2015

Application of spectroscopy and super-resolution microscopy: excited state dynamics of relevant fluorescent dyes and nano-materials, characterization of solar cell materials and diagnosis of neuro-degenerative disease

Ujjal Bhattacharjee
Iowa State University

Recommended Citation

www.manaraa.com

Application of spectroscopy and super-resolution microscopy: Excited state dynamics of relevant fluorescent dyes and nano-materials, characterization of solar cell materials and diagnosis of neuro-degenerative disease

by

Ujjal Bhattacharjee

A dissertation submitted to the graduate faculty

in partial fulfillment of the requirements for the degree of

DOCTOR OF PHILOSOPHY

Major: Physical Chemistry

Program of Study Committee:
Jacob W. Petrich, Major Professor
Xueyu Song
Mark S. Hargrove
Emily A. Smith
Edward Yu

Iowa State University

Ames, Iowa

2015

Dedicated to my parents and wife

TABLE OF CONTENTS

ACKNOWLEDGEMENT

I would have never been able to finish my dissertation without support from my adviser, collaborators, my parents and wife. Collaboration of a great number people contributed immensely in the work discussed in this thesis. It is my great pleasure to take this opportunity to express my gratitude to all of them irrespective of if their name is mentioned or not.

First and foremost, my heartfelt gratitude goes to my thesis adviser Prof. Jacob W. Petrich. I really do not have a proper word to say "Thanks." He is the person who stood by me and assisted throughout this journey. I am grateful for his critical comments after going over this thesis thoroughly. His expertise in optical spectroscopy has taught me so many things and helped to improve my skills preparing me for future endeavors.

Besides my adviser, I express my humble gratitude to of my graduate committee, Dr. Emily A. Smith, Dr. Xueyo Song, Dr. Mark S. Hargrove, and Dr. Edward Yu for their helpful comments and suggestions throughout the years. I express my special thanks to Dr. Emily Smith and her group members, Dr. Michael Lesoine, Aleem Sayed, Daniel Freppon, Jonathan Bobbit, and Deyny Mendivelso for their support in many of my works what would have not been possible without their valuable suggestions and contribution. It was a good experience to work with Michael and Aleem on some of the STED projects. I appreciate the contribution of Daniel Freppon and Jonthan Bobbit in the projects addressing solar cell materials.

I am taking this opportunity to express my humble thanks to Dr. Javier Vela and his group members, especially, Long Men, Dr. Feng Zhu, Yijun Guo, Sam Alvarado, and Pat Dilsaver. I am indebted to them for synthesizing many of the important materials that I have worked with. I highly

encouragement and thoughtful guidance to choose the spectroscopy field as my future pursuit. I am happy to acknowledge my debt to Dr. Rathindra N. Ghosh, who truly inspired me and helped me to stay motivated throughout my difficult times. I am thankful to Dr. Sudipta Modak, who truly introduced the beauty in the field of chemical sciences in my school days.

I enjoyed the years I stayed in Ames owing to many friends I had. I am grateful to my previous roommates and friends, Debasis Mandal, Upamanyu Ray, and Harish Subramani for sharing unforgettable moments with me. I want to express my gratitude to Dr. Sugam Sharma and Hritu Sandilya, not only for their friendship, but also for being great source of support. I am grateful to my friends in Ames, Dr. Debabrata Mukherjee, Payel Mukherjee, Dr. Chiranjit Choudhury, Dr. Sancharini Das, Arindam Roy, Pratik Chatterjee and others for their wonderful company.

I am so grateful and so lucky to have loving and encouraging parents like my parents. My mom and Dad are my sources of strength. My wife, Sudipta, has been always by my side during ups and downs throughout this journey. I am indebted to her for all the sacrifices she has made for me and unconditional support. The word "Thank you" means nothing that I can use to express my gratitude towards them.

CHAPTER 1. INTRODUCTION

General Introduction

Photophysics of inorganic materials and organic molecules in complex systems have been extensively studied with absorption and emission spectroscopy.[1-4] Steady-state and time-resolved fluorescence studies are commonly carried out to characterize excited-state properties of fluorophores. Although steady-state fluorescence measurements are widely used for analytical applications, time-resolved fluorescence measurements provide more detailed information about excited-state properties and the environment in the vicinity of the fluorophore. Many photophysical processes, such as photoinduced electron transfer (PET), rotational reorientation, solvent relaxation, and energy transfer, occur on a nanosecond (10^{-9} s) timescale, thus affecting the lifetime of the fluorophores. Moreover, time-resolved microscopy methods, such as lifetime-imaging, combine the benefits of the microscopic measurement and information-rich, time-resolved data. Thus, time-resolved fluorescence spectroscopy combined with microscopy can be used to quantify these processes and to obtain a deeper understanding of the chemical surroundings of the fluorophore in a small area under investigation. This thesis discusses various photophysical and super-resolution microscopic studies of organic and inorganic materials, which have been outlined below.

Thesis Organization

Chapter 1. As several chapters of this thesis are manuscripts that have been published, submitted for publication, or in the final stages of redaction, and hence present background material from a specialist's point of view, this chapter briefly provides additional important background information on the systems and topics covered: atto-dyes; CdSe-CdS giant quantum

dots; room-temperature ionic liquids; lipid bilayers; bovine spongiform encephalopathy; lipofuscin; poly-3-hexylthiophene; lead-halide perovskites.

Chapter 2 discusses basic principles of fluorescence spectroscopy and microscopy techniques that are used, along with methods of analysis of the experimental data.

Chapter 3 describes the interaction of ATTO dyes with tryptophan and Au-CdS nano composites.

Chapter 4 presents the use of stimulated emission depletion (STED) microscopy for the study of CdSe-CdS giant quantum dots. A brief discussion about the combination of STED microscopy and fluorescence correlation spectroscopy (FCS) to study room-temperature ionic liquids is also presented.

Chapter 5 demonstrates the utility of fluorescence scans of the retina for the diagnosis of bovine spongiform encephalopathies (BSE).

Chapter 6 describes the use of steady-state, time- and polarization-resolved fluorescence techniques to characterize materials of interest for photovoltaic devices. Two important systems are considered: poly (3-hexylthiophene) (P3HT) and lead halide perovskites.

Background Information on Topics Covered

ATTO-dyes

ATTO dyes are typically derivatives of coumarins, rhodamines, carbopyronins and oxazines. For example, the structures of ATTO 590 (a rhodamine derivative) and ATTO 655 (an oxazine derivative) are given in **Figure 1**. ATTO dyes have been designed to absorb over a broad spectral range, currently 390 nm to 740 nm (λ_{max} of absorption spectra). This is an important feature of these dyes for their use in stimulated emission depletion (STED) microscopy. For STED, a dye should meet at least the following criteria: it should have a high absorbance at the wavelength of the excitation beam but none at the wavelength of the STED beam (*i.e.*, the

depletion beam); the wavelength of the STED beam must be contained in the emission spectrum in order to induce stimulated depletion of emission; the dye must have a high fluorescence quantum yield and be photostable. The ATTO dyes are known for their high extinction coefficients and fluorescence quantum yields. For example, ATTO 590 has a fluorescence quantum quantum yield of 0.8. This enables their use in single-molecule detection applications and high-resolution microscopies, such as photoactivated localization microscopy (PALM), stochastic optical reconstruction microscopy (STORM), and STED. The ATTO dyes are very
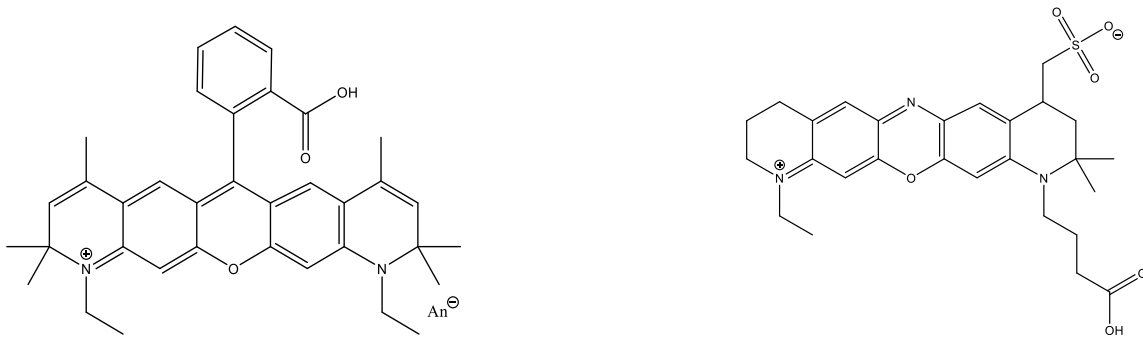
Figure 1. Structure of ATTO 590 (left) and ATTO 655 (right).

photostable under prolonged irradiation, unlike many common fluorescent labels, *e.g.* fluorescein. The less photostable fluorescent dyes pose a serious limitations for high-resolution microscopies. To obtain an acceptable signal-to-noise ratio, it is often necessary to use high excitation intensities and long exposure times.

In addition to imaging applications, the ATTO dyes have been used widely for fluorescence resonance energy transfer (FRET)[5-9] and fluorescence correlation spectroscopy.[10-12] The fluorescence of many red-absorbing ATTO dyes is quenched by electron donors (*e.g.*, tryptophan or guanine) or by nanomaterials *via* photoinduced electron transfer.[13] By taking advantage of this quenching behavior, ATTO 655 has been used to probe biochemical processes in oligonucleotides or polypeptides. The charge separation and the charge recombination rate between ATTO 655 and

tryptophan are 4.0×10^{11} and 5.0×10^{12} s^{-1}, respectively.[14] ATTO 590 forms two types of charge transfer complexes with tryptophan, where charge transfer occurs completely, and an intermediate charge transfer complex, where charge transfer is less efficient. Formation of an exciplex between tryptophan and ATTO 590 has also been observed in ATTO-tryptophan conjugate which quenches the ~350 nm fluorescence of tryptophan.[15]

Gold-cadmium Sulfide Heterostructures

Hybrid nanoparticles[16-21] are important because of their applicability in many technologically important areas such as energy conversion[22] and catalysis.[23, 24] Au-CdS is known to act as a photocatalyst for chemical reactions, most importantly for photochemical hydrogen production.[25-30] The tunable absorption of the solar light and the very fast (sub-20 fs) charge transfer from the semiconductor to the metal made metal-semiconductor hybrids very exciting.[31] The optical properties of the semiconductors can be taiolored by changing material, shape, size etc. It has been reported, furthermore, that excitation of plasmons in metal nanostructures can induce the transfer of hot electrons into the semiconductors, which makes them an interesting candidates for light harvesting materials owing to tunability of their absorption.[32-39] Direct contact between the metal and the semiconductor in the semiconductor-metal monohybrids facilitates the electron injection from metal to semiconductor because the electron transfer rate can overcome the rate of the electron-electron scattering (~hundreds of fs).[40] Furthermore, a selective excitation of either the semiconductor or the metal domain is possible as depicted in **Figure 2** because the energy associated with the excitonic transition of CdS nanoparticles is much different from that of the surface plasmonic resonance (SPR) in Au.[41] Furthermore, the use of NPs as donors and acceptors for FRET applications is also becoming increasingly common.[42-48] ATTO dyes are also known to be efficient candidates for FRET with CdSe/ZnS dots.[49] Thus, all other possible interaction with the nanoparticles between the dyes and the nanoparticles should be examined.

Fang and co-workers have studied the effectiveness of Au-CdS nano heterostructures in the photocatalysis reaction to convert amplex red to resorufin in presence of H_2O_2.[24] Alternatively, one can study the effectiveness as catalyst by the studying quenching of fluorophores by electron transfer where the only difference is that the electron transfer takes place in excited state of the fluorophore. In chapter 3b, we studied the inter-molecular quenching of fluorecence of different ATTO dyes by Au-CdS nanohybrids using selective excitation of Au or CdS portion of the nano structure and critically examined the proposed mechanism existing in the field of research with these heterostructures.
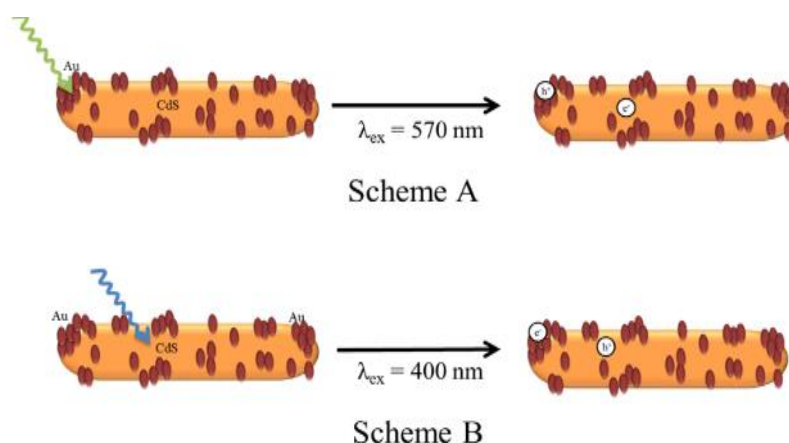
Figure 2. Schematic diagram of Au-CdS nano composite particle. With λex = 570 nm, a charge separation takes place where the electron resides in CdS and the hole remains in Au domain (Scheme A). When excited at 400 nm, both the CdS and gold particles are excited (Scheme B).

CdSe-CdS Giant Quantum Dots

CdSe semiconductor nanocrystals (NCs) have a high quantum efficiency (QE), a size-tunable energy gap, and high photostability at room temperatures. They are used for a wide range of applications such as optoelectronics,[50] biological labelling,[51] and quantum cryptography.[52] The biggest problem that the CdSe colloidal NCs face is intermittent fluorescence at the single-particle level. Their fluorescence intensity is characterized by an interplay between bright and dark

states.[53] The dark periods are reported to follow Lévy statistics.[54] As a consequence, ''off'' events dominate the fluorescence signal as they are of the order of the observation time.[55] In the imaging application of these NCs, specifically in STED microscopy where high laser powers or long acquisition times are often needed, these long-lived dark events present the primary restriction for the use of colloidal NCs. The fluorescence "blinking" is a consequence of Auger recombination, where the energy of one electron-hole pair (exciton) is nonradiatively transferred to another charge carrier.[50] Auger recombination also is known to prevent efficient stimulated emission of isolated NQDs.[56] The rate of Auger recombination is directly dependent on the strength of carrier-carrier Coulomb coupling and the extent of spatial overlap between the electron and hole wave functions involved in the Auger transition.[57-59] Several attempts have been made
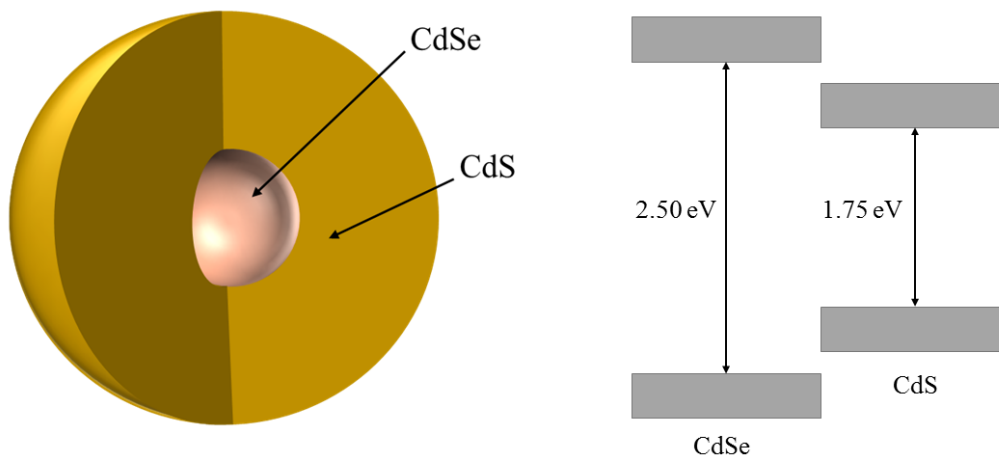
Figure 3. A schematic diagram of CdSe-CdS giant quantum dots (left). The band energies (right) suggest upon photoexcitation electrons in CdSe can move to CdS shell leading to delocalization of electrons to CdS shell.

to reduce Auger recombination by addressing the two factors. Based on the first factor, elongated NCs has been used[60] and organic molecules acting as charge compensators[61] or charge mediators

at the NC surface, separating electrons and holes between the core and the shell regions of core-shell heterostructured NCs that exhibit so-called type-II or quasi-type-II localization regimes,[62, 63] has been utilized. On the otherhand, by considering second factor, a "smooth" confining potential resulting from a graded composition of the NC interfacial layer, has been formed.[64] Giant NQDs (g-NQDs) with 10−20 monolayers of CdS (shell) and 2−5 nm CdSe core, exhibit suppression of luminescence intermittency and effective suppression of Auger recombination.[65-68] The suppression of Auger recombination increases emission efficiencies and the lifetimes of biexcitons, or even multiexcitons of a very high order (13th and possibly higher), and contribute to optical gain. Radiative lifetime components of multiexcitons in gNQDs were observed at 4 K.[69] As an added benefit for STED application, multiexcitons can undergo more effective stimulated emission because of lower threshold for stimulated emission of the multiexcitons than biexcitons and, indeed, many dye molecules.[67] Only a few reports are available on application of STED microscopy on quantum dots.[70] The improved spatial resolution, though, was a result of stimulated absorption to higher energy excited states in the Mn doped ZnSe NQDs rather than stimulated depletion.[70]

In Chapter 4a, we discuss luminescence depletion (LD) imaging using CdSe/14CdS g-NQDs with a lateral spatial resolution of 40 ± 10 nm.[71] It is proposed that stimulated emission and excited-state absorption mechanisms may work either independently or synergistically to provide depletion. A 7-fold improvement over the diffraction barrier was generated at an air interface.

Room Temperature Ionic Liquids (RTIL)

Room temperature ionic liquids (RTILs) form a very important class of solvents owing to their low vapor pressure, high thermal stability, and their interesting catalytic activities. Many,

but all, can be used as "green solvents." They have attracted interest for their ability to help break down cellulose to glucose,[72] which is important for green fuel industry to make ethanol. Ionic liquids can be engineered by the proper choice of cations and anions to tune their properties and make them suitable for many applications and fundamental studies. They are thus referred to as "designer solvents."

Despite their growing use, their structural properties have not yet been fully deciphered. Some experimental and theoretical studies suggest that they are much more structured compared to conventional solvents. This heterogeneity mainly arises as the organic cationic part segregates in small domains over a spatial scale of a few nanometers. The spatially heterogeneous structure has been predicted by molecular dynamics (MD) studies from different groups.[73-78] The first experimental characterization of these nanodomains comes from X-ray diffraction measurements, the presence of low-Q peak in the scattering is consistent with a correlation length at one or two times the long axis of the cation, which predicted the scale of the heterogeneous domains (1.3 -2.7 nm) and their thermal behavior for immidazolium ionic liquids.[79-85] However, some of the conclusions have been questioned by recent neutron scattering experiments and theoretical studies.[86, 87] By small angle neutron scattering experiment it was found that the peak occurs at longer length scale than what was predicted by the previously MD simulation studies of ionic liquids, and that the magnitude of the scattering from this peak is comparable with that from the remainder of the amorphous ionic liquids, suggesting that the peak comes from the second coordination shells of the ions along the vector of alkyl-chain substituents as the anisotropy of the cation increases, and that there is little or no long-range correlated nanostructure in these ionic liquids.[87]

Lipid Bilayers

The lipid bilayer is the basis for the structure that forms the foundation for cellmembrane. Although the lipid bilayers can be observed under electron microscopy, specialized techniques, such as x-ray diffraction and freeze-fracture electron microscopy, are often needed to reveal the details of its organization. The lipid, that is, fatty molecules are the primary constituent of lipid bilayers. They are amphiphilic. They have a hydrophilic head-group and a hydrophobic fatty acid tail. The most common membrane lipids are the phospholipids. A schematic diagram of phospholipids is given in **Figure 4**. The length and saturation of the fatty acid tails are usually different which gives them the ability to pack against one another, thus, affecting the fluidity. Phospholipid vesicles can self-assemble into fluid planar bilayers on solid supports as depicted in **Figure 4**.[88-90] There are several reports which suggest that between the support and the headgroups of the lower leaflet of the bilayer a thin water layer (1-2 nm) is trapped which acts as a lubricant allowing the bilayer to remain fluid.[91-94] As a result, planar supported membranes retain most of the properties of free vesicles or even cell membranes when the appropriate surface components are present. Various methods, such as electron spin resonance (ESR) spectroscopy, have been used to measure the motion of individual lipid molecules and their different parts. It has been established that phospholipid molecules in synthetic bilayers very rarely migrate from one leaflet to the other (flip-flop). On the contrary, lipid molecule readily exchange places with their neighbors within a monolayer. This gives rise to rapid lateral diffusion, with a diffusion coefficient of about 10^{-8} -10^{-9} cm²/sec, which also varies based on the supporting material. The fluidity of a lipid bilayer depends on the composition of the bilayer and temperature. A synthetic bilayer made from a single type of phospholipid changes from a liquid state to a two-dimensional rigid crystalline (or gel) state at a characteristic freezing point. This change of state is called a phase transition, and the temperature at which it occurs is lower (that is, the mmembrane becomes more
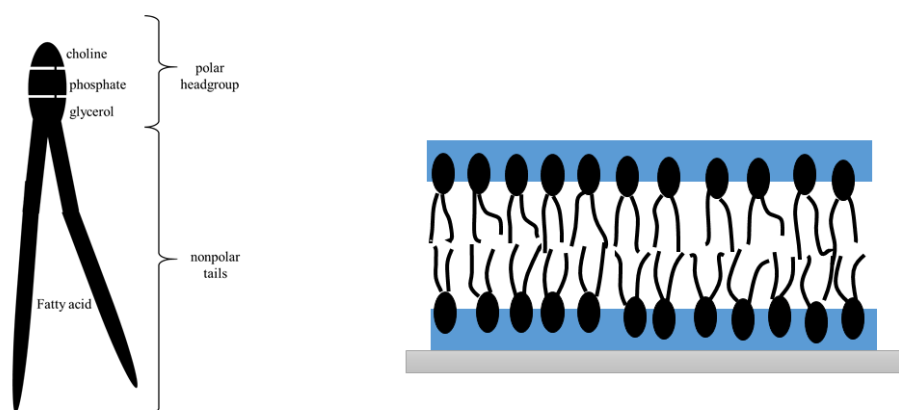
Figure 4. A schematic diagram for lipids; it shows the polar headgroup and nornpolar fatty acid tails (left). A schematic illustrating lipid bilayer (right); it shows the water trapped between lower leaflet and the substrate which contributes towards the mobility of the lipid molecules.

difficult to freeze) if the hydrocarbon chains are short or have double bonds. In chapter 4b, we discuss STED-FCS experiments on POPC membrane. We propose that this can serve as an easy and effective method to identify nanoscale heterogeneity.

Bovine Spongiform Encephalopathy (BSE)

Transmissible spongiform encephalopathies (TSE) are progressive, neurodegenerative disorders that impact the central nervous system (CNS).[95-98] The most general characteristic of these diseases is the generation of sponge-like texture in brain, the others being, neuronal loss, astrocytosis and amyloid plaque formation.[99, 100] These diseases can transmit from one animal to another by prion (proteinacious infectious particle). Prion protein (PrP) are abnormally shaped protein lacking nucleic acid. The biochemical indication of prion diseases is the presence of abnormal metabolism and accumulation of prion protein, where PrP transforms into PrPsc. PrPsc is not soluble in detergent and is partially resistant to protease.[101] Prion protein (PrP) exists in two forms, normal (PrPc) and its pathological isoform which is protease resistant (PrPres).[99, 101] The conversion of PrP to PrPsc happens by conformation change where the alpha-helical content goes

down and simultaneous increase in beta sheet contents.[101] Due to the conformational change, tyrosin moieties become more accessible to solvent. Tyr-Tyr-Arg motif in misfolded prion protein can be selectively used to detect distribution of the PrPsc, and may show path to new diagnosis and therapeutic cures.[102] There have been few reports where antibodies (phosphatidylinositol-specific phospholipase C (PIPLC) or the monoclonal anti-prion protein (PrP) antibody 6H4[103] or antigen-binding fragments (Fabs))[104] directed predominantly against PrPC can reduce production or destroy pre-existing PrPSc in scrapie-infected cell in vitro and can inhibit the propagation of scrapie in transgenic mice in vivo.[105] Most abundant expression of PrPc is seen in the CNS tissue of mammals. It is believed that interaction between PrPres with PrPc enhances a shape change in the protein itself.[99] The structural malformation of this protein changes its function and thus, results in cell damage. Though there are several representatives of TSE diseases, bovine spongiform encephalopathy (BSE) or more commonly known, "mad cow" is the most fatal transmissible neurodegenerative disease. In 1987, the first case of BSE was reported by Wells *et al.*[106] Few years later, in 1994, the first case of Creutzfeldt-Jakob disease (CJD) were found and they were labeled new variant (v) in Britan.[107] Numerous PrP amyloid plaques surrounded by a halo of intense spongiform degeneration was observed in their brain. Subsequently several cases have been reported in USA, Australia or Japan. BSE is believed to be related to the variant (vCJD) in humans. Human vCJD patients had the same kind of prion protein gene mutation as found in an atypical form of bovine spongiform encephalopathy.[108] Incubation time was found to be similar for BSE and vCJD in non_Tg RIII mice.[109] With the increasing use of immunological tests, variant features of pathological and molecular signatures of cattle BSE were reported,[110-115] colloquially referred as "*atypical BSE*."[116] These unusual BSEs can be categorized in two groups based on the

relative molecular mass (Mm) of the unglycosylated PrP^{res} band with respect to that of classicasl BSE (C-type). One that has higher Mm is called H-type, the other being L-type, with lower Mm.[117]

The new variant Creutzfeldt-Jakob disease (vCJD) is believed to be transmitted from cattle through consumption of infected tissue. BSE is infectious but not contagious because it is not excreted. Ruminant brain and spinal cord is reported to contain highest infectivity of prion protein.[118, 119] BSE may be transmitted through contact with infected tissue, body fluids, or contaminated medical instruments. The oral route of infection is, however, the most probable path for BSE transmission to humans.[120-122] The prohibition of specified risk material (SRM; in cattle it includes: brain, eyes (retina), trigeminal ganglia, the spinal cord, the dorsal root ganglia, mesentery, intestines and tonsils.) in human food supply is considered to be very critical.[118] Among the other representatives of TSE, scrapie is the most widespread affecting sheep and goats. It is characterized by a gradual onset. The typical disease characteristics, including unthriftiness, compulsive itching, balance and ambulatory abnormalities, convulsions, and eventual death, however, are seen in advanced cases. At present, there is BSE and the most common form of control is quarantine, euthanasia, and proper disposal of the carcass.

Lipofuscin. Lipofuscin is a yellow-brown pigment that undergoes age-related progressive accumulation mainly in postmiotic cells, such as neurons, cardiac muscle and retinal epithelium.[123-129] Lipofuscin is granular, heterogeneous, high-molecular weight complex aggregate of intracellular material. The biochemistry, mechanism of formation, fluorescence emission and composition of lipofuscin are still a matter of debate in spite of extensive studies. Usually the formation of lipofuscin is associated with the cross linking of carbonyl-amino compound,[124] though it can be produced from different types of biological materials as a product of various side reactions of essential biological processes. The most interesting characteristics of

lipofuscin is its yellowish-orange autofluorescence under UV or blue light which leads to its easy detection.

As a result spontaneous and experimentally induced Creutzfeldt-Jakob's disease (CJD) amount of fluorescent lipofuscin increases in CNS tissues. Boellaard *et al*. have indiacted relationship between lipofuscin production, a decline in autophagocytosis activity, and the experimental induction of CJD in mice.[130] In addition, there are several reports in literature demonstrating link between neurological disease produced by TSEs to eye damage and subsequent accumulation of lipofuscin.[130-138]

Owing to the presence of fluorescence of lipofuscin, autofluorescence from different types of tissue can be differentiated by fluorescence spectroscopy. The introduction of specified risk materials (SRM), during the meat processing has become a concern because of bovine spongiform encephalopathy (BSE). Thus, developing technology for monitoring CNS tissue in meat and other food products as well as for diagnosing animals for TSEs will be increasingly important in securing the safety of the world's food supply. In chapter 5, we examined the use of fluorescence spectral scan to identify BSE. Our data demonstrates that the fluorescence spectra from BSE-positive retinas are more intense compared to the BSE-negative retinas. We propose the finding can be utilized for noninvasive examination of some neurological disease, such as BSE.

Poly (3-hexylthiophene) (P3HT)

Π-conjugated polymers were discovered in 1967 by Alan J. Heeger, Alan MacDiarmid, and Hideki Shirakawa.[139, 140] Ever since, these materials have garnered tremendous interest by research communities, mainly due to electrical and optical properties similar to metals or semiconductors. They also retain the useful mechanical properties of polymers, such as flexibility, ductility, and processing advantages. The semiconducting properties of organic photovoltaics

(OPV) stem from electron delocalization along the conjugated backbone.[141] Electrical conductivity over a broad range, from insulator- to metal-like, can be tuned by reversible "doping" of the
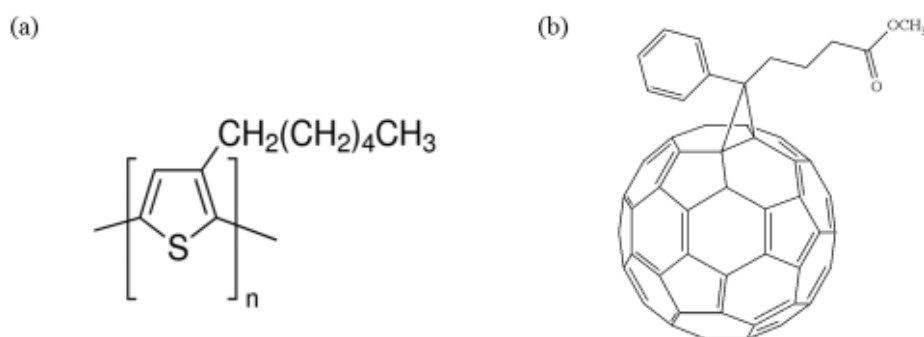
Figure 5. Structure of P3HT (a) and PCBM (b).

conjugated polymers. As every unit in the polymer can be oxidized or reduced, the conducting polymers can be doped as *n*-type (reduced) or as *p*-type (oxidized) to sufficient high density of charge carriers.[142] Among the *n*-type semiconductor polymers, P3HT (poly (3-hexylthiophene)) (**Figure 5**) has been studied the most extensively. After the discovery of photoinduced electron transfer (PET) in the composites of conducting polymers and buckminsterfullerene, C_{60}, and its derivatives (*e.g.*, , PCBM (Phenyl-C61-butyric acid methyl ester) (**Figure 5**)) in 1992,[143, 144] there has been a surge of interest in P3HT/PCBM for their use in solar cells. The efficiency of P3HT/ PCBM solar cells typically lies in the range of 4-6%,[145-149] and it is believed that it can be raised to as high as 9%.[150] The first factor affecting the efficiency of operation is the photoexcitaion of the polymers. This depends on the overlap of the absorption spectrum of the polymers and spectrum of solar radiation, as well as the exctinction coefficient of the polymers. Polymer/C_{60} composites have a wider band gap than semiconductors with absorption of UV radiation. The band gap of the blend is approximately 2 eV.[151] This bandgap can be further
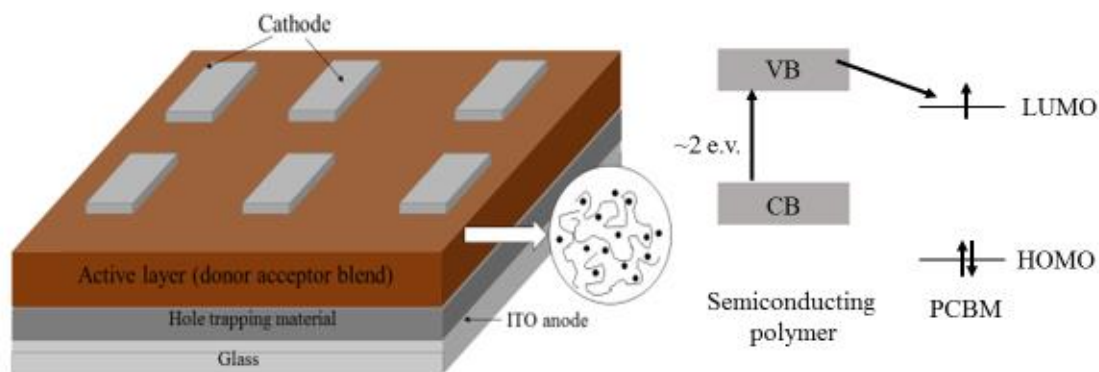
Figure 7. On left, figure shows a typical OPV device, where the active layer is composed of P3HT/ PCBM. On right, conduction (CB) and valance band (VB) energy levels of conducting polymer are presented with respect the HOMO and LUMO energy levels of PCBM. The energy levels shows upon photoexcitation electrons in VB can favorably transferred to PCBM, whereas holes can move in the opposite direction.

tuned without changing the components. For example, it has been reported that a Head-Tail alignment of P3HT has a narrower band gap than a Head-Head alignment,[151] and that the bandgap can be tuned by varying the proportion of PCBM. The second factor influencing the efficiency is the generation of photocarriers and their transfer to the heterojunctions. There have been multiple studies of the charge transfer process between conducting polymers and C_{60}.[152-154] They reported that the charge transfer occurs on a time scale of 50 fs after excitation. The lifetimes of the polymers (>100 ps) suggests the possibility of approaching an efficiency of charge transfer close to unity.[155] Excitation acts as "photodoping." The exciton-diffusion length in P3HT polymers is small (3-8.9 nm),[156] whereas the charge-transfer radius is large (4.8-9 nm).[156] Swift delocalization of excitons in P3HT domains, thus, play an important role to transport charge carriers to the interfaces in addition to diffusion.[157]

There are two important factors involved in exciton separation. One is the binding energy and the other is the internal field in the vicinity of junctions. In organic polymers, dielectric constants are small. This shifts the absorption spectrum to longer wavelength and enhances the difficulties involved in separating excitons. On the other hand, the buildup of electrical potential at the heterojunctions is the result of the thermal equilibrium of the contacted materials. Two materials with different work functions in contact results in electron flow from the one with lower work function to the other, until the Fermi surfaces match. The exciton transport efficiency depends very sensitively upon the nanoscale morphology of the active layer, as disorder existing in the matrix limits the carrier mobility.[158] A more organized morphology, where all P3HT polymer chains align parallel and PCBM adopts a nanocrystal structure, the efficiency of the device increases.[159] In many solution-processed conjugated polymers, self-organization generates complex microstructures in which ordered microcrystalline domains are embedded in an amorphous matrix.[160] Because the most difficult hopping processes (determined by a disordered matrix) limit the charge transport, charge carrier mobility is usually low ($<10\text{-}5$ cm^2 V^{-1} s^{-1}).[161] Sirringhaus *et al*. have shown that self-organization in P3HT results in a lamellar structure with two-dimensional conjugated sheets formed by interchain stacking. The lamellae can be oriented both parallel or normal to the substrate, depending on the processing conditions. The carrier mobility along the two orientations differs by more than a factor of 100, and can reach values as high as 0.1 cm^2 V^{-1} s^{-1}.[162] The morphology of the materials affects electronic structure. A simple Franck-Condon progression is insufficient to fit the absorption and emission spectra of the polymer. The existence of weakly interacting H-aggregate states has been proposed by Spano,[163, 164] and he has proposed a model that describes photophysics of regio-regular P3HT fairly well.[165] In addition, there has been evidence for *J*-aggregate structures, predominantly in P3HT polymers

with higher molecular weight.[166, 167] The two types of aggregates can be identified from the relative intensities of vibronic transitions. Owing to all possible microstructured domains and heterogeneities, the direct and quantitative correlation between their morphology and optoelectronic properties that is desired for engineering of OPV devices is complicated.[168-170] In chapter 6a, use of steady-state and time-resolved fluorescence anisotropy has been used as a tool for characterization of orientations of molecular units in P3HT-based materials.

Lead Halide Perovskites

Organic and inorganic hybrid perovskite solar cells have undergone a rapid evolution of efficiencies from less than 4% in 2009,[171] to a confirmed 16.2%, and then to unconfirmed values as high as 19.3% in 2013.[172] Although the initial use of $CH_3NH_3PI_3$ as a replacement for dyes in dye-sensitized solar cells failed to generate interest because of lower efficiency and instability,[173] solid-state perovskite cells have become a highly active field of research. Perovskites have an ABX_3 structure. Their optical and electronic properties can be tuned by changing A, B, or X. Probably, the most attractive feature of the materials is the possibility of low-cost solution processing for the production of high-performance devices. There are three types of perovskite film architectures in solar cells: mesoporous, planer, and mesoporous/planer hybrid (**Figure 7**).[174] In mesoporous cells, perovskites are incorporated in a mesoporous layer of metal oxide. The morphology of the perovskite is not as important as its ability but to absorb light sufficiently, which requires that the mesoporous layers need to be at least 500 nm thick.[175] On the other hand, in the planer heterojunction architecture, a perovskite layer is deposited with a sandwich configuration (similar to an organic photovoltaic configuration). In this type of cell the morphology of the perovskite layer is very critical because the carriers need to transfer through the layer itself. Thus,

the thickness of the perovskite layer is usually less than 400 nm. One of the main problems in this type of solar cell is current-voltage (IV) hysteresis.[176] To overcome the shortcomings of these two
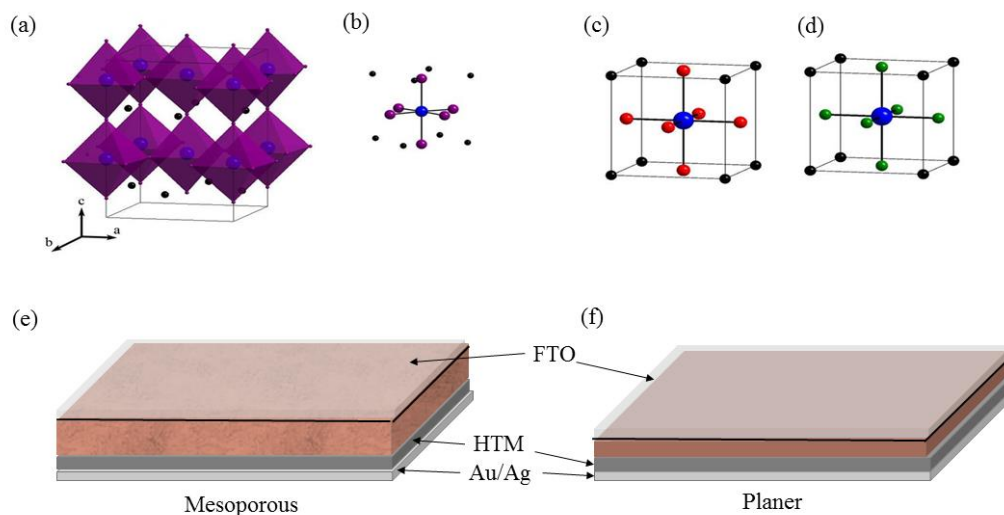
Figure 8. a) crystal structure of $CH_3NH_3PbI_3$, b) shows the coordination of lead center, c) crystal structure of $CH_3NH_3PbBr_3$, d) crystal structure of $CH_3NH_3PbCl_3$, e) Illustrative picture of mesoporous, and f) planer architecture of perovskite solar cells. HTM ─ hole transporting material.

architectures, a third type of architecture has evolved, which has demonstrated high efficiency of the solar cells along with negligible I-V hysteresis. Nevertheless, broadly speaking, the performance of perovskite solar cells depends critically on perovskite composition, crystallinity, and morphology.[175, 177, 178] Similar to organic-polymer-based solar cells, perovskite film uniformity is very important in planar heterojuction solar cells.[179, 180] Film uniformity can be controlled by changing precursor composition, annealing temperature, or using different solvents.[181, 182] Traditionally, solar devices prepared by vapor deposition show higher efficiency than those prepared with solution-processed thin films owing to incomplete, uneven coverage of the perovskite films.[181, 183, 184] Although, some of the best perovskite solar cells prepared to date use a mesoscopic architecture, standard methods for preparation of more controlled and favorable

morphology are not yet available.[185] The use of nanosized perovskites in efficient photoactive layer is possible because of long exciton diffusion lengths. In chapter 6b, we discuss photophysical studies on $CH_3NH_3PbI_3$ and $CH_3NH_3PbBr_3$ nanocrystals with different shapes (dot, rod, and plate or sheet morphologies), both on the single-molecule level and in bulk solution. We showed that dot-, wire-, and sheet-shaped nanocrystals of $CH_3NH_3PbI_3$ display more stable photoluminescence and longer lifetimes (slower charge recombination).

Photovoltaic device performance also improves in the absence of perovskite bulk defects and surface trap states.[176, 186, 187] An explanation of the high open circuit voltage (V_{OC}) can be drawn from a calculation, which shows that despite a large bandgap of 2.2 eV, the dominant defects in $CH_3NH_3PbBr_3$ create only shallow energy levels, indicating a low bulk non-radiative recombination rate.[188] There have been several reports in the literature indicating the presence of trap sates.[171, 189-192] The presence of sub gap states influences the photo-conductivity response in perovskite films. While the planar perovskite films are better in charge carrier mobility, they suffer from limited photovoltage by the sub gap states and low intrinsic doping densities. Temperature dependent shifts in absorption and PL spectra and has been attributed to phase states at different temperatures.[193] In Chapter 6b, we discuseed the PL shift with the aging of perovskite solution. Our data indicated the presence of an extra PL band in freshly prepared samples. The band reappears under laser illumination. We initially postulated two reasons for the appearance of the extra *unwanted* peak at bluer wavelength: one is that under illumination, different crystals are forming; the other, that it arises from a defect. The first option was ruled out based on our *in situ* XRD experiment with laser illumination. Based on spectroscopic results, we changed the synthesic method to obtain defect-free material, which is of prime interest for efficient photovoltaics.

We also studied mixed-halide perovskites, $CH_3NH_3PbBr_{3-x}I_x$ and $CH_3NH_3PbBr_{3-x}Cl_x$, which have tunable optical properties. Although, mixed-halide perovskite films are expected to show a single band at an intermediate wavelength with respect to the corresponding monohalide perovskites, there is a report showing two PL bands in fresh films, though they merge to a single PL band after 21 days.[194] Br-doping enhances the moisture-stability of solar cell devices.[195] In $CH_3NH_3PbBr_{3-x}Cl_x$, the large binding energy of excitons can result in exciton absorption and free-exciton emission.[196] The insertion of both Cl and Br in the perovskite lattice reduces the charge recombination rates in the light absorber film, thus determining Voc of the device. Furthermore, the addition of Br in the perovskite structure can slightly improve the lifetime of the devices. To date, there are only a few reports of studies of these mixed halide perovskites.[197-200] We also studied the phtostability of perovskite materials.

References

1. Valeur, B., *Molecular fluorescence: principles and applications*. Wiley-VCH: Weinheim, 2002.

2. Birks, J. B., *Photophysics of Aromatic Molecules*. Wiley-Interscience: London, 1970.

3. Fleming, G. R., *Chemical Applications of Ultrafast Spectroscopy*. Oxford University Press: London, 1986.

4. Lakowicz, J. R., *Principles of fluorescence spectroscopy*. 3rd ed.; Springer: New York, 2004.

5. Rüttinger, S.; Kapusta, P., *et al*. *J. Fluoresc*. **2010**, *20*, 105.

6. Halivni, S.; Sitt, A., *et al*. *ACS Nano* **2012**, *6*, 2758.

7. Sitt, A.; Even-Dar, N. *J. Phys. Chem. C* **2013**, *117*, 22186.

8. Eggeling, C.; Widengren, J.; Brand, L.; Schaffer, J., *et al*. *J. Phys. Chem. A* **2006**, *110*, 2979.

9.   Bruno, J. G.; Zuninga, M. A., *et al*. *Comb*. *Chem*. *High Throughput Screen*. **2011**, *14*, 622.

10.   Miller, A. E.; Fischer, A. J.; Laurence, T. *PNAS* **2006**, *103*, 11136.

11.   Dertinger, T.; Gregor, I.; von der Hocht, I.; Erdmann, R.; Krämer, B.; Koberling, F. *Proc*. *SPIE* **2006**, *6092*, 609203.

12.   Dertinger, T.; Pacheco, V.; von der Hocht, I.; Hartmann, R., *et al*. *ChemPhysChem* **2007**, *8*, 433.

13.   Doose, S.; Neuweiler, H.; Sauer, M. *ChemPhysChem* **2005**, *6*, 2277.

14.   Zhu, R.; Li, X.; Zhao, X. S.; Yu, A. *J*. *Phys*. *Chem*. *B* **2011**, *115*, 5001-5007.

15.   Bhattacharjee, U.; Beck, C.; Winter, A.; Wells, C.; Petrich, J. W. *The Journal of Physical Chemistry B* **2014**, *118*, 8471-8477.

16.   Wu, K.; Zhu, H.; Liu, Z.; Rodríguez-Córdoba, W.; Lian, T. *J*. *Am*. *Chem*. *Soc*. **2012**, *134*, 10337-10340.

17.   Carbone, L.; Cozzoli, P. D. *Nano Today* **2010**, *5*, 449-493.

18.   Costi, R.; Saunders, A. E.; Banin, U. *Angew*. *Chem*. **2010**, *49*, 4878-4879.

19.   Mokari, T.; Sztrum, C. G.; Salant, A.; Rabani, E.; Banin, U. *Nat*. *Mater* **2005**, *4*, 855−863.

20.   Carbone, L.; Jakab, A.; Khalavka, Y.; Soennichsen, C. *Nano Lett*. **2009**, *9*, 3710-3714.

21.   Korobchevskaya, K. G. C.; Manna, L.; Comin, A. *J*. *Phys*. *Chem*. *C* **2012**, *116*, 26924-26928.

22.   Costi, R.; Saunders, A. E.; Elmalem, E.; Salant, A.; Banin, U. *Nano Lett*. **2008**, *8*, 637-641.

23.   Yin, H., *et al*. *Chem*. *Commun*. **2008**, 4357−4359.

24.   Ha, J. W.; Ruberu, T. P. A.; Han, R.; Dong, B.; Vela, J.; Fang, N. *J*. *Am*. *Chem*. *Soc*. **2014**, *136*, 1398−1408.

25.   Fujishima, A.; Honda, K. *Nature* **1972**, *238*, 37.

26.   Gratzel, M. *Nature* **2001**, *414*, 338.

27.   Cho, I. S.; Chen, Z.; Forman, A. J.; Kim, D. R.; Rao, P. M.; Jaramillo, T. F.; Zheng, X. *Nano Lett*. **2011**, *11*, 4978.

28.   Shankar, K.; Basham, J. I.; Allam, N. K.; Varghese, O. K.; Mor, G. K.; Feng, X.; Paulose, M.; Seabold, J. A.; Choi, K.-S.; Grimes, C. A. *J.Phys*. *Chem*. *C* **2009**, *113*, 6327.

29.   Walter, M. G.; Warren, E. L.; McKone, J. R.; Boettcher, S. W.; Mi, Q.; Santori, E. A.; Lewis, N. S. *Chem*. *Rev*. **2010**, *110*, 6446.

30.   Lewis, N. S. *Science* **2007**, *315*, 798.

31.   Mongin, D.; Shaviv, E.; Maioli, P.; Crut, A.; U., B.; Fatti, N. D.; Vallée, F. *ACS Nano 6*, 7034-7043.

32.   Furube, A.; Du, L.; Hara, K.; Katoh, R.; Tachiya, M. *J*. *Am.Chem*. *Soc*. **2007**, *129*, 14852−14853.

33.   Tian, Y.; Tatsuma, T. *J*. *Am*. *Chem*. *Soc*. **2005**, *127*, 7632−7637.

34.   Lee, J.; Mubeen, S.; Ji, X.; Stucky, G. D.; Moskovits, M. *Nano Lett*. **2012**, *12*, 5014−5019.

35.   Chen, H. M.; Chen, C. K.; Chen, C.-J.; Cheng, L.-C.; Wu, P. C.; Cheng, B. H.; Ho, Y. Z.; Tseng, M. L.; Hsu, Y.-Y.; Chan, T.-S.; Lee, J.-F.; Liu, R.-S.; Tsai, D. P. *ACS Nano* **2012**, *6*, 7362−7372.

36.   Mubeen, S.; Hernandez-Sosa, G.; Moses, D.; Lee, J.; Moskovits, M. *Nano Lett*. **2011**, *11*, 5548-5552.

37.   Lee, Y. K.; Jung, C. H.; Park, J.; Seo, H.; Somorjai, G. A.; Park, J. Y. *Nano Lett*. **2011**, *11*, 4251-4255.

38.   Knight, M. W.; Sobhani, H.; Nordlander, P.; Halas, N. J. *Science* **2011**, *332*, 702−704.

39.   Wu, X.; Thrall, E. S.; Liu, H.; Steigerwald, M.; Brus, L. *J. Phys. Chem. C* **2010**, *114*, 12896-12899.

40.   Hodak, J. H.; Martini, I.; Hartland, G. V. *J. Phys. Chem. B* **1998**, *102*, 6958−6967.

41.   Wu, K.; Rodríguez-Córdoba, W. E.; Yang, Y.; Lian, T. *Nano Lett.* **2013**, *13*, 5255-5263.

42.   Halivni, S.; Sitt, A.; Hadar, I.; Banin, U. *ACS Nano* **2012**, *6*, 2758–2765.

43.   Willner, I.; Willner, B. *Nano Lett.* **2010**, *10*, 3805–3815.

44.   Gill, R.; Willner, I.; Shweky, I.; Banin, U. *J. Phys. Chem. B* **2005**, *109*, 23715–23719.

45.   Sandoghdar, V.; Seelig, J.; Leslie, K.; Renn, A.; Kuhn, S.; Jacobsen, V.; van de Corput, M.; Wyman, C. *Nano Lett.* **2007**, *7*, 685–689.

46.   Alivisatos, A. P.; Gu, W. W.; Larabell, C. *Ann. Rev. Biomed. Eng.* **2005**, *7*, 55–76.

47.   Rogach, A. L.; Klar, T. A.; Lupton, J. M.; Meijerink, A.; Feldmann, J. *J. Mater. Chem.* **2009**, *19*, 1208–1221.

48.   Clapp, A. R.; Medintz, I. L.; Mattoussi, H. *ChemPhysChem* **2006**, *7*, 47–57.

49.   Yin, W.-J.; Shi, T.; Yan, Y. *Appl. Phys. Lett.* **2014**, *104*, 063903.

50.   Klimov, V. I.; Mikhailovsky, A. A.; McBranch, D. W.; Leatherdale, C. A.; Bawendi, M. G. *Science* **2000**, *287*, 1011–1013.

51.   Michalet, X., *et al. Science* **2005**, *307*, 538.

52.   Michler, P., *et al. Nature* **2000**, *406*, 968.

53.   Nirmal, M., *et al. Nature* **1996**, *383*, 802.

54.   Kuno, M., *et al. J. Chem. Phys.* **2000**, *112*, 3117.

55.   Brokmann, X., *et al. Phys. Rev. Lett.* **2003**, *90*, 120601.

56.   García-Santamaría, F.; Brovelli, S.; Viswanatha, R.; Hollingsworth, J. A.; Htoon, H.; Crooker, S. A.; Klimov, V. I. *Nano Lett.* **2011**, *11*, 687-693.

57.   Chepic, D. I.; Efros, A. L.; Ekimov, A. I.; Vanov, M. G.; Kharchenko, V. A.; Kudriavtsev, I. A.; Yazeva, T. V. *J. Lumin*. **1990**, *47*, 113-127.

58.   Wang, L. W.; Califano, M.; Zunger, A.; Franceschetti, A. *Phys*. *ReV.Lett*. **2003**, *91*, 056404.

59.   Klimov, V. I.; McGuire, J. A.; Schaller, R. D.; Rupasov, V. I. *Phys*. *Rev*. *B* **2008**, *77*, 195324.

60.   Htoon, H.; Hollingsworth, J. A.; Dickerson, R.; Klimov, V. I. *Phys*. *Rev*. *Lett*. **2003**, *91*, 227401.

61.   Hohng, S.; Ha, T. *J. Am*. *Chem*. *Soc*. **2004**, *126*, 1324

62.   Nanda, J.; Ivanov, S. A.; Htoon, H.; Bezel, I.; Piryatinski, A.; Tretiak, S.; Klimov, V. I., 99, . *J. Appl*. *Phys* **2006**, *99*, 034309.

63.   Nanda, J.; Ivanov, S. A.; Achermann, M.; Bezel, I.; Piryatinski, A.; Klimov, V. I. *J. Phys*. *Chem*. *C* **2007**, *111*, 15382–15390.

64.   Wang, X.; Ren, X.; Kahen, K.; Hahn, M. A.; Rajeswaran, M.; Maccagnano-Zacher, S.; Silcox, J.; Cragg, G. E.; Efros, A. L.; Krauss, T. D. **2009**, *459*, 686–689.

65.   Chen, Y.; Vela, J.; Htoon, H.; Casson, J. L.; Werder, D. J.; Bussian, D. A.; Klimov, V. I.; Hollingsworth, J. A. *J. Am*. *Chem*. *Soc*. **2008**, *130*, 5026−5027.

66.   Vela, J.; Htoon, H.; Chen, Y.; Park, Y.-S.; Ghosh, Y.; Goodwin, P. M.; Werner, J. H.; Wells, N. P.; Casson, J. L.; Hollingsworth, J. A. *J. Biophotonics* **2010**, *3*, 706−717.

67.   García-Santamaría, F.; Chen, Y.; Vela, J.; Schaller, R. D.; Hollingsworth, J. A.; Klimov, V. I. *Nano Lett*. **2009**, *9*, 3482−3488.

68.   Spinicelli, P.; Buil, S.; Quelin, X.; Mahler, B.; Dubertret, B.; Hermier, J. P. *Phys*. *Rev*. *Lett*. **2009**, *102*, 136801.

69. Htoon, H.; Malko, A. V.; Bussian, D.; Vela, J.; Chen, Y.; Hollingsworth, J. A.; Klimov, V. I. *Nano Lett.* **2010**, *10*, 2401−2407.

70. Irvine, S. E.; Staudt, T.; Rittweger, E.; Engelhardt, J.; Hell, S. W. *Angew. Chem.* **2008**, *47*, 2685−2688.

71. Lesoine, M. D.; Bhattacharjee, U.; Guo, Y.; Vela, J.; Petrich, J. W.; Smith, E. A. *The Journal of Physical Chemistry C* **2013**, *117*, 3662- 3667.

72. Bose, S., Armstrong, D.W., Petrich, J.W. *J. Phys. Chem. B* **2010**, *114*, 8221-8227.

73. Wang, Y.; Voth, G. A. *J. Phys. Chem. B.* **2006**, *110*, 18601-18608.

74. Hu, Z.; Margulis, C. J. *Proc. Natl. Acad. Sci. U. S. A.* **2006**, *103*, 831-836.

75. Lopes, J. N. C.; Padua, A. A. H. *J. Phys. Chem. B.* **2006**, *110*, 3330-3335.

76. Lopes, J. N. C.; Costa Gomes, M. F.; Padua, A. A. H. *J. Phys. Chem. B.* **2006**, *110*, 16816-16818.

77. Urahata, S. M.; Ribeiro, M. C. C. *J. Chem. Phys.* **2004**, *120*, 1855.

78. Wang, Y.; Voth, G. A. *J. Am. Chem. Soc.* **2005**, *127*, 12192-12193.

79. Russina, O.; Triolo, A. *Faraday Discuss.* **2012**, *154*, 97-109.

80. Triolo, A.; Russina, O.; Bleif, H.-J.; Di Cola, E. J. *J. Phys. Chem. B* **2007**, *111*, 4641-4644.

81. Russina, O.; Triolo, A.; Gontrani, L.; Caminiti, R.; Xiao, D.; Hines, L. G., Jr.; Bartsch, R. A.; Quitevis, E. L.; Plechkova, N.; Seddon, K. R. *J. Phys. : Condens. Matter* **2009**, *21*, 424121/1-9.

82. Atkin, R.; Warr, G. G. *J. Phys. Chem. B* **2008**, *112*, 4164-4166.

83. Hayes, R.; Imberti, S.; Warr, G. G.; Atkin, R. *Phys. Chem. Chem. Phys.* **2011**, *13*, 3237-3247.

84. Russina, O.; Triolo, A.; Gontrani, L.; Caminiti, R. *J. Phys. Chem. Lett.* **2012**, *3*, 27-33.

85.   Macchiagodena, M.; Gontrani, L.; Ramondo, F.; Triolo, A.; Caminiti, R. *J. Chem. Phys.* **2011**, *134*, 114521/1-15.

86.   Hardacre, C.; Holbrey, J. D.; Mullan, C. L.; Youngs, T. G. A.; Bowron, D. T. *J. Chem. Phys.* **2010**, *133*, 074510/1−7.

87.   Annapureddy, H. V. R.; Kashyap, H. K.; De Biase, P. M.; Margulis, C. J. *J. Phys. Chem. B* **2010**, *114*, 16838−16846.

88.   Tamm, L. K.; McConnell, H. M. *Biophys. J.* **1985**, *47*, 105-113.

89.   Sackmann, E. *Science* **1996**, *271*, 43-48.

90.   Tampe, R.; Dietrich, C.; Gritsch, S.; Elender, G.; Schmitt, L., *Nanofabrication and Biosystems: Integrating Materials Science, Engineering, and Biology*. Cambridge University Press: New York, 1996.

91.   Bayerl, T. M.; Bloom, M. *Biophys. J.* **1990**, *58*, 357-362.

92.   Johnson, S. J.; Bayerl, T. M.; McDermott, D. C.; Adam, G. W. *Biophys. J.* **1991**, *59*, 289-294.

93.   Koenig, B. W.; Kruger, S.; Orts, W. J.; Majkrzak, C. F. *Langmuir* **1996**, *12*, 1343-1350.

94.   Mou, J. X.; Shao, Z. F. *Biochemistry* **1994**, *33*, 4439-4443.

95.   Kelly, J. W. *Structure* **1997**, *5*, 595.

96.   Tan, S. Y.; Pepys, M. B.; Hawkins, P. N. *Am. J. Kidney Dis.* **1995**, *26*, 267.

97.   Sunde, M.; Serpell, L. C.; Bartlam, M.; Fraser, P. E.; Pepys, M. B.; Blake, C. C. F. *J. Mol. Biol.* **1997**, *273*, 729.

98.   Conway, K. A.; Harper, J. D.; Lansbury, P. T. J. *Biochemistry* **2000**, *39*, 2552.

99.   Hueston, W.; Bryant, C. M. *J. Food. Sci.* **2005**, *70*, R77.

100.   Jeffrey, M.; Goodbrand, I. A.; Goodsir, C. M. *Micron* **1995**, *26*, 277-298.

101.   Prusiner, S. B. *Proc. Natl. Acad. Sci. USA* **1998**, *95*, 13363-13383.

102.   Paramithiotis, E.; Pinard, M.; Lawton, T.; LaBoissiere, S.; Leathers, V. L.; Zou, W.-Q.; Estey, L. A.; Lamontagne, J.; Lehto, M. T.; Kondejewski, L. H.; Francoeur, G. P.; Papadopoulos, M.; Haghighat, A.; Spatz, S. J.; Head, M.; Will, R.; Ironside, J.; O'Rourke, K.; Tonelli, Q.; Ledebur, H. C.; Chakrabartty, A.; Cashman, N. R. *Nat Med* **2003**, *9*, 893-899.

103.   Enari, M.; Flechsig, E.; Weissmann, C. *Proceedings of the National Academy of Sciences* **2001**, *98*, 9295-9299.

104.   Peretz, D.; Williamson, R. A.; Kaneko, K.; Vergara, J.; Leclerc, E.; Schmitt-Ulms, G.; Mehlhorn, I. R.; Legname, G.; Wormald, M. R.; Rudd, P. M.; Dwek, R. A.; Burton, D. R.; Prusiner, S. B. *Nature* **2001**, *412*, 739-743.

105.   Heppner, F. L.; Musahl, C.; Arrighi, I.; Klein, M. A.; Rülicke, T.; Oesch, B.; Zinkernagel, R. M.; Kalinke, U.; Aguzzi, A. *Science* **2001**, *294*, 178-182.

106.   Wells, G. A.; C., S. A.; Johnson, C. T.; Gunning, R. F.; Hancock, R. D.; Jeffrey, M.; Dawson, M.; Bradley, R. *Vet Rec* **1987**, *123*, 638-644.

107.   Cousens, S.; Smith, P. G.; Ward, H.; Everington, D.; Knight, R. S.; Zeidler, M.; Stewart, G.; Smith-Bathgate, E. A.; Macleod, M. A.; Mackenzie, J.; Will, R. G. *Lancet* **2001**, *357*, 1002-1007.

108.   Ironside, J. W. *Brain Pathol.* **1996**, *6*, 379-388.

109.   Bruce, M. E.; Will, R. G.; Ironside, J. W.; McConnell, I.; Drummond, D.; Suttie, A.; McCardle, L.; Chree, A.; Hope, J.; Birkett, C., *et al. Nature (London)* **1997**, *389*, 498-501.

110.   De Bosschere, H.; Roels, S.; Vanopdenbosch, E. *J. Appl. Res. Vet. Med.* **2004**, *2*, 52-54.

111.   Polak, M. P.; Zmudzinski, J. F.; Jacobs, J. G.; Langeveld, J. P. M. *Arch Virol* **2008**, *153*, 69-79.

112.   Buschmann, A.; Gretzschel, A.; Biacabe, A. G.; Schiebel, K.; Corona, C.; Hoffmann, C.; Eiden, M.; Baron, T.; Casalone, C.; Groschup, M. H. *Veterinary Microbiology* **2006**, *117*, 103-116.

113.   Béringue, V.; Bencsik, A.; Le Dur, A.; Reine, F.; Laï, T. L.; Chenais, N.; Tilly, G.; Biacabé, A.-G.; Baron, T.; Vilotte, J.-L.; Laude, H. *PLoS Pathog* **2006**, *2*, e112.

114.   Yamakawa, Y.; Hagiwara, K.; Nohtomi, K.; Nakamura, Y.; Nishijima, M.; Higuchi, Y.; Sato, Y.; Sata, T. **2003**, *56*, 221-222.

115.   Richt, J. A.; Kunkle, R. A.; Alt, D.; Nicholson, E. M.; Hamir, A. N.; Czub, S.; Kluge, J.; Davis, A. J.; Hall, S. M. *Journal of Veterinary Diagnostic Investigation* **2007**, *19*, 142-154.

116.   Stack, M.; Focosi-Snyman, R.; Cawthraw, S.; Davis, L.; Jenkins, R.; Thorne, L.; Chaplin, M.; Everitt, S.; Saunders, G.; Terry, L. *Zoonoses and Public Health* **2009**, *56*, 376-383.

117.   Jacobs, J. G.; Langeveld, J. P. M.; Biacabe, A.-G.; Acutis, P.-L.; Polak, M. P.; Gavier-Widen, D.; Buschmann, A.; Caramelli, M.; Casalone, C.; Mazza, M.; Groschup, M.; Erkens, J. H. F.; Davidse, A.; Zijderveld, F. G. v.; Baron, T. *J. Clin. Microbiol.* **2007**, *45*, 1821-1829.

118.   (EFSA), E. F. S. A. *Quantitative Assessment of the Residual BSE Risk in Bovine-Derived Products, EFSA QRA Report 2004 - working document*; 2005; pp 1-135.

119.   Evaluation of the Potential for Bovine Spongiform Encephalopathy in the United States. In Harvard Center of Risk Analysis, Harvard School of Public Health, and Center of Computational Epidemiology, College of Veterinary Medicine, Tuskegee University, 2001.

120.   Comer, P. J.; Huntly, P. J. *Stat. Methods Med. Res.* **2003**, *12*, 279-291.

121.   Wilesmith, J. W.; Wells, G. A. H.; Cranwell, M. P.; Ryan, J. B. M. *Vet Rec* **1988**, *123*, 638-644.

122.   Wilesmith, J. W.; Ryan, J. B. M. *Vet Rec* **1993**, *132*, 300-301.

123. Sohal, R. S., *Age Pigments*. Elsevier: Amsterdam, 1981.

124. Yin, D. *Free Radical Biology & Medicine* **1996**, *21*, 871-888.

125. Terman, A.; Brunk, U. T. *Acta Pathol., Microbiol., Immunol.* **1998**, *106*, 265-276.

126. Terman, A. *Redox Rep* **2001**, *6*, 15.

127. Tsuchida, M.; Miura, T.; Aibara, K. *Chemistry and Physics of Lipids* **1987**, *44*, 297-325.

128. Strehler, B. L., *Time, Cells, and Aging*. Academic Press: San Diego, 1977.

129. Sundelin, S. P.; Nilsson, S. E. G. *Free Radical Biology & Medicine* **2001**, *31*, 217.

130. Boellaard, J. W.; Schlote, W.; Tateishi, J. *Acta Neuropathologica* **1989**, *78*, 410-418.

131. Foncin, J. F.; Gaches, J.; Le Beau, J. *Revue neurologique* **1964**, *111*, 507-515.

132. Kirschbaum, W. R., *Jakob-Creutzfeldt Disease*. Elsevier: New York, 1968; p 251.

133. Jacobson, S.; Koenig, H.; Ross, E. *J. Neuropathol. Exp. Neurol.* **1967**, *26*, 152-153.

134. Miyashita, M.; Stierstorfer, B.; Schmahl, W. *J. Vet. Med. B* **2004**, *51*, 209-215.

135. Smith, J. D.; Greenlee, J. J.; Hamir, A. N.; Richt, J. A.; Greenlee, M. H. W. *Veterinary pathology* **2009**, *46*, 810-8.

136. Smith, J. D.; Greenlee, J. J.; Hamir, A. N.; Greenlee, M. H. W. *The Veterinary record* **2009**, *165*, 179-81.

137. Hortells, P.; Monzon, M.; Monleon, E.; Acin, C.; Vargas, A.; Bolea, R.; Lujan, L.; Badiola, J. J. *Brain Research* **2006**, *1108*, 188-194.

138. Rubenstein, R.; Gray, P. C.; Wehlburg, C. M.; Wagner, J. S.; Tisone, G. C. *Biochem. Biophys. Res. Commun.* **1998**, *246*, 100-106.

139. Shirakawa, H.; Louis, E. J.; MacDiarmid, A. G.; Chiang, C. K. H. *Chemical Communications* **1977**, 578-580.

140. Chiang, C. K. *Physical Review Letters* **1977**, *39*, 1098-1101.

141.   Pope, M.; Swenberg, C. E., *Electronic Processes in Organic Crystals and Polymers*. 2nd ed.; Oxford Univ.: London, 1999.

142.   Chiang, C. K.; Gau, S. C.; Fincher, J. C. R.; Park, Y. W.; MacDiarmid, A. G. *Appl. Phys. Lett*. **1978**, *33*, 18.

143.   Morita, S.; Zakhidov, A. A.; Yoshino, Y. *Solid State Commun*. **1992**, *82*, 249.

144.   Sariciftci, N. S.; Heeger, A. J.; Krasevec, V.; Venturini, P.; Mihailovic, D.; Cao, Y.; Libert, J.; Bredas, J. L. *Synth.Met*. **1994**, *62*, 107.

145.   Schilinsky, P.; Waldauf, C.; Brabec, C. J. *Applied Physics Letters* **2002**, *81*, 3885-3887.

146.   Padinger, F.; Rittberger, R. S.; Sariciftci, N. S. *Advanced Functional Materials* **2003**, *13*, 85-88.

147.   Ma, W.; Yang, C.; Gong, X.; Lee, K.; Heeger, A. J. *Advanced Functional Materials* **2005**, *15*, 1617-1622.

148.   Reyes, M. -R.; Kim, K.; Dewald, J.; Sandoval, R. -L.; Avadhanula, A.; Curran, S.; Carrol, D. L. *Org.Lett*. **2005**, *7*, 5749-5752.

149.   He, Z.; Zhong, C.; Huang, X.; Wong, W. Y.; Wu, H.; Chen, L.; Su, S.; Cao, Y. *Adv. Mater* **2011**, *23*, 4636-4643.

150.   He, Z.; Zhong, C.; Su, S.; Xu, M.; Wu, H.; Cao, Y. *Nat. Photonics* **2012**, *6*, 591-595.

151.   Cook, S.; Katoh, R.; Furube, A. *J.Phys.Chem.C* **2009**, *113*, 2547-2552.

152.   Lanzani, G.; Zenz, C.; Cerullo, G.; Graupner, W.; Leising, G.; Scherf, U.; Silvestri, S. D. *Synth. Met*. **2000**, *493*, 111-112.

153.   Kraabel, B. D.; J. C. Hummelen, J. C.; Vacar, D.; Moses, D.; Sariciftci, N. S.; Heeger, A. J. *J. Chem. Phys*. **1996**, *104*, 4267.

154.   Kraabel, B.; McBranch, D.; Sariciftci, N. S.; Moses, D.; Heeger, A. J., 256, 733 *Mol. Cryst. Liq. Cryst.* **1994**, *256*, 733.

155.   Heeger, A. J. *Reviews Of Modern Physics* **2001**, *73*, 681-700.

156.   Goh, C.; Scully, S. R.; McGehee, M. D. *J. Appl. Phys.* **2007**, 114503.

157.   Wang, H.; Wang, H.-Y.; Gao, B.-R.; Wang, L.; Yang, Z.-Y.; Du, X.-B.; Chen, Q.-D.; Song, J.-F.; Sun, H.-B. *Nanoscale* **2011**, *3*, 2280-2285.

158.   Noriega, R. *Nat. Mater.* **2013**, *12*, 1038-1044.

159.   Reyes-Reyes, M.; Kim, K.; Carroll, D. L. *Appl. Phys. Lett.* **2005**, *87*, 083506.

160.   Samuelsen, E. J.; Mardalen, J., *Handbook of Organic Conductive Molecules and Polymers* Wiley: Chichester, UK, 1997; Vol. 3.

161.   Kobashi, M.; Takeuchi, H. *Macromolecules* **1998**, *31*, 7273-7278.

162.   Sirringhaus, H.; Brown, P. J.; Friend, R. H.; Nielsen, M. M.; Bechgaard, K.; Langeveld-Voss, B. M. W.; Spiering, A. J. H.; Janssen, R. A. J.; Meijer, E. W.; Herwig, P.; De Leeuw, D. M. *Nature* **1999**, *401*, 685-688.

163.   Spano, F. C. *J. Chem. Phys.* **2005**, *122*, 234701.

164.   Spano, F. C. *J. Chem. Phys.* **2007**, *126*, 159901

165.   Clark, J.; Silva, C.; Friend, R. H.; Spano, F.C. *Phys. Rev. Lett.* **2007**, *98*, 206406.

166.   Martin, T. P.; Wise, A. J.; Busby, E.; Gao, J.; Roehling, J. D.; Ford, M. J.; Larsen, D. S.; Moulé, A. J.; Grey, J. K. 117, 4478−4487. *J. Phys. Chem. B* **2013**, *117*, 4478−4487.

167.   Baghgar, M.; Labastide, J. A.; Bokel, F.; Hayward, R. C.; Barnes, M. D. *J. Phys. Chem. C* **2014**, *118*, 2229-2235.

168.   Ruseckas, A.; Namdas, E. B.; Ganguly, T.; Theander, M.; Svensson, M.; Andersson, M. R.; Inganas, O. *J. Phys. Chem. B* **2001**, *105*, 7624−7631.

169. Theander, M.; Svensson, M.; Ruseckas, A.; Zigmantas, D.; Sundstrom, V.; Andersson, M. R.; Inganas, O. *Chem. Phys. Lett.* **2001**, *337*, 277-283.

170. Jiang, X. M.; Osterbacka, R.; Korovyanko, O.; An, C. P.; Horovitz, B.; Janssen, R. A. J.; Vardeny, Z. V. *Adv. Funct. Mater.* **2002**, *12*, 587−597.

171. Kojima, A.; Teshima, K.; Shirai, Y.; Miyasaka, T. *J. Am. Chem. Soc.* **2009**, *131*, 6050-6051.

172. Green, M. A.; Ho-Baillie, A.; Snaith, H. J. *Nature Photon.* **2014**, *8*, 506-514.

173. Lee, M. M.; Teuscher, J.; Miyasaka, T.; Murakami, T. N.; Snaith, H. J. *Science* **2012**, *338*, 643-647.

174. Zhao, Y.; Zhu, K. *J. Phys. Chem. Lett.* **2014**, *5*, 4175−4186.

175. Choi, J. J.; Yang, X.; Norman, Z. M.; Billinge, S. J. L.; Owen, J. S. *Nano Lett.* **2014**, *14*, 127−133.

176. Snaith, H. J.; Abate, A.; Ball, J. M.; Eperon, G. E.; Leijtens, T.; Noel, N. K.; Stranks, S. D.; Wang, J. T.-W.; Wojciechowski, K.; Zhang, W. *J. Phys. Chem. Lett.* **2014**, *5*, 1511−1515.

177. Dualeh, A.; Tétreault, N.; Moehl, T.; Gao, P.; Nazeeruddin, M. K.; Grätzel, M. *Adv. Funct. Mater.* **2014**, *24*, 3250–3258.

178. Tan, K. W.; Moore, D. T.; Saliba, M.; Sai, H.; Estroff, L. A.; Hanrath, T.; Snaith, H. J.; Wiesner, U. *ACS Nano* **2014**, *8*, 4730–4739.

179. Eperon, G. E.; Burlakov, V. M.; Docampo, P.; Goriely, A.; Snaith, H. J. *Adv. Funct. Mater.* **2013**, *24*, 151–157.

180. Burlakov, V. M.; Eperon, G. E.; Snaith, H. J.; Chapman, S. J.; Goriely, A. *Appl. Phys. Lett.* **2014**, *104*, 091602.

181. Liu, M.; Johnston, M. B.; Snaith, H. J. *Nature* **2013**, *501*, 395–398.

182.   Eperon, G. E.; Burlakov, V. M.; Docampo, P.; Goriely, A.; Snaith, H. J. *Adv. Funct. Mater.* **2013**, *24*, 151–157.

183.   Docampo, P.; Ball, J. M.; Darwich, M.; Eperon, G. E.; Snaith, H. J. *Nat. Commun.* **2013**, *4*, 2761.

184.   Ball, J. M.; Lee, M. M.; Hey, A.; Snaith, H. J. *Energy Environ. Sci.* **2013**, *6*, 1739−1743.

185.   Yang, S.; Zheng, Y. C.; Hou, Y.; Chen, X.; Chen, Y.; Wang, Y.; Zhao, H.; Yang, H. G. *Chem. Mater.* **2014**, *26*, 6705–6710.

186.   Shkrob, I. A.; Marin, T. W. *J. Phys. Chem. Lett.* **2014**, *5*, 1066–1071.

187.   Abate, A.; Saliba, M.; Hollman, D. J.; Stranks, S. D.; Wojciechowski, K.; Avolio, R.; Grancini, G.; Petrozza, A.; Snaith, H. J. *Nano Lett.* **2014**, *14*, 3247–3254.

188.   Shi, T.; Yin, W.-J.; Hong, F.; Zhu, K.; Yan, Y. *Appl. Phys. Lett.* **2015**, *106*, 103902.

189.   Lindblad, R.; Jena, N. K.; Philippe, B.; Oscarsson, J.; Bi, D.; Lindblad, A.; Mandal, S.; Pal, B.; Sarma, D. D.; Karis, O.; Siegbahn, H.; Johansson, E. M. J.; Odelius, M.; Rensmo, H. *J. Phys. Chem. C* **2015**, *119*, 1818-1825.

190.   Buin, A.; Pietsch, P.; Xu, J.; Voznyy, O.; Ip, A. H.; Comin, R.; Sargent, E. H. *Nano Lett.* **2014**, *14*, 6281-6286.

191.   Duan, H.-S.; Zhou, H.; Chen, Q.; Sun, P.; Luo, S.; Song, T.-B.; Bob, B.; Yang, Y., 17, *Phys. Chem. Chem. Phys* **2015**, *17*, 112-116.

192.   Wu, X.; Trinh, M. T.; Niesner, D.; Zhu, H.; Norman, Z.; Owen, J. S.; Yaffe, O.; Kudisch, B. J.; Zhu, X. Y. *J. Am. Chem. Soc.* **2015**, *137*, 2089-2096.

193.   Kao, T. S.; Chou, Y.-H.; Chou, C.-H.; Chen, F.-C.; Lu, T.-C. *Appl. Phys. Lett.* **2014**, *105*, 231108.

194.   Sadhanala, A.; Deschler, F.; Thomas, T. H.; Dutton, S. E.; Goedel, K. C.; Hanusch, F. C.;

Lai, M. L.; Steiner, U.; Bein, T.; Docampo, P.; Cahen, D.; Friend, R. H. *J. Phys. Chem. Lett.* **2014**,

5, 2501-2505.

195.   Noh, J. H.; Im, S. H.; Heo, J. H.; Mandal, T. N.; Seok, S. I. *Nano Lett.* **2013**, *13*, 1764-9.

196.   Kitazawa, N.; Watanabe, Y.; Nakamura, Y. *J. Mater. Sci.* **2002**, *37*, 3585-3587.

197.   Protesescu, L.; Yakunin, S.; Bodnarchuk, M. I.; Krieg, F.; Caputo, R.; Hendon, C. H.;

Yang, R. X.; Walsh, A.; Kovalenko, M. V., ASAP. *Nano Lett.* **2015**.

198.   Papavassiliou, G. C.; Pagona, G.; Karousis, N.; Mousdis, G. A.; Koutselas, I.;

Vassilakopoulou, A. *J. Mater. Chem.* **2012**, *22*, 8271-8280.

199.   Yin, W.-J.; Yan, Y.; Wei, S.-H. *J. Phys. Chem. Lett.* **2014**, *5*, 3625-3631.

200.   Zhang, M.; Yu, H.; Lyu, M.; Wang, Q.; Yun, J.-H.; Wang, L. *Chem. Commun.* **2014**, *50*,

11727-11730.

CHAPTER 2. EXPERIMENTAL TECHNIQUES

In this chapter, several experimental techniques that are employed in the following chapters are elaborated upon.   These are: time-correlated, single-photon counting; fluorescence depolarization; confocal and stimulated emission depletion (STED) microscopies and transient absorption spectroscopy and time-resolved emission spectra.

Time-Correlated, Single-Photon Counting (TCSPC)

This technique for measuring excited-state lifetimes is extremely useful and important because of its relative simplicity and the generally high quality of data that it generates. Assuming a dilute solution excited by a short pulse at $t = 0$, the rate of relaxation of the population, n, of excited molecules can be given by the first-order differential equation[1]

$$\frac{dn}{dt} = -kn \tag{2.1}$$

Integrating eqn 2.1 results in an exponential decay of the excited state population.

$$n_t = n_0 \cdot e^{-\frac{t}{\tau}} \tag{2.2}$$

n_t and n_0 are the excited state populations at time t and t = 0, respectively. τ is the excited state lifetime of the fluorophore and determines the rate constant for the decay of the excited state by the relation , $\tau = 1/k$. Thus fluorescence intensity, I, also follows the exponential decay:

$$I_t = I_0 \cdot e^{-\frac{t}{\tau}} \tag{2.3}$$

The probability, P, of emission a photon after a time delay, Δt by a single molecule with respect to the time of excitation is given by:[1a]

$$P\,(\Delta t) = e^{-\frac{t}{\tau}} \tag{2.4}$$

Thus, the measurement of single-photon emission statistics can reproduce excited state population decay statistics. The time-correlated, single-photon counting (TCSPC) technique is designed to measure low photon fluxes, which permits the determination of the excited-state lifetime.[2] A schematic of this experiment is provided in **Figure 1**.

A pulsed light source with a high repetition rate excites the sample. A very sensitive detector, usually a micro-channel plate (MCP), is used to detect emitted photons by fluorophores. The MCP is capable of responding to a single photon with a well-defined and wavelength independent electric output pulse. A fast photodiode (PD) triggered by the excitation pulse and it is registers a "start" time in the time-to-amplitude converter (TAC). The TAC is analogous to a very precise stopwatch. It measures the delay time between the excitation pulse and the pulse produced from the MCP by the emitted photon. After being started by the reference photodiode, the TAC charges a capacitor with constant current and creates voltage, which linearly varies with time. Upon detection of a fluorescence photon, the MCP generates a "stop" pulse, which stops the voltage ramp of the capacitor. The exact timings of a pulse from MCP (representing time of the photon event) or the reference signal are critical. In order to avoid timing jitter arising from random amplitude magnification inside the detector or changing laser source intensity, the pulses are first passed through constant fraction discriminator (CFD) before they reach to TAC. The accumulated voltage of the capacitor in the TAC is proportional to the time delay between the start pulse and the stop pulse. Subsequently, by an analog-to-digital converter (ADC),[1a] the position of a detected photon on the time axis is recorded from the amplitude of the voltage in TAC. It, then, sends the time information to a multi-channel analyzer (MCA). The MCA is a multichannel array with N channels, where each channel corresponds to an increasing voltage interval. The time of the arrived photon is then interpreted as a channel number in MCA. As the

sample is excited with a high repetition rate light source, the sample is repeatedly excited by pulses; and single photons are counted. Thus, following a number of repetition of single-photon detection events, a histogram, which corresponds to the decay curve, is built up in the MCA. It is very important that during a single detection cycle, only one photon is detected. When many molecules are excited at the same time, a nonlinear distortion in the histogram, known as pile-up, occurs.[2-3] This can be avoided by ensuring that the average count rate at the detector is ~ 5%
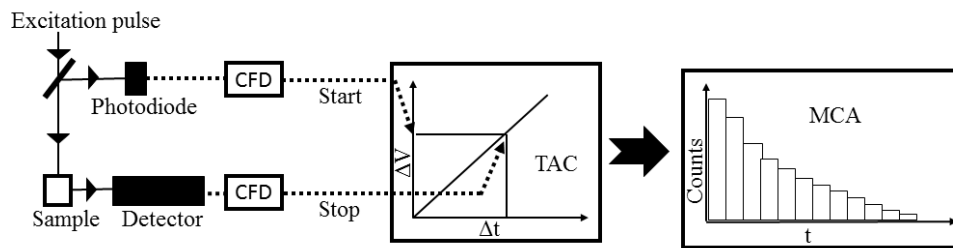
Figure 1.   Illustration of basic principle of time-correlated, single-photon counting method. CFD: constant fraction discriminator; TAC: time-to-amplitude converter; MCA: multi-channel analyzer.

of the repetition rate of the excitation laser, that there is a low excitation pulse energy, and that there is a low fluorophore concentration. The transit time spread of the pulse from the detector limits the temporal resolution of the experiment. With our system as described here, the time resolution is determined by an instrument response function of ~40 ps with a MCP detector.[2-3]

The recorded fluorescence decay profile, *F(t)*, is a convolution of the instrument response *I(t)* and the true fluorescence response to a delta pulse excitation *f(t)*:

$$F(t) = \int_0^\infty I(t - t')f(t')\,dt' \tag{2.5}$$

Scattering the excitation pulse by nondairy coffee creamer is used to measure the instrument response function. The true fluorescence decay profile is obtained by deconvolution of *F(t)* using known *I(t)*.

TCSPC Setup

A schematic diagram of the components of the TCSPC instrument is given in **Figure 2**. A Nd:VO$_4$ laser (Millennia, Spectra Physics) is used to pump homebuilt mode-locked Ti:sapphire oscillator. The mode-locked Ti:sapphire laser can produce short (femtosecond) pulses tunable over a wavelength range of 790 to 880 nm with a repetition rate of 88 MHz. Further details about the Ti:sapphire oscillator is described in the following section. The output from the Ti-sapphire oscillator is modulated by a Pockels cell (Model 350-160, Conoptics Inc.) to reduce the repetition rate to approximately 8.8 MHz. Subsequently, using harmonic generation crystals (Model TP-2000B, U-Oplaz Technologies), the fundamental wavelength of ~800 nm is frequency doubled or tripled. The resulting blue (~ 400 nm) or UV (~ 266 nm) laser used as excitation sources. The
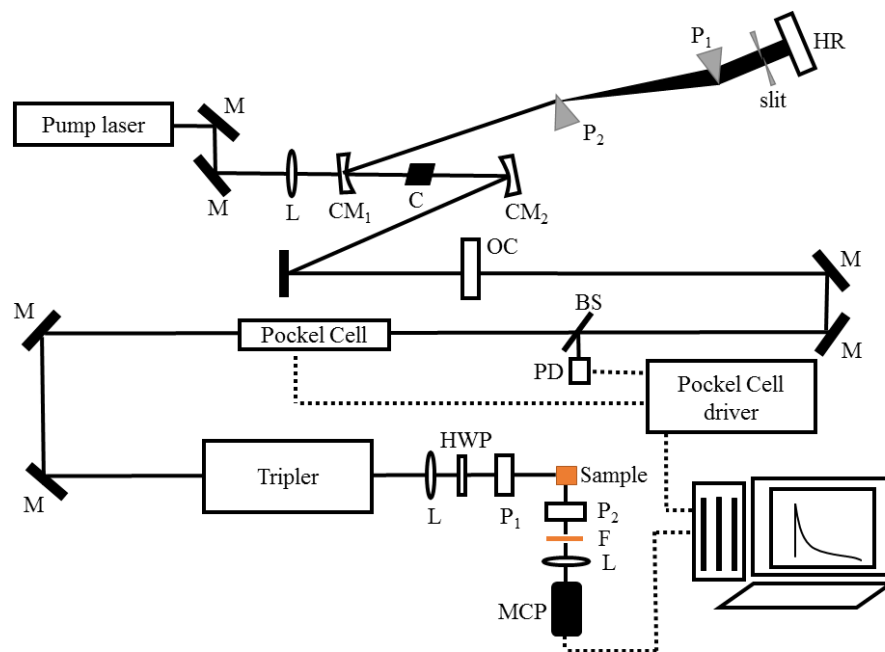
Figure 2. Schematic diagram of TCSPC instrument: M, mirror; L , lens; C, crystal; OC, output coupler; P, prism; BS, beam splitter; PD, photodiode; WP, wave plate; MCP, microchannel plate; F, filter.

polarization of the excitation pulses are made vertical using a half-wave plate and subsequently

passed through a polarizer to ensure high degree of polarization. After the sample, an analyzer is placed at the "magic angle" (54.7°) with respect to excitation polarization. The detector output is amplified with a pre-amplifier before going to the Becker & Hickl photon counting module (Model SPC-630). The SPC module contains the usual building blocks (CFDs, TAC, ADC) together with a large histogram memory integrated on one board. The full-width-at-half-maximum (fwhm) of the instrument response function of the TCSPC system is ~40 – 45 ps. In the following sections some of the fundamentals related to our TCSPC have been discussed.

Ti-sapphire Laser and Mode-Locking. One of the most widely used solid-state lasers use the titanium sapphire, $Ti:Al_2O_3$ as the gain medium. In $Ti:Al_2O_3$ crystals, some of the Al^{+3} ions are replaced by Ti^{+3} ions in the hexagonal crystal structure with the metal ion in the center. Crystalline field produces a triply degenerate $^2T_2$ ground state and a doubly degenerate ^2E excited state, perturbing the electronic energy level of Ti^{+3} ion. Strong crystal field interaction with the 3d electron results in the larger equilibrium Ti-O distance in the upper state compared to that in lower level, thus, producing a wide separation between emission and absorption band with large width. Commonly frequency-doubled Nd:YAG lasers are used to pump owing to its absorption band centered at 490 nm. The peak in the fluorescence spectra is at 780 nm with a 180 nm band width (fwhm) which makes this tunable over a range of 675 nm to 1110 nm. The basic parts of a laser resonator are the gain medium, the pump source, and two end mirrors, such as high reflector (reflectivity, r_1 ~100%) and output coupler (which passes only a small fraction of the trapped light; reflectivity, r_2). Upon population inversion in the gain medium by the pump laser, it amplifies the initial light trapped (noise) in the oscillator. The gain, in a round trip, G can be defined as:

$$G = \frac{I_1}{I_0} = r_1 r_2 e^{2(k-\gamma)L} \tag{2.6}$$

Where, I_0 and I_1 are the initial and final intensities respectively, k and γ are the gain and loss coefficients and L is the cavity length. After several fold of oscillation between the end mirrors if the $G \geq 1$, the cavity will initiate and sustain the emission.

Depending on two boundary conditions, there can be different longitudinal and transverse modes of lasers. From the first boundary condition of phase-matching after one round trip in the cavity, different longitudinal modes are generated as given by the following equation.

$$n\left(\frac{\lambda}{2}\right) = L \tag{2.7}$$

Where the n is a positive integer. The total number if longitudinal modes (N) can be expressed as:

$$N \cong \frac{4L\Delta\lambda}{\lambda_0^2} \tag{2.8}$$

Where λ_0 and $\Delta\lambda$ are the peak maximum and the half width at half maximum of the spontaneous emission band of the gain medium and $\lambda_0^2 \gg \Delta\lambda^2$. Secondly, depending on the other boundary condition that the electromagnetic field goes to zero away from the resonator axis, intensity dependence in the perpendicular plane to the direction of propagation (say, z direction) can be given by,

$$E_{mn}(x,y) = E_0 H_m\left(\frac{\sqrt{2}x}{w}\right) H_n\left(\frac{\sqrt{2}y}{w}\right) e^{-\frac{x^2+y^2}{w^2}} \tag{2.9}$$

Where H_m and H_n are the Hermite polynomials. $m, n = 0$ leads to TEM$_{00}$ mode which has a Gaussian distribution of intensity in x,y plane.

In a Ti:Sapphire laser cavity, millions of longitudinal modes exist. With the help of mode-locking, a constant phase relationship is created among the different modes, thus, making the modes constructively interfere at some point in the cavity and destructively interfere elsewhere. This results in laser pulses, a part of which escapes the laser cavity upon reaching the output coupler each time. The output pulse train consists of pulses separated by the one full round-trip

time of the cavity. Making as many modes oscillating as possible facilitates generation of short pulses. Fourier transform of the spectrum limits the minimum pulse duration, $\Delta\tau_p$ and from the uncertainty principle, one can write,

$$\Delta\tau_p \Delta\upsilon \geq \frac{1}{2\pi} \tag{2.10}$$

The methods of mode-locking broadly fall under two categories, active and passive mode-locking. In our laboratory, we use Kerr-lens mode-locking which is a passive mode-locking technique. Kerr-lens mode-locking which is based on the non-linear intensity-dependent refractive index of a material at high intensity, can produce pulses with pulse duration of as small as few femtoseconds. The refractive index under Kerr effect can be represented as

$$n(r,t) = n_0 + n_2 I(r,t) \tag{2.11}$$

Where n_0 and n_2 are the linear refractive index and non-linear refractive index coefficient respectively and I is the instantaneous beam intensity. Under TEM$_{00}$ laser mode with a Gaussian intensity profile, the center of the beam is more strongly focused than the edges of the beam owing to higher intensity in the center. Thus, placing an aperture at a suitable distance from the Kerr medium in a laser cavity leads to transmission of higher fraction of focused beam while blocking the weaker (CW) portion of the beam. Subsequently, the Kerr medium with an aperture introduces low losses when instantaneous pulse intensity is increased and thus, results mode-locking condition of the laser. In a freely running laser, the Kerr nonlinearity effect can not self-start the mode-locking. Thus, an intensity fluctuation is introduced by perturbing the cavity to initiate the mode-locking. In our laboratory setup, this is achieved by slightly tapping one of the curved mirrors in the cavity. Subsequently, the different frequencies of competing longitudinal modes are swept across producing a strong amplitude modulation due to mode beating. The strongest mode-beating pulse initiates the mode-locking.

Second Harmonic Generation and Sum Frequency Mixing Process. Second harmonic generation and sum or difference frequency mixing processes are second order nonlinear processes, i.e. polarization of the medium is not directly proportional to the electric field E. With approximation Polarization of material can be written in a form of Taylor series,

$$P_i = \varepsilon_0 \left[\sum_j \chi_{ij}^{(1)} E_j + \sum_{jk} \chi_{ijk}^{(2)} E_j E_k + \sum_{jkl} \chi_{ijkl}^{(3)} E_j E_k E_l + \cdots \right] \tag{2.12}$$

or simply the second order term can be given as,

$$P_2 = \varepsilon_0 \chi^{(2)} E^2 \tag{2.13}$$

Now let us consider combination of two photons with frequencies ω_1 and ω_2 ($\omega_1 = \omega_2$ or $\omega_1 \neq \omega_2$). We can write the expression for the field as,

$$E = \left(E_1 e^{-i\omega_1 t} + E_1^* e^{i\omega_1 t} \right) + \left(E_2 e^{-i\omega_2 t} + E_2^* e^{i\omega_2 t} \right) \tag{2.14}$$

The second order nonlinear polarizibility can be written as,

$$P_2 = \varepsilon_0 \chi^{(2)} E^2$$

$$= \varepsilon_0 \chi^{(2)} \left[E_1^2 e^{-i(2\omega_1)t} + (E_1^*)^2 e^{i(2\omega_1)t} + E_2^2 e^{-i(2\omega_2)t} + (E_2^*)^2 e^{i(2\omega_2)t} + 2E_1 E_1^* + 2E_2 E_2^* + \right.$$

$$\left. 2E_1 E_2 e^{-i(\omega_1+\omega_2)t} + 2E_1^* E_2^* e^{-i(\omega_1+\omega_2)t} + 2E_1 E_2^* e^{-i(\omega_1-\omega_2)t} + 2E_1^* E_2 e^{-i(\omega_1-\omega_2)t} \right] \tag{2.15}$$

The First four terms represent the second harmonic generation, that is frequency doubled electromagnetic waves are generated, terms with $(\omega_1 + \omega_2)$ are the sum frequency generation, and the terms with $(\omega_1 - \omega_2)$ represent the difference frequency generation process. From photon's point of view, it can be described by the schematic diagram in **Figure 3**. From the above equation it is quite obvious that when $\omega_1 = \omega_2$, we can only have second harmonic generation. Though there are possibilities of generation of several frequencies, but in order to efficiently generate any of those we have fulfill the phase matching criteria which can be obtained from the energy and momentum conservation of photons. Energy (hω) and momentum (h**k**) conservation in a dispersion free media can be expressed as:

$$\omega_1 + \omega_2 = \omega_3 \tag{2.16}$$

$$\boldsymbol{k}_1 + \boldsymbol{k}_2 = \boldsymbol{k}_3 \tag{2.17}$$

If the refractive index of the medium, n, depends on ω, then k is expressed as $k(\omega) = \omega\, n(\omega)/c$. Thus phase matching criteria for collinear propagation can be rewritten as:

$$\omega_1 n(\omega_1) + \omega_2 n(\omega_2) = \omega_3 n(\omega_3) \tag{2.18}$$

This condition can be satisfied in birefringent medium.
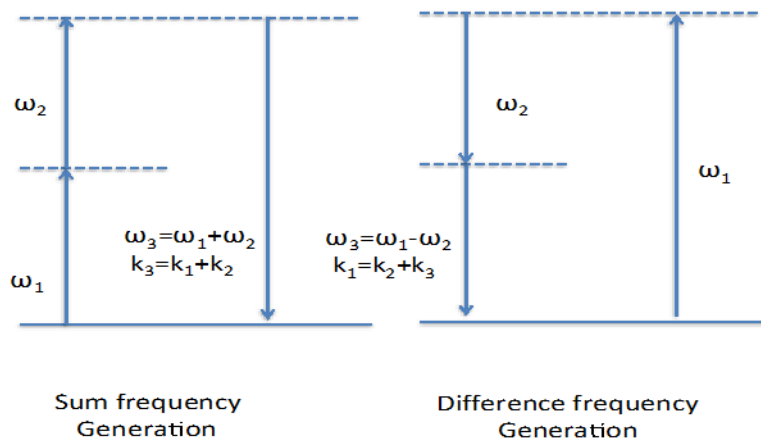
Figure 3. Schematic diagram showing sum frequency and difference frequency generation.

Time-Resolved Fluorescence Depolarization

The average excited-state lifetime of fluorophores is in the order of nanoseconds for many fluorophores, whereas the absorption of a photon by the molecules takes place very fast (essentially instantaneously). Thus, during this time delay between absorption and emission, a molecule, as a whole (global rotational movement) or by part (local motion) can undergo significant angular displacement, which can depolarize the emission of the fluorophore. To elucidate molecular orientation, or to measure time involved with such depolarization processes, the time-resolved fluorescence anisotropy is measured.

If an ensemble of molecules is excited using a polarized laser pulse and fluorescence is detected by using a polarizer before the detector at parallel and perpendicular orientations with respect to excitation polarization, $I_{||}$ and $I_\perp$, the parallel and perpendicular components of the fluorescence are obtained, respectively.

Figure 4 presents a single chromophore and and its transition dipole moment, $\vec{\mu}$, which is a vector coupling the excited state to ground state *via* the radiation field of the electric field of the excitation source. The anisotropy (*r*) is defined as:[4]

$$r = \frac{I_{||} - I_\perp}{I_{||} + 2I_\perp} \qquad (2.19)$$

Let $W(\theta, \phi, t)$ be the probability that $\vec{\mu}$ is at the angles θ and ϕ at a time, t. Assuming the probability evolution operator to be $G(\theta_0, \phi_0 \mid \theta, \phi, t)$, one can write,

$$W(\theta, \phi, t) = \int_0^{2\pi} d\phi_0 \int_0^{\pi} \sin\theta_0 \, d\theta_0 \, W(\theta_0, \phi_0) G(\theta_0, \phi_0 \mid \theta, \phi, t) \qquad (2.20)$$

Let us now assume that at time zero (t = 0) the absorption and emission dipoles are parallel. The molecule shown in the Figure absorbs a photon whose electric field vector ($\vec{\epsilon}$) is polarized along the z-axis with a probability proportional to $|\vec{\mu} \cdot \vec{\epsilon}|^2$. Using normalization condition (eqn 2.21),

$$\int_0^{2\pi} \int_0^{\pi} W(\theta_0, \phi_0) d\phi_0 \, \sin\theta_0 \, d\theta_0 = 1 \qquad (2.21)$$

one can show that the distribution of the excited state molecules at time, t = 0, is:

$$W(\theta_0, \phi_0) = \frac{3}{4\pi} \cos^2\theta_0 \qquad (2.22)$$

$W(\theta_0, \phi_0)$ can also be written in terms of the second Legendre polynomial: $P_2(x) = 1/3 \, (3x^2 - 1)$:

$$W(\theta_0, \phi_0) = \frac{1}{4\pi} [1 + 2P_2(\cos\theta_0)] \qquad (2.23)$$

One can now expand $G(\theta_0, \phi_0 \mid \theta, \phi, t)$ in terms of spherical harmonics and use the normalization condition (eqn 2.24) and boundary condition (eqn 2.25).

$$\int_0^{2\pi} \int_0^{\pi} d\phi \; \sin\theta \; d\theta \; G\left(\theta_0, \phi_0 \mid \theta, \phi, t\right) = 1 \tag{2.24}$$

$$G\left(\theta_0, \phi_0 \mid \theta, \phi, t = 0\right) = \delta(\cos\theta - \cos\theta_0)\delta(\phi - \phi_0) \tag{2.25}$$

Upon solving the equation 2.20 in terms of spherical harmonics one reach to a final equation as,

$$W\left(\theta, \phi, t\right) = \frac{1}{4\pi}\left[1 + 2C_{2,0}(t)P_2(\cos\theta_0)\right] \tag{2.26}$$

Where $C_{2,0}(t)$ is the coefficient of the spherical harmonic expansion with l = 2 and m = 0.

Again, let us assume we have a single fluorophore oriented as shown in the **Figure 4** and we are detecting fluorescence emission along the y-axis. Thus, we can only detect light that is polarized along the x- and z-axes. Probability of a molecule being in excited state is K(t), which is usually a decaying exponential. Subsequently, fluorescence intensities for one molecule in parallel or perpendicular directions are given by,

$$\mathcal{I}_{\parallel}(\theta, \phi, t) \propto \mu^2 \cos^2\theta \; K(t) \tag{2.27}$$

$$\mathcal{I}_{\perp}(\theta, \phi, t) \propto \mu^2 \; \sin^2\theta \cos^2\phi \; K(t) \tag{2.28}$$

If we now consider an ensemble of such molecules, then using equation 2.26 we calculate the appropriate average as,

$$I_{\parallel}(t) \propto \int_0^{2\pi} \int_0^{\pi} d\phi \; \sin\theta \; d\theta \; \mathcal{I}_{\parallel}(\theta, \phi, t) \; W\left(\theta, \phi, t\right) \tag{2.29}$$

$$I_{\perp}(t) \propto \int_0^{2\pi} \int_0^{\pi} d\phi \; \sin\theta \; d\theta \; \mathcal{I}_{\perp}(\theta, \phi, t) \; W\left(\theta, \phi, t\right) \tag{2.30}$$

Furthermore, it can be shown that,

$$I_{\parallel}(t) = \left[\frac{1}{3} + \frac{4}{15}C_{2,0}(t)\right]K(t) \tag{2.31}$$

$$I_{\perp}(t) = \left[\frac{1}{3} - \frac{2}{15}C_{2,0}(t)\right]K(t) \tag{2.32}$$

Putting the calculated values for $I_{\parallel}(t)$ and $I_{\perp}(t)$ in equation 2.19, we can show that,

$$r(t) = \frac{2}{5} C_{2,0}(t) \tag{2.33}$$

From boundary and normalization condition we know that at time, t = 0, $C_{2,0}(t = 0) = 1$; thus,

$r(t = 0) = \frac{2}{5}$. Also, it must be true that K(t) $= I_{\parallel}(t) + 2I_{\perp}(t)$, since fluorescence is is emitted

along all three Cartesian axes Therefore, using anisotropy rather than the more commonly used

polarization, $P(t) = I_{\parallel}(t) - I_{\perp}(t)/I_{\parallel}(t) + I_{\perp}(t)$, one is always certain to normalize

depolarizing effects to the excited-state lifetime, which is the most trivial source of depolarization.

However, under the constraint that the rotational motion of the molecule is much longer than the

lifetime of the excited species, use of the polarization is acceptable. If one measures the

fluorescence with the analyzer set at some arbitrary angle, α, with respect to the direction of

parallel polarization, it can be shown that,

$$I_{\alpha}(t) = \cos^2\alpha \, I_{\parallel}(t) + \sin^2\alpha \, I_{\perp}(t) \tag{2.34}$$

Thus, to get true lifetime without any effect from rotational motion, one should orient the analyzer

at an angle of 54.7°, which is commonly known as "magic angle." Under this condition one can

decouple the lifetime, K(t), from the rotational motion. This is because 54.7° is the angle at which

the parallel intensity is equal to two times the perpendicular intensity. Furthermore, one can derive

a general equation which is independent of shape of the molecule or nature of the $<P_2>$ and is

directly the correlation function for the second Legendre polynomial of the dipole reorientation

angle:

$$r(t) = \frac{2}{5} \langle P_2[\hat{\mu}(0) \cdot \hat{\mu}(t)] \rangle \tag{2.35}$$

The fluorescence anisotropy, $r(t)$, at time t after the excitation of the fluorophore

can also be defined as[5]

$$r(t) = r_0 e^{-\frac{t}{\tau_r}} \qquad (2.36)$$

If the fluorophore can be considered as a rigid rotator, the τ_r can be calculated by the Stokes-Einstein-Debye relation:[6]

$$\tau_r = \frac{\eta V}{k_B T} \qquad (2.37)$$

Where η, V, k_B, and T are viscosity of solvent, molecular volume of the fluorophores, Boltzmann's constant, and the absolute temperature respectively. Equation 2.37 assumes a continuum model for the solvent. There is possibility that the rotational motion of a fluorophore is restricted and at time, $t = \infty$, there is a residual anisotropy (r_∞), then a one can rewrite the eqn 2.36 as,

$$r(t) = (r_0 - r_\infty) e^{-\frac{t}{\tau_r}} + r_\infty \qquad (2.38)$$

In the case of nonspherical molecules and when there are possibilities of having various angular movements, the *r(t)* can be represented by multiexponential functions as given in eqn 2.39

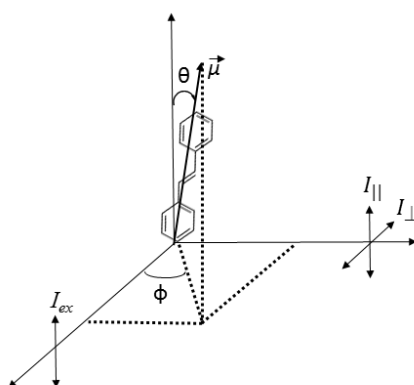$$r(\text{t}) = \sum_i r_i e^{-\frac{t}{\tau_{r(i)}}} \qquad (2.39)$$

Figure 4. Coordinate system used for fluorescence anisotropy. The dye is first excited by a polarized laser pulse. A second polarizer is placed before the detector at the parallel or perpendicular orientation with respect to that of the excitation polarizer.

Time-resolved fluorescence anisotropy of dye molecules in solution is a widely used technique for studying the tumbling or rotational motion of the molecule on the picosecond to nanosecond time scale.[5a] Information about the microscopic motions can also be recovered from time-dependent fluorescence anisotropy *r(t)*.[7]

Confocal and STED Microscopy.

In light microscopy, the resolution is defined by the minimum distance *r* at which two points can be distinguished. Quantitatively, by the Raleigh criterion, two point sources are regarded as just-resolved when the principal diffraction maximum of one image coincides with the first minimum of the other. Ernst Abbe first demonstrated that the diffraction of light determines the image resolution. In the lateral direction the resolution, r_{x-y}, is given as:

$$r_{x-y} = \frac{\lambda}{2 \cdot NA} \tag{2.40}$$

The axial (perpendicular to image plane) resolution, r_z, can be written as:

$$r_z = \frac{2 \cdot \lambda}{NA^2} \tag{2.41}$$

λ is the wavelength of light, and NA is the numerical aperture of the objective used. The resolution of optical instrumentation is also a function of the quality of the optics and of the stability of the instrumentation for the imaging platform. (The above mentioned diffraction limit holds for ideal optics and instrumentation. Under real laboratory situations, the resolution is often lower than that calculated.) Small excitation wavelengths and large NA-objectives contribute to better resolution. Optics with limited defects and very flat surfaces are necessary to approach diffraction-limited performance. As elucidated in the schematic given in **Figure 5c,** the flatness of a reflecting surface is important reducing distortion of the wave-front of the incident laser beam.[8] Such distortions affect the complex modes, such as a doughnut profile more

significantly.[9] Thus, high quality optical elements as thick as 6 mm have been used to minimize the degradation of beam profiles.[8, 10]

Two techniques, wide-field and raster scan, are generally used for the construction of an image. In wide-field imaging, a large sample area (on the order of 0.1 mm) can be observed. Whereas, in raster scanning, a specimen is scanned through a point of light by moving it in a raster pattern, that is, point-by-point; and subsequently an image is reconstructed (**Figure 5a** and **5b**). Thus, in raster scanning, often a long imaging time is required, depending on the image size, the number of pixels needed to create the image, and the time it takes to get the spectroscopic parameter of interest, such as lifetime at a single point. On the other hand, collection times for wide-field imaging can be much faster (ms-μs). Two types of cameras, charged-coupled device (CCD) and metal-oxide semiconductor (CMOS), are used for collection of a wide-field image. Avalanche photodiodes (APDs) and photo-multiplier tubes (PMTs) are used for raster scanning, as these detectors give the time information of the collected photons in addition to their number.[11] PMTs are often more suitable for measurements on the picosecond to nanosecond time scales. In wide-field imaging, the optics and the physical dimension of the camera sensor determine the pixel size (image area/number of pixels involved). In contrast, the pixel size in raster scanning can be easily varied by changing image size and the number of pixel.

The Nyquist criterion is usually taken into account during raster scanning. The Nyquist criterion limits the pixel size to be at least half the size of the spatial resolution of the instrument to preserve all the information content of the measurement.[12] Using a pixel size smaller than the Nyquist criterion does not enhance resolution of an image. This knowledge is critical to avoid unnecessarily long imaging times.
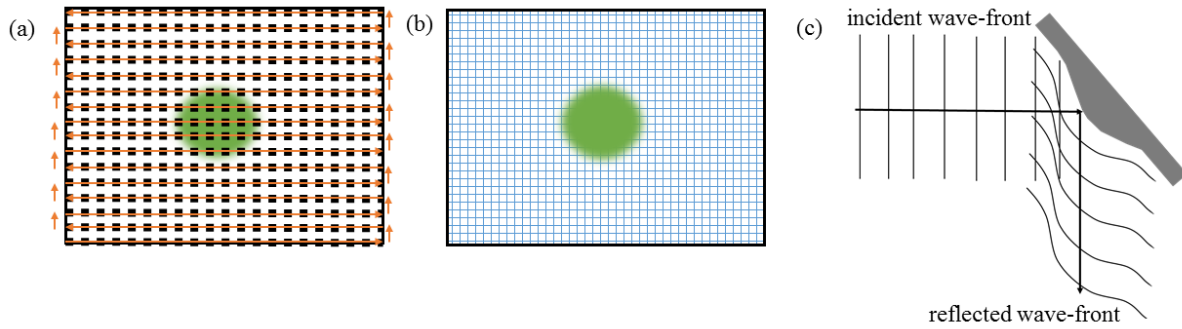
Figure 5. a) Shows point by point scanning, then from the information stored the whole image is reconstructed. b) Shows the wide-field imaging technique, where the whole image is collected together, c) Shows how imperfections on the surfaces of the optics can lead to wave-front distortion.

The confocal technique was first put forward by Minsky in 1957. There, the field of view is limited by a pinhole placed before detector. Thus, only light from the focal plane can reach the detector placed after the pinhole; and light from all other, out-of-focus planes is blocked, as shown in **Figure 6**. In the confocal fluorescence microscopy, the contribution from a point (x, y) to the signal is two-fold. In the first step, excitation light needs to illuminate the point (x, y), which can be represented by the illumination point-spread-function (PSF) $h_{ex}(x,y)$. Secondly, the fluorescence photons emitted from (x, y) have to propagate to the detector pinhole. This is described by a similar PSF, $h_{det}(x,y)$. Confocal imaging is determined by the product of both PSFs as:[13]

$$h_{conf}(x,y) = h_{ex}(x,y) \, \Theta \, h_{det}(x,y) \approx h_{ex}^2 \qquad (2.42)$$

The right-hand-side can be approximated when the Stokes shift is small compared to the excitation wavelength.

The squared single lens PSF nature of the fluorescence imaging has significant benefits, as can be seen by the following example. Let us assume that the illumination probability is 0.1

for a point. Thus, for confocal imaging this probability will contribute as squared, 0.01. This suggests the several advantages of such arrangements of optical components: light scattering from specimen is lowered reducing the blurring of image, improved signal to noise ratio, reduction of depth of field, possibility of Z-scan, and possibility quantitative studies of optical properties of the specimen.[14] The pinhole is mounted on the image plane and aligned with microscope axis. Thus, if it is misaligned or the pinhole size is lower than the corresponding size with a diffraction-limited spot, the number of collected photons is severely reduced. Therefore, an "optimum" aperture (rejecting the photons from the outer rings of the Airy disk) is required for effective operation of the confocal system. Furthermore, slight misalignment of the pinhole can induce aberration of the image. Polarization of the excitation beam also plays a vital role in the image. The output of many lasers might not be completely polarized. A linear polarized light can be obtained by passing the laser through a polarizer. However, with time, the intensity after the polarizer can vary as two polarization components can vary in proportion. An easy way to scramble the polarization is to use a quarter wave-plate before microscope. Image quality is also affected by vibration of the optical components. Floating table is used to dampen the vibration.

Intensity images can be used to obtain structural and morphological information,[15] and information about the properties such as diffusion rates of biological materials.[16] In addition pulsed-laser excitation can provide information about the excited-state lifetime of the emitters, which can be effected by different cellular conditions, such as pH[17] or proximity to other amino acids or nucleic acids.

Sub-diffraction Imaging Using Stimulated Emission Depletion. Although electron- and scanning-probe microscopy techniques can produce much higher resolution than the diffraction limit (~300 nm for λ_{ex} = 600 nm) in the visible spectral range, the investigation of living cells is not possible as the sample has to be dehydrated and kept in an evacuated chamber. Fluorescence

imaging techniques, however, can be carried out under physiological conditions with, often, an added benefit of simplified sample preparation. Sub-diffraction images can be constructed in the wide-field format by techniques such as stochastic optical reconstruction microscopy (STORM)[18] and photo-activated localization microscopy (PALM).[19] STORM[18d] and PALM[19a] take the advantage of the stochastic nature of "on" or "off" events from fluorescent labels or endogenous fluorophores. Fluorescence emission is localized with image reconstruction algorithms resulting in a spatial resolution of ~20 nm or better in the lateral direction.

To obtain sub-diffraction spatial resolution in raster imaging, stimulated emission depletion (STED)[20], and ground state depletion (GSD) have been used.[21] In these techniques, a doughnut-shaped beam is used to deplete the emission from the periphery of a Gaussian-shaped excitation beam, permitting the collection of signal only from the undepleted center (**Figure 6**). To achieve the doughnut shaped STED beam, the Gaussian beam is passed through a vortex phase plate which imprints a helical 0-2π phase ramp on the beam's wavefront and, subsequently, when the beam is focused, destructive interference leads to a central zero intensity region.[22] The emitters in the periphery of the Gaussian excitation beam go to the ground state by stimulated depletion in STED, to a higher-energy excited state in stimulated absorption, or to long-lived dark states in GSD. The signal intensity remaining at the doughnut's center can be made to be a sub-diffraction size.

The stimulated depletion under illumination by light with a wavelength that matches the energy gap between ground state (S_0) and first excited state (S_1) is the alternate relaxation pathway to spontaneous emission. Neglecting the vibrational relaxation rates, one can write:

$$\frac{d[S_1]}{dt} = k_{ex}[S_0] - (k_{SE} + k_{STE})[S_1] \qquad (2.43)$$

Where k_{ex}, k_{SE}, and k_{STE} are the rate constants for excitation, spontaneous emission, and stimulated emission, respectively; and $[S_0]$ and $[S_1]$ are the population in ground state and first excited state. Furthermore, we can write the individual rate constants as,

$$k_{ex}= \sigma_{ex}\cdot\gamma_{ex}\cdot I_{ex} \qquad (2.44)$$

$$k_{STE}= \sigma_{STE}\cdot \gamma_{STE}\cdot I_{STED} \qquad (2.45)$$

$$k_{SE}=1/\tau_{SE} \qquad (2.46)$$

Where σ, γ, I, and τ_{SE} are cross section, reciprocal photon energy, intensity, and fluorescence lifetime respectively. The stimulated emission rate can be tuned by changing the light intensity. Let us now assume, pulsed excitation and STED beam are applied successively. Usually, a temporal delay of tens of picoseconds is kept between the two pulses for optimum efficiency. We can write the initial conditions as $[S_1]$ (t_0) =1 and $[S_1]$ $(t = \infty) = 0$. Thus eqn 2.43 can be solved as

$$[S_1](t) = e^{-(k_{SE}+k_{STE})t} \qquad (2.47)$$

With a rectangular pulse with pulse width of τ_p , $[S_1]$ after each pulse can be expressed as

$$[S_1](I_{STED}) = e^{-k_{SE}\tau_p+k_{STE}\tau_p} \qquad (2.48)$$

This shows the STED can work efficiently under the condition, $k_{STE} \gg k_{SE}$.

The fwhm of the effective PSF resulting from the overlap of STED beam on the top of excitation beam gradually becomes narrower with increasing value of the saturation factor, $\xi = I_{STED}/I_{sat}$, where Isat is the STED intensity at which half of the initial fluorescence is depleted. The lateral resolutions can usually be obtained 50-nm regime with sufficient power in the depletion beam, though resolution down to ten nanometer has been reported.[21a, 23] In principle, unlimited resolution enhancement can be observed as I_{STED} reaches infinity. The lateral resolution in presence of the STED beam, Δr, at a given STED power can be calculated using the formula,

$$\Delta r = \frac{\lambda}{2n \, \sin \alpha \sqrt{1+\xi}} \tag{2.49}$$

The resolution of STED imaging can be further enhanced by time-gating the decay, that is, by removing photons from time channels that have not been completely or sufficiently depleted.[10, 20c, 24] It also ensures removal of fast scattered light and long-lived fluorescence background.

The biggest challenge in employing this technique is to obtain a perfect doughnut. It is very important that one obtains a doughnut where the intensity at the center is less than 1% of the intensity of the maxima. The doughnut and excitation profile uniformity and the overlap between STED and excitation beam, also play very vital roles to achieve best resolution. An optimal doughnut is ensured by checking the image obtained by scanning gold nanoparticles (~5 nm) with the doughnut beam. The relative timing of the excitation and STED beam is critical. Also, the polarization of both the beams should be the same. The depletion percentage should be calculated with different powers of the STED beam. Then considering possible photo-bleaching of the fluorophores, and background fluorescence from absorption of STED beam, an optimum power for STED imaging should be attained. The image resolution is checked by scanning commercially available fluorescence microsphere beads. Sometimes, astigmatism present in the optical systems result in enhancement of resolution only along one direction. Also, to remove artifacts from the outermost periphery of the excitation beam where the fluorescence have not been depleted, slightly under filling the objective can be proven beneficial. But one should remember that under filling the objective with excitation beam decreases resolution of a confocal image. Arguably, the most critical criteria of an efficient STED instrument is the stability of the optics and the laser profile, as movement as small as few nanometers can degrade the image resolution.
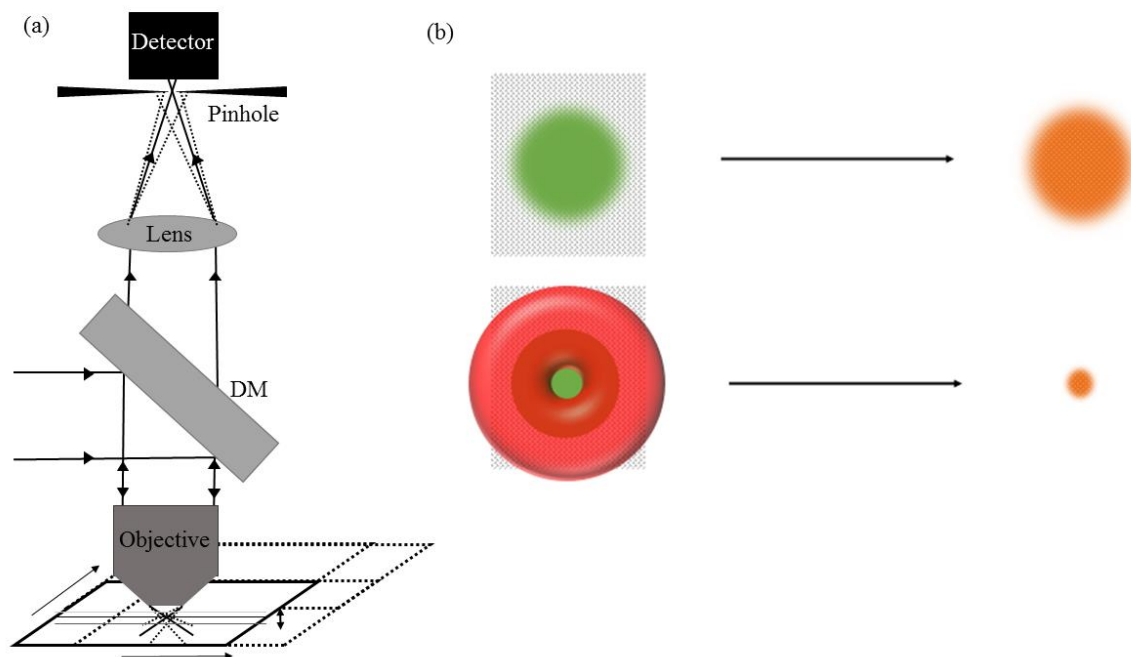
Figure 6. a) A schematic illustration of confocal scanning stage microscopy. b) A schematic diagram showing fwhm of the effective PSF decreases in STED imaging method.

Transient Absorption Spectroscopy and Time-resolved Emission Spectra (nanosecond).
Transient absorption in nanosecond regime is a widely used technique to study photo-physics of molecules, such as triplet-state (T_1) lifetimes in organic molecules, trap-state lifetimes in important materials, and kinetics of transient reaction intermediates. The peak intensity of the absorption spectra of such transient species is directly proportional with the population. The absorption at time t, is related to the transmitted light intensity by the expression: $A_t = -\log(I_t/I_0)$. Where, I_0 is the reference intensity when there is not any transient species, that is, before excitation with laser pulse. The time dependent absorbance can be fit to a sum of exponentials: $A_t = \sum_i a_i exp^{-k_i t}$. The average lifetime thus can be given as: $\tau = \sum_i 1/k_i$.

The nanosecond transient absorption instrument used in our laboratory is made of the following components. The pump source is a pulsed laser, Surelite II (Continuum). It is a Q-switch laser with pulse width of 5ns, repetition rate is 20 Hz and fundamental wavelength is 1064nm. The other harmonic wavelengths (532 nm, 355 nm, and 266 nm) can be produced using harmonic-generation crystal/s. As described earlier, proper phase matching condition is necessary to effectively produce higher-harmonic wavelengths. The laser wavelength is cleaned up by placing proper dichroic mirrors in the 45^0 arrangement as shown in the **Figure 7**. A collimated white light from a xenon lamp is used as a probe beam. Thus, the absorbance spectra in a broad range of wavelengths can be monitored. A UV filter is placed in the probe beam to minimize the sample degradation. The focused probe beam and the pump beam are spatially and temporally overlapped on the sample. Subsequently, unabsorbed light goes to spectrograph which splits the light into different wavelengths in different horizontal direction and their corresponding intensities are measured by an ICCD (intensified charge coupled device) camera. ICCD camera is a gated CCD camera, which is effective for time resolved experiments, where intensification takes place synchronously with laser excitation. CCD is a silicon-based semiconductor chip composed of a two-dimensional matrix of photo sensors, and each element correspond to a pixel of an image area. Higher the intensity, higher will be the charge stored. Subsequently, a full absorption is obtained at different times from the excitation pulse. Alternatively, this instrument can also be used to collect time-resolved emission spectra (TRES), only difference being the absence of the probe beam. Construction of TRES has been widely used to quantitatively describe solvation function. Although in nanosecond scale, solvation is rarely observed unless the solvent is highly viscous, the time dependent wavelength shift of the emission maxima can be utilized to characterize

emission from a trap state in inorganic materials. The emission spectra can be fit with multi-peak line shape functions and the different excitation recombination rates can be calculated.
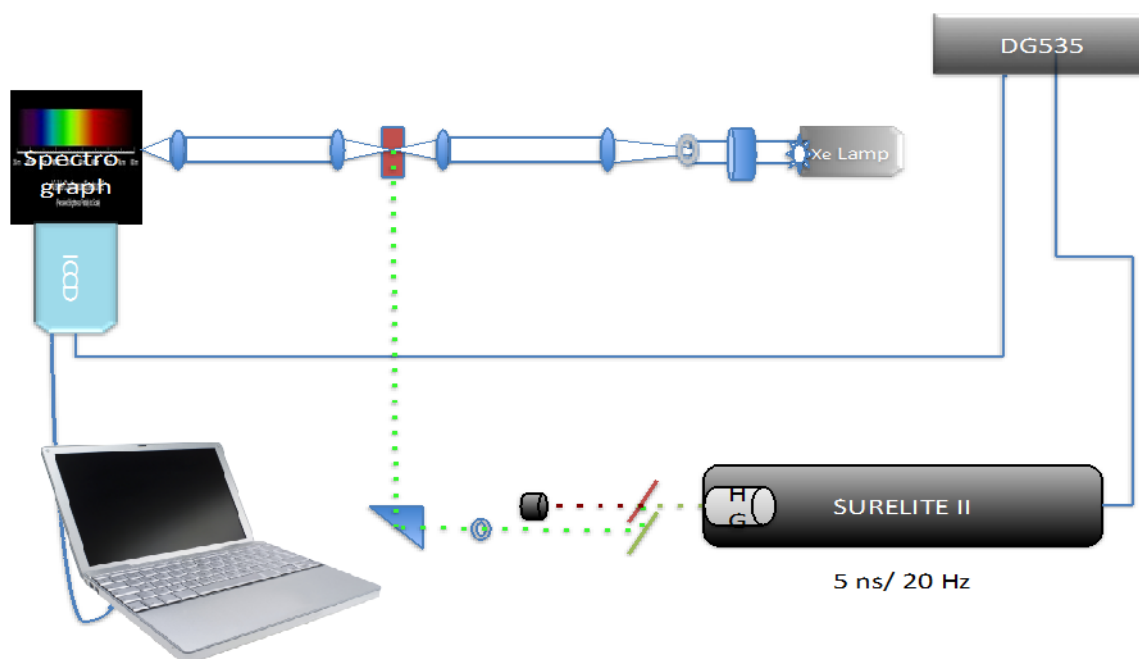
Figure 7. Schematic diagram of laser flash photolysis setup.

Q-switching. Q-switching is a widely used technique to generate short (nanosecond) pulses by modulating intra-cavity losses in laser cavity. As soon as the pumping begins inside the laser cavity, the population reaches a steady state, in the meantime, the laser beam starts growing and energy will come out of the system if gain is higher than the cavity losses and gain duration is sufficient. But as beam grows, stimulated emission takes place and inversion in population density starts to reduce to a lower steady state value where the reduced gain is equal to losses. Let us assume, t_s is the time required to reach the new equilibrium state. Typically the values of t_s range from 1 ns to 1μs. In solid-state lasers generally the upper level lifetime, τ_u is significantly higher than t_s. From the equation, $N_u = N_j\Gamma_{ju}/\gamma_u = N_j\Gamma_{ju}\tau_u$, where N_j is the density in the state j from which the energy is to be transferred, Γ_{ju} is the pumping rate from level j to upper level and γ_u is the decay

rate from the level u, laser cavities with such solid state gain medium the laser output reaches the

saturation intensity (I_{sat}) long before the upper state population, N_u reaches the maximum potential,

that is laser actually operates with gain much lower than the maximum possible value, when laser

cavity is not in place. So the trick is that if we pump the gain medium for τ_u without the cavity and

then suddenly switch the cavity in place, a momentary high-energy pulse can be produced. This

gain is well above the steady state gain. Thus, very quickly stimulated emission will get the hold

back, the laser output energy will die very quickly. This is known as Q switching. When the cavity

is not in place, it is with low Q and suddenly it switches to high Q when cavity is in place. To

produce high inversion in population in density to implement Q switching, one needs the following

requirements, (i) $\tau_u > t_s$, (ii) the pumping flux duration has to be longer than cavity buildup time, at

least for a duration of τ_u, (iii) initial cavity losses should be high enough for pumping duration so

that there is no beam growth, and (iv) switching process (low Q to high Q) should be fast enough

to extract the energy that was stored during low Q condition. Followings are the pictorial

representation of the Q-switching process.

Laser cavity rate equation can be given as[25]

$$\frac{d\phi}{dt} = \frac{c\phi g_0}{\eta}\left(\frac{L}{d}\right) - \frac{\phi}{t_c} \tag{2.50}$$

Where ϕ is the total number of photons with laser frequency v inside the laser cavity, t_c is cavity

decay time, η refractive index of the medium where laser beam is travelling, and L is cavity length.

Let us define $\tau = t/t_c$. Subsequently, the eqn 2.50 becomes,

$$\frac{d\phi}{d\tau} = \phi\left[\left(\frac{g_0}{\eta d/cLt_c}\right) - 1\right] = \phi\left(\frac{g_0}{g_{th}} - 1\right) \tag{2.51}$$

From eqn. 2.50, if $g_0 = g_{th}$, $d\phi/d\tau = 0$, that is g_{th} is a steady state gain in a continuous wave

laser. M is total population difference in the gain medium at any instant during Q-switching

process. M=ΔN_{ul}.V, where ΔN_{ul} is the population difference and V is mode volume within the gain

medium. Now if we replace gain by variable M in eqn. 2.50, as g_0/g_{th}= M/M$_{th}$ where M$_{th}$ total population inversion at threshold, i.e. when cavity gain equals the losses, we get

$$\frac{d\phi}{d\tau} = \phi\left(\frac{M}{M_{th}} - 1\right) \tag{2.52}$$

When a photon is emitted by stimulated emission, the population of upper state decreases by 1 and population of ground state increases by 1, so overall change in population is by a factor of 2, Thus we can write,

$$\frac{dM}{d\tau} = -2\left[\phi\frac{M}{M_{th}}\right] \tag{2.53}$$

From eqn 2.52 and 2.53 we can conclude that rate of decrease in population inversion is twice that of increase in number of photons due to stimulated emission. Now dividing eqn 2.52 by equation 2.53 we get

$$\frac{d\phi}{dM} = \left(\frac{M_{th}}{2M} - \frac{1}{2}\right) = \frac{1}{2}\left(\frac{M_{th}}{M} - 1\right) \tag{2.54}$$

Integrating the above equation we get

$$\phi - \phi_0 = \frac{1}{2}\left[M_{th}\ln\frac{M}{M_0} - (M - M_0)\right] \tag{2.55}$$

M_0 is the initial population difference; and if we assume ϕ_0 is zero, we can get the equation that describes the relation of number of photon in the cavity to the inverted population at any instant of time. Again, for a time t>>t_c there will no photon exist in the cavity, so we can write the equation as

$$\frac{M_f}{M_0} = e^{(M_f - M_0)/M_{th}} \tag{2.56}$$

Which leads to the equation, which gives the fraction of initial energy that is converted to laser energy,

$$\frac{M_0 - M_f}{M_0} = 1 - e^{(M_f - M_0)/M_{th}} \tag{2.57}$$

This clearly suggests higher the M_0 is before the Q switching; more energy can be extracted from the cavity as laser pulse.

Q-Switching by Electro-Optic Shutter. Inside the laser cavity laser is forced to operate on only one polarization. The beam propagating within the cavity makes double pass through the Pockels cell (PC) and a quarter wave plate ($\lambda/4$). When there is no voltage in the Pockels cell, it does not add any rotation to the polarization, only the $\lambda/4$ adds $45°$ rotation during one pass. Thus, after two passes the beam comes

back to polarizer with $90°$ rotated polarization, thus gets rejected and hence, no oscillation takes place. But during high Q condition, PC with 3600V also adds $45°$ rotation to the polarization, thus after double pass through $\lambda/4$ and PC, total rotation is $180°$, thus horizontal polarization comes back as horizontal polarization, thus oscillation takes place.
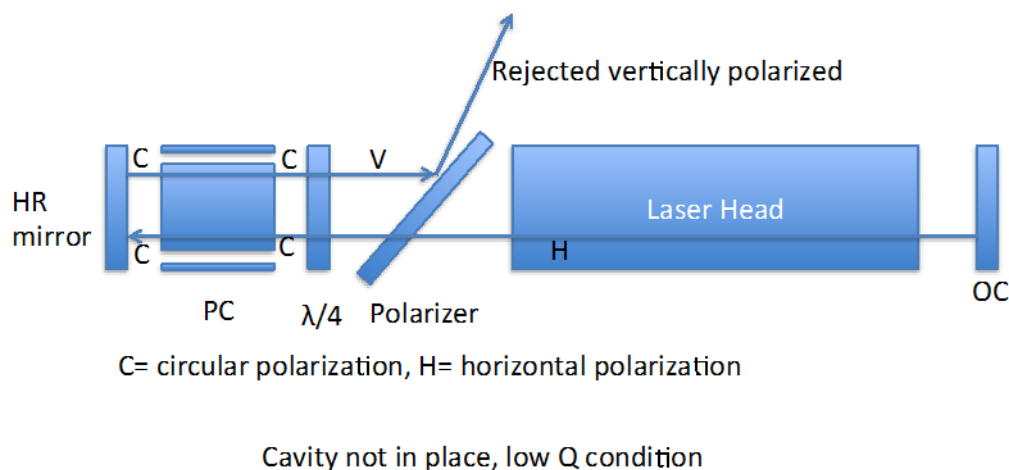

Figure 7. A schematic diagram of Q-switching by electro-optic shutter. HR, high reflector; OC, output coupler; PC, Pockels cell; $\lambda/4$, quarter wave plate.

References

1.   (a) Tkachenko, N. V.; Lemmetyinen, H., *Springer Ser. Fluoresc.* **2008,** *5*, 195; (b) Holzwarth, A. R., *Meth. Enzymol.* **1995,** *246*, 334.

2. (a) Becker, W., *Advanced time-correlated single photon counting techniques*. Springer: Berlin: New York, 2005; (b) O'Connor, D. V.; Phillips, D., *Time-correlated single photon counting*. Academic Press: Orlando, Florida, 1984.

3. Tkachenko, N. V., *Optical spectroscopy : methods and instrumentations*. 1st ed.; Elsevier: Amsterdam: Boston, 2006.

4. (a) Cross, A. J.; Fleming, G. R., *Biophysical Journal* **1984,** *46*, 45-56; (b) Fleming, G. R.; Morris, J. M.; Robinson, G. W., *Chemical Physics* **1976,** *17*, 91-100.

5. (a) Fleming, G. R., Chemical Applications of Ultrafast Spectroscopy. University Press: Oxford, London, 1986; (b) O'Connor, D. V.; Phillips, D., *Time-correlated single photon counting*. Academic Press: Orlando, Florida, 1984; (c) Fleming, G. R.; Knight, A. E. W.; Morris, J. M.; Robbins, R. J.; Robinson, G. W., *Chem. Phys. Lett.* **1977,** *51*, 399.

6. Van Holde, K. E.; Johnson, W. C.; Ho, P. S., Prentice Hall: New Jersey, 1998.

7. Maiti, N. C.; Krishna, M. M. G.; Britto, P. J.; Periasamy, N., *J. Phys. Chem. B* **1997,** *101*, 11051.

8. Lauterbach, M., *Fast STED Microscopy*. Universität Göttingen, Göttingen, 2009.

9. Boruah, B. R.; Neil, M. A., *Optics Express* **2006,** *14*, 10377-10385.

10. Lesoine, M. D.; Bhattacharjee, U.; Guo, Y.; Vela, J.; Petrich, J. W.; Smith, E. A., *The Journal of Physical Chemistry C* **2013,** *117*, 3662- 3667.

11. (a) Auksorius, E.; Boruah, B. R.; Dunsby, C.; Lanigan, P. M. P.; Kennedy, G.; Neil, M. A. A.; French, P. M. W., *Opt. Lett.* **2008,** *33*, 113-115; (b) Bückers, J.; Wildanger, D.; Vicidomini, G.; Kastrup, L.; Hell, S. W., *Opt. Express* **2011,** *19*, 3130-3143.

12. (a) *The Digital Image. In Optical Imaging Techniques in Cell Biology*. CRC Press: 2006; (b) Gao, Y.; Grey, J. K., *Journal of the American Chemical Society* **2009,** *131*, 9654-9662.

13.   (a) Wilson, T., *Confocal Miccroscopy*. Academic Press: London, 1990; (b) Wilson, T.; Sheppard, C. J. R., Theory and Practice of Scanning Optical Microscopy. Academic Press: London, 1984.

14.   *Handbook of Biological Confocal Microscopy*. Plenum Press: New York, 1990.

15.   (a) Madisen, L.; Zwingman, T. A.; Sunkin, S. M.; Seung Wook, O.; Zariwala, H. A.; Hong, G.; Ng, L. L.; Palmiter, R. D.; Hawrylycz, M. J.; Jones, A. R.; Lein, E. S.; Hongkui, Z., *Nature Neuroscience* **2010,** *13*, 133-140; (b) Eng, J.; Lynch, R. M.; Balaban, R. S., *Biophysical Journal* **1989,** *55*, 621-630.

16.   Arora, N.; Mainali, D.; Smith, E. A., *Analytical & Bioanalytical Chemistry* **2012,** *404*, 2339-2348.

17.   (a) Tantama, M.; Hung, Y. P.; Yellen, G., *Journal of the American Chemical Society* **2011,** *133*, 10034-10037; (b) Islam, M.; Honma, M.; Nakabayashi, T.; Kinjo, M.; Ohta, N., *International Journal of Molecular Sciences* **2013,** *14*, 1952-1963; (c) Orte, A.; Alvarez-Pez, J. M.; Ruedas-Rama, M. J., *ACS Nano* **2013,** *7*, 6387-6395.

18.   (a) Bates, M.; Huang, B.; Dempsey, G. T.; Zhuang, X., *Science* **2007,** *317*, 1749- 1753; (b) Huang, B.; Jones, S. A.; Brandenburg, B.; Zhuang, X., *Nat. Meth.* **2008,** *5*, 1047-1052; (c) Huang, B.; Wang, W.; Bates, M.; Zhuang, X., *Science* **2008,** *319*, 810-813; (d) Rust, M. J.; Bates, M.; Zhuang, X., *Nat. Meth.* **2006,** *3*, 793-796.

19.   (a) Betzig, E.; Patterson, G. H.; Sougrat, R.; Lindwasser, O. W.; Olenych, S.; Bonifacino, J. S.; Davidson, M. W.; Lippincott-Schwartz, J.; Hess, H. F., *Science* **2006,** *313*, 1642-1645; (b) Boldt, K.; Bruns, O. T.; Gaponik, N.; Eychmüller, A., *The Journal of Physical Chemistry B* **2006,** *110*, 1959-1963.

20.   (a) Klar, T. A.; Hell, S. W., *Opt. Lett.* **1999,** *24*, 954-956; (b) Hell, S. W.; Wichmann, J., *Opt. Lett.* **1994,** *19*, 780-782; (c) Syed, A.; Lesoine, M. D.; Bhattacharjee, U.; Petrich, J. W.; Smith, E. A., *Photochemistry and Photobiology* **2014**.

21.   (a) Bretschneider, S.; Eggeling, C.; Hell, S. W., *Physical Review Letters* **2007,** *98*, 218103; (b) Hell, S. W.; Kroug, M., *Appl. Phys. B* **1995,** *60*, 495-497.

22.   Keller, J.; Schönle, A.; Hell, S. W., *Opt. Express* **2007,** *15*, 3361–3371.

23.   (a) Wildanger, D.; Medda, R.; Kastrup, L.; Hell, S. W., *Journal of Microscopy* **2009,** *236*, 35-43; (b) Wildanger, D.; Rittweger, E.; Kastrup, L.; Hell, S. W., *Opt. Express* **2008,** *16*, 9614-9621; (c) Willig, K. I.; Kellner, R. R.; Medda, R.; Hein, B.; Jakobs, S.; Hell, S. W., *Nat. Methods* **2006,** *3*, 721-723; (d) Willig, K. I.; Keller, J.; Bossi, M.; Hell, S. W., *New Journal of Physics* **2006,** *8*, 106.

24.   Lesoine, M. D.; Bose, S.; Petrich Jacob, W.; Smith, E. A., *J. Phys. Chem. B* **2012,** *116*, 7821-7826.

25.   Silfvast, W. T., *Laser Fundamentals*. 2nd ed.; Cambridge University Press: 2004.

CHAPTER 3a. TRYPTOPHAN AND ATTO 590: MUTUAL FLUORESCENCE QUENCHING AND EXCIPLEX FORMATION

A paper published in The *Journal of Physical Chemistry B*

Ujjal Bhattacharjee,[1,2] *Christie Beck,*[1] *Arthur Winter,*[1] *Carson Wells,*

and *Jacob W. Petrich**[1,2]

ABSTRACT

Investigation of fluorescence quenching of probes, such as ATTO dyes, is becoming an increasingly important topic owing to the use of these dyes in super-resolution microscopies and in single-molecule studies. Photoinduced electron transfer is their most important nonradiative pathway. Because of the increasing frequency of the use of ATTO and related dyes to investigate biological systems, studies are presented for inter- and intra-molecular quenching of ATTO 590 with tryptophan. In order to examine intra-molecular quenching, an ATTO 590-tryptophan conjugate was synthesized. It was determined that tryptophan is efficiently quenching ATTO 590 fluorescence by excited-state charge transfer and two charge transfer complexes are forming. In addition, it was discovered that an exciplex (whose lifetime is 5.6 ns) can be formed between tryptophan and ATTO 590, and it is suggested that the possibility of such exciplex formation should be taken into account when protein fluorescence is monitored in a system tagged with ATTO dyes.

─────────────────────────

[1]Department of Chemistry, Iowa State University, Ames, IA

[2]U.S. Department of Energy Ames Laboratory, Ames, IA

* To whom correspondence should be addressed. Email: jwp@iastate.edu

KEYWORDS

Fluorescent probe, electron transfer, ATTO dyes, ATTO-Tryptophan conjugate, Stern-Volmer, excited-state potential energy surface.

INTRODUCTION

Because of their experimentally desirable features of, for example, high quantum yield and photochemical stability, ATTO dyes such as ATTO 590 (**Figure 1**) are finding ever growing applications as probes for biological studies using fluorescence-based techniques[1-3] in, for example, super-resolution microscopies[4-6] and single-molecule measurements.[7-9] It is important, however, to understand how possible interactions with the environment can affect the ATTO photophysics. Marmé *et al*. observed fluorescence quenching of red absorbing ATTO dyes in the presence of amino acids.[10] They noted that tryptophan proved to be the most efficient quencher of ATTO fluorescence. They attributed the quenching to the production of a ground-state ATTO-tryptophan complex, which they concluded was nonfluorescent. This conclusion was based upon their observation that static quenching is dominant. Zhu *et al*. carried out transient absorption experiments of ATTO 655 in the presence of tryptophan in aqueous solution.[11] Assuming that the standard redox potential of the oxazine dye (MR 121) is similar to that of ATTO 655, they searched for photoinduced electron transfer from tryptophan to ATTO 655. They, however, were unable to find any evidence of a charge separated species, thus concluding that it decayed faster than the time resolution of their instrument, 150 fs. Using a similar system, Yu and coworkers reported two charge separation rates, which they interpreted in terms of two different charge-separated complexes.[12]

Stimulated by these studies, we performed further experiments with ATTO 590 in order to elucidate inter- and intramolecular quenching processes with tryptophan. Our results do not

support the existence of nonfluorescent ground-state complexes in the concentration range investigated, but they are consistent with excited-state electron transfer being the predominant mechanism for fluorescence quenching. Unfortunately, the time resolution of our transient absorption spectrometer was not sufficient to observe the charge separated species.

In the course of these studies, we also investigated the quenching of *tryptophan fluorescence* by ATTO 590, which quenches fluorescence very efficiently by means of formation of an exciplex in ATTO-tryptophan conjugate. This is consistent with the work of Rivarola *et al.*, reported exciplex formation of excited-state indole derivatives and monosubstituted benzenes in cyclohexane.[13] (In the case of benzonitrile and chlorobenzene, a charge transfer interaction with indole is, however, suggested to be more likely.) In a similar study by Previtali and coworkers, indole derivatives including tryptophan were found to form exciplexes in solutions of reverse micelles solutions made with the cationic surfactant benzylhexadecyldimethylammonium chloride in benzene, particularly at low molar ratio water/surfactant.[14] There is also evidence of exciplex formation with tryptophan and alcoholic solvents.[15-17] To our knowledge, our report is the first of tryptophan exciplex formation with a commonly used fluorescent label, ATTO 590, in aqueous solution. This finding is particularly relevant for a thorough and correct interpretation of fluorescence data in biological systems tagged with such dyes.

EXPERIMENTAL

Materials. ATTO 590 (free carboxy acid) was purchased from ATTO-TEC GmbH, Siegen, Germany, and L-tryptophan was purchased from Sigma Aldrich. They were used as received. All the experiments were done in 10-mM phosphate buffer at pH 7.

Preparation of the Conjugate of ATTO 590 and Tryptophan. 0.3 mg (0.0015 mmol) L-tryptophan was dissolved in 1 mL of 1-M NaHCO₃ solution. 0.5 mg (0.00063 mmol) of ATTO

590 NHS ester, dissolved in 50 µL DMF, was added to the reaction vessel. After 2.5 hours of stirring at ambient temperature in the dark, the solvent was removed *in vacuo*. The product was purified on a preparatory TLC plate (1000 microns, Analtech Silica) in the dark in 1:1 MeOH:CHCl$_3$. The bottom fluorescent spot (R_f = 0.44) was isolated. EI/MS, formula C$_{48}$H$_{49}$N$_4$O$_6$ requires mass of 777.3652 (observed, 777.3646).

Steady-State Measurements. Absorbance was recorded with an Agilent 8453 UV Vis spectrometer with 1-nm resolution. Steady-state fluorescence measurements were done with a Spex Fluoromax-4 with a 3- or 4-nm bandpass and corrected for lamp spectral intensity and detector response. To avoid reabsorption, reemission effects or dye aggregation, concentrations were kept near 1 µM in all measurements.

Lifetime Measurements. Measurements of excited state lifetimes were carried out with the time-correlated single-photon counting (TCSPC) technique. The apparatus for time-correlated single-photon counting is described elsewhere.[18] The fundamental from a homemade mode-locked Ti-sapphire oscillator was modulated by a Pockels cell (model 350-160, Conoptics Inc.) to reduce the repetition rate to 8.8 MHz. An excitation wavelength of 415 nm or 266 nm was used. The second and third harmonics were obtained from the 830 nm fundamental by means of a U-Oplaz Technologies (Model TP-2000B) doubler/tripler. Recently a Becker & Hickl photon counting module (model SPC-630) has been employed. With the system described, the full-width at half-maximum of the instrument response (IRF) is ∼40-50 ps. Generally, for lifetime experiments 65,000 counts were taken in the peak channel unless it mentioned. A cuvette of 3-mm or 1-cm path length was used for the time-resolved measurement, depending upon the sample. Different filters were also chosen to see fluorescence decay of a particular band. The

decay parameters were determined by fitting to a sum of exponentials after deconvolution of instrument response function.

Calculations. DFT computations (B3LYP/ STO-3G) were used to compute the energies of the ATTO-Trp conjugate. A PCM water solvation model was employed. At this low level of theory, the energies may be underestimated due to DFT having difficulties calculating dispersion forces. The computed lowest energies for the 5' and 6' open and stacked forms of the conjugate are shown (Supplementary Material), along with their energies (in kcal/mol) and energy differences between the open and stacked forms. The energy differences of the open and stacked forms of both isomers lie within 5 kcal/mol, which is within the measurable error of Gaussian. Because of this, it is difficult to draw quantitative conclusions about the conformations. On the other hand, the calculations are consistent with the notion that the ATTO-Trp conjugate can exist in many conformations, including those that are stretched and stacked. We invoke such geometries in our discussion of lifetime data below. All DFT computations were done with Gaussian 09. The hybrid B3LYP functional was used, which consists of the Becke three-parameter exchange functional[19] with the correlation functional of Lee, Yang, and Parr.[20]

RESULTS AND DISCUSSION

Steady-State Measurements. **Figure 2** presents the absorption spectra of ATTO 590 in pH 7 buffer in the presence and absence of tryptophan. Marmé *et al.* proposed formation of a nonfluorescent ground-state complex responsible for static quenching of tryptophan and ATTO 590.[10] They calculated the association constant, K, to be 50, which implies that in a mixture of 50-mM tryptophan and a micromolar solution of ATTO dye, about half of the ATTO 590 should exist in complexed form. As it is very unlikely that the ATTO monomer and an ATTO-Trp complex would have the same absorption spectra, we would expect a noticeable change in the

absorption spectra in the presence of 50-mM tryptophan. This, however, was not the case. The absorption spectra of ATTO 590 are essentially the same regardless of the concentration of tryptophan in pH 7 buffer, from which we conclude that there is no significant formation of a ground-state complex. Furthermore, even for the ATTO-tryptophan conjugate, where ground-state complex formation would have been more facile, the ATTO 590 monomer absorption spectrum is conserved.

The situation of ATTO 590 and tryptophan in this work stands in clear contrast to, for example, the documented example of oxazine and tryptophan, examined by Sauer and coworkers[21], which do form a ground-state complex, as evidenced by about a 10-nm red shift in the absorption of oxazine as the concentration of tryptophan is increased from 0 to 50 mM. Over this range of tryptophan concentration, the absorption spectrum of oxazine also changes in shape and intensity. On the other hand, the spectra of ATTO 590 are unchanged both in shape and intensity within the resolution of our absorption spectrometer ($\pm$ 1 nm) over the entire range of tryptophan concentration and in the ATTO 590-tryptophan conjugate (**Figure 2**).

On the other hand, the possibility of excited-state charge transfer is possible when the two chromophores are sufficiently near. Namely, the fluorescence spectra of the conjugate and of ATTO 590 in the presence or absence of tryptophan show one emission maximum at 610 nm for excitation at any wavelength corresponding to absorption by the ATTO 590 chromophore. When, however, the conjugate is excited (at λ_{ex} = 266 nm), a new fluorescence band with a maximum at 455 nm (**Figure 3**) is observed; and, simultaneously, the "normal" fluorescence maximum of tryptophan, ~350 nm, is strongly quenched. We did not observe the same band with ATTO 590 dissolved in 50-mM tryptophan solution in pH 7-buffer, which is not surprising, as the average distance between ATTO 590 and Trp is greater (~60 Å) than that in the conjugate

(~10 Å), in other words, 50-mM is not concentrated enough compared to the "effective concentration" of tryptophan in the conjugate, which is estimated to be ~110 mM by inspection of the Stern-Volmer plot (**Figure 5**).

The excitation spectra of the conjugate are given in **Figure 4**. When emission is collected at 630 nm, the excitation spectrum agrees very well with the ATTO 590 absorption spectrum. But when the emission is collected at 460 nm, the excitation spectrum differs completely from the absorption spectrum. This indicates that an exciplex is forming between tryptophan and ATTO 590. This band is not a result of excimer formation between two tryptophans as is demonstrated by its absence in a solution of 50-mM tryptophan containing no ATTO 590 (**Figure 3**).

Di Mascio and coworkers[22] have observed spectra similar to that displayed in **Figure 3** for photo-oxidized tryptophan. It is highly unlikely that our spectrum arises from such a product. The experimental conditions employed in this work are considerably different than ours. Di Mascio and coworkers irradiate their sample with 500 W for 3 hours. They also maintain their sample in an environment that is very rich in oxygen. On the other hand, we excite our sample with only a 3- or 4-nm bandpass of very low intensity light in a fluorometer; and the spectrum is acquired in a few minutes. In addition, we obtain the *same* spectrum when the sample is deoxygenated (**Figure 5**).

Time-Resolved Experiments. **Table I** summarizes excited-state lifetime data for ATTO 590 as a function of tryptophan concentration and makes comparisons with the ATTO-Trp conjugate and ATTO-phalloidin (**Figure 1b**), a commonly used probe in biological studies.[6] The weights for the shortest and the intermediate lifetimes of ATTO 590 increase with increasing tryptophan concentration. A Stern-Volmer plot was constructed from the data in **Table I** quantifying the

quenching efficiency of tryptophan. A quenching constant of 0.03 ± 0.01 M^{-1} was obtained (**Figure 6a**). The ATTO-Trp conjugate and the ATTO-phalloidin are also included on this plot, for completeness, to provide an indication of the "effective concentration" of tryptophan in the two complexes. (The same Stern-Volmer plot was constructed from the steady-state data. As the steady-state data are simply the time integrals of the time-resolved data, and as the quenching constant obtained from the time-resolved data is obtained from the *average lifetime*, which is identical to the fluorescence quantum yield, it is not surprising that the steady-state Stern-Volmer plot yields exactly the same result (**Figure 6b**)).

Table II and Table III present the lifetimes of the ATTO-50-mM Trp mixture and ATTO-Trp conjugate respectively as a function of temperature. In pH 7 buffer, uncomplexed ATTO has a single-exponential and *temperature independent* lifetime of 3.7 ns. Addition of tryptophan to the ATTO solution shortens the ATTO lifetime.

In order to simplify the analysis, it was convenient and instructive to use the temperature dependent lifetimes of the ATTO-50-mM Trp mixture as a model. The data were always well fit to the same three lifetime components with varying weights. Namely, there is always a 400-ps component in the presence of tryptophan; unquenched ATTO provides a 3.7-ns component, as stated above; and there is a component of intermediate duration, which is well described by 1.9 ns. These lifetime components are all well reproduced by the ATTO-Trp conjugate, which serves as a self-consistency check of the analysis, only the intermediate lifetime component was 1.0 ns for conjugate. The transient data, along with the absorption and excitation spectra referred to earlier are inconsistent with the claim [10] of the formation of a *nonfluorescent* ground-state complex, whose presence would be expected to generate a single-exponential fluorescence decay whose intensity, but not lifetime, decreased with increasing tryptophan concentration.

We interpret the weights of the lifetimes, a_1, a_2, and a_3, to be directly proportional to three types of ground-state configurations between ATTO and Trp: a_1, to configurations in which charge transfer does not occur at all; a_3, to a configuration in which charge transfer is as rapid as it can be (400 ps); and a_2, to intermediate configurations in which charge transfer is possible but is not as efficient as in a_3. Consequently, plots of $\ln(a_i/a_j)$ vs. $1/T$ can be used to obtain the standard free energy differences among these three populations (**Figures 7a and b**). **Table IV** summarizes the values of standard thermodynamic quantities obtained from the fits.

We performed lifetime measurement of the ATTO 590-Trp conjugate using $\lambda_{ex} = 415$ nm and 266 nm (**Figure 8a**). No excitation-wavelength dependence was observed when only fluorescence from ATTO 590 was monitored. But when $\lambda_{ex} = 266$ nm and $\lambda_{em} = 400\text{-}530$ nm, a lifetime 5.6 ns was observed (**Figure 8b**). (In this case, 20,000 counts were obtained in the peak channel for the lifetime owing to the lower fluorescence intensity). A growth (or induction) time should be observed for the transient fluorescence of an exciplex, corresponding to its formation; but we only observe an exponential decay, indicating that the exciplex is formed too rapidly to be detected with our instrumentation. With 266 nm excitation, either tryptophan or ATTO 590 is excited. When tryptophan is excited, it forms an exciplex with ATTO 590; and when ATTO is excited it follows the same decay path as obtained with 415 nm excitation.

Finally, as there is large overlap between the absorption spectrum of ATTO 590 and the fluorescence spectrum of tryptophan, there is also a possibility of fluorescence resonance energy transfer (FRET). But with the time resolution of our instrument we could not find any growth time in ATTO 590 fluorescence exciting at 266 nm.

The data from **Tables I-IV** are summarized schematically by the potential energy surface given in **Figure 9.**

CONCLUSIONS

Stimulated by the work of Marmé *et al*. we monitored the quenching of ATTO 590 by tryptophan. Seeing no change in absorption spectra in presence of tryptophan, we can conclude that there is not any ground state complex formation. We saw three-exponential decays in presence of tryptophan. The fast component of the three-exponential decays is attributed to a conformation which form the most effective the charge-separated species among the other conformations. We found out that when tryptophan is excited, it forms an exciplex in presence of ATTO dyes and the lifetime of the exciplex is 5.6 ns, this is potentially responsible for quenching of tryptophan fluorescence by ATTO 590. This exciplex fluorescence should be taken into account for monitoring tryptophan fluorescence in presence of tagging ATTO dyes. This information can also be utilized to detect proximity of tryptophan to the ATTO labels in biological systems, though a detailed study would be required to conclude something quantitatively.

ACKNOWLEDEMENTS

REFERENCES

1. Lehmann, A. D.; Parak, W. J.; Zhang, F.; Ali, Z.; Roecker, C.; Nienhaus, G. U.; Gehr, P.; Rothen-Rutishauser, B. Fluorescent–Magnetic Hybrid Nanoparticles Induce a Dose-Dependent Increase in Proinflammatory Response in Lung Cells in Vitro Correlated with Intracellular Localization. *Small* **2010**, *6*, 753-762.

2. Salerno, D.; Daban, J.-R. Comparative Study of Different Fluorescent Dyes for the Detection of Proteins on Membranes Using the Peroxyoxalate Chemiluminescent Reaction. *Journal of Chromatography B* **2003**, *793*, 75-81.

3. Freeman, R.; Finder, T.; Gill, R.; Willner, I. Probing Protein Kinase (CK2) and Alkaline Phosphatase with CdSe/ZnS Quantum Dots. *Nano Lett*. **2010**, *10*, 2192-2196.

4. Rittweger, E.; Rankin, B. R.; Westphal, V.; Hell Stefan, W. Fluorescence Depletion Mechanisms in Super-Resolving Sted Microscopy. *Chemical Physics Letters* **2007**, *442*, 483-487.

5. Heilemann, M.; Van de Linde, S.; Mukherjee, A.; Sauer, M. Super-Resolution Imaging with Small Organic Fluorophores. *Angewandte Chemie, International Edition* **2009**, *48*, 6903-6908.

6. Lesoine, M. D.; Bose, S.; Petrich Jacob, W.; Smith, E. A. Supercontinuum Stimulated Emission Depletion Fluorescence Lifetime Imaging. *J Phys Chem B* **2012**, *116*, 7821-7826.

7. In *Biophotonics 2007: Optics in Life Science*, Proceedings of SPIE- The International Society for Optical Engineering, Popp, J.; Bally, G. v., Eds. 2007; pp 66331Z/1-66331Z/12.

8. Ross, J.; Buschkamp, P.; Fetting, D.; Donnermeyer, A.; Roth, C. M.; Tinnefeld, P. Multicolor Single-Molecule Spectroscopy with Alternating Laser Excitation for the Investigation of Interactions and Dynamics. *Journal of Physical Chemistry B* **2007**, *111*, 321-326.

9. Miller, A. E.; Fischer, A. J.; Laurence, T.; Hollars, C. W.; Saykally, R. J.; Lagarias, J. C.; Huser, T. Single-Molecule Dynamics of Phytochrome-Bound Fluorophores Probed by Fluorescence Correlation Spectroscopy. *Proc. Natl. Acad. Sci.* **2006**, *103*, 11136-11141.

10. Marmé, N.; Knemeyer, J.-P.; Sauer, M.; Wolfrum, J. Inter- and Intramolecular Fluorescence Quenching of Organic Dyes by Tryptophan. *Bioconjugate Chemistry* **2003**, *14*, 1133–1139.

11. Zhu, R.; Li, X.; Zhao, X. S.; Yu, A. Photophysical Properties of Atto655 Dye in the Presence of Guanosine and Tryptophan in Aqueous Solution. *J. Phys. Chem. B* **2011**, *115*, 5001-5007.

12. Sun, Q.; Lu, R.; Yu, A. Structural Heterogeneity in the Collision Complex between Organic Dyes and Tryptophan in Aqueous Solution. *J. Phys. Chem. B* **2012**, *116*, 660-666.

13. Rivarola, C.; Bertolotti, S. G.; Borsarelli, C. D.; Cosa, J. J.; Previtali, C. M.; Neumann, M. G. Hydrogen Bonding and Charge Transfer Interactions in Exciplexes Formed by Excited Indole and Monosubstituted Benzenes in Cyclohexane. *Chemical Physics Letters* **1996**, *262*, 131-136.

14. Borsarelli, C. D.; Bertolotti, S. G.; Previtali, C. M. Exciplex-Type Behavior and Partition of 3-Substituted Indole Derivatives in Reverse Micelles Made with

Benzylhexadecyldimethylammonium Chloride, Water and Benzene *Photochemistry and Photobiology* **2001**, *73*, 97-104.

15. Vekshin, N.; Vincent, M.; Gallay, J. Excited-State Lifetime Distributions of Tryptophan Fluorescence in Polar Solutions. Evidence for Solvent Exciplex Formation. *Chem. Phys. Lett.* **1992**, *199*, 459-464.

16. Hershberger, M. V.; Lumry, R. W. The Photophysics of 5-Methoxyindole. A Non-Exciplex Forming Indole: Additional Evidence for Two Classes of Exciplexes. *Photochem. Photobiol.* **1976**, *23*, 391-397.

17. Hershberger, M. V.; Lumry, R. W.; Verall, R. The 3-Methylindole/N-Butanol Exciplexes: Evidence for Two Exciplex Sites in Indole Compounds. *Photochemistry and Photobiology* **1981**, *33*, 609-617.

18. Chowdhury, P. K.; Halder, M.; Sanders, L.; Calhoun, T.; Anderson, J. L.; Armstrong, D. W.; Song, X.; Petrich, J. W. Dynamic Solvation in Room-Temperature Ionic Liquids. *J Phys Chem B* **2004**, *108*, 10245-10255.

19. Becke, A. D. Density-Functional Exchange-Energy Approximation with Correct Asymptotic Behavior. *Physical Review A* **1988**, *38*, 3098-3100.

20. Lee, C. T.; Ynag, W. T.; Parr, R. G. Development of the Colle-Salvetti Correlation-Energy Formula into a Functional of the Electron Density. *Physical Review B* **1988**, *37*, 785-789.

21. Doose, S.; Neuweiler, H.; Sauer, M. A Close Look at Fluorescence Quenching of Organic Dyes by Tryptophan. *ChemPhysChem* **2005**, *6*, 2277-2285.

22. Ronsein, G. E.; Oliveira, M. C. B.; Miyamoto, S.; Medeiros, M. H. G.; Mascio, P. D. Tryptophan Oxidation by Singlet Molecular Oxygen [O_2 ($^1\Delta_g$)]: Mechanistic Studies

Using ^{18}O-Labeled Hydroperoxides, Mass Spectrometry, and Light Emission Measurements. *Chemical Research in Toxicology* **2008**, *21*, 1271-1283.

Table I. Fluorescence Lifetimes of ATTO 590

Species	τ_1 (ns)	a_1	τ_2 (ns)	a_2	τ_3 (ns)	a_3	$<\tau>$ (ns)
ATTO 590	3.7	1					
ATTO 590, 1.5 mM Trp	3.7	0.87	2.6	0.06	0.4	0.07	3.4
ATTO 590, 10 mM Trp	3.7	0.53	2.7	0.28	0.4	0.19	2.8
ATTO 590, 30 mM Trp	3.7	0.25	2.1	0.48	0.4	0.27	2.0
ATTO 590, 50 mM Trp	3.7	0.15	1.9	0.51	0.4	0.34	1.7
ATTO 590-Trp conjugate	3.7	0.08	1.0	0.53	0.4	0.39	1.0

Emission was collected at $\lambda_{em} > 550$ nm. The ATTO 590 concentration was maintained at 1 μM. Lifetime values have a ± 5% error. $<\tau>$ is proportional to the fluorescence quantum yield and is given by $<\tau> = \Sigma\, a_i\, \tau_i$.

Table II. Temperature Dependence of ATTO 590 Lifetimes in the Presence of 50-mM

Tryptophan

Temp (^{0}C)	τ_1 (ns)	a_1	τ_2 (ns)	a_2	τ_3 (ns)	a_3	$<\tau>$ (ns)
5	3.7	0.23	1.9	0.44	0.4	0.33	1.8
22	3.7	0.15	1.9	0.51	0.4	0.34	1.7
45	3.7	0.08	1.9	0.6	0.4	0.32	1.6
65	3.7	0.04	1.9	0.66	0.4	0.30	1.5
85	3.7	0	1.9	0.69	0.4	0.31	1.4

Table III. Temperature Dependence of ATTO 590-Trp Conjugate Lifetimes

Temp (^{0}C)	τ_1 (ns)	a_1	τ_2 (ns)	a_2	τ_3 (ns)	a_3	$<\tau>$ (ns)
5	3.7	0.11	1.0	0.64	0.4	0.25	1.2
22	3.7	0.08	1.0	0.53	0.4	0.39	1.0
45	3.7	0.07	1.0	0.29	0.4	0.64	0.8
65	3.7	0.06	1.0	0.16	0.4	0.78	0.7
85	3.7	0.05	1.0	0.10	0.4	0.86	0.6

Table IV. ΔG^0 obtained from the fit to plots of $\ln(a_i/a_j)$ vs. $1/T$ at 298 K [a]

ATTO-Trp conjugate

	ΔH^0 (kcal/mol)	ΔS^0 (kcal/mol-K)	ΔG^0 (kcal/mol)
$a_3 \leftrightarrow a_2$	8.0	0.027	0.006
$a_2 \leftrightarrow a_1$	- 3.1	- 0.007	-0.094
$a_3 \leftrightarrow a_1$	4.8	0.019	-0.090

ATTO-50-mM Trp mixture

	ΔH^0 (kcal/mol)	ΔS^0 (kcal/mol-K)	ΔG^0 (kcal/mol)
$a_2 \leftrightarrow a_3$	-1.8	-0.007	0.029
$a_1 \leftrightarrow a_2$	7.6	0.028	-0.074
$a_1 \leftrightarrow a_3$	5.5	0.020	-0.049

[a] a_1 corresponds to the species with the shortest lifetime, which is fixed in the fitting procedure to 0.4 ns; a_2, to a species with an intermediate lifetime, which is fixed to 1.9 or 1.0 ns, and a_3, to the unquenched lifetime of ATTO, which was determined to be 3.7 ns (see **Tables I-III**).

a)

b)
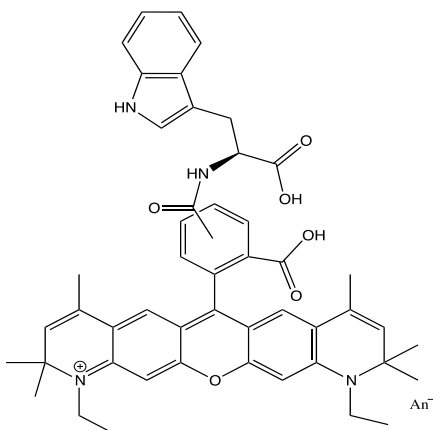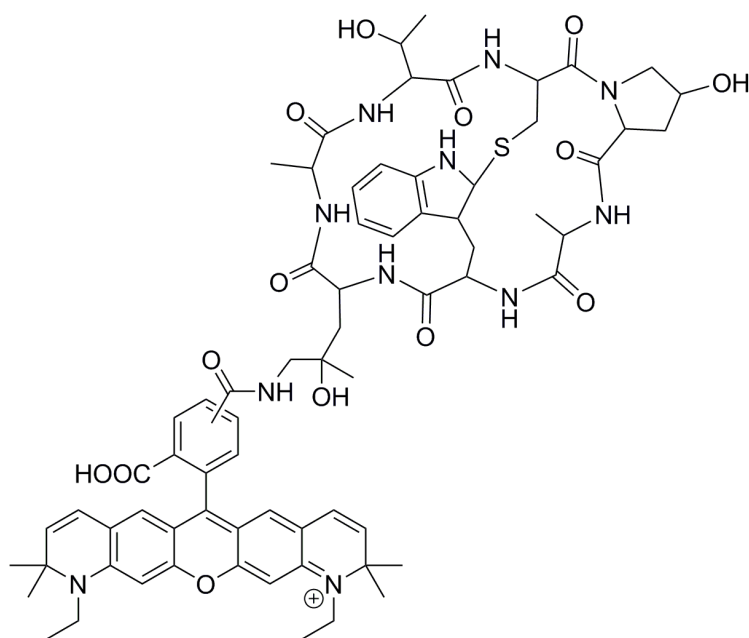
Figure 1.

a) Structure of the conjugate of ATTO 590 and L-tryptophan.

b) Structure of ATTO 590-phalloidin.
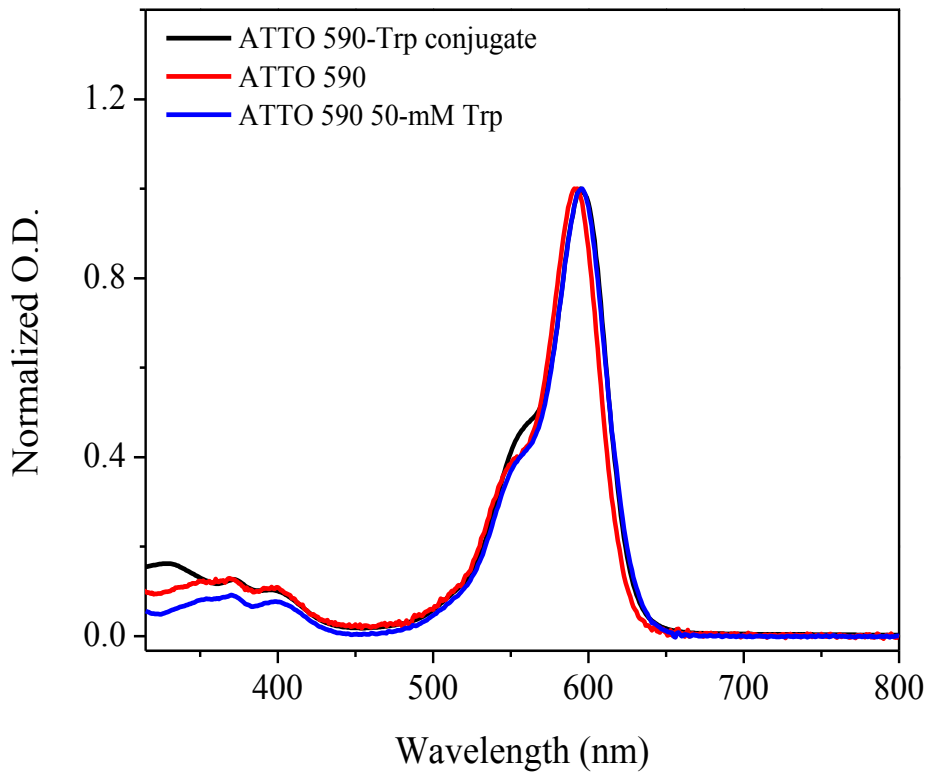
Figure 2.

Normalized absorption spectra of:

a) ATTO 590-tryptophan conjugate (black);

b) ATTO 590 (red);

c) ATTO 590 in the presence of 50-mM tryptophan (blue) in pH 7 buffer.

The concentration of ATTO 590 was kept constant at 1 μM. Spectrum c was collected by using

50-mM tryptophan as a blank. The spectra were normalized with respect to that of ATTO 590-

tryptophan conjugate. The maximum O.D. values were 0.119 and 0.118 for b and c, respectively.

That the optical density of the ATTO, or its spectrum, does not change as a function of

tryptophan concentration is important for eliminating the possibility of a ground-state complex between the two chromophores.
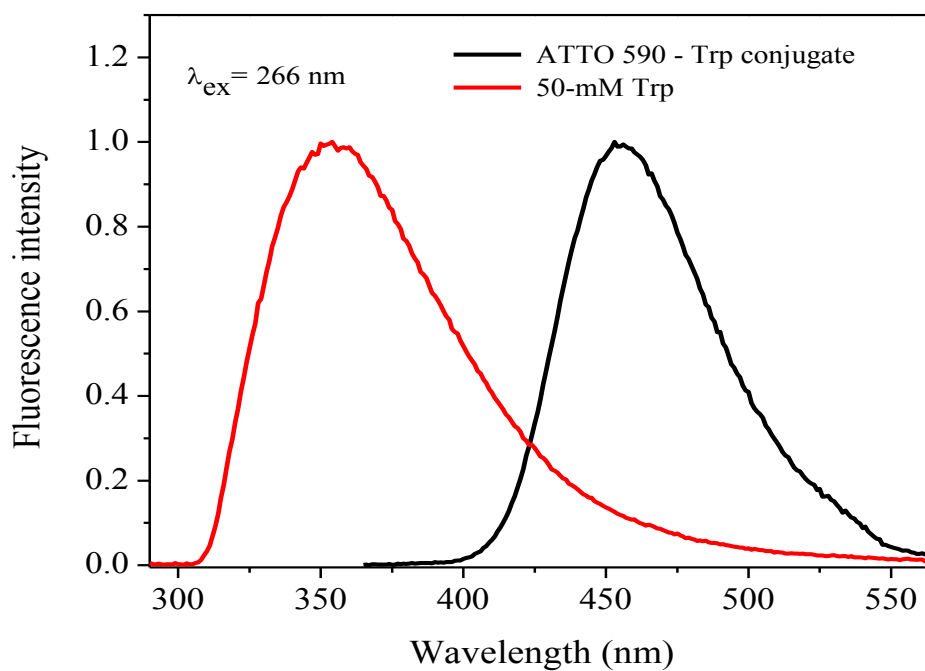
Figure 3.

Exciplex fluorescence of the ATTO 590-tryptophan conjugate, λ_{ex} = 266 nm. The control experiment performed in the absence of tryptophan demonstrates that the band at 455 nm is not a result of an excimer of tryptophan.
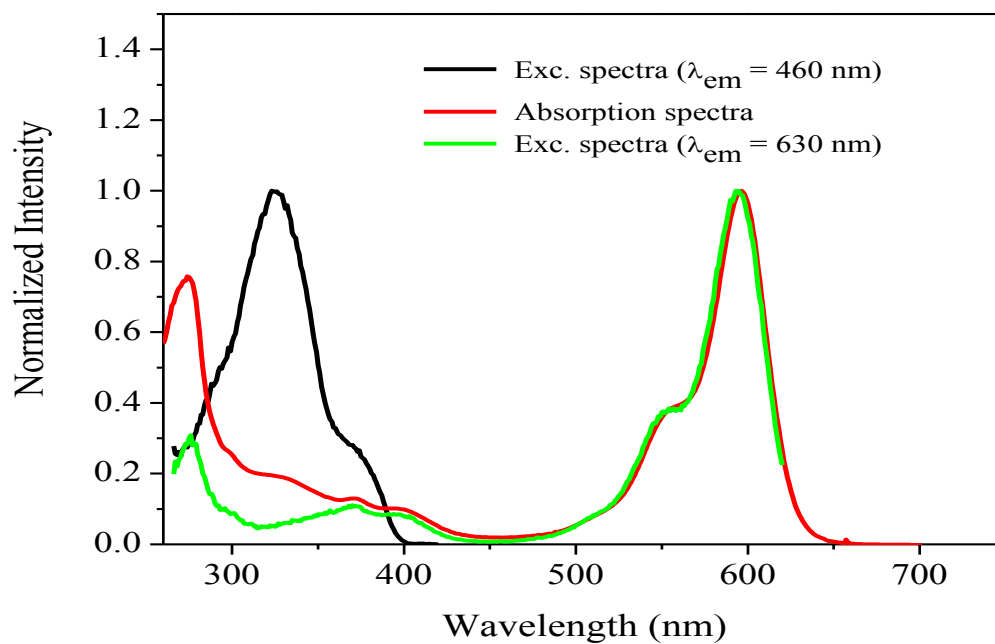
Figure 4.

Excitation spectra of the ATTO 590-tryptophan conjugate:

a) emission collected at 460 nm (black), corresponding to the exciplex fluorescence;

b) emission collected at 630 nm (green), corresponding to ATTO 590 fluorescence;

c) absorption spectra of the conjugate (red).

Note the superposition of the green and the red spectra.
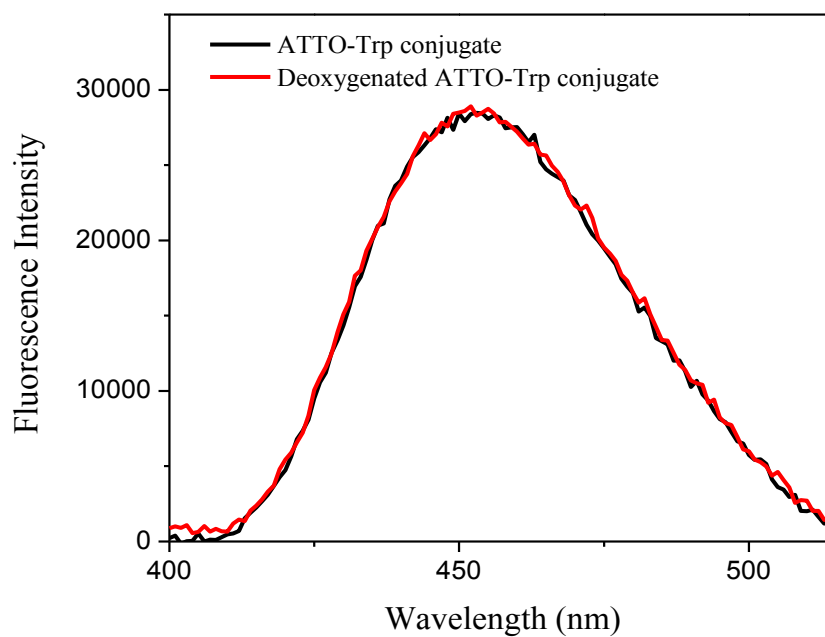
Figure 5.

Fluorescence spectra of the ATTO 590-tryptophan conjugate in pH 7 buffer, λ_{ex} = 266 nm:

a) with ambient oxygen concentration (black);

b) after deoxygenation (red)

The deoxygenation was carried out by bubbling Ar gas through the solution in an air-tight

cuvette for 30 minutes.
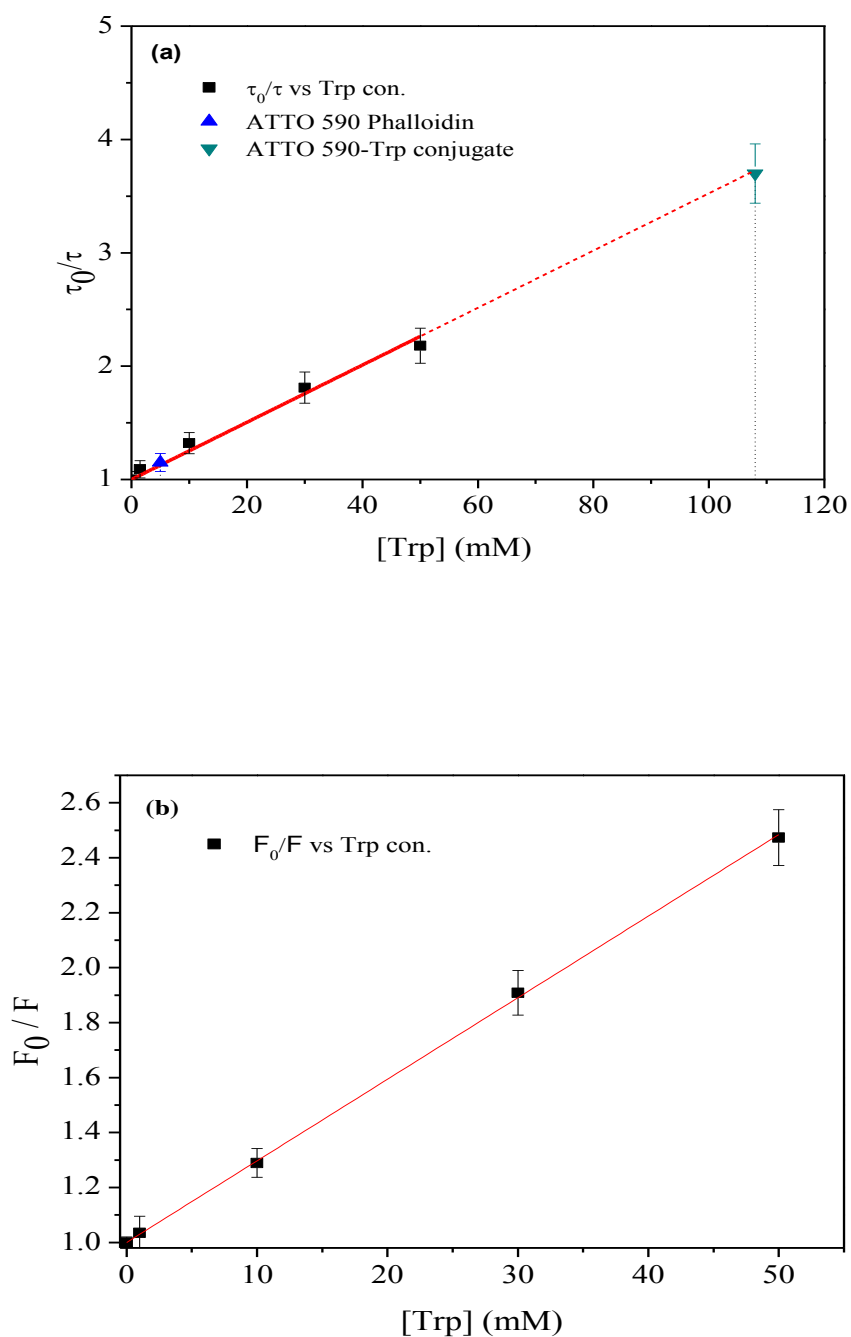
Figure 6.

a) Stern-Volmer plot of the average lifetime of ATTO 590 as a function of tryptophan concentration. The plot shows the "effective concentration" of tryptophan in the ATTO 590-Trp

conjugate and in ATTO 590-phalloidin: *i.e*., these two species are positioned on the straight line obtained to construct the Stern-Volmer plot according to their average fluorescence lifetimes.

b) Stern-Volmer plot of the same species as in a), but based upon the steady-state data. Both methods yield the same quenching constant of 0.03 ± 0.01 M^{-1}.

Figure 7.

a) Plot of the natural logarithm of the ratio of the amplitudes as a function of temperature in the ATTO 590-50-mM Trp mixture.

b) Plot of the natural logarithm of the ratio of the amplitudes as a function of temperature in the ATTO 590-Trp conjugate.
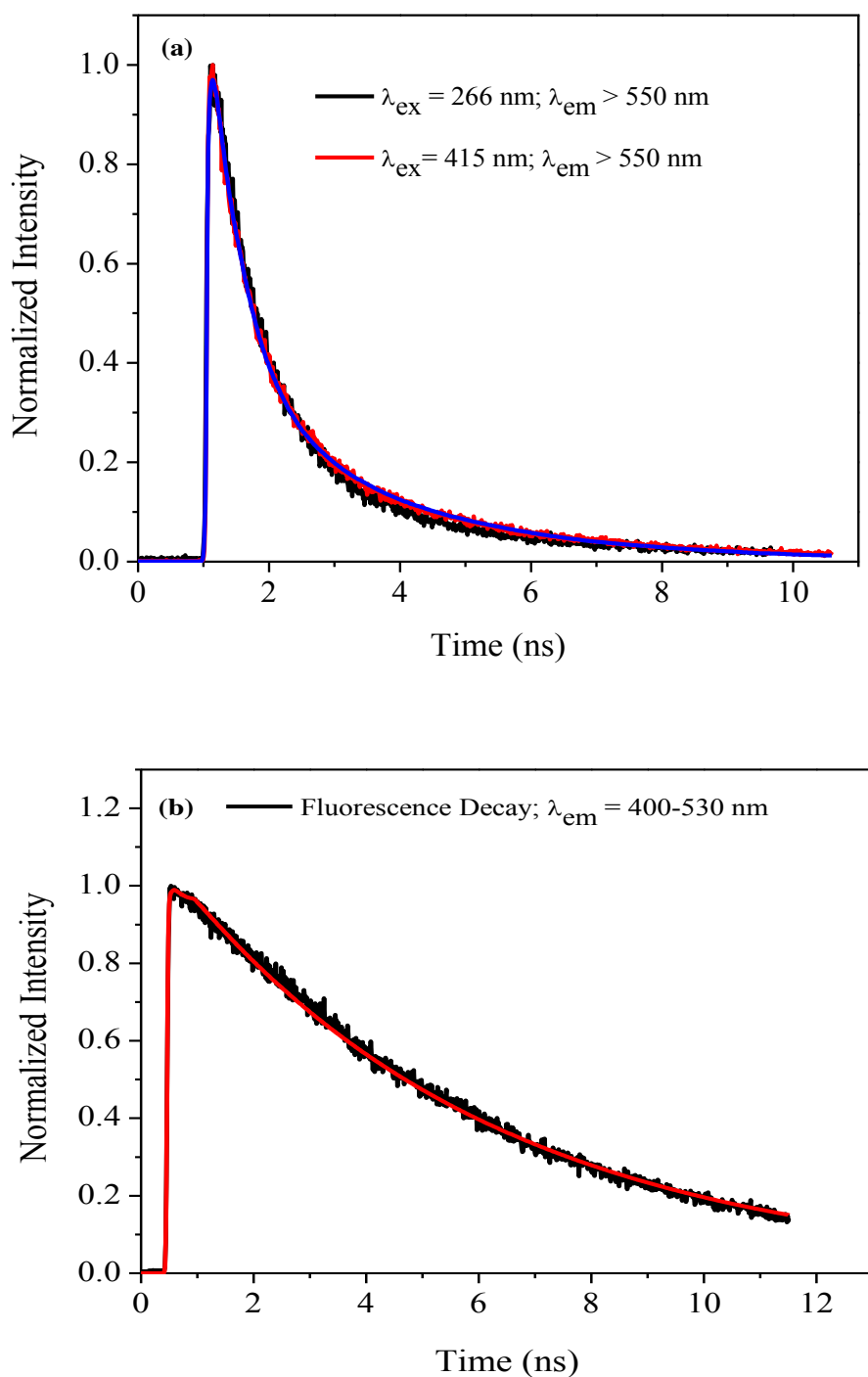
Figure 8.

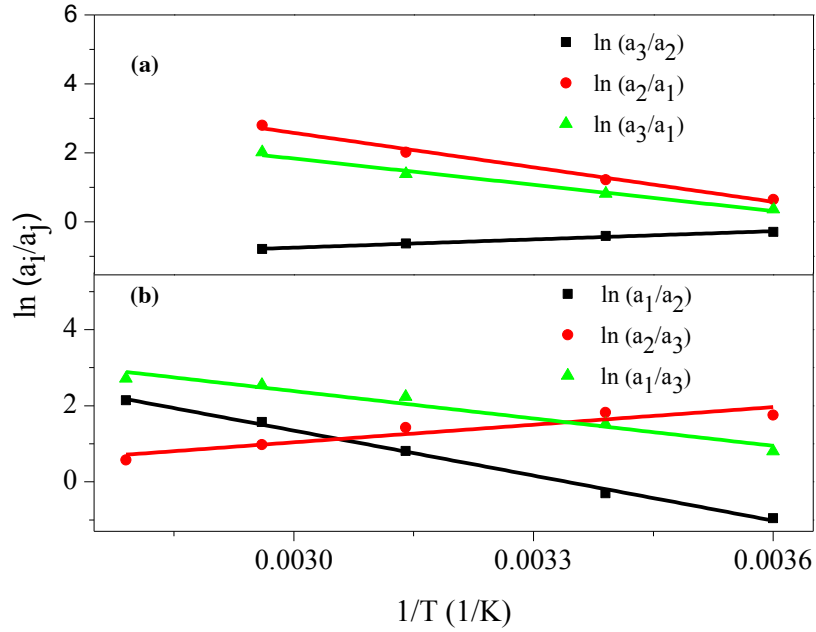a)   Lifetime decay of the excited state of the conjugate. Emission was collected using a 550

nm long-pass filter to monitor only ATTO fluorescence.

λ_{ex} = 266 nm (black); λ_{ex} = 415 nm (red), τ_1 = 3.7, a_1 = 0.08; , τ_2 = 1.0, a_2 = 0.53; τ_3 = 0.4, a_3 = 0.39; $\langle\tau\rangle$ = 1.0 ns.

Visual inspection of the two decay curves indicates that there is no significant excitation wavelength dependence when only ATTO fluorescence is considered.

b)   Exciplex lifetime decay (black); fit to the decay, τ = 5.6 ns (red).

λ_{ex} = 266 nm. The fluorescence was collected with a filter combination permitting transmission in the window from 400-530 nm. 20,000 were collected in the peak channel.
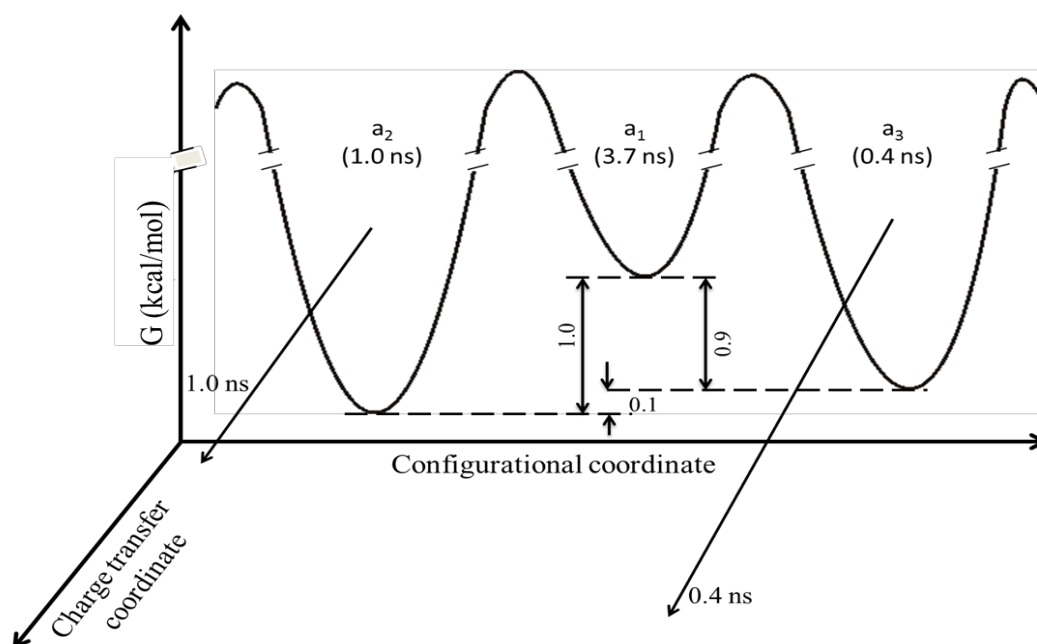
Figure 9.

A schematic diagram for the excited-state potential energy surface of ATTO 590-Trp conjugate as a function of a configurational coordinate and a charge transfer coordinate. The three wells arise from the preexisting ground-state conformations (see Supplementary Material). We have categorized these conformations into three different groups, yielding lifetimes of 3.7 ns (a_1), 1.0 ns (a_2), and 0.4 ns (a_3), based upon the efficiency of charge transfer from ATTO to Trp in each conformation. The size of the arrows along the charge transfer coordinate qualitatively indicates the efficiency of charge transfer. The magnitudes of the barriers are unknown, and hence the break marks are provided.

CHAPTER 3b. QUENCHING OF THE FLUORESCENCE OF ATTO DYES BY Au-CdS NANOPARTICLES

Manuscript under preparation for publication

Ujjal Bhattacharjee,[1,2] Long Men,[1] Sam Alvarado, Javier Vela[1,2], and Jacob W. Petrich[1,2]*

KEYWORDS

Au-CdS; ATTO dyes; quenching; photoinduced electron transfer

ABSTRACT

Metal-semiconductor nano-hybrids, such as Au-CdS, have emerged as very important class of materials for their use in photochemical hydrogen production and other catalysis reactions. The most unique feature of these particles is the possibility of selective excitation of either CdS or the Au domains in the hybrid particles. Furthermore, upon excitation with different wavelength these particles can remain as oppositely charged. Here we studied photophysical interaction of these particles with the widely used ATTO dyes. We have observed that the fluorescence of the dyes quenched by these particles due to photoinduced electron transfer and based on the wavelength of excitation, the nature of the charge transfer complex differ. Our findings suggest that the effectiveness of photocatalyst can be alternatively studied by some simple quenching experiments. Also, due to growing use of the ATTO dyes in fluorescence resonance energy transfer (FRET) with nanoparticles, all the possible photophysical processes should be studied.

---

[1]Department of Chemistry, Iowa State University, Ames, IA

[2]U.S. Department of Energy Ames Laboratory, Ames, IA

INTRODUCTION

Hybrid nanoparticles[1] have attracted considerable attention because of their applicability in many technologically important areas such as energy conversion[2] and catalysis.[3] Au-CdS has been reported in several papers as a photocatalyst for chemical reactions, most importantly for photochemical hydrogen production.[4] Metal-semiconductor hybrids are used because the absorption of solar light can be tuned in these materials and the charge transfer from the semiconductor to the metal is very fast, less than20 fs.[5] The possibility of changing the material, shape, size, or other parameters of the semiconductor enables one to tailor its optical properties. It has been shown, furthermore, that excitation of plasmons in metal nanostructures can induce the transfer of hot electrons into the semiconductors, making them interesting candidates for light harvesting materials because their absorption is tunable.[6] In semiconductor-metal monohybrids, as the metal and the semiconductor are directly in contact, the electron injection from metal to semiconductor occurs with higher efficiency. This is because the electron transfer rate can overcome the rate of the electron-electron scattering (~hundreds of fs).[7] Alternatively, the efficient electron transfer happens *via* plasmon induced metal-to-semiconductor interfacial charge-transfer transition (PICTT) pathway as proposed by Lian and co-workers.[8] As the energy associated with the excitonic transition of CdS nanoparticles is much different from that of the surface plasmonic resonance (SPR) in Au, a selective excitation of either the semiconductor or the metal domain is possible.[9]

We have studied the photophysical interaction of Au-CdS nanoparticles with ATTO dyes. ATTO dyes are used extensively in single-molecule spectroscopies and super-resolution microscopies.[10] They are excellent fluorescence probes. They have high fluorescence quantum

yields, are photostable, exhibit significant Stokes shifts; and a considerable range of them covering the visible absorption and emission spectrum is commercially available.

Photoinduced electron transfer (PET) to amino acids is a known nonradiative pathway for ATTO dyes.[11] It has been reported that PET is most effective in the red-absorbing ATTO dyes. Fang and Vela and co-workers studied the effectiveness of Au-CdS nanoparticles specially designed to have Au nanoparticles attached to CdS nanorods. The particles were designed to serve as photocatalyst for the conversion of amplex red to resorufin in the presence of H_2O_2.[3b] Two distinct mechanisms has been proposed for charge separation in the nano-hybrids depending on excitation wavelength.[3b, 9] Using selective excitation of Au or CdS portion of the nano-structure, and studying effect on quenching on different dyes one can critically examine the proposed mechanism existing in the field of research with these metal-semiconductor nanoparticles. Furthermore, the use of NPs as donors and acceptors for FRET applications is also becoming increasingly common.[12] ATTO dyes have been shown to be efficient candidate for FRET with CdSe/ZnS quantum dots.[13] Thus, it's important to know all other possible interaction with the nanoparticles. In this work we studied inter-molecular quenching of two different ATTO dyes (ATTO 590 (**Figure 1a**) and ATTO 655 (**Figure 1b**)) with Au-CdS nano-hybrids where Au nanparticles are deposited on CdS nanorods.

MATERIALS AND METHODS

Materials. ATTO 590 and ATTO 655 (free carboxy acid) were obtained from ATTO-TEC. Cadmium oxide (99.998%), sulfur (99.999%) and tetramethylammonium hydroxide pentahydrate (98%) were obtained from Alfa Aesar. Octadecylphosphonic acid (ODPA) was purchased from PCI Synthesis. Trioctylphosphine oxide (TOPO) (99%); dodecylamine (98%) and

didodecyldimethylammonium bromide (98%) were purchased from Sigma-Aldrich. Trioctylphosphine (TOP) (97%) and gold (III) chloride (99%) were purchased from Strem. All chemicals were used as received unless specified otherwise.

Synthesis of Colloidal CdS Nanorods. CdO (105 mg, 0.81 mmol), TOPO (1.375 g, 3.56 mmol), and ODPA (535 mg, 0.94 mmol) were taken into a three-neck round bottom flask with a glass-coated stir bar. The flask, fitted with a stainless steel thermocouple, condenser and septum was sealed and connected to a Schlenk line. The mixture was subsequently heated to 100 °C using a heating mantle and kept under vacuum for 15 min. After that, the apparatus was refilled with dry argon and heated to 320 °C resulting in a colorless solution. The mixture was then cooled down to 120 °C, placed under vacuum for 15 min, and heated to 300 °C. We injected TOP (1.20 mL, 2.7 mmol) into the flask. The mixture again heated to 320 °C followed by addition of TOPS solution (1.00 mL, 2.2 mmol). Then, the mixture was cooled down to 315 °C for 85 min. After that, the reaction mixture was taken down from the heating mantle and cooled to room temperature. Then we diluted the nanorods with toluene (5 mL) and isolated adding a 1:1 v/v iso-propanol/nonanoic acid (24 mL) mixture followed by centrifugation (5,000 rpm for 10 min). The product was redispersed in toluene.

Synthesis of Colloidal Au-CdS. Optical density (O.D.) of CdS nanorod solution in toluene at 470 nm was checked to obtain a desired concentration. 15 mL of the solution was kept in a sealed three-neck round bottom flask and degassed, refilled with dry argon, and stored in the dark for 12 h. Gold (III) chloride ($AuCl_3$) (28 mg, 0.08 mmol), dodecylamine (117 mg, 0.63 mmol) and didodecyl dimethyl ammonium bromide (74 mg, 0.16 mmol) were added in 18 mL of anhydrous toluene in the dark under a dry atmosphere and then sonicated for 5 min. This gold solution was injected dropwise to the CdS solution under equilibrium in an oil bath at 40 °C in

the dark and under an argon atmosphere. After the complete addition of the gold solution, the reaction was allowed to continue for 15 min. The purification of nonvolatile products were carried out by precipitation with a 1:1 mixture of acetone and methanol (30 mL) and centrifugation (4500 rpm for 10 min). The product thus formed was redispersed in toluene.

Transfer of Au-CdS Hybrid Heterostructures to Water. The product was dissolved in 10 mL of toluene and 10 mL of distilled water was added. Tetramethyl ammonium hydroxide pentahydrate (300 mg, 1.65 mmol) and DL-mercaptosuccinic acid (50 mg, 0.33 mmol) were added and the resulting mixture was stirred overnight in the dark. Subsequently, the aqueous layer was separated and washed with acetone to ensure removal of the excess ligands. The product was readily redispersed in water.

DFT calculation. The molecular orbital energies were computed using density functional theory (DFT). First, the geometry of the molecules was optimized using a 6-311G(d) basis set. Calculations were performed assuming the dye molecules in vacuum. The TPSS (Tao, Perdew, Staroverov, Scuseria) functional was employed. To obtain E_{HOMO}, E_{ex} (excitation energy) was calculated with the help of TD-DFT.[14] The calculations were performed on ATTO 655 and on TAMRA (owing to its highly similar optical properties and molecular structure with those of ATTO 590).

Steady-State Measurements. An Agilent 8453 UV Vis spectrometer with 1-nm resolution was used to record absorbance. Steady-state fluorescence measurements were carried out with a Spex Fluoromax-4 with a 3- or 4-nm bandpass and was corrected for lamp spectral intensity and detector response. Concentrations were kept near 0.1 μM in all measurements, to avoid reabsorption effects, reemission effects, or dye aggregation.

Lifetime Measurements. Measurements of excited-state lifetimes were performed with the time-correlated singlephoton counting (TCSPC) technique. The apparatus for time-correlated, single-photon counting has been described previously.[11] The fundamental (~800 nm) from a homemade mode-locked Ti-sapphire oscillator was passed through a Pockels cell (model 350-160, Conoptics Inc.) to reduce the repetition rate to 8.8 MHz. 400 nm excitation wavelength, used for some of the experiments, was obtained from the fundamental using a U-Oplaz Technologies (Model TP-2000B) doubler/tripler. A Becker & Hickl photon counting module (model SPC-630) is used. This apparatus produces an instrument function (IRF) with a full-width at half-maximum (fwhm) of ~40-50 ps. For the experiments with excitation wavelength of 570 nm, a supercontinuum laser (Fianium Ltd.) with 570±5 nm bandpass filter was used. Repetition rate of the laser is 1 MHz and the fwhm of the IRF is ~190 ps. A quartz cuvette of 3-mm or 1-cm path length was used. The decay parameters were obtained by fitting the decay to sum of exponentials after deconvolution of IRF from the decay.

RESULTS AND DISCUSSION

Steady-State Measurements. A transmission electron-microscopy (TEM) image of CdS nanorods with deposited Au nanoparticles is given in **Figure 1c**. The average (± one standard deviation) length and diameter of the nanohybrids were found to be 134.5(±11.5 nm) and 6.0 (±0.7) nm respectively. The diameter of the gold nanoparticles was in a range of 2.5 - 6.5 nm. A schematic diagram of the nano heterostructure is given in **Figure 1d**. The absorption spectrum of the nano-composite particle is shown in **Figure 2**. The spectrum is comprised of the characteristic, continuous excitonic absorption due to the CdS nanorods and surface plasmon resonance band of the Au nanoparticle, thus, showing that the optical properties of the original components are retained.[5, 9] This features permit the selective excitation of the CdS (λ_{ex} = 400 nm) or the Au

domains (λ_{ex} = 570 nm) of the composite. **Figure 3** presents the photoluminescence spectrum of Au-CdS nano hybrids. Both the band-edge and trap-state emissions are highly quenched by fast (~20 fs in Au-CdS[5] and ~3.4 ps in Pt-CdS) interfacial electron transfer.[1a, 9] The reported recombination rate is very slow in Pt-CdS nano hybrids: ~1.2 ± 6 μs. Similar rates are expected for Au-CdS. Thus, during the interaction of the heterostructure with the dye, the Au-CdS particles remain essentially charge-separated. The fluorescence spectra of ATTO dyes is broadened (**Figure 4a**) in presence of the Au-CdS particles. This broadening is indicative of a strong electronic interaction between the nanohybrids and ATTO dyes. Lian and co-workers[15] propose such an interaction between Au and CdS.

We further examined the possibility of formation of ground-state complexes between Au-CdS and ATTO dyes by taking fluorescence spectra with varying wavelength (**Figure 4b**). The excitation spectrum of ATTO dye in presence of Au-CdS matches with absorption of ATTO dye as well (data not shown). We observed a gradual decrease of fluorescence intensity with the increasing amount of Au-CdS in the solution, and it is quantitatively given by a Stern-Volmer plot (**Figure 4c**). We used both 400 nm and 570 nm as excitation wavelength for doing the experiment. The quenching is occurring by photoinduced electron transfer as further confirmed by time resolved data.

Time-Resolved Experiments. **Quenching Experiment with λ_{ex} = 570 (Scheme A).** We have measured the lifetime of ATTO 590 with increasing concentration of the Au-CdS concentration (**Figure 5a**). The concentration of Au-CdS was predicted from the absorption spectrum of the material at 470 nm.[16] **Table I** summarizes excited-state lifetime data for ATTO 590 excited with 570 nm. The emission decays can be best represented by a bi-expoential function, where one component represents the contribution from the charge separated species between Au-

CdS and ATTO 590 (0.93 ns) where the other being contribution from unquenched dye molecules (3.7 ns). We see with increasing concentration, weight of the first component gradually increases. A similar Stern-Volmer plot was generated plotting average lifetime with the concentration of the Au-CdS nanoparticles (**Figure 5b**). The Stern-Volmer constant (0.04 μM^{-1}) thus obtained, matches with the one obtained using steady state results. Which further confirms absence of any ground state complex between Au-CdS and ATTO 590. Based on the calculated energy levels of the ATTO 590 (calculation was carried out with TAMRA because of similar molecular structure and optical properties), LUMO level is much higher in energy than the conduction band (CB) of CdS (**Figure 6**). So reductive electron transfer from CdS to ATTO is impossible. Also due to presence of negative charge on CdS,[17] the electron transfer from excited state of ATTO to CdS domain is unfavorable.[18] This can be further verified by a control experiment with CdS nanorods (with no gold); there CdS is not be charged. Electron transfer between Au and dye has not been reported in an intermolecular mixture of the Au particle and dye. There are only few reports in the literature suggesting electron transfer from an organic dye to gold cores only when short linkers (2–8 atoms) were used in polar solvents.[19] But due to presence of positive charge on the gold domains, electron transfer can be favored.[17-18] Also, chance of resonance energy transfer (RET) between the dye and the Au is very less due to average distance between the two moieties and poor overlap between fluorescence spectra of the dyes (mainly ATTO 655) and plasmonic absorption. Secondly, we performed a control experiment with Au nanoparticles which did not show quenching of fluorescence. If RET had been the mechanism behind the quenching with Au-CdS under 570 nm excitation, we should have observed it in presence of Au. This strongly suggests electron transfer from excited state of ATTO 590 to the Au.

As the extent of quenching in different ATTO dyes can change based on where they absorb as reported by Marmé *et al.*,[20] and also ATTO 655 has more suitable absorption and emission wavelengths for high resolution microscopy applications, we carried out identical experiments on ATTO 655, more red absorbing dye. We only performed the experiments with an excitation wavelength of 570 nm to excite both the dye and Au plasmonic band and the effect excitation of CdS on ATTO 655 could not be checked as the dye does not absorb 400 nm. We observed that though the population of charge transfer species is similar to that obtained with ATTO 590 under similar quencher concentration (**Table II**), the lifetime of the charge transfer species is much slower, 1.1 ns (compared to 1.8 ns in unquenched dye). The Stern-Volmer plot (**Figure 7**) constructed with average lifetime of ATTO 655 with varying concentration of the nano-hybrid yield a Stern-Volmer constant value of 0.01 μM^{-1}. Based on the energy of relative ATTO dyes, the ATTO 655 should be quenched more if we consider TAMRA as an alternative of 590. Here we conclude our TD-DFT calculation did not produce a transition energy precise enough for the comparison between the two dyes, as evidenced from the fact that the calculated wavelength TD-DFT did not match the experimental wavelengths.

Quenching Experiment with λ_{ex} = 400 (Scheme B). A similar experiment was carried out using excitation wavelength of 400 nm (**Figure 8a**). In this case, the component representing the charge transfer between ATTO 590 and Au-CdS has a lifetime of 0.23 ns (**Table III**). Hence, this observation clearly indicates the type of charge transfer complex formed between Au-CdS and ATTO 590 differs with different excitation wavelengths, namely 570 nm (plasmonic band of Au) and 400 nm (excitonic band in CdS). The population of the charge transfer species by excitonic excitation of CdS in Au-CdS is also much higher. The Stern-Volmer constant value is about 4 times higher than that obtained when we induce excitation of the SPR band in the nano-composite

(**Figure 8b**). These observations supports the observation by Lian and co-workers, that photogenerated electrons and holes appear to be more active and longer-lived when generated at CdS than when generated at Au.[9] When 400 nm wavelength is used to induce plasmonic transition, and thus when the nanohybrids remain charge separated according to schematic B (**Figure 1d**), electron transfer to CdS domain from the ATTO dye is solely responsible for the quenching. The relative energy level of the dye molecular orbital and CdS CB, strongly support electron transfer. As the gold domains remain as negatively charged, as reported in the literature,[18] the charge transfer to Au becomes highly unfavorable.

To confirm our hypothesis, we performed a control study with CdS nanorods with ATTO dyes under both 400 nm and 570 nm. First, with 400 nm excitation, we did not observe quenching with the similar concentration of CdS as in the experiments with the metal-semiconductor nanohybrids. Thus, we can conclude that in Au-CdS nanohybrids, the presence of positive charge on CdS domain is important for effective electron transfer. Secondly, under 570 nm excitation the yield of internal charge transfer (between Au and CdS) is less (~24%). Consequently, many nanohybrid moieties would be present without any charge separation in the solution under 570 nm.[3b] So the quenching of ATTO dyes observed with 570 nm could be a result of electron transfer from ATTO to CdS domain in the particles without prior charge separation. This possibility has been nullified by a control experiment with 570 nm as CdS does not absorb 570 nm. As we did not see quenching by CdS under 570 nm excitation, in the nano-hybrids quenching is not occurring due to charge transfer between ATTO and CdS domain. Furthermore, we did not see quenching in the solution mixture of Au nanoparticles and ATTO dye. Thus, the positive charge on Au domains in nano-hybrids under 570 nm excitation makes the electron transfer between ATTO dyes and Au particle facile.

CONCLUSION

Stimulated by the work Lian and co-workers, we monitored the quenching of ATTO 590 and ATTO 655 dyes in presence of Au-CdS hetrostructures in solution mixture. Though the optical properties of the individual components of nanohybrid Au-CdS is retained, but in presence of one another their ability towards PET, an indirect measure of photocatalytic efficiency, changes significantly. Under excitation wavelength of 400 nm, PET takes place between the dye and the CdS domain in the hybrid particle. Whereas, under 570 nm excitation, there are possibilities of electron transfer between Au domain in the charge separated nanohybrids or the CdS domains in neutral particle and the ATTO dye. The photoinduced processes in the dye and Au-CdS systems are complicated and it can be controlled, for example, by the choice of the dye, excitation wavelength, distance between the dye and nanohybrids. This shows that Au-CdS can be considered as adaptable constituent for photoactive devices. However, it is important to examine and understand their interactions with dyes comprehensively to use them. Especially the charge-transfer processes require further thorough studies in order to find out in detail the effect of solvent polarity, particle size, length and packing density of the dyes on the charge separation and recombination. As another application of this work, in future, we can perform stimulated emission depletion (STED) experiment with dye attached to the nanoparticle, and study the photophysics along the length of the particle with resolution much below the diffraction limit.[10a]

REFERENCES

1.   (a) Wu, K.; Zhu, H.; Liu, Z.; Rodríguez-Córdoba, W.; Lian, T., *J. Am. Chem. Soc.* **2012,** *134*, 10337-10340; (b) Carbone, L.; Cozzoli, P. D., *Nano Today* **2010,** *5*, 449-493; (c) Costi, R.; Saunders, A. E.; Banin, U., *Angew. Chem.* **2010,** *49*, 4878-4879; (d) Mokari, T.; Sztrum,

C. G.; Salant, A.; Rabani, E.; Banin, U., *Nat. Mater* **2005**, *4*, 855−863; (e) Carbone, L.; Jakab, A.; Khalavka, Y.; Soennichsen, C., *Nano Lett.* **2009,** *9*, 3710-3714; (f) Korobchevskaya, K. G. C.; Manna, L.; Comin, A., *J. Phys. Chem. C* **2012**, *116*, 26924-26928.

2. Costi, R.; Saunders, A. E.; Elmalem, E.; Salant, A.; Banin, U., *Nano Lett.* **2008,** *8*, 637-641.

3. (a) Yin, H., *Chem. Commun.* **2008**, 4357−4359; (b) Ha, J. W.; Ruberu, T. P. A.; Han, R.; Dong, B.; Vela, J.; Fang, N., *J. Am. Chem. Soc.* **2014,** *136*, 1398−1408.

4. (a) Fujishima, A.; Honda, K., *Nature* **1972,** *238*, 37; (b) Gratzel, M., *Nature* **2001,** *414*, 338; (c) Cho, I. S.; Chen, Z.; Forman, A. J.; Kim, D. R.; Rao, P. M.; Jaramillo, T. F.; Zheng, X., *Nano Lett.* **2011,** *11*, 4978; (d) Shankar, K.; Basham, J. I.; Allam, N. K.; Varghese, O. K.; Mor, G. K.; Feng, X.; Paulose, M.; Seabold, J. A.; Choi, K.-S.; Grimes, C. A., *J.Phys. Chem. C* **2009**, *113*, 6327; (e) Walter, M. G.; Warren, E. L.; McKone, J. R.; Boettcher, S. W.; Mi, Q.; Santori, E. A.; Lewis, N. S., *Chem. Rev.* **2010,** *110*, 6446; (f) Lewis, N. S., *Science* **2007,** *315*, 798.

5. Mongin, D.; Shaviv, E.; Maioli, P.; Crut, A.; U., B.; Fatti, N. D.; Vallée, F., *Acs Nano 6*, 7034-7043.

6. (a) Furube, A.; Du, L.; Hara, K.; Katoh, R.; Tachiya, M., *J. Am.Chem. Soc.* **2007,** *129*, 14852−14853; (b) Tian, Y.; Tatsuma, T., *J. Am. Chem.Soc.* **2005,** *127*, 7632−7637; (c) Lee, J.; Mubeen, S.; Ji, X.; Stucky, G. D.; Moskovits, M., *Nano Lett.* **2012,** *12*, 5014−5019; (d) Chen, H. M.; Chen, C. K.; Chen, C.-J.; Cheng, L.-C.; Wu, P. C.; Cheng, B. H.; Ho, Y. Z.; Tseng, M. L.; Hsu, Y.-Y.; Chan, T.-S.; Lee, J.-F.; Liu, R.-S.; Tsai, D. P., *ACS Nano* **2012,** *6*, 7362−7372; (e) Mubeen, S.; Hernandez-Sosa, G.; Moses, D.; Lee, J.; Moskovits, M., *Nano Lett.* **2011,** *11*, 5548-5552; (f) Lee, Y. K.; Jung, C. H.; Park, J.; Seo, H.; Somorjai, G.

A.; Park, J. Y., *Nano Lett.* **2011,** *11,* , 4251-4255; (g) Knight, M. W.; Sobhani, H.; Nordlander, P.; Halas, N. J., *Science* **2011,** *332*, 702−704; (h) Wu, X.; Thrall, E. S.; Liu, H.; Steigerwald, M.; Brus, L., *J. Phys.Chem. C* **2010,** *114*, 12896-12899.

7.   Hodak, J. H.; Martini, I.; Hartland, G. V., *J. Phys. Chem. B* **1998,** *102*, 6958−6967.

8.   Wu, K.; Chen, J.; McBride, J. R.; Lian, T., *Science* **2015,** *349*, 632-635.

9.   Wu, K.; Rodríguez-Córdoba, W. E.; Yang, Y.; Lian, T., *Nano Lett.* **2013,** *13*, 5255-5263.

10.   (a) Lesoine, M. D.; Bhattacharjee, U.; Guo, Y.; Vela, J.; Petrich, J. W.; Smith, E. A., *The Journal of Physical Chemistry C* **2013,** *117* (7), 3662-3667; (b) Syed, A.; Lesoine, M. D.; Bhattacharjee, U.; Petrich, J. W.; Smith, E. A., *Photochemistry and Photobiology* **2014,** *90* (4), 767−772.

11.   Bhattacharjee, U.; Beck, C.; Winter, A.; Wells, C.; Petrich, J. W., *The Journal of Physical Chemistry B* **2014,** *118* (29), 8471-8477.

12.   (a) Clapp, A. R.; Medintz, I. L.; Mattoussi, H., *ChemPhysChem* **2006,** *7*, 47–57; (b) Rogach, A. L.; Klar, T. A.; Lupton, J. M.; Meijerink, A.; Feldmann, J., *J. Mater. Chem.* **2009,** *19*, 1208–1221; (c) Alivisatos, A. P.; Gu, W. W.; Larabell, C., *Ann. Rev. Biomed. Eng.* **2005,** *7*, 55–76; (d) Sandoghdar, V.; Seelig, J.; Leslie, K.; Renn, A.; Kuhn, S.; Jacobsen, V.; van de Corput, M.; Wyman, C., *Nano Lett.* **2007,** *7*, 685–689; (e) Gill, R.; Willner, I.; Shweky, I.; Banin, U., *J. Phys. Chem. B* **2005,** *109*, 23715–23719; (f) Willner, I.; Willner, B., *Nano Lett.* **2010,** *10*, 3805–3815; (g) Halivni, S.; Sitt, A.; Hadar, I.; U., B., *ACS Nano* **2012,** *6*, 2758–2765.

13.   Kaiser, U.; Jimenez de Aberasturi, D.; Malinowski, R.; Amin, F.; Parak, W. J.; Heimbrodt, W., *Applied Physics Letters* **2014,** *104*, 041901.

14.   Zhang, M., *J. Phys. Chem. A* **2007,** *111*, 1554-1561.

15.   Yang, Y.; Rodríguez-Córdoba, W.; Xiang, X.; Lian, T., *Nano Lett*. **2011,** *12*, 303-309.

16.   Yu, W. W.; Qu, L.; Guo, W.; Peng, X., *Chem. Mater*. **2003,** *15*, 2854-2860.

17.   Xu, W.; Jain, P. K.; Beberwyck, B. J.; Alivisatos, A. P., *J. Am.Chem. Soc*. **2012,** *134*, 3946.

18.   Barazzouk.S.; Kamat.P.V.; Hotchandani.S., *J. Phys. Chem.B* **2005,** *109*, 716.

19.   (a) Ipe, B. I.; Thomas, K. G., *J. phys. Chem. B* **2004,** *108*, 13265-13272; (b) Ipe, B. I.; Thomas, K. G.; Barazzouk, S.; Hotchandani, S.; kamat, P. V., *J. phys. Chem. B* **2002,** *106*, 18-21.

20.   Marmé, N.; Knemeyer, J.-P.; Sauer, M.; Wolfrum, J., *Bioconjugate Chemistry* **2003,** *14* (6), 1133-1139.

Table I

Excited state lifetimes of ATTO 590 in presence of Au-CdS with λ_{ex}= 570 nm

	τ_1	a_1	τ_2	a_2	$< \tau >$
ATTO	3.7				3.7
ATTO + 3.5 μM Au-CdS	3.7	0.86	0.9	0.14	3.3
ATTO + 6.5 μM Au-CdS	3.7	0.75	0.9	0.25	3.0
ATTO + 11 μM Au-CdS	3.7	0.61	0.9	0.39	2.6
ATTO + 19 μM Au-CdS	3.7	0.48	0.9	0.52	2.2

Table II

Excited state lifetimes of ATTO 655 in presence of Au-CdS with λ_{ex}= 570 nm

	τ_1	a_1	τ_2	a_2	$<\tau>$
ATTO	1.9				1.9
ATTO + 2.5 μM Au-CdS	1.9	0.86	1.1	0.14	1.7
ATTO + 4.5 μM Au-CdS	1.9	0.71	1.1	0.29	1.6
ATTO + 7 μM Au-CdS	1.9	0.57	1.1	0.43	1.5
ATTO + 15.3 μM Au-CdS	1.9	0.46	1.1	0.54	1.4

Table III

Excited state lifetimes of ATTO 590 in presence of Au-CdS with λ_{ex}= 400 nm

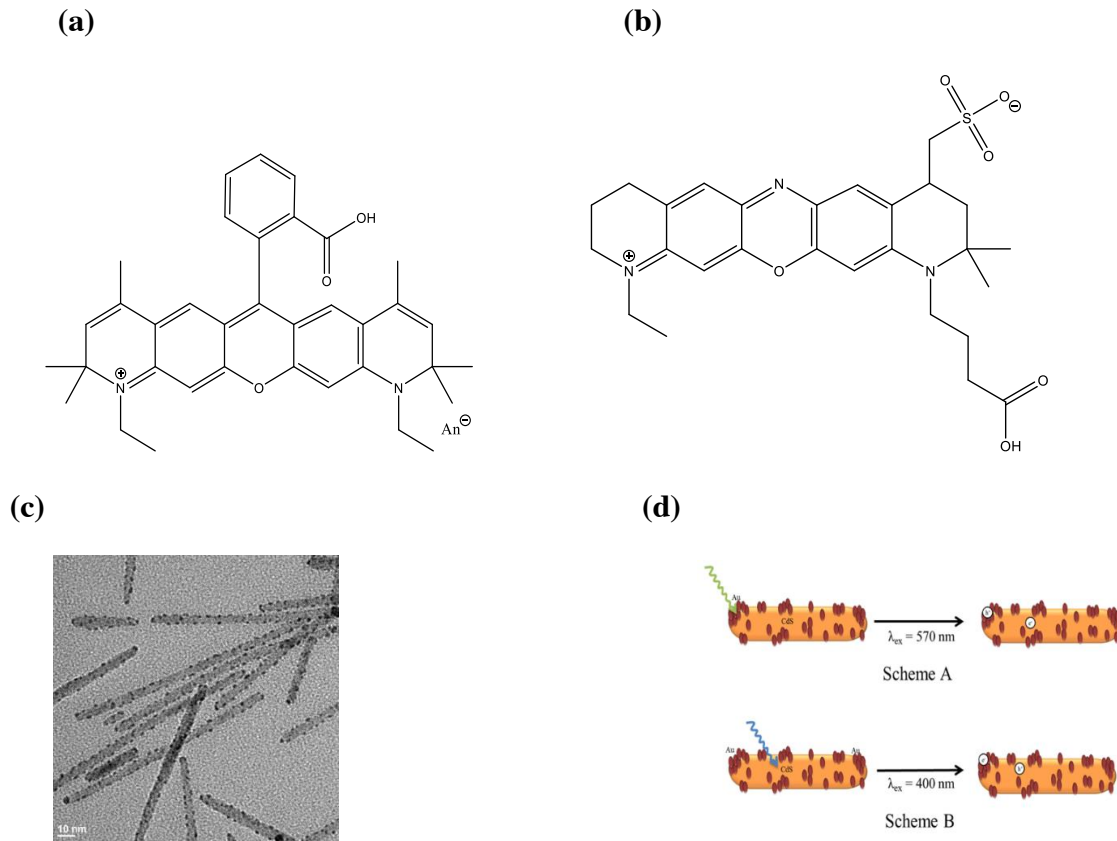|	τ_1	a_1	τ_2	a_2	$<\tau>$
ATTO	3.7				3.7
ATTO + 2.5 μM Au-CdS	3.7	0.72	0.2	0.28	2.7
ATTO + 4.5 μM Au-CdS	3.7	0.61	0.2	0.39	2.4
ATTO + 7 μM Au-CdS	3.7	0.59	0.2	0.41	2.2
ATTO + 15.3 μM Au-CdS	3.7	0.23	0.2	0.77	1.0

(a)

(b)

(c)

(d)

Figure 1.

a) Structure of ATTO 590.

b) Structure of ATTO 655.

c) TEM image of Au-CdS nanorods.

d) A schematic diagram of Au-CdS nano composite particle. With λ_{ex} = 570 nm, a charge separation takes place where the electron resides in CdS and the hole remains in Au domain (Scheme A). When excited at 400 nm, both the CdS and gold particles are excited. It leads to electron transfer from CdS to gold.
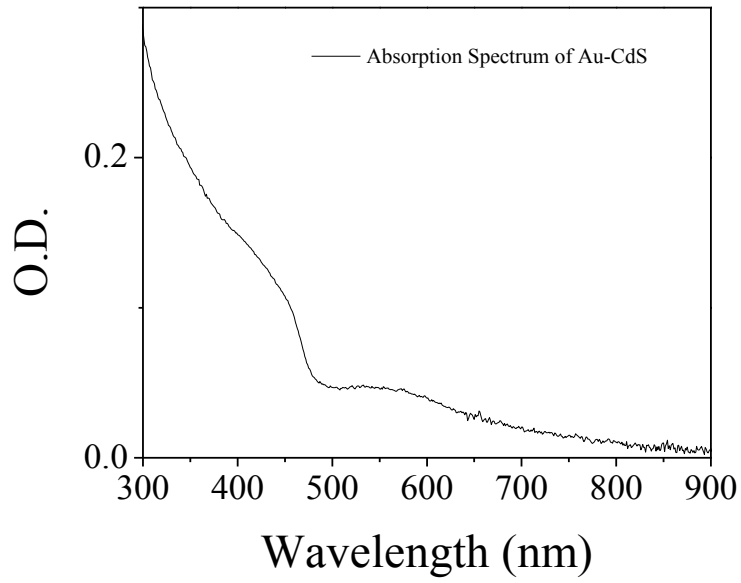
Figure 2.

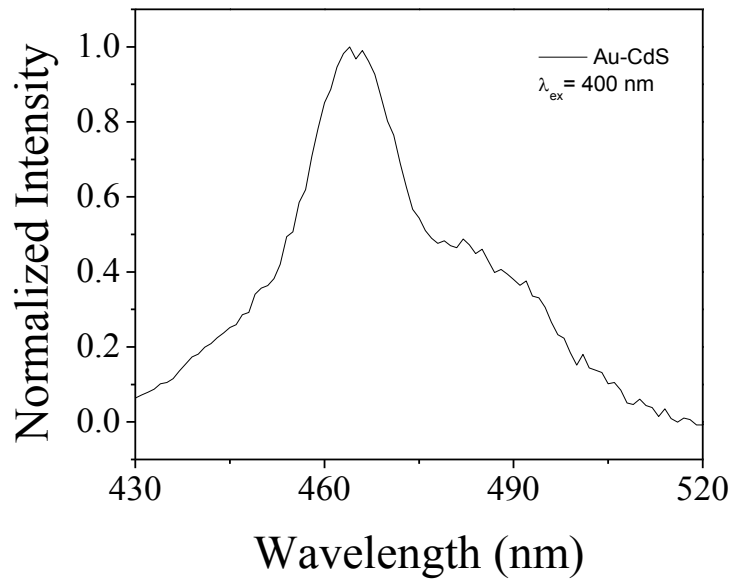Normalized absorption spectra of Au-CdS nanorods.

Figure 3.

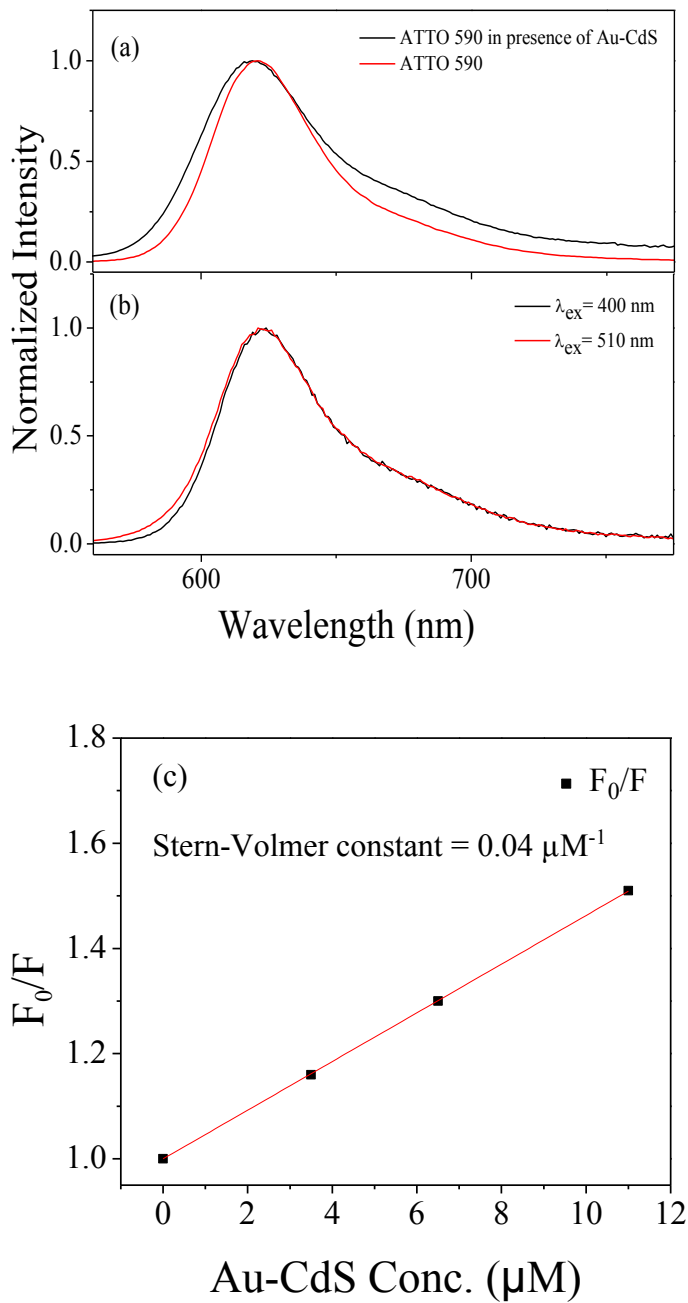Normalized photoluminescence spectrum of Au-CdS nanorods, $\lambda_{ex} = 400$ nm.

Figure 4.

a) Fluorescence spectra of ATTO 590 in presence (black) and absence (red) of Au-CdS in water (red).

b) Fluorescence spectra of ATTO 590 in presence of Au-CdS in aqueous solution excited at $\lambda_{ex} =$ 400 nm (black) and $\lambda_{ex} =$ 510 nm (red).

c) Stern-Volmer plot of the ATTO 590 as a function of CdS-Au concentration based upon the steady-state data, $\lambda_{ex} =$ 570 nm.

Figure 5.

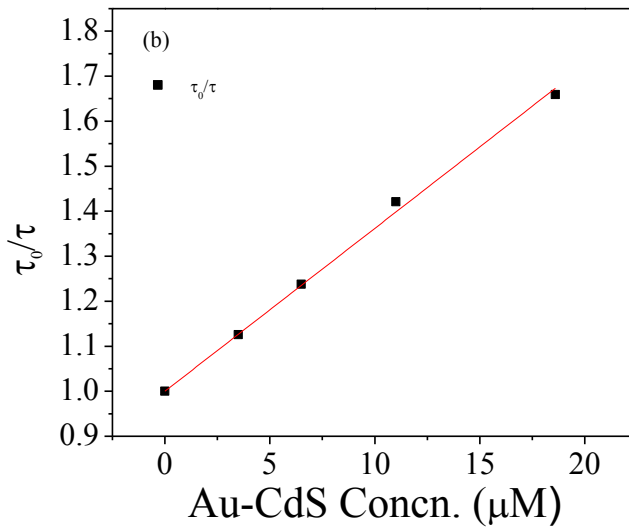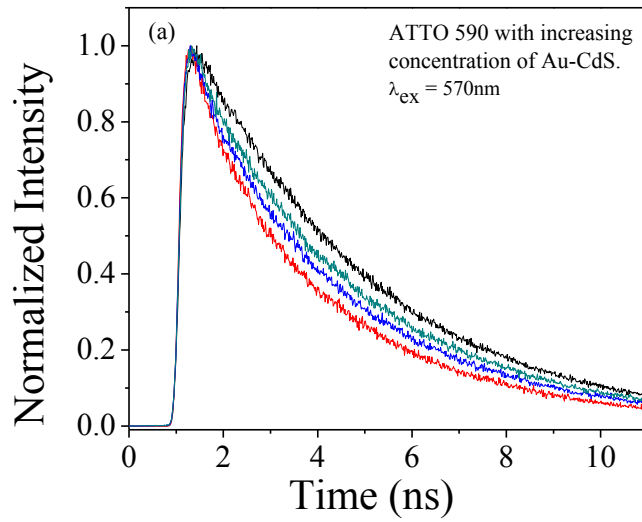Stern-Volmer plot of the average lifetime of ATTO 590 as a function of CdS-Au concentration,

λ_{ex} = 570 nm.

Both the stern-volmer plots (based on steady-state and average lifetime) yielded same stern-volmer

constant of $0.04~\mu M^{-1}$.
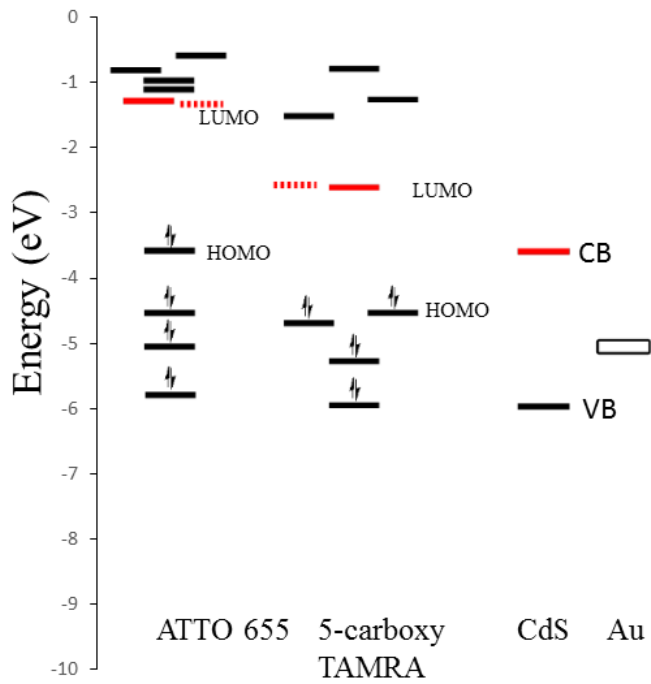
Figure 6.

Energy levels of the molecular orbitals of the dye studied, ATTO 655 and TAMRA (due to similarity in the molecular structure and optical properties with ATTO 590). Also the energy of the conduction band (CB) and valance band (VB) of CdS and Au work function is included to compare the potential for electron transfer. All the energies are with respect to vacuum.

Figure 7.

Stern-Volmer plot of the average lifetime of ATTO 655 as a function of CdS-Au concentration,

$\lambda_{ex} = 400$ nm.

The stern-volmer yielded a stern-volmer constant of 0.01 μM^{-1}.

Figure 8.

Stern-Volmer plot of the average lifetime of ATTO 590 as a function of CdS-Au concentration,
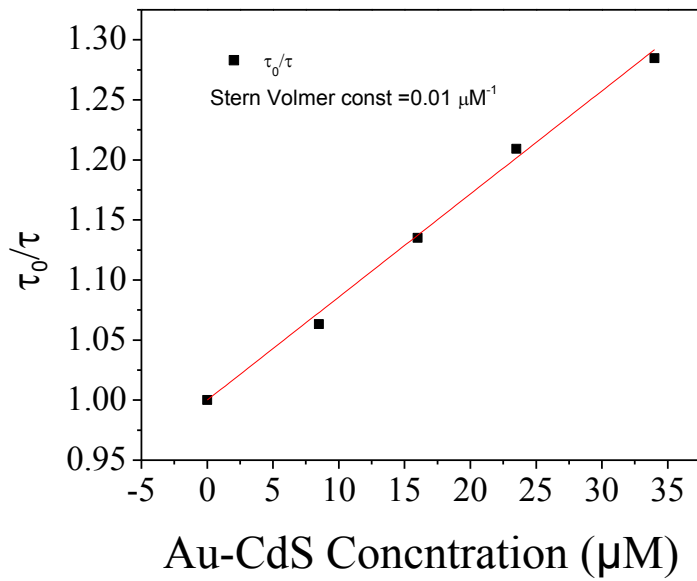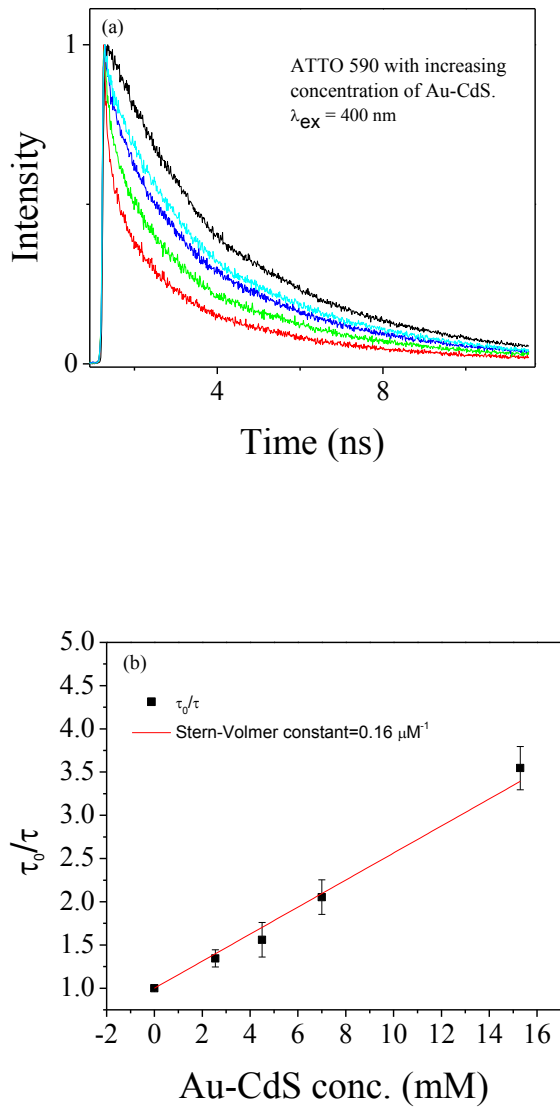
λ_{ex} = 400 nm.

The stern-volmer yielded a stern-volmer constant of 0.16 μM^{-1}.

CHAPTER 4a. SUBDIFFRACTION, LUMINESCENCE-DEPLETION IMAGING OF ISOLATED, GIANT, CdSe/CdS NANOCRYSTAL QUANTUM DOTS

A paper published in The *Journal of Physical Chemistry C*

Michael D. Lesoine[1,2], Ujjal Bhattacharjee[1,2], Yijun Guo[1,2], Javier Vela[1,2], Jacob W. Petrich[1,2], and Emily A. Smith[1,2*]*

ABSTRACT

Subdiffraction spatial resolution luminescence depletion imaging was performed with giant CdSe/14CdS nanocrystal quantum dots (g-NQDs) dispersed on a glass slide. Luminescence depletion imaging used a Gaussian shaped excitation laser pulse overlapped with a depletion pulse, shaped into a doughnut profile, with zero intensity in the center. Luminescence from a subdiffraction volume is collected from the central portion of the excitation spot, where no depletion takes place. Up to 92% depletion of the luminescence signal was achieved. An average full-width at half-maximum of 40 ± 10 nm was measured in the lateral direction for isolated g-NQDs at an air interface using luminescence depletion imaging; whereas the average

_____

full-width at half-maximum was 450 ± 90 nm using diffraction-limited, confocal luminescence imaging. Time-gating of the luminescence depletion data was required to achieve the stated spatial resolution. No observable photobleaching of the g-NQDs was present in the measurements, which allowed imaging with a dwell time of 250 ms per pixel to obtain images with a high signal-to-noise ratio. The mechanism for luminescence depletion is likely stimulated emission, stimulated absorption, or a combination of the two. The g-NQDs fulfill a need for versatile, photostable tags for subdiffraction imaging schemes where high laser powers or long exposure times are used.

INTRODUCTION

Lateral spatial resolution using visible wavelengths is limited by diffraction to ~250 nm in far-field optical microscopy.[1-4] There are several imaging techniques available to circumvent this constraint. Near-field techniques with a probe in close proximity to the sample can be used, but the probe can be too invasive for some applications.[5] In addition to using a near-field technique, there are several far-field techniques that have been developed. Stochastic optical reconstruction microscopy and several similar techniques utilize intermittent on/off states to limit the number of fluorophores emitting in a diffraction limited volume, and to generate a series of images that are reconstructed into a high resolution image.[6] Stimulated emission depletion (STED) microscopy uses point-spread function engineering, and can yield measurements with high spatial and temporal resolution.[7-15] STED uses a doughnut shaped depletion beam that spatially and temporally overlaps a Gaussian shaped excitation beam. The depletion beam is tuned to the red edge of a fluorophore's emission spectrum providing depletion of the signal at

the periphery of the Gaussian excitation profile. The resulting signal from the center of the excitation profile is below the diffraction limit.

In order to achieve subdiffraction spatial resolution imaging with STED, high laser powers or long acquisition times may be required. These conditions may lead to significant photobleaching of most small molecule fluorophores, which can degrade the achieved spatial resolution.[16-17] Nanocrystal quantum dots (NQDs) display the highest photostability of the prominently used fluorescent labels,[18-19] making them an ideal fluorophore for STED. On the other hand, Auger recombination, for example, is known to prevent efficient stimulated emission of isolated NQDs.[20] Stimulated emission can outpace Auger recombination in close-packed solids and highly concentrated colloidal solutions,[21-22] but extended solids have limited utility as tags for imaging applications.

Hell and coworkers demonstrated 45-nm spatial resolution along a single axis for clusters of Mn-doped ZnSe QDs using a depletion beam with two nodes having zero intensity between them.[23] They attributed the improved spatial resolution to stimulated absorption to higher-lying excited states.[24] Clusters of QDs were necessary for their study to avoid excessive exposure times as sufficient signal could not be obtained with isolated QDs due to a long lifetime (about 90 μs) of the luminescence transition.

So-called giant NQDs (g-NQD) with 10 to 20 monolayers of CdS shell added onto a 2- to 5-nm CdSe core exhibit suppression of luminescence intermittency (*i.e.*, blinking) and almost complete suppression of Auger recombination.[25-28] The suppression of Auger recombination has the effect of increasing the lifetime of biexcitons and even allowing the observation of multiexciton states.[29] Radiative lifetime components of excitons, biexcitons, and up to 6th-order multiexcitons in g-NQDs were observed with excitation powers on the order of 1 kW cm^{-2} at 4

K.[29] Furthermore, biexcitons and multiexcitons can undergo more effective stimulated emission, with the multiexcitons having a lower threshold for stimulated emission than biexcitons and indeed many dye molecules.[26]

Here, we report luminescence depletion (LD) imaging using CdSe/14CdS g-NQDs with a lateral spatial resolution of 40 ± 10 nm. It is proposed that stimulated emission and excited-state absorption mechanisms may work either independently or synergistically to provide depletion. A 7-fold improvement over the diffraction barrier was generated at an air interface with excitation and depletion powers of 50 pJ and 2 nJ, respectively.

EXPERIMENTAL

Sample Preparation and Characterization

The g-NQDs have been previously described.[30] A dilute solution of CdSe/14CdS g-NQDs (average particle size 13 ± 2 nm as measured by transmission electron microscopy) in toluene was deposited on a glass slide (474030-9000-000, Carl Zeiss Microscopy, Thornwood, NY) and the solvent allowed to evaporate. The sample was dried in ambient conditions for 30 min before any measurements were performed.

Blinking statistics for the g-NQDs were determined by comparing the percent of time the signal was in a binary high (on) or low (off) state using sequential 25-ms measurements over a 95-s time window. Depletion efficiencies for the g-NQDs were measured as the attenuation of the luminescence signal after illumination with the excitation and depletion wavelengths compared to the signal with illumination of only the excitation wavelength. The depletion power was varied and sequential 250-ms measurements over a 45-s time window were collected. Depletion was also observed with a CMOS camera (Moticam 2, Motic, British Columbia,

Canada) by illuminating a single QD with the excitation beam and blocking and unblocking the LD beam. Photobleaching rates for the g-NQDs were measured by illuminating the samples with the excitation beam at the same position and taking sequential time measurements over 3.5 minutes. For all measurements described above, the beams had a Gaussian profile.

Imaging

The imaging system used for these studies has been described previously.[31] Minor changes to the system are described below. The excitation and depletion beams derive from a SC laser, (SC-450-pp-he, Fianium, Southampton, UK), which has its output split into two paths using a polarizing beam splitter cube (DMLP605R, Thorlabs, Newton, New Jersey). Filters are used to select the excitation and LD wavelengths, which are shown in Figure 1. Measurements were performed using 50 pJ for excitation and 2 nJ for LD, as measured before the microscope objective. The LD beam was shaped into a doughnut with a vortex-phase plate. The beams are expanded and collimated before being recombined using a dichroic mirror (ZT594RDC, Chroma, Bellows Falls, Vermont). The collinear pulses are reflected via a dichroic mirror (635-70BPDC, Chroma) to an oil immersion objective and the resulting luminescence is directed to the detection path. The signal is sent to two stacked emission filters (FF01-629/56-25, Semrock, Rochester, New York) and subsequently through a 100 micron pinhole (NT36-392, Edmund Optics, Barrington, NJ) and a hybrid PMT (HPM-100-40, Becker and Hickl, Berlin, Germany) coupled to a single-photon counting card (SPC-830, Becker and Hickl).

Raster scanning of a 1×1 micron (64×64 pixels) or 2×2 micron (128×128 pixels) region was used to generate the images. Images were collected at room temperature. All data were collected with Single Photon Counter v9.30 software (Becker & Hickl) and analyzed

further using SPCImage (Becker & Hickl) or MATLAB version 2011b (Mathworks, Natick, MA). A time window of 3.3 ns with 64 time channels and a dwell time of 250-ms per pixel were used. Time-gating was used to obtain the best spatial resolution, as further outlined below. Image-J 1.44p (National Institutes of Health, USA) was used to take cross-sections of contiguous pixels in the collected images and Origin (OriginLab, Northampton, MA) was used to perform all other data processing. All reported uncertainties are one standard deviation.

RESULTS AND DISCUSSION

Luminescence Depletion Efficiencies of g-NQDs

The goal of this work was to explore the ability of giant nanocrystal quantum dots (g-NQDs) to serve as photostable tags for subdiffraction imaging techniques that require high laser powers and/or long exposure times. In practice, this required determining the experimental conditions, including wavelengths, laser powers, acquisition times, and signal gating, necessary for subdiffraction imaging using g-NQDs. As observed in Figure 1, the g-NQDs display the characteristic broad excitation curve (blue curve). The excitation wavelengths (green curve) were chosen to be as far red-shifted as possible in order to limit scattering, photodamage, and background luminescence in future applications where this may be an issue, such as in the case of biological samples, without compromising the desired signal collection. The amount of spectral overlap between the g-NQD's narrow emission profile (yellow curve) and the depletion wavelengths (red curve) had to be carefully balanced. A too small overlap would lead to inefficient depletion, while an unnecessarily large overlap would cause an unwanted decrease in signal collection from a narrow detection window (black curve). LD occurs with the chosen

excitation and depletion wavelength (Figure 1 inset). In this instance, both the excitation and depletion beams were Gaussian shaped, and the data reveal that the depletion is reversible.

The optimum power of the depletion beam results in 100% LD efficiency without excessive exposure of the sample to high photon fluxes, thus limiting sample heating and damage. In order to determine the optimal power for the depletion beam, the attenuation of the luminescence signal for isolated g-NQDs was recorded for varying depletion powers (Figure 2). The depletion efficiency increases with increasing depletion power up to the maximum output of the laser used for these studies (2.0 nJ). At the highest power, a 92% depletion was calculated after correcting for a 3% contribution to the luminescence signal caused by the depletion beam. The mechanism of the high depletion efficiency could be stimulated emission, stimulated absorption, or both. Stimulated absorption has been shown for Mn-Doped ZnSe NQDs.[23] A definitive assignment of the mechanism will, however, require further experiments that are beyond the scope of this work.

Determination of G-NQDs On/off Time and Photobleaching Rates

A zero or low frequency of blinking events is desirable for raster scan imaging to maintain the generated image's integrity. For an imaging application, a dwell time that is too short relative to the blinking characteristics of the nanoparticle will result in an undesired false negative at that pixel, on the other hand, it is not desirable to ensure there are no false negatives, as excessive imaging times may result. The blinking characteristics of the g-NQDs must be known to set a dwell time per pixel that limits false negatives and to quantify the probability of recording a false negative at an acceptable imaging speed. Therefore, the luminescence signal of isolated g-NQDs was recorded over a time window of 95 s using an excitation power of 50 pJ.

Representative data from ten randomly chosen g-NQDs are shown in Figure 2. The average percent on-time for all nanoparticles was 98.40 ± 0.04%. Hollingsworth and coworkers reported an on-time of greater than 99% and between 99 to 80% of the total analysis time as corresponding to non-blinking and largely-non-blinking g-NQDs, respectively.[27] The percentage of particles with on-times greater than 99% was 90% and the average off-time for these particles was 100 ± 200 ms. While the percentage of particles with on-times between 99 to 80% was 10%.

No observable photobleaching was observed on the time-scale of any of the measurements performed, which included an extended 3.5-minute illumination of the g-NQDs. This allowed for dwell times per pixel not possible with typical fluorescent dyes used for STED, including the 250 ms dwell time used for subsequent experiments.

Subdiffraction Spatial Resolution using g-NQDs.

The confocal and LD images of 12 quantum dots are shown in Figure 4. The confocal images were recorded using only the excitation beam, while both the excitation and depletion beams were incident upon the sample for the LD images. The improvement in the spatial resolution of the LD images is evident by the smaller feature size. In the confocal images, there are occasional rows of lower luminescence intensity compared to the rest of the pixels representing the g-NQD. This is attributed to a few intermittent blinking periods, characteristic of even the best g-NQDs. The amount of intermittent blinking recorded in the LD images is significantly lower than in the confocal images, and is only observed for g-NQD number 6. This is expected since the total time used to collect the nanoparticle's luminescence signal (not the

time the nanoparticle is exposed to the laser) in the LD mode is 97.7 ± 0.8 % shorter than that used to collect the confocal image.

Cross-sections were measured for each g-NQD shown in Figure 4, and representative cross-sections are shown in Figure 5. The confocal cross-sections were best fit to Gaussians, while the LD cross-sections were best fit to Lorentzians. This is consistent with previously reported STED data using small fluorophores.[11,31-32] The representative cross-sections in Figure 5 show a resolution enhancement, as defined by the full-width at half-maximum (fwhm), from 398 nm for the confocal mode to 43 nm for the LD mode. The average fwhm values for 12 g-NQDs are given in Table 1. The average cross section is 450 ± 90 nm and 40 ± 10 nm for the confocal and LD modes, respectively. For comparison, the actual "physical" average particle size measured by transmission electron microscopy was 13 ± 2 nm.

In order to achieve the 40 ± 10 nm spatial resolution in the LD imaging mode, we had to time-gate the data. The average fwhm of the LD cross-sections prior to applying the time-gate was 90 ± 20 nm. A representative confocal and LD decay curve is shown in Figure 6. The applied time-gate is represented by the two vertical lines. The signal prior to 600 ps is higher in the LD curve than the confocal curve. This is likely the result of scatter due to the STED beam, which degrades the spatial resolution. A time-gate at 500 ps was previously applied to STED images using small molecule fluorophores because depletion was incomplete at earlier times.[31] At long times the decay curve is primarily dominated by noise that does not convey useful information. While gating the signal significantly improved the LD image, gating the confocal data did not significantly alter the average fwhm of the confocal data set (Figure 6 bottom).

Two lifetime components were extracted from the LD data (2400 ± 800 ps and 300 ± 100 ps). If components with lifetimes greater than 3000 ps were present, they were not measured due

to the narrow time window used in these experiments to limit imaging times. One or both of the lifetime components may originate from multiexcitons. Htoon et al.[29] measured higher-order excitons in similar g-NQD at 4K using a $21\times$ lower power density than used in the current study (21 kW cm^{-2} for the excitation beam). The percentage of the short component decreased from 70 $\pm$ 6% to 50 $\pm$ 10% for the confocal to LD imaging formats, respectively (Figure 6).

The overall quality of the confocal and luminescence decay curves are similar (Figure 6). In a previous experiment using small dye molecules, the noise in the STED decay curve was higher compared to that obtained in the confocal experiment.[31] This was because far fewer molecules were probed by STED, and this reduced the signal. For the small molecule fluorophores, the dwell time per pixel was limited to 5 ms due to excessive photobleaching at longer dwell times. The photostabilty of the g-NQDs allows the dwell time per pixel to be increased, increasing the signal and improving the quality of the decay curve. A 250 ms dwell time was used for these studies, but shorter dwell times could be used to increase the imaging speed, particularly if data are recorded with fewer time channels (i.e., if time-gating is applied but lifetimes are not extracted), while still generating high-quality images with good signal-to-noise ratios.

CONCLUSIONS

Luminescence depletion images of CdSe/14CdS giant nanocrystal quantum dots (g-NQDs) with 13 $\pm$ 2 nm particle size show a spatial resolution of 40 $\pm$ 10 nm. The mode of the resolution enhancement is through depletion of the g-NQDs luminescence, suggested to be the result of stimulated emission and absorption working individually or in concert. Time-correlated, single-photon counting detection allowed the signal to be time-gated, which is

required for achieving 40-nm spatial resolution images. Critical for obtaining this result, is that photobleaching was not observed, permitting high quality measurements with extended dwell times that would be difficult to obtain under conditions where photobleaching was present. We conclude that g-NQDs show great promise as robust fluorescent labels for subdiffraction measurements in densely populated systems.

ACKNOWLEDGEMENTS

REFERENCES

(1)   Abbe, E. *Archiv für Mikroskopische Anatomie* **1873**, *9*, 413.

(2)   Strutt, J. W. *Phil. Mag.* **1874**, *XLVII*, 81.

(3)   Strutt, J. W. *Phil. Mag.* **1874**, *XLVII*, 193.

(4)   Strutt, J. W. *Phil. Mag.* **1879**, *VIII*, 261.

(5)   Binnig, G.; Quate, C. F.; Gerber, C. *Phys. Rev. Lett.* **1986**, *56*, 930.

(6)   Rust, M. J.; Bates, M.; Zhuang, X. *Nat. Methods* **2006**, *3*, 793.

(7)   Hell, S. W.; Wichmann, J. *Opt. Lett.* **1994**, *19*, 780.

(8)   Klar, T. A.; Hell, S. W. *Opt. Lett.* **1999**, *24*, 954.

(9)   Klar, T. A.; Engel, E.; Hell, S. W. *Phys. Rev. E* **2001**, *64*, 066613.

(10)   Bain, A. J.; Marsh, R. J.; Armoogum, D. A.; Mongin, O.; Porrès, L.; Blanchard-Desce, M. *Biochem. Soc. Trans.* **2003**, *31*, 1047.

(11)   Vicidomini, G.; Moneron, G.; Han, K. Y.; Westphal, V.; Ta, H.; Reuss, M.; Engelhardt, J.; Eggeling, C.; Hell, S. W. *Nat. Methods* **2011**, *8*, 571.

(12)   Donnert, G.; Keller, J.; Medda, R.; Andrei, M. A.; Rizzoli, S. O.; Lührmann, R.; Jahn, R.; Eggeling, C.; Hell, S. W. *Proc. Natl. Acad. Sci. U.S.A.* **2006**, *103*, 11440.

(13)   Willig, K. I.; Keller, J.; Bossi, M.; Hell, S. W. *New J. Phys.* **2006**, *8*, 106.

(14)   Willig, K. I.; Kellner, R. R.; Medda, R.; Hein, B.; Jakobs, S.; Hell, S. W. *Nat. Methods* **2006**, *3*, 721.

(15)   Rittweger, E.; Han, K. Y.; Irvine, S. E.; Eggeling, C.; Hell, S. W. *Nat. Photonics* **2009**, *3*, 144.

(16)   Wildanger, D.; Medda, R.; Kastrup, L.; Hell, S. W. *J. Micros.* **2009**, *236*, 35.

(17)   Hotta, J.-i.; Fron, E.; Dedecker, P.; Janssen, K. P. F.; Li, C.; Müllen, K.; Harke, B.; Bückers, J.; Hell, S. W.; Hofkens, J. *J. Amer. Chem. Soc.* **2010**, *132*, 5021.

(18)   Chen, F.; Gerion, D. *Nano Letters* **2004**, *4*, 1827.

(19)   Boldt, K.; Bruns, O. T.; Gaponik, N.; Eychmüller, A. *The Journal of Physical Chemistry B* **2006**, *110*, 1959.

(20)   García-Santamaría, F.; Brovelli, S.; Viswanatha, R.; Hollingsworth, J. A.; Htoon, H.; Crooker, S. A.; Klimov, V. I. *Nano Letters* **2011**, *11*, 687.

(21)   Klimov, V. I.; Mikhailovsky, A. A.; Xu, S.; Malko, A.; Hollingsworth, J. A.; Leatherdale, C. A.; Eisler, H. J.; Bawendi, M. G. *Science* **2000**, *290*, 314.

(22)   Zhang, C.; Xu, J.; Zhu, T.; Zhang, F.; Tan, Z.; Schiff, S. J.; Su, H.; Gao, S.; Wang, A. Y. *Physical Review B* **2009**, *80*, 035333.

(23)   Irvine, S. E.; Staudt, T.; Rittweger, E.; Engelhardt, J.; Hell, S. W. *Angewandte Chemie International Edition* **2008**, *47*, 2685.

(24)   He, Y.; Wang, H.-F.; Yan, X.-P. *Analytical Chemistry* **2008**, *80*, 3832.

(25)   Chen, Y.; Vela, J.; Htoon, H.; Casson, J. L.; Werder, D. J.; Bussian, D. A.; Klimov, V. I.; Hollingsworth, J. A. *Journal of the American Chemical Society* **2008**, *130*, 5026.

(26)   García-Santamaría, F.; Chen, Y.; Vela, J.; Schaller, R. D.; Hollingsworth, J. A.; Klimov, V. I. *Nano Letters* **2009**, *9*, 3482.

(27)   Vela, J.; Htoon, H.; Chen, Y.; Park, Y.-S.; Ghosh, Y.; Goodwin, P. M.; Werner, J. H.; Wells, N. P.; Casson, J. L.; Hollingsworth, J. A. *Journal of Biophotonics* **2010**, *3*, 706.

(28)   Spinicelli, P.; Buil, S.; Quélin, X.; Mahler, B.; Dubertret, B.; Hermier, J. P. *Physical Review Letters* **2009**, *102*, 136801.

(29)   Htoon, H.; Malko, A. V.; Bussian, D.; Vela, J.; Chen, Y.; Hollingsworth, J. A.; Klimov, V. I. *Nano Letters* **2010**, *10*, 2401.

(30)   Guo, Y.; Marchuk, K.; Sampat, S.; Abraham, R.; Fang, N.; Malko, A. V.; Vela, J. *The Journal of Physical Chemistry C* **2011**, *116*, 2791.

(31)   Lesoine, M. D.; Bose, S.; Petrich, J. W.; Smith, E. A. *The Journal of Physical Chemistry B* **2012**.

(32)   Fitzpatrick, J. A. J.; Yan, Q.; Sieber, J. J.; Dyba, M.; Schwarz, U.; Szent-Gyorgyi, C.; Woolford, C. A.; Berget, P. B.; Waggoner, A. S.; Bruchez, M. P. *Bioconj. Chem.* **2009**, *20*, 1843.

Table 1. Full-width at half-maximum (fwhm) values obtained for cross-sections of g-NQDs obtained in the images shown in **Figure 4**.

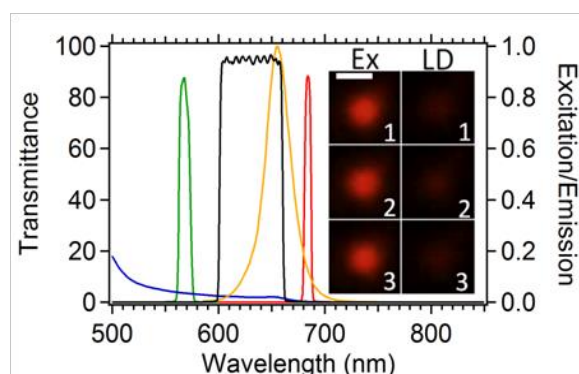| g-NQD Number from Figure 4	Confocal fwhm (nm)	Luminescence Depletion (time-gated) fwhm (nm)
1	550	34
2	479	35
3	525	42
4	432	30
5	612	44
6	355	33
7	397	38
8	310	51
9	398	43
10	370	45
11	463	55
12	494	62
Average	450 ± 90	40 ± 10

Figure 1. The CdSe/14CdS g-NQDs excitation (blue line) and emission (orange line) spectra and the transmission curves for the microscope's filters. The laser pulses are selected with interference filters with the excitation (green line) and LD (red line) filters centered at 570 ± 10 nm and 684 ± 8 nm, respectively. The band-pass of the LD filter allows significant overlap with the g-NQDs emission spectrum while avoiding unwanted excitation. Two stacked emission filters (black line) centered at 629 ± 56 nm allow the signal to be transmitted to the detection path. The inset shows the QDs LD is reversible with successive images from top to bottom of a single quantum dot obtained with excitation beam illumination (left column) or excitation plus depletion beam illumination (right column), where all beams were Gaussian shaped. The scale-bar is 500 nm.
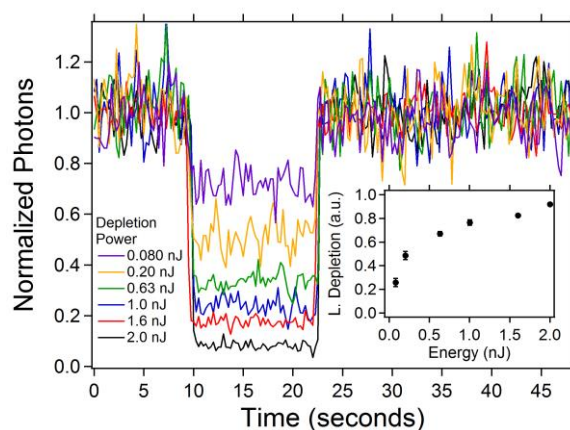
Figure 2. The g-NQD depletion efficiency was measured using continuous illumination with the 50 pJ excitation beam, and overlapping the depletion beam after approximately 10 s had elapsed. The depletion powers ranged from 0.08 to 2 nJ. The data were corrected for a small component of luminescence generated by the depletion beam, but did not need correction for photobleaching. The inset shows the fraction of LD versus depletion laser power.
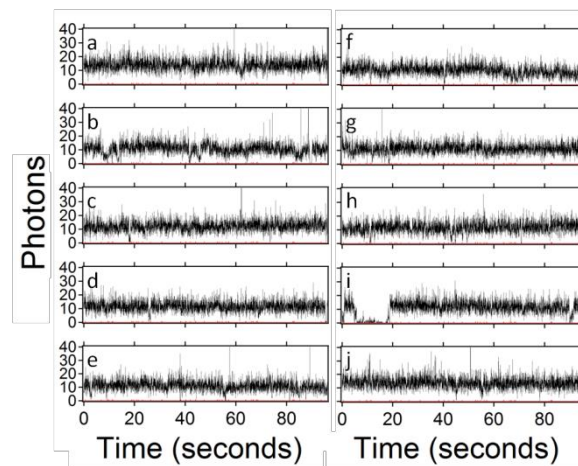
Figure 3. Graphs of the luminescence intensity versus time for 10 individual g-NQDs labeled a to j. The luminescence intensity was integrated every 25 ms for a total of 95 s. The excitation power was the same as used for collecting the LD images (50 pJ). The QD was considered off if the signal dropped below 5 counts for 3 adjacent data points. The data show g-NQDs under the experimental conditions used here were 90 % non-blinking with on-times greater than 99 % and 10 % largely non-blinking with on-times between 99 % and 80 %.
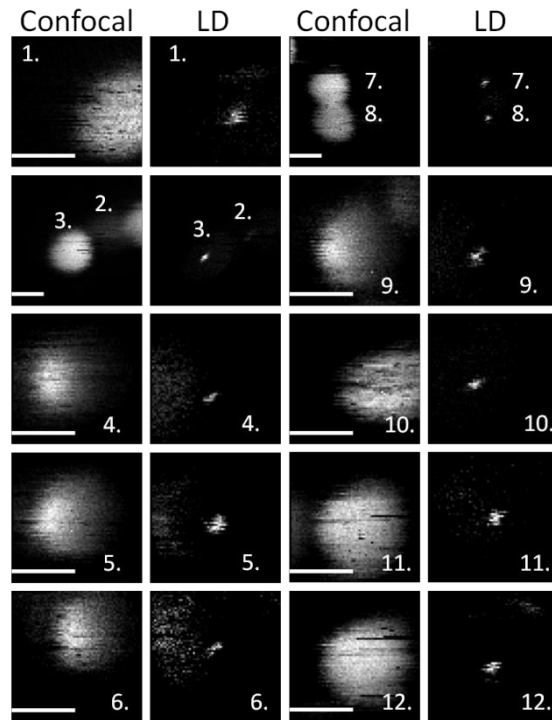
Figure 4. Images of 12 g-NQDs measured in the confocal and LD modes. The confocal images were collected after blocking the depletion beam, and the toroid shaped depletion beam was unblocked to generate the LD images. The scan direction was vertical. Scale-bars are all equal to 500 nm.
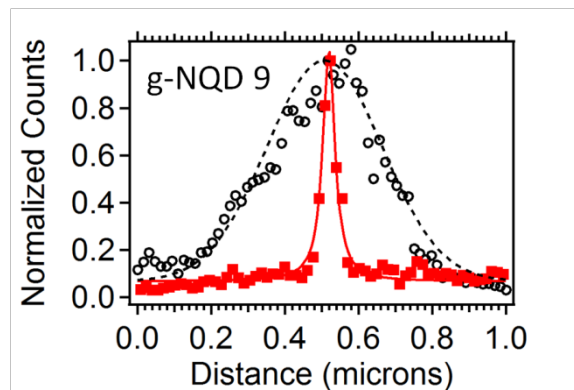
Figure 5. Representative cross-sections and associated fits for a g-NQD in confocal (open circles, Gaussian fit with 398 fwhm) and time-gated LD (solid squares, Lorentzian fit with 43 nm

fwhm) modes. The time-gate applied to the LD images yields an improvement of 2.25 fold over the ungated LD data. A 7× average lateral resolution improvement is observed for the time-gated STED data over the system's diffraction limit.
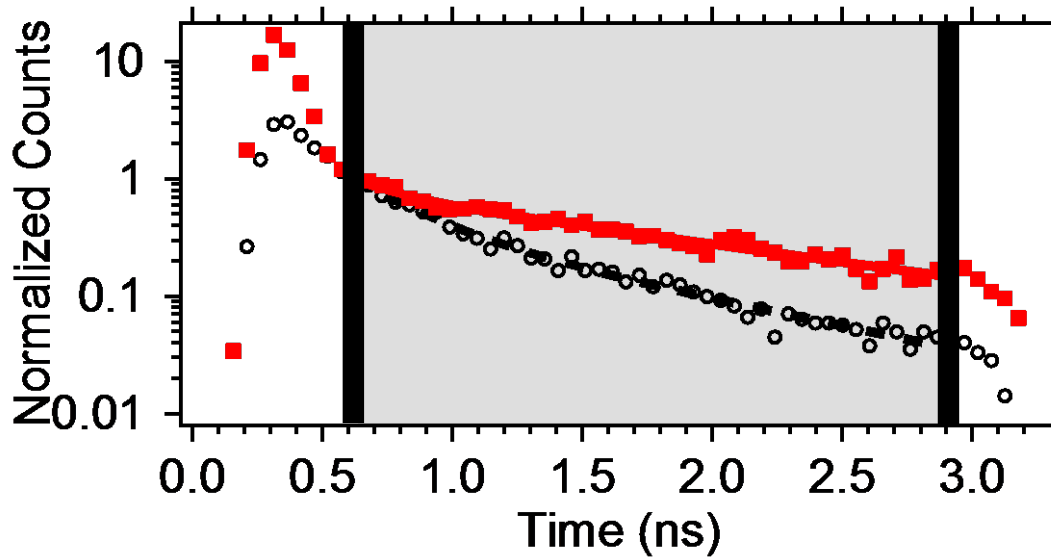
	A_1 (%)	Tau_1 (ps)	A_2 (%)	Tau_2 (ps)
Confocal	70 ± 6	260 ± 40	30 ± 6	1500 ± 400
LD	50 ± 10	300 ± 100	50 ± 10	2400 ± 800

Confocal   LD   Confocal (Time-gated)   LD (Time-gated)
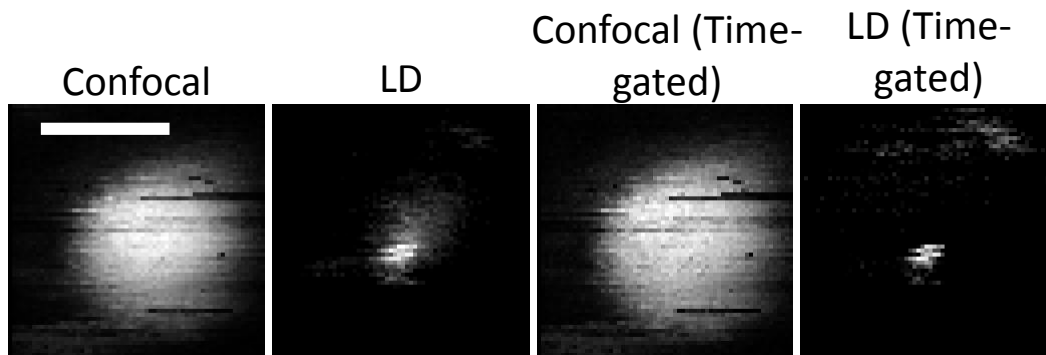
Figure 6. Top: Representative confocal (open circles with dotted line fit) and LD (solid squares with solid line fit) luminescence decay curves are shown at the top of the figure. The vertical lines represent the time-gate that was applied to the LD images in Figure 4. The data have been normalized to the value at 600 ps. Bottom: The two left images show confocal and LD data prior to applying the time-gate and the two right confocal and LD images show the effects of applying the time-gate. The scale-bar is equal to 500 nm

CHAPTER 4b. FLUORESCENCE CORRELATION SPECTROSCOPY MEASUREMENT COMBINED WITH STED MICROSCOPY: A TOOL FOR DETECTION OF SMALL SCALE HETEROGENEITIES

ABSTRACT

Stimulated emission depletion microscopy has emerged as a very interesting and highly applicable technique. The superiority of this technique over traditional confocal microscopies is primarily based on the sub-diffraction resolution. The other aspect, if all the techniques used with confocal microscopy can also be performed with STED microscopy with an added benefit of resolution, still remains open to research. Here we study effectiveness of STED on FCS measurements. This ingenious combination can open up a scope to study heterogeneous domains whose size is much below the diffraction limit of visible light, in different systems. We have found, STED-FCS experiments works with its full potential in two dimensional system, such as, in lipid bilayers. Whereas, in systems where the fluorophores can diffuse in three dimension, improvement of resolution by STED over the existing confocal technique is nominal. This somewhat presents a limitation of this combined technique.

INTRODUCTION

Confocal fluorescence correlation spectroscopy (FCS) has been used for to characterize the microscopic heterogeneity of samples by measuring the diffusion of a fluorescent probe. In all the experiments that have been reported to date, the focal spotsize was around 300-400 nm. Thus, the confocal technique may not be appropriate for the study of nanoscale heterogeneous domains in systems such as ionic liquids (ILs) and lipid bilayers. Spatially heterogeneous structure in ILs have been predicted by molecular dynamics (MD) studies from different groups.[1] The presence of low-Q peaks in X-ray diffraction measurements of immidazolium ILs is consistent with a correlation length of one or two times the long axis of the cation. The scale of the heterogeneous domains for immidazolium ionic liquids has thus been predicted to be 1.3-2.7 nm.[2] Shaw *et al*. used confocal FCS for several pyrrolidinium ionic liquids (ILs) with different organic chain length.[3] They showed the presence of bimodal diffusion of the probe (rhodamine 6G) in ILs with small alkyl chains, such as, tris-(2-hydroxyethyl)-methylammonium methylsulfate (HEMA), might not be apparent in confocal FCS measurements. In similar studies, Bhattacharyya and coworkers[4] and Samanta and his group[5] studied ILs by confocal FCS and proposed the existence of heterogeneity in some of the ionic liquids.

Here, we combine two techniques, super-resolution stimulated emission depletion (STED) microscopy and FCS. This provides the advantage of looking at a very small portion of sample. Recently, Hell and coworkers studied diffusion of ATTO 647N-labelled phosphoethanolamine and sphingomyelin in plasma membrane.[6] They found that sphingolipids and glycosylphosphatidylinositol-anchored proteins are trapped in cholesterol-mediated molecular

complexes dwelling within < 20-nm diameter areas by combining FCS with STED. In confocal FCS the anomalous diffusion was not observed, as it was averaged out.

We have performed preliminary STED-FCS measurements on an IL with a short alkyl chain, HEMA, and on a very viscous organic solvent, glycerol, which serves as a control for experiments with ionic liquids. We expected that our super-resolution stimulated emission depletion (STED) microscope with 40-nm spatial resolution would be able to detect the very small heterogeneous domains.[7] We have observed, however, that STED resolution enhancement does not work efficiently when there is possible motion along the axial direction (that is, perpendicular to the focal plane). Thus, we did not observe any heterogeneity in HEMA by STED-FCS with a small resolution enhancement over confocal measurements. Furthermore, to study the effectiveness of the combined STED-FCS technique, we have carried out experiments on lipid bilayers. Lipid bilayers appear to be a two dimensional system with respect to the full width at half-maximum of the confocal volume along the perpendicular direction to the sample plane. Thus, in essence, movement of the probes along the axial direction is restricted. We have observed the STED-FCS works effectively in lipid bilayers and we can detect heterogeneity present in lipid bilayers where confocal-FCS is unable to detect the bimodal diffusion as it averages out in a confocal volume of ~300 nm.

MATERIALS AND METHODS

Instrumentation. In our STED microscope, the diffraction-limited excitation beam (570 nm) is overlapped with a doughnut-shaped STED beam (700 nm).   As spontaneous emission in the periphery is depleted by the ring of the STED beam, only the fluorophores present in the center can emit light, which makes the effective point spread function (PSF) go well below diffraction limit, which is given by, $d=\lambda/(2\times N.A.)$. The spatial resolution STED microscopy is given by, $d =$

$\lambda/(2N.A.\sqrt{I/I_s + 1}\,)$, where I is the intensity of STED laser and I_s is the intensity at which 50% of fluorophores are quenched. The details of the apparatus are given elsewhere.[8] The only modification is that we are using a 100-μm pinhole in the detection side instead of the collection fiber. We measure resolution of our instrument by scanning 40-nm fluorescent beads (FluoSpheres red, 40 nm, Invitrogen, Grand Island, NY), and the resolution is 40 ± 10 nm.

For FCS, the data are collected in "fifo" mode, which registers microtime (time lag between laser pulse and the arrival of photon) and macrotime (time from beginning of the experiment) for each photon in a time-tagged data file. This gives us the ability to know the timing of photons over a broad dynamic range. From the microtime of the photons, a fluorescence lifetime histogram can be generated. Macrotime along with microtime can give us dynamics over 10 ms with a picosecond time resolution upon autocorrelation of the number of photons detected at different times. This photon counting mode is preferable to the systems that uses continuous wave laser, as we can use time-gating to block out initial scattering or long-time background fluorescence. Such gating often improves the autocorrelation.[9] As in our STED system, the best resolution is obtained by time-gating some hundreds of picosecond at the beginning, for STED-FCS, we use our TAC parameters to discard photons in first 500 ps. The correlation function $G(\tau)$ is given by:

$$G(\tau) = \frac{\langle \delta F(0)\delta F(\tau)\rangle}{\langle F\rangle^2} \tag{1}$$

where $\langle F\rangle$ is the average number of counts and $\delta F(\tau)$ is the fluctuation in counts at a delay τ around the mean value, $\langle F\rangle$, $\delta F(\tau) = \langle F\rangle - F(\tau)$. Becker & Hickl software generates the autocorrelation function by generating a histogram of the coincidence of photons at a time τ between original time-tagged data and the data with a temporal shift by τ.

Data Analysis. Chromophores experiencing different local environments, diffusion in the focal volume can be described by a three dimensional Gaussian function is given by,[10]

$$G(\tau) = \frac{1}{N} \sum_{i=1}^{n} a_i \left(1 + \frac{\tau}{\tau_{D_i}}\right)^{-1} \left(1 + \frac{\tau}{k^2 \tau_{D_i}}\right)^{-1/2} \tag{2}$$

where N is the mean number of molecules, a_i is the contribution of the ith local environment component to the total amplitude of the autocorrelation function, τ_D is the characteristic diffusion time, and $k = \omega_z/\omega_{xy}$, where ω_z and ω_{xy} are the axial and radial dimensions of the confocal volume. The diffusion coefficient, D, is related to τ_D by, $\tau_D = \omega_{xy}/4D$. When i = 1, the model reduces to the case for normal three-dimensional diffusion and when i = 2, a bi-modal diffusion model is obtained.

The other way to represent anomalous diffusion is by noting that the mean square displacement of the molecule's diffusion $<r>^2$ is not linear with time but, rather follows a power law in time τ: [11]

$$\langle r \rangle^2 = 4D'\tau^\alpha \tag{3}$$

where D' is the average diffusion coefficient. The anomalous diffusion exponent, α, gives the degree of hindrance to free diffusion. For free Brownian diffusion, $\alpha = 1$; and for hindered diffusion, $\alpha < 1$. With this anomalous coefficient, α, equation 2 becomes:

$$G(\tau) = \frac{1}{N} \left(1 + \left(\frac{\tau}{\tau_D}\right)^\alpha\right)^{-1} \left(1 + \frac{1}{k^2} \left(\frac{\tau}{\tau_D}\right)^\alpha\right)^{-1/2} \tag{4}$$

We fit the normalized correlation function with Origin 8.1, with τ_D replaced by $\omega_{xy}/4D$. We scan gold nanoparticles to find the PSF for the confocal spot in the XY dimension with the same experimental conditions, which helps us to fix ω_{xy} for the confocal correlation data. Similarly we can fix k to avoid having too many parameters by scanning gold nanoparticles in the XZ dimension. From confocal data, we can find the diffusion coefficient of fluorophores in glycerol (control). For STED-FCS data, we can fix everything but the ω_{xy} for glycerol to find the radial resolution in

STED-FCS. For glycerol, we use the 3D normal diffusion model with single modality, because if we use equation 4, it gives α close to 1. Our plan is to use equation 4 to ionic liquid in both confocal and STED data, and find out how α changes from confocal to STED data.

Materials

Ionic Liquids. Glycerol was obtained from Fisher scientific, and the ionic liquids were obtained from Sigma Aldrich. The ionic liquids are purified passing through a column as described elsewhere.[12] Fluorescence from the impurity in the ionic liquid impurity is checked for. The ionic liquids are dried rigorously under vacuum prior to use. The fluorescent dye ATTO 590 and alexa fluor 594 were obtained from ATTO-TEC (Germany) and Invitrogen, respectively.

Lipid bilayers (POPC membrane). Fused silica coverslips were purchased from Spi Supplies. 1-Palmitoyl-2-oleoyl-sn-glycerol-3- phosphatidylcholine (**Figure1a**) (POPC, Tm = -2 °C) was obtained from Avanti Polar Lipids (Birmingham, AL). Planar lipid bilayers supported on fused silica surfaces were developed using standard vesicle fusion procedures, which have been detailed elsewhere.[13] POPC Lipid mixtures were dissolved in chloroform in glass centrifuge tubes. The total lipid concentration was fixed at 0.5 mg/mL. The solutions were mixed well to ensure homogeneity. The chloroform was then evaporated to near dryness under an inert atmosphere of nitrogen. The samples were subsequently placed into a vacuum desiccator for 2.5 h for complete removal of residual chloroform. In the vials containing them, 50-mM sodium phosphate buffer, pH 8.0, was added in such a way that the final lipid concentration would be 0.3 mM. The lipids were then kept in solution *via* agitation for 15 min forming large mulitilamellar vesicles. Extrusion of the large mulitilamellar vesicle solution was carried out with Avanti Mini-Extruder to form

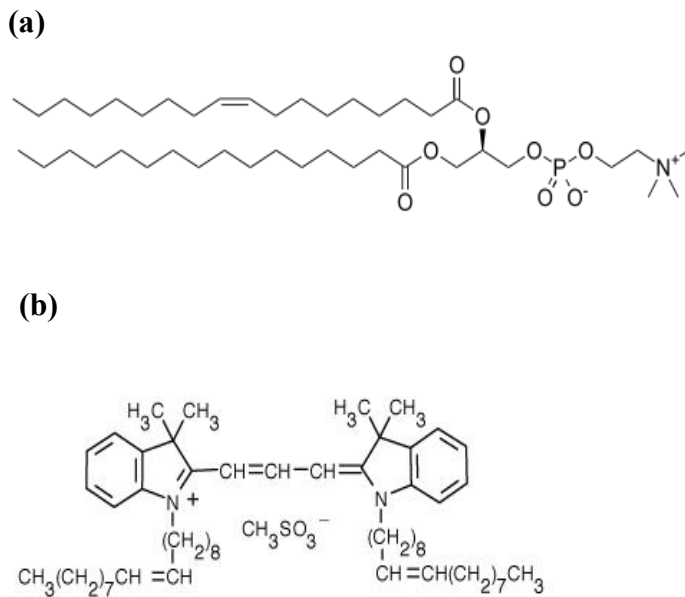small unillamellar vesicles. The holder block of the extruder was kept at a

(a)

(b)

Figure 1. a) Structure of 1-Palmitoyl-2-oleoyl-sn-glycerol-3- phosphatidylcholine (POPC), b) structure of DiI, and c) absorption (blue) and emission (red) spectra of DiI.

temperature greater than room temperature ($28°C$), which is critical for the successful generation of vesicles from phospholipids with a phase transition temperature above room temperature. A drop of the vesicle solution (100 µL) was placed on the bottom of a Petri dish, and a dried fused silica microscopic slide was placed on top of the drop. The Petri dish was incubated on a $28°C$ hot plate for 30-45 min. As a final step, the slide was carefully removed from the Petri dish and was placed into a homemade cell, which was filled with the phosphate buffer. We used lipophilic DiI (Invitrogen Molecular Probes) (**Figure 1b**) as a probe for studying diffusion. 50 µL of a nanomolar dye solution was incorporated in the cell and incubated for 10 min to enable dye molecules to penetrate the membrane. Subsequently, the slide containing the membrane was washed in the

liquid cell with the phosphate buffer at least 5 times to eliminate any contribution to the fluorescence from free dye in buffer.

RESULTS AND DISCUSSION

Lifetime Data. We measured lifetime of coumarin 153 dye in glycerol and HEMA (**Figure 2**) with our TCSPC setup as described elsewhere.[14] If the heterogeneity is so prominent, we should see more than one exponential of fluorescence decay in HEMA and excitation wavelength dependence of emission maximum. With HEMA, we saw single exponential decay just as it is in control glycerol and in steady state experiment also we did not see any wavelength dependence. This suggests either there is no heterogeneity in HEMA or the scale of heterogeneity is so small that it is being averaged out. It makes our STED-FCS experiment very desirable where we can look at very small portion of the ionic liquid.

Confocal- and STED-FCS Data. To calibrate our instrument with a known system, we chose alexa fluor 594 in water. The confocal FCS result is given in **Figure 3**. We found diffusion coefficient to be 443 μm^2/s. For rhodamine 6G the diffusion coefficient is known to be 426 μm^2/s.[15] This similarity in diffusion coefficients confirms that our choice of excitation intensity is good[16] and that the confocal volume is calibrated. The only problem
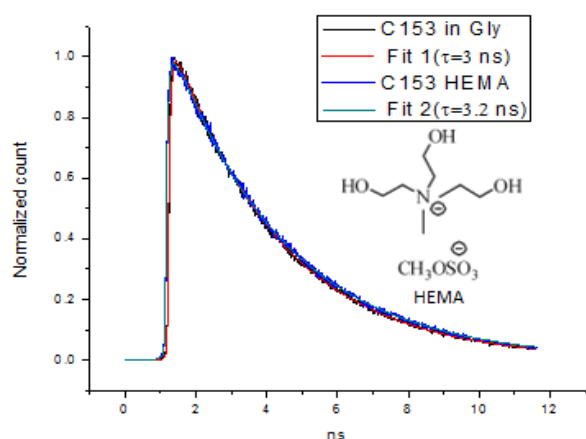
Figure 2. Lifetime decay of coumarin 153 in glycerol and HEMA; the inset shows structure of HEMA.

that we face is that the repetition rate of our laser (2MHz) is not high enough, as a long time is required to obtain high-quality data (1-2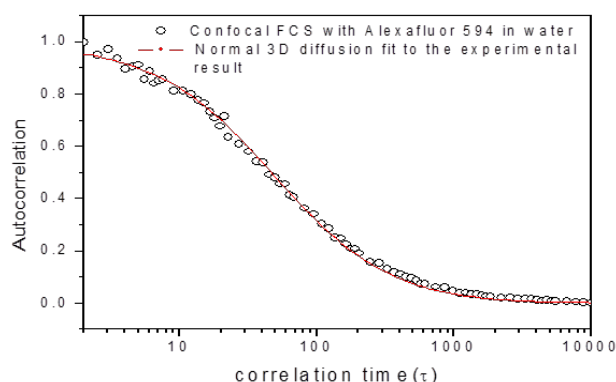 hrs). We characterized our confocal spot size by scanning gold nanoparticles, which gave us a full-width at half-maximum (fwhm) in the XY plane of 300-310 nm; the fwhm in the XZ plane is 900nm. To verify that the heterogeneity is a result of molecular structure of ionic liquid and not viscosity, we did experiments taking a conventional solvent with high viscosity (glycerol) as a control for the

Figure 3. Confocal FCS with alexa fluor 594 in water.

ionic liquids. **Figure 4** presents the confocal and STED-FCS measurement with alexa fluor 594 in glycerol. After following the fitting procedure described in data analysis section, we found ω_{xy} to be 250 nm. Under the same experimental conditions (glycerol as embedding medium), we measured the spatial resolution to be 50-60 nm. Similarly, in HEMA, only a nominal reduction of focal area with STED over confocal was calculated. Even under STED-FCS we did not find any heterogeneity in small chain IL, HEMA.

Thus, we have seen that the effect of STED on FCS is not much pronounced with a bulk sample. The prime reason is the presence of diffusion along axial direction in the focal volume. The doughnut shaped STED is not uniform throughout the axial direction of confocal volume, thus, not effective to enhance the resolution throughout the axial direction. This suggests necessity of a two dimensional samples for effective enhancement of resolution by STED beam in FCS

experiments. In a 2D film the diffusional motion of the molecules is restricted only to the plane of the glass slide, with negligible motion in axial direction. This somewhat restricts the applicability
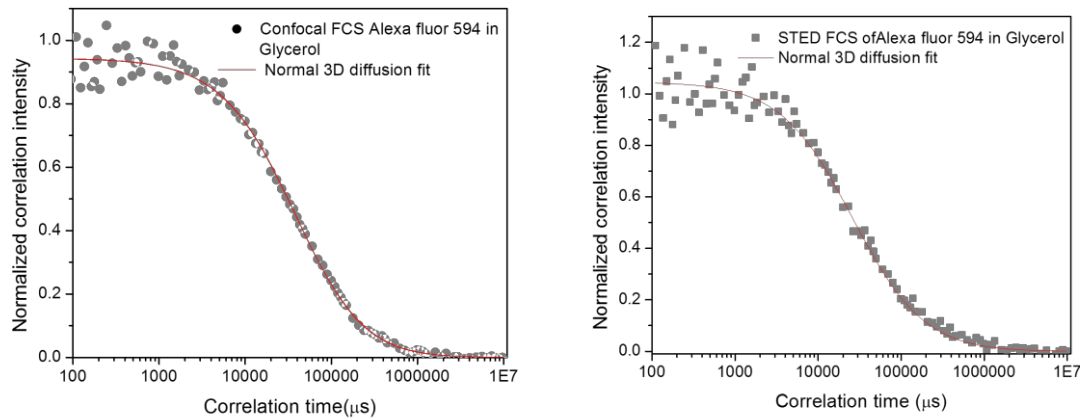
Figure 4: (*Left*) Confocal FCS with alexa fluor 594 in glycerol (gray dot) and fitting of the experimental curve with normal 3D diffusion(red line); (*Right*) STED-FCS with alexa fluor 594 in glycerol (gray box) and fitting of the experimental curve with normal 3D diffusion(red line).

of the combined STED-FCS method. We thus studied diffusion of lipophilic dyes in lipid membrane. The thickness of lipid bilayers has been reported as ~ 20 nm. Thus with respect to 900 nm fwhm of STED profile along XZ plane, the lipid membrane samples essentially becomes 2D. We can easily neglect any diffusional motion in the direction perpendicular to XY-plane.

The **Figure 5** shows the fluorescence image of POPC membrane on fused silica microscopic slides. The mobility of the prepared membranes were examined with the help of fluorescence recovery after photo-bleaching (FRAP) experiment. When average diffusion

constant (D) is faster than 10^{-8} cm^2/s, we concluded that we are obtaining contribution from diffusion of dye in free form, that is, in solution. Whereas, a diffusion coefficient slower than 10^{-10} cm^2/s reflects a non-mobile, ill formed membrane.[13a] We obtained a diffusion coefficient of 10^{-9} cm^2/s using FRAP experiment, thus, suggesting formation of well-defined membrane whose size is big enough with respect to the beam diameter. We have collected FCS data both in presence and

Figure 5. Fluorescence image of POPC membrane.

absence of depletion beam. As evident in **Figure 6a,** going from the confocal to STED mode of data collection, the mean correlation time, is shifting towards faster time scale. As the lipid bilayer can be safely assumed to be 2D, for the fitting of FCS data we have used 2D diffusional equation, as given by,

$$G(\tau) = \frac{1}{N}\left(1 + \left(\frac{\tau}{\tau_D}\right)^{\alpha}\right)^{-1} \tag{5}$$

Upon replacing τ_D by $\omega_{xy}/4D$, we obtain:

$$G(\tau) = \frac{1}{N}\left(1 + \left(\frac{8\ln 2 \cdot D \cdot \tau}{\omega_{xy}{}^2}\right)^{\alpha}\right)^{-1} \tag{6}$$

As described earlier, during the fitting of the confocal-FCS data, the beam diameter (ω_{xy}) was fixed as 300 nm. As heterogeneous domains in lipid bilayers are very small compared to ω_{xy}, we can assume that we see an averaged out diffusion, thus α can be set to 1. Henceforth, we obtained the diffusion coefficient (D) of the lipid bilayer to be **3 μ^2/s**. Hell and coworkers reported 5 μ^2/s diffusion coefficient value for a lipid bilayer membrane (DOPC). During fitting of the STED-FCS curve the diffusion coefficient obtained from confocal mode was kept constant and the ω_{xy}, anomaly coefficient (α) was kept free to vary. This returned a value of the ω_{xy} and α as **81 nm** and
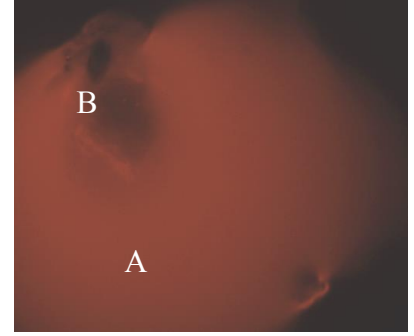
0.97. Thus, we observed the effect of stimulated depletion very effectively. On the contrary, we can fix ω_{xy} to the value obtained from scanning fluorescent beads (50 nm), which changes the average diffusion constant from the value obtained from confocal mode, which can well be true as the in STED mode we are looking at small fraction of the confocal area. The microscopic diffusion coefficient can be different form average diffusion coefficient obtained from a larger area. But, considering our system, a well formed lipid bilayer, we do not expect the diffusion
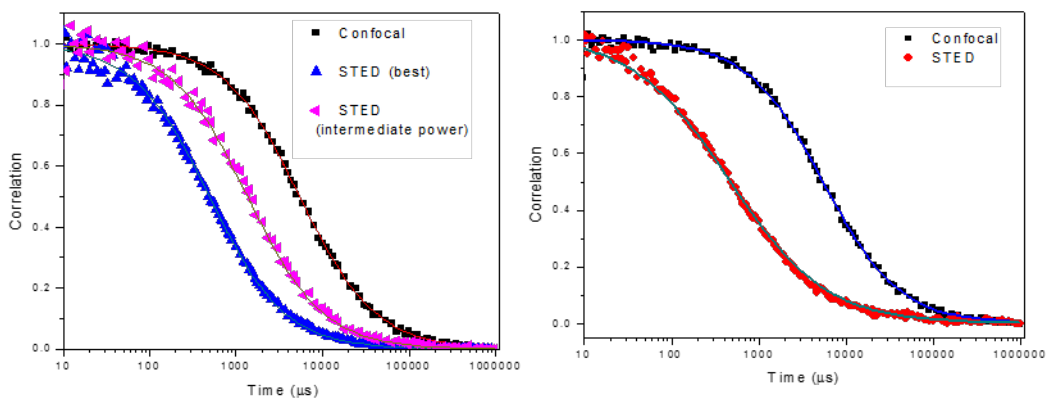
Figure 6. a) Confocal- (black) and STED- (with 4 nJ (blue) and 1 nJ (pink) peak power) FCS with DiI in lipid bilayer at point A in figure 5. b) Confocal- (black) and STED- ((red) with 4 nJ peak power) FCS with DiI in lipid bilayer at point B in **Figure 5**.

coefficient to vary when we are looking at sub-diffraction area. We further tested the effect of STED laser power. We carried out the FCS with an intermediate STED pulse energy of 1 nJ (instead of 4 nJ, a power used for maximum STED resolution for our system). As expected we observed an intermediate shift of the correlation curve towards faster time. Our proposal that the STED-FCS is much superior technique over confocal FCS to examine heterogeneity domains which are very small, was further studied. We carried out STED-FCS experiment on a region labeled as B (**Figure 5**) where we observed presence of some defects. **Figure 6b** shows the correlation curved obtained using STED-FCS technique. Consistent with data obtained from well-formed bilayer, we observed the correlation shifting towards faster time at

point B also. Using the fitting method described earlier, we obtained the ω_{xy} and α as **85 nm** and **0.78** respectively. The value of less than unity of anomaly coefficient suggests hindered diffusion in that region. This observation has only been possible because of smaller effective measurement area with STED mode. This heterogeneity was not observed by confocal-STED as the small scale heterogeneities are averaged in a much bigger area.

CONCLUSION

Thus, from the observations it is evident that the STED-FCS works most efficiently in 2D samples, where the movement along the axial direction is restricted. We have performed experiments with bulk ionic liquids, we observed nominal improvement of resolution. Whereas with lipid bilayers, the calculated focal area (ω_{xy}= ~ 80 nm) is significantly lower than the diffraction limited confocal mode. Our results indicates towards the power of STED-FCS experiment to study very small scale heterogeneity in membranes. The STED-FCS can be used as an effective tool to detect defects in lipid bilayers; thus can one can have a better control to form defect free lipid bilayers. We also propose that if one can make a thin layer of ionic liquids, the ingenuous STED-FCS can be used for detection of very small scale heterogeneity in ILs like HEMA where confocal FCS is unable to find the structured nature.

REFERENCES

1.   (a) Wang, Y.; Voth, G. A., *J. Am. Chem. Soc.* **2005,** *127*, 12192-12193; (b) Wang, Y.; Voth, G. A., *J. Phys. Chem. B.* **2006,** *110*, 18601-18608; (c) Hu, Z.; Margulis, C. J., *Proc. Natl. Acad. Sci. U. S. A.* **2006,** *103*, 831-836; (d) Lopes, J. N. C.; Padua, A. A. H., *J. Phys. Chem. B.* **2006,** *110*, 3330-3335; (e) Lopes, J. N. C.; Costa Gomes, M. F.; Padua, A. A. H., *J. Phys. Chem. B.* **2006,** *110*, 16816-16818; (f)

Urahata, S. M.; Ribeiro, M. C. C., *J. Chem. Phys.* **2004,** *120*, 1855; (g) Canongia Lopes, J. N. A.; Padua, A. A. H., *J. Phys. Chem. B*. **2006,** *110*, 3330.

2.   (a) Atkin, R.; Warr, G. G., *J. Phys. Chem. B* **2008,** *112*, 4164-4166; (b) Hayes, R.; Imberti, S.; Warr, G. G.; Atkin, R., *Phys. Chem. Chem. Phys.* **2011,** *13*, 3237-3247; (c) Macchiagodena, M.; Gontrani, L.; Ramondo, F.; Triolo, A.; Caminiti, R., *J. Chem. Phys.* **2011,** *134*, 114521/1-15; (d) Russina, O.; Triolo, A., *Faraday Discuss.* **2012,** *154*, 97-109; (e) Russina, O.; Triolo, A.; Gontrani, L.; Caminiti, R., *J. Phys. Chem. Lett.* **2012,** *3*, 27-33; (f) Russina, O.; Triolo, A.; Gontrani, L.; Caminiti, R.; Xiao, D.; Hines, L. G., Jr.; Bartsch, R. A.; Quitevis, E. L.; Plechkova, N.; Seddon, K. R., *J. Phys. : Condens. Matter* **2009,** *21*, 424121/1-9; (g) Triolo, A.; Russina, O.; Bleif, H.-J.; Di Cola, E. J., *J. Phys. Chem. B* **2007,** *111*, 4641-4644.

3.   Guo, J.; Baker, G. A.; Hillesheim, P. C.; Dai, S.; Shaw, R. W.; Mahurin, S. M., *Phys. Chem. Chem. Phys.* **2011,** *13*, 12395-12398.

4.   Sasmal, D. K.; Mandal, A. K.; Mondal, T.; Bhattacharyya, K., *J. Phys. Chem. B* **2011,** *115*, 7781-7787.

5.   Patra, S.; Samanta, A., *J. Phys. Chem. B* **2012,** *116*, 12275-12283.

6.   Eggeling, C.; Ringemann, C.; Medda, R.; Schwarzmann, G.; Sandhoff, K.; Polyakova, S.; Belov, V. N.; Hein, B.; Middendorff, C. V.; Schönle, A.; Hell, S. W., *Nature* **2009,** *457*, 1159.

7.   (a) Lesoine, M. D.; Bhattacharjee, U.; Guo, Y.; Vela, J.; Petrich, J. W.; Smith, E. A., *The Journal of Physical Chemistry C* **2013,** *117*, 3662- 3667; (b) Syed, A.; Lesoine, M. D.; Bhattacharjee, U.; Petrich, J. W.; Smith, E. A., *Photochemistry and Photobiology* **2014**.

8.   Lesoine, M. D.; Bose, S.; Petrich Jacob, W.; Smith, E. A., *J. Phys. Chem. B* **2012,** *116*, 7821-7826.

9.   Földes-Papp, Z.; Liao, S.-C. J.; You, T.; Barbieri, B., *Current Pharmaceutical Biotechnology* **2009,** *10*, 532-542.

10.   (a) Krichevsky, O.; Bonnet, G., *Rep. Prog. Phys.* **2002,** *65*, 251; (b) Mahurin, S. M.; Dai, S.; Barnes, M. D., *J. Phys. Chem. B* **2003,** *107*, 13336.

11.   (a) Bouchaud, J.-P.; Georges, A., *Phys. Reports* **1990,** *195*, 127-193; (b) Saxton, M. J., *Biophys. J.* **1994,** *66*, 394-401; (c) Feder, T. J.; Brust-Mascher, I.; Slattery, J. P.; Baird, B. A.; Webb, W. W., *Biophys. J.* **1996,** *70*, 2767-2773.

12.   Earle, M. J.; Gordon, C. M.; Plechkova, N. V.; Seddon, K. R.; Welton, T., **2007,** *79*, 758.

13.   (a) Smith, E. A.; Coym, J. W.; Cowell, S. M.; Tokimoto, T.; Hruby, V. J.; Yamamura, H. I.; Wirth, M. J., *Langmuir* **2005,** *21*, 9644-9650; (b) Brian, A. A.; McConnell, H. M., *Proc. Natl. Acad. Sci. USA* **1984,** *81*, 6159-6163; (c) Cremer, P. S.; Boxer, S. G., *J. Phys. Chem. B* **1999,** *103*, 2554-2559.

14.   Chowdhury, P. K.; Halder, M.; Sanders, L.; Calhoun, T.; Anderson, J. L.; Armstrong, D. W.; Song, X.; Petrich, J. W., *J. Phys. Chem. B* **2004,** *108* (29), 10245-10255.

15.   Petrasek, Z.; Schwille, P., *Biophys. J.* **2008,** *94*, 1437.

16.   Gregor, I.; Patra, D.; Enderlein, J., *Chem. Phys.Chem.* **2005,** *6*, 164-170.

CHAPTER 5. FLUORESCENCE SPECTROSCOPY OF THE RETINA FOR THE SCREENING OF BOVINE SPONGIFORM ENCEPHALOPATHY

Ujjal Bhattacharjee[†,‡] *Catherine Graham,*[§] *Stefanie Czub,*[§] *Sandor Dudas,*[§] *Mark A. Rasmussen,*[‡] *Thomas A. Casey,*[†]

and Jacob W. Petrich*[†,‡]

ABSTRACT

Transmissible spongiform encephalopathies (TSE) are progressive, neurodegenerative disorders, of which bovine spongiform encephalopathy (BSE) is of special concern because it is infectious and debilitating to humans. The possibility of using fluorescence spectroscopy to screen for BSE in cattle was explored. Fluorescence spectra from the retinas of experimentally infected BSE-positive cattle with clinical disease were compared with those from both sham-inoculated and non-inoculated BSE-negative cattle. The distinct intensity difference of about 4- to 10-fold between the spectra of the BSE-positive and the BSE-negative (sham-inoculated and non-

---

[†]Department of Chemistry, Iowa State University, Ames, Iowa, United States.

[‡]U.S. Department of Energy Ames Laboratory, Ames, Iowa, United States.

[§]Canadian Food Inspection Agency, National Center for Animal Disease, Lethbridge Laboratory, Alberta, Canada.

[‡]Leopold Center, Iowa State University, Ames, Iowa, United States.

* email address: jwp@iastate.edu; FAX: 001-515-294-0105

inoculated) eyes suggests the basis for a means of developing a rapid, noninvasive examination of BSE in particular and TSEs in general.

KEYWORDS: Transmissible spongiform encephalopathy, bovine spongiform encephalopathy, retinal scan, fluorescence spectroscopy, lipofuscin.

INTRODUCTION

Transmissible spongiform encephalopathies (TSEs) are well-known neurological disorders resulting in deterioration of the central nervous system of animals, including humans. The most general characteristics of these diseases are the spongiform changes in the brain, neuronal loss, astrocytosis and amyloid plaque formation.[1] The biochemical signature of prion diseases is the presence of abnormal metabolism and accumulation of prion protein, that is, the conversion of PrP to PrP^{Sc}, which is not soluble in detergent and is partially protease resistant.[2]

The TSE of most concern for the food supply is bovine spongiform encephalopathy (BSE), a fatal neurodegenerative transmissible disease in cattle. It is thought to be associated with variant Creutzfeldt-Jakob disease (vCJD) in humans. The oral route of infection is considered to be the most probable path for transmission of BSE to humans. In order to reduce the risk of human exposure, specified risk material (SRM, e.g. brain and spinal cord) from cattle is removed during slaughter and processing. Prohibition of SRM in the human food chain is considered of critical importance for protection of consumers from BSE. Regulations regarding SRM have been promulgated by the European Commission (Annex V Commission Regulation (EC) No. 999/2001) and for the United States by the Food Safety and Inspection Service (99 CFR 310.22). Many other countries have also banned bovine CNS tissues from meat products and its presence is cause for import rejection and international trade disputes. Developing faster, light-based technology for

monitoring CNS tissue in meat and other food products as well as for screening for TSEs will be increasingly important in securing the safety of the world's food supply. It is also important to diagnose and monitor the frequency of prion disease in cattle, particularly those meant for human consumption.

Fluorescence spectroscopy is highly sensitive and is widely used technique in biology.[8-12] It has been employed in our laboratory for various food safety applications. We have used it to screen for fecal contamination on beef carcasses by exploiting the presence of highly fluorescent chlorophyll metabolites.[13] We have, furthermore, observed that CNS tissues fluoresce much more intensely than non-CNS tissues,[14-16] thus providing a means of detecting CNS tissue in food products. The relatively high fluorescence intensity of CNS tissues is attributed to the accumulation of lipofuscin, which is a highly fluorescent, heterogeneous, yellow-brown material.[17-22]

We subsequently combined the power of fluorescence spectroscopy and the fluorescent properties of CNS tissue to the problem of diagnosing TSEs in animal tissue. In particular, we previously addressed the problem of scrapie, a widespread TSE affecting sheep and goats. It is not, however, infectious to humans. Though there have been several efforts to develop spectral examinations of eyes to assess the extent of macular degeneration and other abnormalities,[23-31] only a few reports in the literature address the potential of using retinal scans for the diagnosis of TSEs.[32-36] Adhikary *et al.*[37] and Bose *et al.*[38] studied scrapie-infected sheep and mice eyes, respectively, by fluorescence spectroscopy. This work was inspired by substantial documentation linking neurological disease produced by TSEs to eye damage and the accumulation of lipofuscin.[39-45] Retinas from scrapie-positive sheep were compared with those from scrapie-negative sheep, and distinct differences in the fluorescence intensity and spectroscopic signatures

were observed. The characteristic fluorescence in the scrapie-positive retina was suggested to be due to the accumulation of lipofuscin. It was concluded that the eye, in particular the retina, is a useful tissue for noninvasive examination of some neurological pathologies, such as scrapie. Here, we provide the first report of a novel, fluorescence-based method of retinal scanning for BSE infection in cattle, which may lead to a nonlethal and noninvasive means to identify BSE infection in cattle upon further development.

EXPERIMENTAL

Animals and disease diagnosis. The experiments were performed with a total of 20 right eyes from 20 different cattle (of known age) obtained from several sources (Canadian Food Inspection Agency- National Center for Animal Disease,(CFIA-NCAD) Lethbridge sample bilaterally symmetric tissue of the head by formalin fixing the left specimen and keeping the right specimen for fresh/frozen). Eleven of the animals were BSE-positive (of three types namely C, H and L). Nine were BSE-negative: 1 from Canadian Food Inspection Agency National Center for Animal Disease (CFIA-NCAD, Lethbridge); 3 from a local abattoir in Lethbridge, Canada; and 5 from Sierra for Medical Science, California.

Cattle from the specific pathogen-free (SPF) herd at the CFIA-NCAD, Lethbridge, were used for experimental inoculation of bovine spongiform encephalopathy (BSE). All protocols for animal work related to these inoculation experiments and the handling and housing of the animals involved met or exceeded the standards set by the Canadian Council for Animal Care and the Canadian Biosafety Standards and Guidelines. All work involving BSE positive material was conducted in BSL 3 containment laboratories as per the Biosafety Standards and Guidelines for Canada. In cattle BSE-challenge experiments, all animals were challenged in BSL 3 containment and housed for no less than 4 weeks, after which they were moved to isolated pens outside of

containment until the presentation of clinical disease. At this point, animals were moved back into containment for the duration of the experiment.

The animals selected for inoculation were a cross breed of Black Angus and Hereford. Both steers and heifers were used for inoculation. The eyes that were analyzed were from cattle inoculated during two separate experiments. In the first experiment, performed from 2005-2007, 1 mL of 10% w/v BSE-positive brain homogenate (in phosphate-buffered saline at pH 7.4) was injected intra-cranially into 4-month-old calves. (The brain homogenate of the first 5 cases of indigenous BSE in Canada was used to inoculate these animals (**Table S1**).) Each of these cases has undergone extensive molecular characterization and each were deemed to be classical BSE (cBSE).[46] After inoculation, the cattle were housed in isolated pens at the CFIA-NCAD Lethbridge until they presented progressive clinical signs consistent with BSE. Animals were euthanized by lethal injection and underwent an extensive *post mortem* examination during which samples, including the eyes, were collected for immediate analysis or for future work. In the second experiment, brain homogenate (1 mL of 10% w/v in PBS pH 7.4) from Canadian field cases of classical (C), high (H), and low (L) type atypical BSE were intra-cranially inoculated into 2 animals each (*i.e.*, 6 BSE-positive animals, **Table S2**). Brain samples from each of these cases have been extensively characterized and typed based on these properties.[46] Cattle inoculated were 4-month-old Black Angus Hereford cross breeds from the CFIA-NCAD SPF herd. Animals were kept in isolated pens until the presentation of progressive clinical signs consistent with BSE were observed. They were then euthanized *via* lethal injection and sampled extensively during a comprehensive *post mortem* examination. One additional animal (**Table S3**) was intra-cranially inoculated with 1 mL of 10% w/v known BSE- negative, bovine-brain homogenate. One eye from each animal inoculated was collected and stored at -80°C until it was used for spectral analysis.

Other control eyes (*i.e.*, BSE-negative tissue) were collected at a local abattoir or obtained from Sierra for Medical Science (California) (**Table S3**). Eyes from the abattoir were of various breeds and between 24 and 30 months old and tested BSE negative by the methods described below. The eyes from BSE-negative cattle purchased from Sierra for Medical Science were from 29-months old animals and they were harvested from a slaughterhouse where slaughtering was carried out following USDA guidelines. The animals were subjected to *ante-mortem* and *post-mortem* inspections, and all the animals passed the inspections. The animals were certified to be free of disease and fit for human consumption. Molecular characterization of the disease associated prions using Western blot was also completed to determine type of the BSE present in the 11 BSE-positive animals (Table S4).

Rapid Test Platforms Used to Confirm Successful Experimental Transmission of BSE.

    Prionics Check Priostrip. This is an immuno-chromatographic assay based on protease digestions to purify selectively disease-associated PrP^{Sc}. Surviving PrP^{Sc} is allowed to bind with anti-PrP antibodies conjugated to colored latex beads. The bead solution is drawn up on an immuno-chromatographic strip with a second anti-PrP antibody immobilized on it. Colored beads, which are bound to PrP^{Sc}, bind to the immobilized antibody causing accumulation of color at the antibody location on the strip. The optical density (OD) is determined, and OD values above a kit-defined cutoff are deemed positive for BSE.

    IDEXX Herd Check ELISA. This ELISA is based on specific binding of misfolded, disease-associated PrP^{Sc} using the Seprion ligand. After allowing PrP^{Sc} to bind to ligand-coated wells, an anti-PrP antibody conjugated to horse-radish peroxidase (HRP) is allowed to bind to any PrP^{Sc} immobilized in the wells. TMB (3,3′,5,5′-tetramethylbenzidine) substrate is

added to facilitate a color-change reaction catalyzed by the HRP enzyme. If a sample contains PrP^{Sc}, HRP will be present in the well causing a color change, increasing the optical density (OD) in the sample well. Samples wells with an OD above the run-specific cutoff OD are considered positive for BSE.

Western Blot Information. The Western blot used to type BSE is based on the Prionics Check Western blot kit with some modifications. Briefly, 10% brain-stem homogenates in Prionics homogenization buffer were digested with proteinase K (PK) in mild or stringent conditions. Mild digestion was done following the Prionics Check Western kit digestion conditions; 100 µL of 10% sample homogenate was mixed with 10 µL of Digestions Buffer and 10 µL of Prionics Check Western PK and incubated at 48°C for 40 minutes. Stringent digestion conditions require a higher pH and increased amount of PK; 100 µL of 10% sample homogenate was mixed with 10 µL of 1-M Tris-HCl (pH 8.0) and 10 µL of 10mg/mL PK (Roche) and incubated at 48°C for 40 minutes. Digestions were stopped by adding 10 µL of Prionics Check Western Digestion Stop Solution and 100 µL of 2x SDS PAGE sample buffer. Samples were mixed well, boiled at 95°C for 5 minutes, and then separated on a 12% SDS-PAGE gel. Proteins in the gel were then transferred to a PVDF membrane (Millipore) and detected with anti-PrP specific mouse monoclonal antibodies 6H4 (Prionics) and P4 (AbD Serotec).

Immuno-Histochemistry (IHC) Information. Fresh tissue was placed in 10% neutral buffered formalin for at least 24 hours and then put into 98-99% formic acid (VWR) for 1 hour. Tissue was then rinsed and the pH was neutralized with 10% neutral buffered formalin (Fisher Scientific). Samples were processed to remove water and infiltrate the tissue with parafin (Leica), the tissue was then mounted in a paraffin block; and sections were cut on a microtome and fixed to slides for immuno-histochemistry (IHC) and histology. The slides were heated to remove the

wax, re-hydrated, treated with 3% hydrogen peroxide to quench endogenous peroxidases, and then placed in 98-99% formic acid for 5 min. The slides were rinsed with Tris Buffered Saline (TBS) (Dako) several times to adjust the pH to between 7 and 8, placed in a stainless-steel rack, covered with Citrate Target Retrieval solution (Dako), and autoclaved at $122 \pm 1\ {}^{0}C$ at 16 psi for 25 min. The slides were cooled to room temperature and incubated in Tris Buffered Saline with Tween (TBST) (Dako) for at least 5 min before proceeding to immuno-detection.

The following steps for immuno-detection were done manually or on an autostainer; slides were blocked with 5% normal goat sera (Dako) for 15 minutes at room temperature and placed in the required dilution of primary antibody for 1 h at 37 ${}^{o}C$ or overnight at 4 ${}^{o}C$. After incubation in mouse anti-PrP antibody, slides were rinsed with TBST and transferred to EnVision + HRP Labelled Anti-Mouse Polymer solution (Dako) for 30 minutes at room temperature. Slides were then rinsed with TBST and water and were developed in fresh 3,3'-diaminobenzidine (DAB) (Sigma) solution until the desired level of development was reached. Slides were then rinsed in water, counter-stained with hematoxylin, dehydrated, and cover-slipped for microscopic evaluation.

Sample Preparation. Globes were kept frozen at -80${}^{o}C$ until use, at which time they were thawed at room temperature. After dissecting the globes, the retina was removed and was stretched out flat on a microscopic slide, making a surface area of roughly 15 mm x 15 mm, allowed to dry for a few minutes and no further solution was added. To ensure safe handling of the infected samples, the slides were covered with another slide, and the edges were sealed with nail polish that was nonfluorescent under our optical conditions.

Steady-State Measurements. Steady-state fluorescence spectra were obtained with a SPEX Fluoromax-4 (ISA Jobin-Yvon/SPEX, Edison, NJ) with a 5-nm band-pass for both

excitation and emission and corrected for lamp spectral intensity and detector response. The sample was maintained in a front-faced orientation. Based on previous work[37] , 470 nm was chosen for the excitation wavelength (λ_{ex}). An interference filter centered on 470 nm was placed in the excitation beam to ensure spectral purity. Emission was collected at wavelengths (λ_{em}) greater than 505 nm using a cutoff filter before the detector to eliminate scattered light. In addition, fluorescence spectra were obtained using horizontal-vertical (HV) orientations, respectively, using two polarizers placed before and after the sample, further ensuring complete elimination of scattered light.

RESULTS AND DISCUSSION

We carried out the fluorescence experiments on the retinas of the right eyes of 20 different animals, where 11 were BSE-positive and 9 were BSE-negative. In the animals diagnosed as BSE-negative in CFIA-NCAD, Lethbridge, there was no labeling representative of PrP[Sc] in brain sections and retina when they were examined after IHC testing. Similarly, there was no evidence of spongiform pathology in the brains. In contrast, the BSE-positive animals showed spongiform changes in the brain and had PrP[Sc] immuno-staining in IHC testing of brain sections and the retina.[47] The BSE positive cattle were all challenged intra-cranially (IC) with C, H or L type positive BSE brain homogenate. While this is not the natural route for the transmission for BSE, at the later stages of disease, PrP[Sc] distribution and clinical disease are very similar in IC and orally challenged cattle. It is well known that the different BSE types have PrP[Sc] with unique biochemical characteristics and some variation in dissemination. Retinas from the BSE positive cattle included in this study all had PrP[Sc] deposition in the retina as detected by IHC.

Figures 1a and b present a comparison of the fluorescence spectra of the retina from BSE-positive and BSE-negative tissue upon excitation at 470 nm. **Figure 1a** presents spectra from the

162

right eye of cattle whose ages are known to within 3 months. The BSE-positive cattle are divided in two groups: five from 27 (24) to 30 (27) months old (post-BSE-challenge age in parentheses), referred to as being in the "latter stages of infection," see **Table S1**; and six from 22 (19.5) to 25 (22) months old (post-BSE-challenge age in parentheses), referred to as being in the "early stages of infection," see **Table S2**. The early-stage tissues exhibited a 5- to 8-fold increase in the fluorescence intensity with respect to the age-matched negative control tissues. Comparison with age-matched tissue is important, as it has been shown that lipofuscin increases with age.[48-50] The increase of lipofuscin with age may have more confounding effects in natural cases of BSE. Cattle with naturally acquired BSE are usually 5 years of age or older. In order to ensure that significant spectral differences in cattle greater than 5 years old with and without BSE are appearing as a result of disease, the age-matched experiment as with clinical-diseases will most likely suffice.

Latter-stage BSE positive retina tissues afforded fluorescence intensities 6- to 11-fold greater than those of the corresponding age-matched animals. Two peak maxima lying from 560 to 565 nm and from 575 to 600 nm were noted. These spectral characteristics are more prominent, however, in scrapie-infected sheep retinas.[37] These distinct peaks were not observed in the spectra of murine retina.[38]

Lipofuscin accumulates in randomly distributed granules dispersed in the retinas of sheep eyes,[37] and we expect the same to be true for bovine eyes. As the experimental configuration permits only 1.5% of the surface area of the retina to be examined, we attempted to gauge the effect of this heterogeneity by interrogating two random portions of each retina. Within experimental error, the positive tissues were all more fluorescent than their age-matched counterparts. The composite of all spectra is included given in **Figure 1b.** For completeness, the spectra from the four BSE-negative eyes (of uncertain age, 24-30 months) obtained from the

Lethbridge abattoir are included in **Figure 1b**. Their low fluorescence intensities fall in the range of the BSE-negative age-matched samples.

Figure 2a presents a plot of the average fluorescence intensities of both positive early- and latter-stage retinas and of negative retinas with respect to the ages of the animals. As the age of the animals falls within a window of about three months, error bars of ± 1.5 months are provided. **Figure 2a** also indicates that the fluorescence intensity of BSE-positive tissue is significantly greater than that of the corresponding BSE-negative age-matched tissue. The observation in **Figure 2a** illustrates the screening power of this fluorescence-based method. The early-stage cattle can be readily distinguished from the latter-stage ones. Both were inoculated intra-cranially, but the former were not allowed to progress to the same extent of clinical disease. They had a less widespread and intense distribution of PrP^{Sc} in the brainstem tissue at the level of the obex (see **Figure 2b** and **2c**). IHC of the eyes indicated a smaller deposition of PrP^{Sc} in the retina than in the C-type BSE-inoculated animals listed in **Table S1**. In conclusion, it is evident that there is a significant difference in the fluorescence intensity of the retinas from BSE-positive compared to BSE-negative cattle. Hence, we suggest that this spectral difference could be used as a screening tool to identify BSE infection in cattle. The next step towards a screening tool for BSE in cattle would be to design and test an instrument to obtain retinal spectra from live cattle or cattle immediately *post mortem*. A noninvasive, high-throughput screening tool such as this would allow for routine testing to identify cattle with a high likelihood of being BSE positive. Early detection, removal, and destruction of these BSE infected cattle would help to promote animal health and increase food safety.

ACKNOWLEDGEMENTS

REFERENCES

1.   Jeffrey, M.; Goodbrand, I. A.; Goodsir, C. M., Pathology of the Transmissible Spongiform Encephalopathies with Special Emphasis on Ultrastructure. *Micron* **1995**, *26*, 277-298.

2.   Prusiner, S. B., Prions. *Proc. Natl. Acad. Sci. USA* **1998**, *95*, 13363-13383.

3.   Ironside, J. W., Review: Creutzfeldt-Jacob Disease. *Brain Pathol.* **1996**, *6*, 379-388.

4.   Cousens, S.; Smith, P. G.; Ward, H.; Everington, D.; Knight, R. S.; Zeidler, M.; Stewart, G.; Smith-Bathgate, E. A.; Macleod, M. A.; Mackenzie, J.; Will, R. G., Geographical Distribution of Variant Creutzfeldt-Jakob Disease in Great Britain, 1994-2000. *Lancet* **2001**, *357*, 1002-1007.

5.   Comer, P. J.; Huntly, P. J., TSE Risk Assessments: A Decision Support Tool. *Stat. Methods Med. Res.* **2003**, *12*, 279-291.

6.   E. F. S. A., Quantitative Assessment of the Residual BSE Risk in Bovine-Derived Products, EFSA QRA Report 2004 - working document. *EFSA J.* **2005**, *307*, 1-135.

7.   Harvard Center of Risk Analysis, and Harvard School of Public Health, and Center of Computational Epidemiology, College of Veterrinary Medicine, Tuskegee University. Evaluation of the Potential for Bovine Spongiform Encephalopathy in the United States, 2001. (November 26). Access at http://www.fsis.usda.gov/Science/Risk_Assessments/.

8.   Christensen, J.; Nørgaard, L.; Bro, R.; Engelsen, S. B., Multivariate Autofluorescence of Intact Food Systems. *Chem*. *Rev*. **2006**, *106*, 1979 - 1994.

9.   Wold, J. P.; Mielnik, M., Nondestructive Assessment of Lipid Oxidation in Minced Poultry Meat by Autofluorescence Spectroscopy. *J*. *Food Sci*. **2000**, *65*, 87-95.

10.   Wold, J. P.; Mielnik, M.; Pettersen, M. K.; Aaby, K.; Baardseth, P., Rapid Assessment of Rancidity in Complex Meat Products by Front Face Fluorescence Spectroscopy. *J*. *Food Sci*. **2002**, *67*, 2397-2404.

11.   Olsen, E.; Vogt, G.; Ekeberg, D.; Sandbakk, M.; Petterson, J.; Nilsson, A., Analysis of the Early Stages of Lipid Oxidation in Freeze-stored Pork Back Fat and Mechanically Recovered Poultry Meat. *J*. *Agric*. *Food Chem*. **2005**, *53*, 338-348.

12.   Olsen, E.; Vogt, G.; Veberg, A.; Ekeberg, D.; Nilsson, A., Analysis of Early Lipid Oxidation in Smoked, Comminuted Pork of Poultry Sausages with Spices. *J*. *Agric*. *Food Chem*. **2005**, *53*, 7448-7457.

13.   Ashby, K. D.; Wen, J.; Chowdhury, P.; Casey, T. A.; Rasmussen, M. A.; Petrich, J. W., Fluorescence of Dietary Porphyrins as a Basis for Real-Time Detection of Fecal Contamination on Meat. *J*. *Agric*. *Food Chem*. **2003**, *51*, 3502-3507.

14.   Chowdhury, P. K.; Halder, M.; Choudhury, P. K.; Kraus, G. A.; Desai, M. J.; Armstrong, D. W.; Casey, T. A.; Rasmussen, M. A.; Petrich, J. W., Generation of Fluorescent Adducts of Malondialdehyde and Amino Acids: Toward an Understanding of Lipofuscin. *Photochem*. *Photobiol*. **2004**, *79*, 21-25.

15.   Schönenbrücher, H.; Adhikary, R.; Mukherjee, P.; Casey, T. A.; Rasmussen, M. A.; Maistrovich, F. D.; Hamir, A. N.; Kehrli, M. J.; Richt, J.; Petrich, J. W., Fluorescence-Based

Method, Exploiting Lipofuscin, for Real-Time Detection of Central Nervous System Tissues on Bovine Carcasses. *J. Agric. Food Chem.* **2008**, *56*, 6220–6226.

16. Adhikary, R.; Schonenbrucher, H.; Rasmussen, M. A.; Casey, T. A.; Hamir, A. N.; Kehrli, M. E.; Richt, J. A.; Petrich, J. W., A Comparison of the Fluorescence Spectra of Murine and Bovine Central Nervous System and Other Tissues. *Photochem. Photobiol.* **2009**, *85*, 1322-1326.

17. Yin, D., Biochemical Basis of Lipofuscin, Ceroid, and Age Pigment-Like Fluorophores. *Free Radical Biol. Med.* **1996**, *21*, 871-888.

18. Boellaard, J. W.; Schlote, W.; Tateishi, J., Neuronal Autophagy in Experimental Creutzfeldt-Jakob's Disease. *Acta Neuropathol.* **1989**, *78*, 410-418.

19. Terman, A.; Brunk, U. T., Lipofuscin: Mechanisms of Formation and Increase with Age. *Acta Pathol., Microbiol., Immunol.* **1998**, *106*, 265-276.

20. Tsuchida, M.; Miura, T.; Aibara, K., Lipofuscin and Lipofuscin-Like Substances. *Chem. Phys. Lipids* **1987**, *44*, 297-325.

21. Curtis, H. J., *Biological Mechanisms of Aging*. Charles C. Thomas: Springfield, IL, 1966.

22. Strehler, B. L., *Time, Cells, and Aging*. Academic Press: San Diego: San Diego, 1977.

23. Holz, F. G.; Bellman, C.; Staudt, S.; Schutt, F.; Volcker, H. E., Fundus Autofluorescence and Development of Geographic Atrophy in Age-related Macular Degeneration. *Invest. Ophthalmol. Visual Sci.* **2001**, *42*, 1051-1056.

24. Hortells, P.; Monzon, M.; Monleon, E.; Acin, C.; Vargas, A.; Bolea, R.; Lujan, L.; Badiola, J. J., Pathological Findings in Retina and Visual Pathways Associated to Natural Scrapie in Sheep. *Brain Res.* **2006**, *1108*, 188-194.

25.	Smith, R. T.; Nagasaki, T.; Sparrow, J. R.; Barbazetto, I.; Koniarek, J. P.; Bickmann, L. J., Photographic Patterns in Macular Images: Representaion by a Mathematical Model. *J. Biomed. Opt.* **2004**, *9*, 162-172.

26.	Rubenstein, R.; Gray, P. C.; Wehlburg, C. M.; Wagner, J. S.; Tisone, G. C., Detection and Discrimination of PrP[Sc] by Multi-Spectral Ultraviolet Fluorescence. *Biochem. Biophys. Res. Commun.* **1998**, *246*, 100-106.

27.	Surguchev, A.; Surguchov, A., Conformational Diseases: Looking into the Eyes. *Brain Res. Bull.* **2010**, *81*, 12-24.

28.	Smith, R. T.; Gomes Nuno, L.; Barile, G.; Busuioc, M.; Lee, N.; Laine, A., Lipofuscin and Autofluorescence Metrics in Progressive STGD. *Invest. Ophthalmol. Visual Sci.* **2009**, *50*, 3907-14.

29.	Delori, F. C., Autofluorescence Method to Measure Macular Pigment Optical Densities Fluorometry and Autofluorescence Imaging. *Arch. Biochem. Biophys.* **2004**, *430*, 156-162.

30.	Schweitzer, D.; Hammer, M.; Schweitzer, F.; Anders, R.; Doebbecke, T.; Schenke, S.; Gaillard, E. R., In Vivo Measurement of Time-resolved Autofluorescence at the Human Fundus. *J. Biomed. Opt.* **2004**, *9*, 1214-1222.

31.	Schmitz-Valckenberg, S.; Holz, F. G.; Bird, A. C.; Spaide, R. F., Fundus Autofluorescence Imaging. *Retina* **2008**, *28*, 385-409.

32.	Greenlee, J. J.; Smith, J. D.; Greenlee, M. H. W.; Nicholson, E. M., Clinical and Pathologic Features of H-type Bovine Spongiform Encephalopathy Associated with E211K Prion Protein Polymorphism. *PLoS One* **2012**, *7*, e38678.

33.	Smith, J. D.; Greenlee, J. J.; Hamir, A. N.; Greenlee, M. H. W. Altered Electroretinogram b-wave in a Suffolk Sheep Experimentally Infected with Scrapie. *Vet. rec.* **2009**, *165*, 179-181.

34.   Smith, J. D.; Greenlee, J. J.; Hamir, A. N.; Richt, J. A.; Greenlee, M. H. W., Retinal Function and Morphology are Altered in Cattle Infected with the Prion Disease Transmissible Mink Encephalopathy. *Vet. Pathol.* **2009**, *46*, 810-8.

35.   Greenlee, J. J.; Hamir, A. N.; Greenlee, M. H. W., Abnormal Prion Accumulation Associated with Retinal Pathology in Experimentally Inoculated Scrapie-affected Sheep. *Vet. Pathol.* **2006**, *43*, 733-739.

36.   National Scrapie Surveillance Plan, APHIS, USDA, access at http://www.aphis.usda.gov/vs/nahss/sheep/national_scrapie_surveillance_plan_08192008.pdf.

37.   Adhikary, R.; Mukherjee, P.; Krishnamoorthy, G.; Kunkle, R. A.; Casey, T. A.; Rasmussen, M. A.; Petrich, J. W., Fluorescence Spectroscopy of Retina for Diagnosis of Transmissible Spongiform Encephalopathies. *Anal. Chem.* **2010**, *82*, 4097-4101.

38.   Bose, S.; Schönenbrücher, H.; Richt, J. r.; Casey, T. A.; Rasmussen, M. A.; Kehrli, J., M.; Petrich, J. W., Fluorescence Spectroscopy of Retina from Scrapie-infected Mice. *Photochem. Photobiol.* **2013**, *89*, 864-868.

39.   Gaillard, E. R.; Atherton, S. J.; Eldred, G.; Dillon, J., Photophysical Studies on Human Retinal Lipofuscin. *Photochem. Photobiol.* **1995**, *61*, 448-453.

40.   Docchio, F.; Boulton, M.; Cubeddu, R.; Ramponi, R.; Barker, P. D., Age-related Changes in the Fluorescence of Melanin and Lipofuscin Granules of the Retinal Pigment Epithelium: a Time-resolved Fluorescence Spectroscopy Study. *Photochem. Photobiol.* **1991**, *54*, 247-253.

41.   Dillon, J.; Zheng, L.; Merriam, J. C.; Gaillard, E. R., Transmission of Light to the Aging Human Retina: Possible Implications for Age-related Macular degeneration. *Exp. Eye Res.* **2004**, *79*, 753-759.

42.   Mata, N. L.; Weng, J.; Travis, G. H., Biosynthesis of a Major Lipofuscin Fluorophore in Mice and Humans with ABCR-mediated Retinal and Macular Degeneration. *Proc. Natl. Acad. Sci. U.S.A.* **2000**, *97*, 7154-7159.

43.   Boulton, M.; Docchio, F.; Dayhaw-Barker, P.; Ramponi, R.; Cubeddu, R., Age-related Changes in the Morphology, Absorption and Fluorescence of Melanosomes and Lipofuscin Granules of the Retinal Pigment Epithelium. *Vision Res.* **1990**, *30*, 1291-1303.

44.   Gaillard, E. R.; Zheng, L.; Merriam, J. C.; Dillon, J., Age-related Changes in the Absorption Characteristics in the Primate Lens. *Invest. Ophthalmol. Visual Sci.* **2000**, *41*, 1454-1459.

45.   Glickman, R. D., In *Progress in Brain Research;* Ripps, K. H. H., Wu, S., Eds., 2001; pp 699-712.

46.   Dudas, S.; Yang, J.; Graham, C.; Czub, M.; McAllister, T. A.; Coulthart, M. B.; Czub, S. *PLoS One* **2010**, *5*, e10638.

47.   Wells, G. A.; Wilesmith, J. W., The Neuropathology and Epidemiology of Bovine Spongiform Encephalopathy. *Brain Pathol.* **1995**, *5*, 91-103.

48.   Delori, F. C.; Staurenghi, G.; Arend, O.; Dorey, C. K.; Goger, D. G.; Weiter, J. J., In Vivo Measurement of Lipofuscin in Stargardt's Disease-Fundus Flavimaculatus. *Invest. Ophthalmol. Visual Sci.* **1995**, *36*, 2327-2331.

49.   Wing, G. L.; Blanchard, G. C.; Weiter, J. J., The Topography and Age Relationship of Lipofuscin Concentration in the Retinal Pigment Epithelium. *Invest. Ophthalmol. Visual Sci.* **1978**, *17*, 601-607.

50.   Mukherjee, P.; Bose, S.; Hurd, A. A.; Adhikary, R.; Schonenbrucher, H.; Hamir, A. N.; Richt, J. A.; Casey, T. A.; Rasmussen, M. A.; Petrich, J. W., Monitoring the Accumulation of

Lipofuscin in Aging Murine Eyes by Fluorescence Spectroscopy. *Photochem*. *Photobiol*. **2009**, *85*, 234-238.
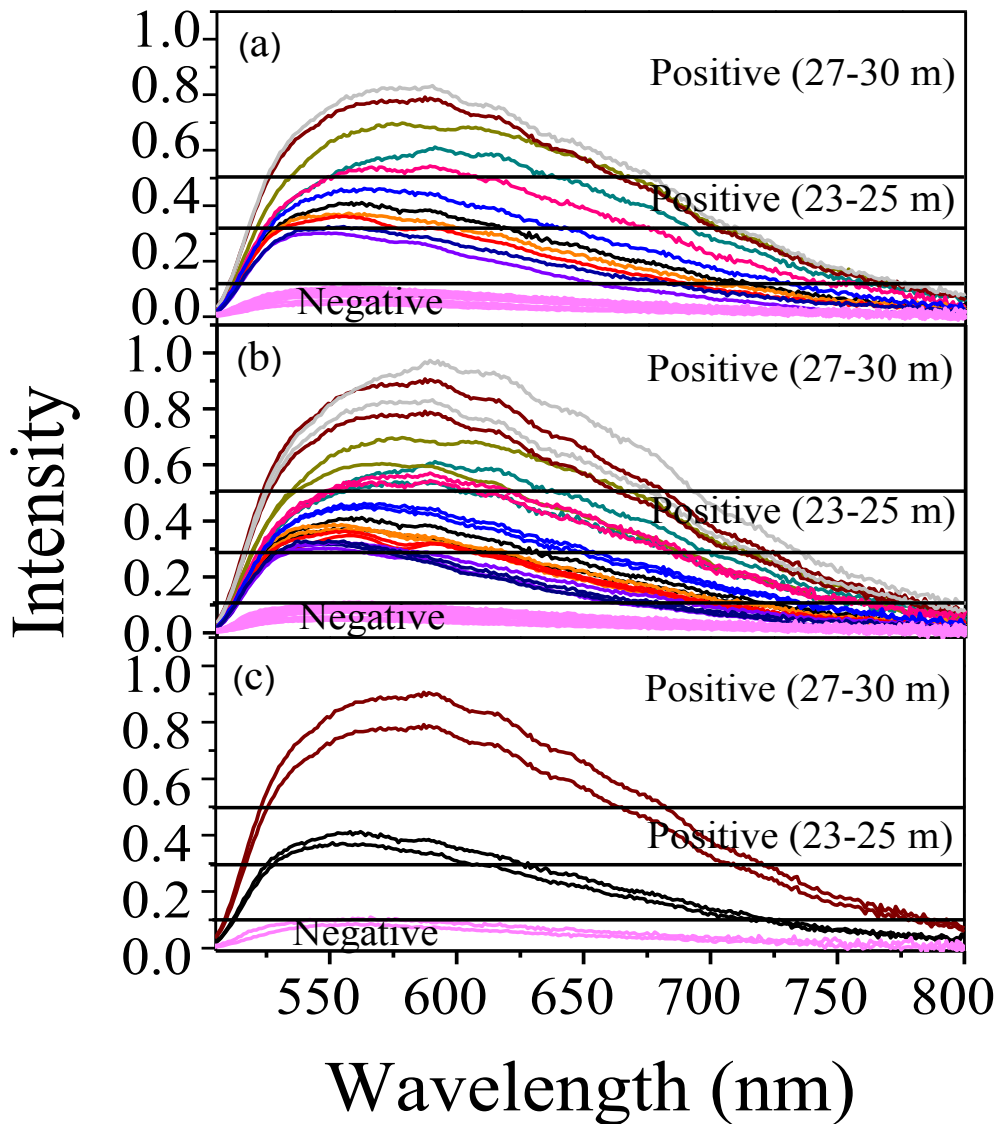
Figure 1. Throughout panels a, b, and c, each retina is associated with a specific color in order to facilitate comparisons. The age in months (m) is indicated. In each panel, a horizontal line is drawn to delineate regions of very low, intermediate, and high fluorescence intensity.

(a) Fluorescence spectra of the retinas from BSE-positive and BSE-negative animals. $\lambda_{ex} = 470$ nm. There is a 4- to 10-fold increase in the peak fluorescence intensity in the positive samples

with respect to the negative ones owing to a higher accumulation of lipofuscin, which is attributed to BSE infection. Spectra of one portion (~5 mm x 1 mm) of an entire (~ 15 mm × 15 mm) retinal sample.

(b) Same as (a), except that two randomly selected portions of each retina is presented in order to gauge the spectral and intensity variations across the tissue.

(c) A subset of (b) presenting the fluorescence spectra of both the portions of retina from the three representative eyes, one of "latter-stage" (brown), one of "early stage" (black), and one of negative eyes (magenta).
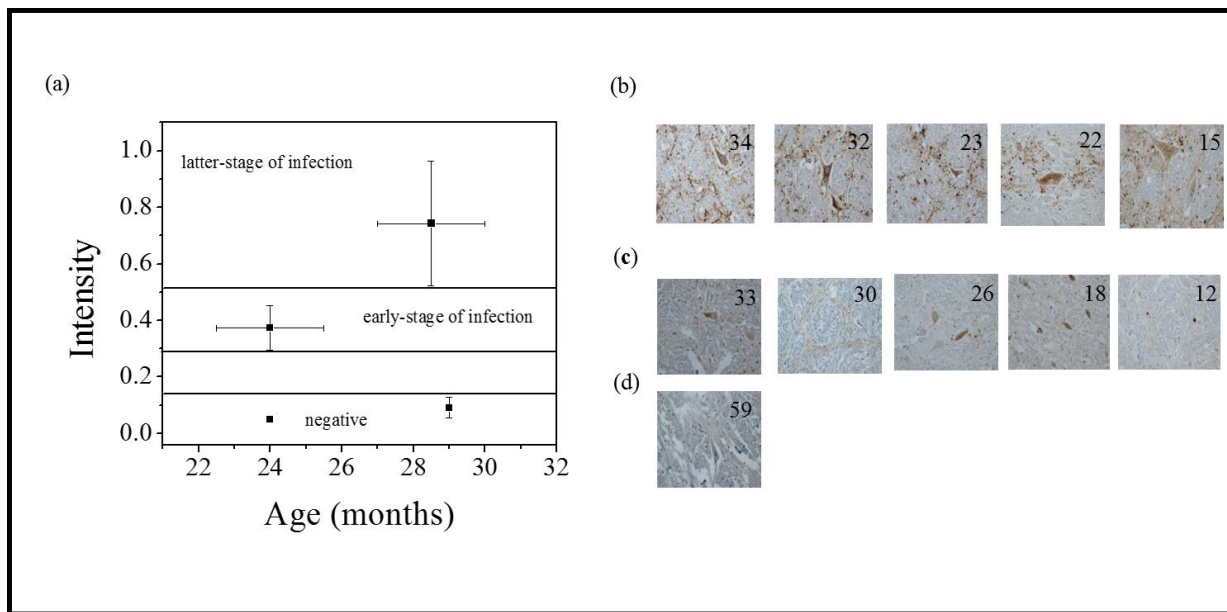
Figure 2. Comparison of the fluorescence intensity of retinas with IHC images.

(a) Maximum fluorescence intensity *vs*. age in months for all the data presented in Figure 1b. λ_{ex} = 470 nm. The average maximum intensity ± one standard deviation is plotted. This Figure demonstrates that the increase in fluorescence intensity owing to BSE infection is significantly larger than that owing to age.

(b) IHC images of the brainstems (at the level of the obex) for the latter-stage BSE positive cattle. Prion protein specific immuno-staining detected high amounts of PrP^{Sc} deposition in the brains of these later stage BSE positive cattle. The corresponding eyes from these animals also show a much higher fluorescence intensity compared to the early-stage BSE positive eyes.

(c) IHC images of the brainstems (at the level of the obex) for the remaining BSE infected cattle. Prion protein specific immuno-staining is detecting PrP^{Sc} aggregates indicative of BSE but to a much lower degree compared to the later stage BSE positive cattle (panel b).

(d) IHC images of the brainstem (at the level of the obex) of a representative BSE negative control (sham-inoculated) after prion protein specific immuno-staining. No detection of aggregated PrP^{Sc} is evident in this normal brain sample.

The numbers labelling the images in panels b, c, and d are the last two digits of the animals' ID numbers.

CHAPTER 6a. CHARACTERIZING ELECTRIC FIELD EXPOSED P3HT THIN FILMS USING POLARIZED-LIGHT SPECTROSCOPIES

A paper submitted to *The Journal of Physical Chemistry B*

Ujjal Bhattacharjee,[§,1,2] Moneim Elshobaki, [§,3,4] Kalyan Santra,[1,2] Jonathan M. Bobbitt,[1,2] Sumit Chaudhary,[3] Emily A. Smith,[1,2] and Jacob W. Petrich[1,2]*

ABSTRACT

The Π-conjugated polymer, P3HT (poly (3-hexylthiophene)) has been widely used as a polymer donor in the active layer in organic photovoltaic devices. Although high power conversion efficiencies have been achieved with P3HT-based devices, structural details, such as orientation of polymer units, extent of H- and J-aggregation, and heterogeneity are not yet fully understood. P3HT polymer chains are known to form heterogeneous domains in thin films by stacking in lamellar layers. Depending on the polymer molecular weight, these P3HT units can undergo both inter- and intra-molecular coupling. Thus, to enhance carrier mobility, different

---

[1]Department of Chemistry, Iowa State University, Ames, IA, USA

[2]U.S. Department of Energy Ames Laboratory, Ames, IA, USA

[3]Materials Science & Engineering Department, Iowa State University, Ames, IA, USA.

[4] Physics Department, Mansoura University, Mansoura, Egypt.

[§] Contributed equally to this work.

[*] To whom correspondence should be addressed. Email: jwp@iastate.edu.

measures have been taken to render the films more homogeneous and ordered. One such measure is to apply an electric field while the sample dries in order to align the polymeric units. We have examined the use of polarized fluorescence and Raman spectroscopy for characterizing the order of P3HT molecules in a thin film. We found, using steady-state and time-resolved fluorescence anisotropy, that one can effectively determine preferential orientations of the units in a thin film. We also found that the ratio of H- and J-coupling changes when the films are exposed to an electrical field oriented at different angles relative to the substrate during the drying process. Measurements of the polarization dependence of the Raman scattered light are sensitive to the polymer orientation. Although the sensitivity is not as good, the polarized Raman measurements are consistent with the fluorescence measurements.

INTRODUCTION

Π-conjugated polymers (π-CP) have been of considerable interest and applicability since their discovery.[1, 2] The combination of the properties of metals and semiconductors, mechanical properties such as tensile strength, ductility, *etc.,* and the ease of processing gives these materials a very important role in the development of organic photovoltaic (OPV) devices. Among the polymers used for solar cells, P3HT (poly (3-hexylthiophene)), is the most extensively studied. The efficiency of P3HT (donor)/phenyl-C61-butyric acid methyl ester (acceptor) solar cells typically lies in the range of 4-6 %;[3-7] and in similar polymers, such as poly[[4,8-bis[(2-ethylhexyl)oxy] benzo [1,2- b:4,5-b′]dithiophene-2,6-diyl] [3-fluoro-2- [(2- ethylhexyl) carbonyl] thieno [3,4-b] thiophenediyl]] (PTB7), an efficiency as high as ~10% has been achieved.[8]

The two main challenges that P3HT-based solar cells face are: (1) poor overlap between the absorption spectrum of P3HT and the solar spectrum; and (2) structural defects. The first can

be somewhat alleviated by making the film thicker, ensuring sufficient absorption of solar light. On the other hand, owing to the small exciton-diffusion length and the large charge-transfer radius (4.8-9 nm), excitons reach interfaces by swift delocalization in P3HT domains instead of by diffusion.[9] Disorder in the polymer matrix, however, limits the carrier mobility.[10] Studies directed towards reducing structural disorder and, thus, increasing carrier mobility are fundamental to enhancing the efficiency of these materials. Thermal annealing,[11-13] solvent annealing,[14, 15] slow growth,[16] and the use of high boiling solvents[17, 18] and solvent additives[19, 20] have been explored as a means to attenuate the problem. Electric fields have previously been used to align[21] or to generate a particular morphology of nanomaterials.[22] Thus, applying an electric field during preparation of polymer films can probably affect the orientation of polymer units and the concomitant change in charge mobility.[23] Understanding the molecular ordering of P3HT is critical when using these thin films as active layers in various electronic devices.

Here we investigate the use of steady-state and time-resolved fluorescence anisotropy along with polarized Raman spectroscopy to characterize the orientation of the polymer units. Barnes and coworkers have studied P3HT nanofibers with polarized time- and wavelength-resolved fluorescence microscopy.[24] They showed that the dominant inter-chain exciton coupling (H-aggregation) in low-molecular-weight nanofibers changes to predominantly intra-chain coupling (J-aggregation) for high molecular-weight nanofibers.[24] In thin films, P3HT remains a weakly coupled H-aggregate,[25, 26] although varying amounts of inter- and intra-chain coupling can be observed depending on the molecular weight, processing conditions, and other parameters.[27] We show that an applied electric field can change the ratio of inter-chain to intra-chain coupling in the polymer and that these orientational changes can be effectively probed by spectroscopic techniques using polarized light.

EXPERIMENTAL

Solution preparation. Neat P3HT (92% regio-regular) with molecular weight 70 kDa (1-Materials, Inc., Dorval, Québec, Canada) was dissolved in 1, 2-dichlorobenzene (DCB) with a dilution of 20 mg/ml. The solutions were stirred at 850 rpm on a hot plate at 50°C and then filtered.

Substrate preparation under an E-field. Indium tin oxide (ITO)-coated glass slides (25-mm × 25-mm) (Delta Technologies, Loveland, CO) were cleaned following the method described by Chaudhary *et al*.[28] The solution-processed π-CP based films were subjected to an electric field immediately after they were formed by spin coating at 500 rpm for 40 s while they were still wet. This was accomplished by placing the coated substrates around a van de Graaf dome in three different orientations: 0°, 45°, and 90° relative to the normal of the surface of the dome (**Figure 1**). The field strength was approximately 5.88 kV/m at the surface of the generator's dome, and the films were kept at a distance of approximately 1 cm from the surface of the dome.

Steady-state fluorescence measurements: Excitation anisotropy. These were performed with a Spex Fluoromax-4 with a 4- or 5-nm excitation and emission bandpass and corrected for lamp spectral intensity and detector response. The steady-state spectra were collected using a front-faced orientation. Glan-Thompson polarizers were appropriately placed before and after the sample. A 550-nm long-pass filter was used to eliminate scattered light. Excitation spectra were collected with a 720 ± 5-nm interference filter. To obtain the excitation anisotropy spectra, the films were excited with vertically polarized light, and emission polarized both parallel and perpendicular to the excitation polarization was collected. The anisotropy (*r*) was computed as[29, 30]:

$$r = \frac{I_{||} - I_{\perp}}{I_{||} + 2I_{\perp}} \tag{1}$$

(Note that the anisotropy differs from a frequently used quantity, the polarization, by the presence of the 2 in the denominator. The factor of two normalizes the difference in $I_{||}$ and $I_{\perp}$ to the excited-state lifetime of the fluorophores, since the denominator in eqn 1 is proportional to the excited-state lifetime.[29, 30])

Because the grating and optics of a monochromator may be sensitive to polarization, a correction factor must also be determined. Such a factor, g, is obtained by taking the ratio of two spectra of a dye in solution. (Here we used ATTO 655 in water, as its absorption and emission spectra overlapped those of P3HT). Insofar as the dye can be considered to be freely rotating on the time scale of the measurement, $I_{||}$ and $I_{\perp}$ should be identical, regardless of the excitation polarization. Any differences in $I_{||}$ and $I_{\perp}$ must thus be attributed to the monochromator and detection optics. As discussed in our previous work and that of other groups,[31-34] the steady-state anisotropy, corrected for instrumental polarization dependence, is thus given by:

$$r = \frac{I_{V,V} - g\,I_{V,H}}{I_{V,V} + 2\,g\,I_{V,H}} \tag{2}$$

Where the notation $I_{V,V}$ indicates fluorescence obtained using excitation light polarized vertically to the plane of the table and collected vertically to the plane of the table. $I_{V,H}$, similarly, indicates vertical excitation and horizontal collection. The correction factor is given as: $g = \frac{I_{H,V}}{I_{H,H}} = \frac{I_{V,V}}{I_{V,H}}$. Measurements were repeated at least three times. The optical system was optimized

by comparing results with those obtained from the excitation anisotropy of hypericin, which emits in the same region and which we had reported previously.[31]

Time-resolved fluorescence measurements. These were obtained with the time-correlated, single-photon counting (TCSPC) technique. The apparatus for time-correlated, single-photon counting is described elsewhere.[35] Our system provides an instrument response function whose full-width at half-maximum (FWHM) is ~40-50 ps. Experiments were performed in a front-faced orientation. The samples were excited with vertically polarized light and a second polarizer was inserted in between the sample and the detector. The polarizer was oriented parallel and perpendicular to the excitation polarizer. Crossed polarizers provided an extinction of 10^5. An interference filter at 720 ± 5 nm was used to collect photons, to be consistent with the steady-state measurements. Fluorescence lifetimes were measured with a polarizer oriented at "the magic angle," 54.7˚ to the vertical in order to prevent depolarizing events from skewing the measured fluorescence lifetime.[36] For each sample, fluorescence lifetime and anisotropy decays were measured at three random locations on the sample. Fluorescence decays were best fit to two decaying exponentials, after deconvolution with the instrument response function. The time-dependent anisotropy, *r(t)*, was constructed using the eqn. 1 and was well described by a single-exponential decay. The parallel and the perpendicular traces were collected for equal amounts of time, during which the incident excitation power remained constant. This resulted in the overlap of the "tails" of the parallel and perpendicular traces at sufficiently long times, thus obviating the need for "tail matching."[30, 34]

Raman measurements. All Raman spectra were collected using a lab-built microscope system (Leica, Wetzlar, Germany) with a 532-nm laser excitation (Sapphire SF 532-nm 150 mW, Coherent, Santa Clara, CA) after the fluorescence measurements were completed. The

laser beam was expanded with a 10× beam expander in order to backfill a 10× Leica microscope objective with a 0.25 numerical aperture. The laser spot size after the objective was 1.6 ± 0.2 μm. The objective was used for focusing and collecting the Raman scattering from the epidirection and then directed to a side port on the microscope where it was focused onto an f/1.8i HoloSpec spectrograph (Kaiser Optical Systems, Ann Arbor, MI). A Newton 940 (2048 × 512 pixels) charged-coupled device (CCD) was used to detect the Raman signal (Andor Technology, Belfast, UK).

Raman spectra were collected at 5 different locations from the center of each P3HT film under ambient laboratory conditions. An XY translation-stage (ProScan, Prior Scientific, Rockland, MA) controlled by a lab-developed LabVIEW program (2010 version, National Instruments, Austin, TX) was used to move 1 mm to each new location. The spectra were collected for 10 s with 2 accumulations and illuminated with 1.09×10^4 W/cm^2, which is a low enough power density to avoid film degradation.[37] The power density used is equivalent to 8.05×10^4 suns, and two accumulations were used in order to remove cosmic rays.

Polarized Raman spectra were also collected on the P3HT films from the center of the film. The excitation polarization was controlled by a half-wave plate, and was set to p-polarization. A linear polarizer was placed at the side port of the microscope to collect either s- or p-polarized Raman scattering. A second linear polarizer set 45° to the collection polarizer was placed before the spectrometer to correct the spectrometer response function.[38] The ratio of the scattered light intensity with the detection polarizer set to s (I_s) to the intensity with the detection polarizer set to p (I_p) was calculated. Benzene was used to test the instrument setup (I_s/I_p 0.035 ± 0.009 at 991 cm^{-1}, 0.77 ± 0.02 at 1171 cm^{-1} and 0.783 ± 0.009 at 1588 cm^{-1}), and similar ratios

were obtained to those found in literature.[38, 39] The polarized spectra were collected for 30 s with 2 accumulations at a power density of 1.32×10^4 W/cm^2.

Igor Pro 6.36 (Wavemetrics, Lake Oswego, OR) was used to correct for background and to analyze the Raman spectra. The spectra were fit with a linear baseline and to a Gaussian function from 1250 to 1550 cm^{-1} with Igor Pro's batch fitting macro. The full-width at half-maximum (FWHM) and peak amplitudes were extracted from the fits.

RESULT AND DISCUSSION

Steady-state fluorescence measurements. Spano, Barnes, and coworkers have shown that two vibronic transitions in the steady-state fluorescence spectra of P3HT are exquisitely sensitive to the state of aggregation of the polymer chains: the 0-0 transition at ~650 nm and the 0-1 transition at ~720 nm.[40] In particular, the ratio between the intensities of these bands ($S_r = I_{0-0}/I_{0-1}$) is indicative of whether the polymer chain is an H- or a J-aggregate.[41] In H-aggregation, the columbic interaction arising from the side-by-side stacking of the chromophores between the chains of the crystalline films is suggested to suppress the 0-0 transition, yielding $S_r < 1$.[41] In contrast, in J-aggregation, the head-to-tail conformation of chromophores is suggested to enhance a one-dimensional intrachain interaction, increasing the intensity of the 0-0 band, yielding $S_r > 1$.[41, 42] In addition, emission spectra exhibit red shifts for H-aggregation; blue shifts, for J-aggregation.

Polarized emission spectra of neat P3HT films are presented in **Figure 2**. The results are summarized in **Table I**. For emission collected parallel to the excitation polarization (**Figure 2a**), the 0-0 peak of the normalized steady-state spectra decreased with increasing angle of the applied E-field, and was always less than 1. Such low values of S_r, coupled with the spectral red-shift with increasing E-field angle, suggest H-aggregation. In contrast, for emission

collected perpendicular to the excitation polarization, S_r was consistently higher than for the parallel case. This suggests an increase of J-aggregation, which is consistent with the attendant spectral blue shift with E-field angle (**Figure 2b**). Thus, the polarized emission spectra are sensitive to the extent of H- and J- aggregation of the film, induced by the applied electric field.

Figure 3 (right ordinate) presents the fluorescence excitation spectrum (with parallel orientation of excitation and emission polarizers) of a P3HT film in the absence of an applied electric field. The maximum of the 0-0 transition is ~615 nm. The fluorescence excitation anisotropy spectra, constructed as described above, of P3HT films prepared at angles of 0°, 45°, and 90° with respect to the E-field, are presented in **Figure 3 (left ordinate).** In all cases, the anisotropy decreases from 0.35-0.40 (0.40 being the theoretical maximum[29]) at the reddest edge of the excitation spectrum (~690 nm), to 0.10-0.17 at the bluest part of the excitation spectrum that we excited, 400 nm. Our ability to attain an anisotropy near the theoretical upper limit confirms the proper alignment of our apparatus and good extinction of the excitation and analyzer polarizers. Most importantly, however, there is a clear and reproducible decrease in the anisotropy of the entire spectrum in going from an angle of the applied electric field of 0˚ to 90˚. The lowest values of the anisotropy occur when there is no applied electric field. Thus, the 0°-film exhibits the maximum anisotropy, that is, preferential orientation of the polymeric units in the plane parallel to the substrate which may lead to high horizontal carrier mobility

Time-resolved fluorescence measurements: Fluorescence lifetime and anisotropy decays. Time-resolved polarized emission of P3HT films is presented in **Figure 4**. The parameters for the decay of the fluorescence lifetime and anisotropy of the P3HT films are summarized in **Table II**. The average fluorescence lifetimes are 0.31, 0.25, 0.32, and 0.28 ns for the films made with E-field at 0°, 45°, 90°, and with no E-field, respectively. Time-resolved

anisotropies of the films yield $r(0)$ values, that is, the anisotropies at $t = 0$, similar to those obtained from the steady-state measurements (**Table II**), as expected. This result provides another check on the accuracy of the steady-state anisotropy measurements presented in **Figure 3**. The fluorescence depolarization times, *i.e.*, the decay of the anisotropy, are on the order of a nanosecond. This is not attributed to rotational motion of the polymer film but rather to electronic coupling between the chromophores in the polymer, for which there is precedent for organic molecules.[34, 43]

Raman measurements. Raman spectroscopy can be used to characterize polymer-based organic photovoltaic device morphology by measuring changes in the full-width at half-maximum (FWHM) and the resulting polarization of the scattered light.[37-39, 44-47] **Table III** presents measured parameters for the P3HT carbon-carbon double bond peak at 1450 cm^{-1} for films prepared in the absence of an external electric field, or with an electric field oriented in the noted directions. These parameters were also measured for a P3HT crystal. All films have statistically similar peak maxima and FWHM values; the ratio, however, of the polarized Raman scattered light is statistically lower for the 0°, 45°, and 90° films, indicating greater anisotropy compared to the film prepared in the absence of an electric field (**Table III**). An example of the data is presented in **Figure 5**. Based on the work of Kleinhenz *et al*. and the polarized Raman data, there is an increasing order of the axis of the polymer backbone toward the orientation of the polarization of the excitation light for the 0°, 45°, and 90° films. The film prepared in the absence of an electric field (E = 0) has a statistically similar ratio of the polarized Raman scattered light as the P3HT crystal, indicating similar anisotropies. The polarized Raman measurements are more sensitive to the polymer orientation than the 1450 cm^{-1} peak FWHM values, which have been used extensively in the literature. Both fluorescence anisotropy and

polarized Raman measurements show increasinganisotropy for the samples prepared in the electric field. The polarized Raman measurements, however, show no distinction between the 0°, 45°, and 90° films, indicating the fluorescence anisotropy measurement is a more sensitive technique in these cases.

CONCLUSIONS

We have shown that the P3HT polymer units can be oriented when the films are subjected to an electric field of ~5.88 kV/m as they dried and that this orientation can be probed effectively by steady-state and time-resolved fluorescence anisotropy measurements. The highest degree of ordering, as quantified by the limiting anisotropy (r_0 for the steady-state measurement; $r(0)$, for the time-resolved measurement), is attained when the electric filed is parallel to the film, as depicted in **Figure 1**. The polarized emission spectra are also sensitive to the orientation of the electric field (**Figure 2** and **Table I**) as quantified by the ratio of the first two vibronic transitions, which are in turn related to the extent of H- or J-aggregation. Finally, polarized Raman experiments suggest differences between the samples in the presence and absence of electric field. Taken as a whole, these results suggest that the polymeric units of P3HT can be ordered with an electric field, that this ordering can be probed and quantified by spectroscopies using polarized light, and that applying an electric field in excess of 5.88 kV/m to drying films of P3HT could be beneficial in improving the performance of organic solar cells.

ACKNOWLEDGEMENTS

Table I

Ratio of the Intensity of the 0-0 to 0-1 Vibronic Bands of P3HT, S_r, as a Function of Electric Field Orientation for Emission Collected Parallel and Perpendicular to the Excitation Polarization[a]

S_r, parallel	S_r, perpendicular	Electric field angle [b]
0.89 ± 0.02	0.71 ± 0.01	E = 0
0.81 ± 0.01	0.98 ± 0.02	0°
0.77 ± 0.01	0.88 ± 0.02	45°
0.76 ± 0.01	0.85 ± 0.02	90°

[a] Data summarized from the polarized fluorescence spectra presented in **Figure 2**.

[b] Angles are defined for the applied electric field (E ≠ 0) as defined in **Figure 1**.

Table II

Fluorescence Anisotropy Parameters

for Oriented P3HT Films (λ_{ex} = 425 nm and λ_{em} = 720 nm)

E-field direction [a]	r_0 [b]	$r(0)$ [c]	τ_D (ns) [c]	τ_F (ns) [d]
0°	0.17 ± 0.01	0.18 ± 0.02	1.6 ± 0.4	0.31 ± 0.06
45°	0.15 ± 0.01	0.16 ± 0.01	1.3 ± 0.4	0.25 ± 0.06
90°	0.13 ± 0.01	0.12 ± 0.01	0.5 ± 0.3	0.32 ± 0.06
reference (*i.e.*, E = 0)	0.11 ± 0.02	0.09 ± 0.02	0.7 ± 0.3	0.28 ± 0.05

[a] See **Figure 1** for the definitions of the angles specifying the E-field orientations.

[b] r_0 is the steady-state anisotropy: $-0.2 \leq r_0 \leq 0.4$

[c] Fluorescence anisotropy decays are constructed from eqn 1 and fit to a single exponential of the form: $r(t) = r(0)exp(-t/\tau_D)$. $r(0)$ is the anisotropy at time zero (*i.e.*, the limiting anisotropy): $-0.2 \leq r(0) \leq 0.4$.[29] At the same excitation wavelength, r_0 should equal $r(0)$. τ_D is the fluorescence depolarization time, *i.e.*, the 1/e time at which the parallel and perpendicular curves coalesce. Factors that contribute to depolarization are molecular motion (such as rotational diffusion) or nonradiative events such as interactions between electronic states of different polarization.

[d] τ_F, the average fluorescence lifetime, *i.e.*, $<\tau_F> = A_1\tau_1 + A_2\tau_2$, where the A_i and the τ_i are the amplitudes and lifetimes of the two components in the double-exponential fit used to fit the fluorescence decay.

Table III

Peak Maximum, FWHM and Ratio of the s-Polarized to p-Polarized Scattered Light

Intensity (I_s/I_p) for the 1450 cm^{-1} Band of P3HT

P3HT	Peak Max (cm^{-1})	FWHM (cm^{-1})	I_s/I_p
film, 0°	1450.1 ± 0.1	31.6 ± 0.3	0.49 ± 0.01
film, 45°	1449.8 ± 0.2	31.9 ± 0.4	0.490 ± 0.009
film, 90°	1449.88 ± 0.07	31.5 ± 0.2	0.499 ± 0.008
film, E = 0	1449.7 ± 0.2	32.1 ± 0.4	0.521 ± 0.007
crystal, E = 0	1453.5 ± 0.1	31.3 ± 0.3	0.512 ± 0.009
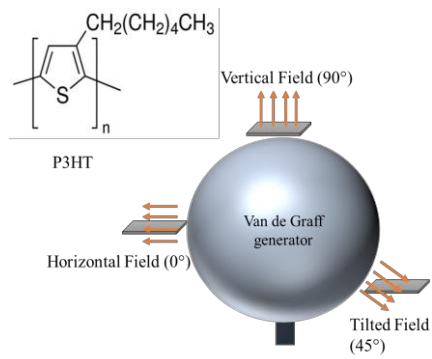
Figure 1. Diagram of the van de Graff electric-field generator, showing the sample placement and directions of the electric field relative to the sample. Also included is the structure of P3HT.
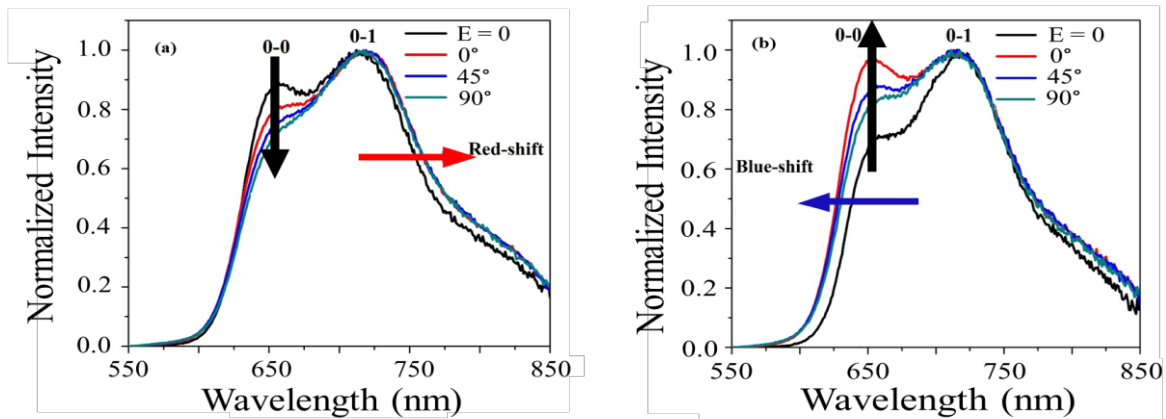
Figure 2. Polarized fluorescence emission spectra of P3HT thin films: **(a)** emission parallel, and **(b)** perpendicular to the polarization of the 520 nm excitation beam. The spectra are normalized at the 0-1 vibronic transition. $S_r = I_{0-0}/I_{0-1}$. For **(a)** $S_r = 0.81$, 0.77, 0.76 and 0.89 for angles of 0°, 45°, and 90° and for the control (E = 0), respectively. Changing the electric field orientation from 0° to 90° decreases I_{0-0}, and hence S_r, as indicated by the direction of the black arrow. This change in electric field also induces a red shift in the spectra, as indicated by the direction of the red arrow. For **(b)** $S_r = 0.98$, 0.88, 0.85, and 0.71, for angles of 0°, 45°, and 90° and for the control (E = 0), respectively. From reference (E = 0) film to the films exposed to E-field, I_{0-0} increases, and hence S_r, as indicated by the direction of the black arrow. This change in electric field also induces a blue shift in the spectra, as indicated by the direction of the blue arrow.
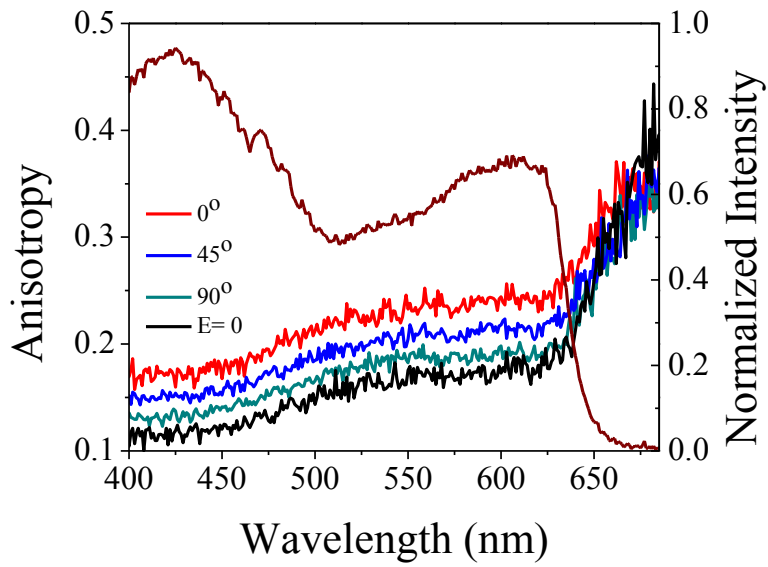
Figure 3. Fluorescence excitation spectrum of a P3HT film collected with parallel orientation of excitation and emission polarizers) (brown curve, right ordinate). Fluorescence excitation anisotropy of P3HT films prepared under different orientations of the applied electric field (left ordinate). $\lambda_{em} = 720$ nm.
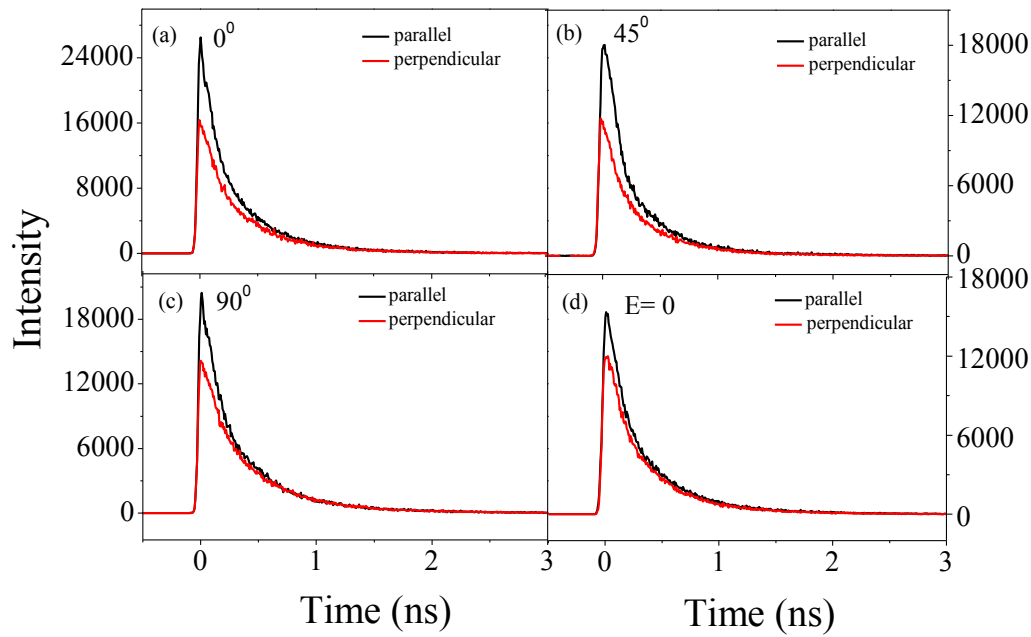
Figure 4. Time-resolved polarized emission of P3HT films prepared under (a) 0°, (b) 45°, (c) 90°, (d) and E = 0 with the emission polarizer parallel to the excitation polarizer (black), and the emission polarizer perpendicular to the excitation polarizer (red). $\lambda_{ex} = 425 \pm 10$ nm, and $\lambda_{em} = 720 \pm 5$ nm.

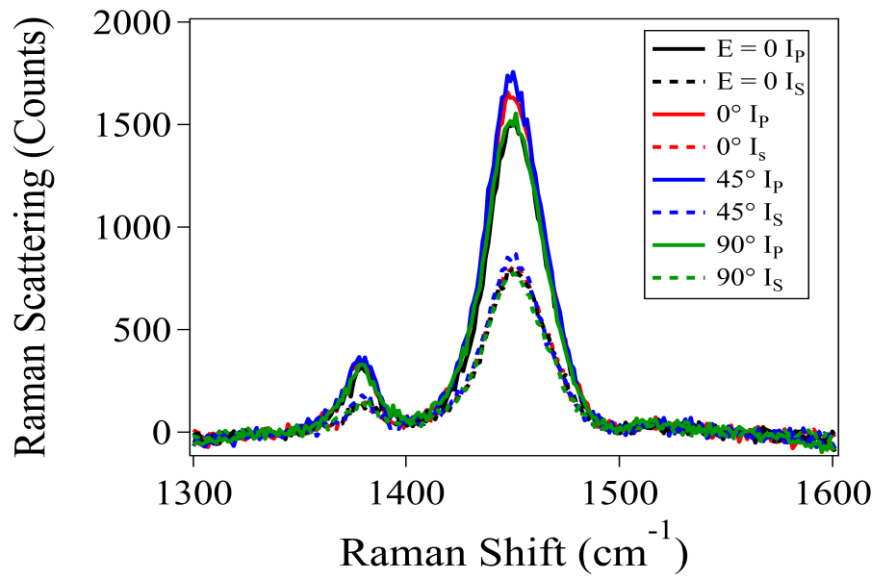**Figure 5.** Polarized Raman spectra for P3HT films oriented under an electric field.

REFERENCES

1.   Shirakawa, H.; Louis, E. J.; MacDiarmid, A. G.; Chiang, C. K. H. *Chemical Communications* **1977**, 578-580.

2.   Chiang, C. K. *Physical Review Letters* **1977**, *39*, 1098-1101.

3.   Schilinsky, P.; Waldauf, C.; Brabec, C. J. *Applied Physics Letters* **2002**, *81*, 3885-3887.

4.   Padinger, F.; Rittberger, R. S.; Sariciftci, N. S. *Advanced Functional Materials* **2003**, *13*, 85-88.

5.   Ma, W.; Yang, C.; Gong, X.; Lee, K.; Heeger, A. J. *Advanced Functional Materials* **2005**, *15*, 1617-1622.

6.   Reyes, M. -R.; Kim, K.; Dewald, J.; Sandoval, R. -L.; Avadhanula, A.; Curran, S.; Carrol, D. L. *Org. Lett.* **2005**, *7*, 5749-5752.

7.   He, Z.; Zhong, C.; Huang, X.; Wong, W. Y.; Wu, H.; Chen, L.; Su, S.; Cao, Y. *Adv. Mater.* **2011**, *23*, 4636-4643.

8.   He, Z.; Zhong, C.; Su, S.; Xu, M.; Wu, H.; Cao, Y. *Nat. Photonics* **2012**, *6*, 591-595.

9.   Wang, H.; Wang, H.-Y.; Gao, B.-R.; Wang, L.; Yang, Z.-Y.; Du, X.-B.; Chen, Q.-D.; Song, J.-F.; Sun, H.-B. *Nanoscale* **2011**, *3*, 2280-2285.

10.   Noriega, R. *Nat. Mater.* **2013**, *12*, 1038-1044.

11.   Liu, Y. X.; Summers, M. A.; Edder, C.; Frechet, J. M. J.; McGehee, M. D. *Advanced Materials* **2005**, *17*, 2960.

12.   Ma, W. L.; Yang, C. Y.; Gong, X.; Lee, K.; Heeger, A. J. *Advanced Functional Materials* **2005**, *15*, 1617-1622.

13.   Oklobia, O.; Shafai, T. S. *Solar Energy Materials and Solar Cells* **2014**, *122*, 158-163.

14.   Miller, S.; Fanchini, G.; Lin, Y.-Y.; Li, C.; Chen, C.-W.; Su, W.-F.; Chhowalla, M. *Journal of Materials Chemistry* **2008**, *18*, 306-312.

15.   Li, G.; Yao, Y.; Yang, H.; Shrotriya, V.; Yang, G.; Yang, Y. *Advanced Functional Materials* **2007**, *17*, 1636-1644.

16.   Mihailetchi, V. D.; Xie, H.; de Boer, B.; Popescu, L. M.; Hummelen, J. C.; Blom, P. W. M.; Koster, L. J. A. *Appl Phys Lett* **2006**, *89*, 012107.

17.   Ma, W.; Yang, C.; Gong, X.; Lee, K.; Heeger, A. J. *Advanced Functional Materials* **2005**, *15*, 1617-1622.

18.   Bao, Z.; Dodabalapur, A.; Lovinger, A. J. *Appl Phys Lett* **1996**, *69*, 4108-4110.

19.   Chen, F.-C.; Tseng, H.-C.; Ko, C.-J. *Appl Phys Lett* **2008**, *92*, 103316.

20.   Moon, J. S.; Takacs, C. J.; Cho, S.; Coffin, R. C.; Kim, H.; Bazan, G. C.; Heeger, A. J. *Nano Letters* **2010**, *10*, 4005-4008.

21.   He, H.; Cai, W.; Lin, Y.; Chen, B. *Langmuir* **2010**, *26*, 8925-8932.

22.   Petchsang, N.; McDonald, M. P.; Sinks, L. E.; Kuno, M. *Advanced Materials* **2013**, *25*, 601-605.

23.   Ismail (Elshobaki), M. R. *Tailoring Device-Scale Properties in Organic Electronics: Morphological, Optical and Electrode-Interface Related Approaches*. Ph. D. Dissertation, Iowa State University, Ames, IA, 2015.

24.   Baghgar, M.; Labastide, J. A.; Bokel, F.; Hayward, R. C.; Barnes, M. D. *J. Phys. Chem. C* **2014**, *118*, 2229-2235.

25.   Clark, J.; Silva, C.; Friend, R. H.; F.C, S. *Phys. Rev. Lett.* **2007**, *98*, 206406.

26.   Paquin, F.; Latini, G.; Sakowicz, M.; Karsenti, P.-L.; Wang, L.; Beljonne, D.; Stingelin, N.; Silva, C. *Phys. Rev. Lett.* **2011**, *106*, 197401.

27.   Sirringhaus, H.; Brown, P. J.; Friend, R. H.; Nielsen, M. M.; Bechgaard, K.; Langeveld-Voss, B. M. W.; Spiering, A. J. H.; Janssen, R. A. J.; Meijer, E. W.; Herwig, P.; De Leeuw, D. M. *Nature* **1999**, *401*, 685-688.

28.   Elshobaki, M.; Anderegg, J.; Chaudhary, S. *ACS Appl. Mater. Interfaces* **2014**, *6*, 12196-12202.

29.   Fleming, G. R.; Morris, J. M.; Robinson, G. W. *Chemical Physics* **1976**, *17*, 91-100.

30.   Cross, A. J.; Fleming, G. R. *Biophysical Journal* **1984**, *46*, 45-56.

31.   Das, K.; Dertz, E.; Paterson, J.; Zhang, W.; Kraus, G. A.; Petrich, J. W. *J. Phys. Chem. B* **1998**, *102*, 1479-1484.

32.   Valeur, B.; Weber, G. *Photochem. Photobiol.* **1977**, *25*, 441-444.

33.   Eftink, M. R.; Selvidge, L. A.; Callis, P. R.; Rehms, A. A. *J. Phys. Chem.* **1990**, *94*, 3469.

34.   Rich, R. L.; Chen, Y.; Neven, D.; Negrerie, M.; Gai, F.; Petrich, J. W. *J. Phys. Chem.* **1993**, *97*, 1781-1788.

35.   Bhattacharjee, U.; Beck, C.; Winter, A.; Wells, C.; Petrich, J. W. *J. Phys. Chem. B* **2014**, *118*, 8471-8477.

36.   Fleming, G. R., Chemical Applications of Ultrafast Spectroscopy. In University Press: Oxford,London, 1986.

37.   Lesoine, M. D.; Bobbitt, J. M.; Carr, J. A.; Elshobaki, M.; Chaudhary, S.; Smith, E. A. *J. Phys. Chem. C* **2014**, *118*, 30229-30237.

38.   Zhao, J.; McCreery, R. L. *Langmuir* **1995**, *11*, 4036-4040.

39.   McCreery, R. L., *Raman Spectroscopy for Chemical Analysis*. John Wiley & Sons: 2005; Vol. 225.

40.   Clark, J.; Silva, C.; Friend, R. H.; Spano, F. C. *Phys. Rev. Lett.* **2007**, *98*, 206406.

41.   Spano, F. C.; Jenny, C.; Silva, C.; Friend, R. H. *The Journal of Chemical Physics* **2009**, *130*, 074904.

42.   Niles, E. T.; Roehling, J. D.; Yamagata, H.; Wise, A. J.; Spano, F. C.; Moulé, A. J.; Grey, J. K. *J. Phys. Chem. Lett.* **2012**, *3*, 259-263.

43.   Ruggiero, A. J.; Todd, D. C.; Fleming, G. R. *J. Am. Chem. Soc.* **1990**, *112*, 1003-1014.

44.   Gao, Y.; Martin, T. P.; Niles, E. T.; Wise, A. J.; Thomas, A. K.; Grey, J. K. *J. Phys. Chem. C* **2010**, *114*, 15121-15128.

45.   Tsoi, W. C.; James, D. T.; Kim, J. S.; Nicholson, P. G.; Murphy, C. E.; Bradley, D. D.; Nelson, J.; Kim, J. S. *J. Am. Chem. Soc.* **2011**, *133*, 9834-9843.

46.   Veerender, P.; Saxena, V.; Chauhan, A. K.; Koiry, S. P.; Jha, P.; Gusain, A.; Choudhury, S.; Aswal, D. K.; Gupta, S. K. *Sol. Energy Mater. Sol. Cells* **2014**, *120*, 526-535.

47.   Kleinhenz, N.; Rosu, C.; Chatterjee, S.; Chang, M.; Nayani, K.; Xue, Z.; Kim, E.; Middlebrooks, J.; Russo, P. S.; Park, J. O.; Srinivasarao, M.; Reichmanis, E. *Chem. Mater.* **2015**, *27*, 2687-2694.

CHAPTER 6b. MIXED HALIDE ORGANOLEAD PEROVSKITES: THE ROLE OF EXCESS PRECURSOR ON PHOTOLUMINESCENCE STABILITY

Modified from a paper to be submitted to *ACS Nano*

Ujjal Bhattacharjee,[‡,1,2] Long Men,[‡,1,2] Daniel J. Freppon,[‡,1,2] Feng Zhu,[1] Emily A. Smith,[,1,2] Javier Vela[*,1,2] Jacob W. Petrich,[*,1,2]*

KEYWORDS

mixed-halide perovskites; nanocrystals; surface traps

ABSTRACT

There has been a tremendous effort to drive solution-based perovskite solar cells towards higher efficiency, reaching approximately 20% recently. Nevertheless, there are still challenges, the most important of which are currently to increase their photo-, thermal- or moisture stability. We have synthesized perovskite materials doped with different percentages of other halides, such as bromide in I- perovskites and chloride in Br- Perovskites. The band gap has been engineered by changing the percent composition of dopants to give an empirical composition of $CH_3NH_3Pb(I_{1-x}Br_x)_3$ and $CH_3NH_3Pb(Br_{1-x}Cl_x)_3$. It is shown that the band gap can be tuned reproducibly over

[1]Department of Chemistry, Iowa State University, and [2]Ames Laboratory, Ames, Iowa 50011

[‡]Contributed equally to this paper.

* To whom correspondence should be addressed. Email: vela@iastate.edu , esmith1@iastate.edu, jwp@iastate.edu.

almost the entire visible spectrum. One important aspect of this work is that we made perovskite nanoparticles that show better photoluminescence behaviors than the bulk material. The presence of other halide dopants in perovskites is known to have better moisture stability. In response to photo-stability issues, we carried out different steady-state and time-resolved spectroscopic studies to characterize the material prepared using a 1:3:3 ratio of PbX_2, CH_3NH_3X and surfactant. We established that the presence of excess precursor (CH_3NH_3X and surfactant) during synthesis gives rise to different photoluminescence (PL) peaks having different excited-state lifetimes, which is not desirable for optimal use of these materials in solar cells. It is hypothesized that the PL blinking observed in single particle studies can possibly be linked to the defects. In order to test this hypothesis, the synthesis was changed to a ratio of 1:1.5:1.5 of lead halide and precursors. This yielded pristine PL peaks of perovskite, suggesting the removal of defects. The origin of different PL in the presence of excess precursor and illumination was further characterized using XRD coupled with laser illumination.

INTRODUCTION

Extremely rapid progress in the development of organometal halide perovskite solar cells has been demonstrated since 2013, when energy conversion efficiencies reached a confirmed value of 16.2% and an unconfirmed value of 19.3%. Furthermore, a wide range of fabrication approaches and device concepts have been introduced.[1] If the stability of the perovskite-based photovoltaics is improved further, perovskite solar cells have the potential to become dominant means of obtaining low-cost solar power[3] and to match the capability and capacity of existing technologies in the future.[4] Perovskite are known for their absorption of solar light over a broad range of wavelengths and ambipolar diffusion behavior. Organometal halide perovskites have also stimulated interest in designing thin-film, mesoscopic solid-state, solar cells.[5] 12−15% efficiencies have

been reported. A simple planar heterojunction solar cell with an active layer formed with perovskite by vapor deposition has been shown to possess solar-to-electrical power conversion efficiencies of ~15%.[6] Efficient thin film hybrid photovoltaics have also been developed.[7]

A series of organic–inorganic hybrid metal halide perovskites with the general formulation AMX_3 (X= Cl, Br, I), where A is the methylammonium ($CH_3NH_3^+$) or formamidinium ($HC(NH_2)_2^+$) cation and M is Sn or Pb, has been reported. Among the organometal halide perovskites, the one with the general composition $CH_3NH_3PbX_3$ has become an extremely attractive semiconductor material owing to its low production cost and exceptionally good photovoltaic performance. It is reported to form high voltage solar cells in conjunction with organic hole conductors.[8] The electronic and optical properties of these perovskites are easily tunable over a broad range by changing the halide. $CH_3NH_3PbI_3$ perovskites have a bandgap of 1.5 eV (820 nm),[9] whereas, $CH_3NH_3PbBr_3$ perovskites have a bandgap of 2.3 eV (540 nm).[10] Moreover, by replacing the methylammonium cation in this perovskite with the slightly larger formamidinium cation, a bandgap tunable between 1.48 and 2.23 eV results. The 1.48 eV-bandgap perovskite is believed to be the most suitable for single junction solar cells.[11] A mixture of formamidinium ($HN=CHNH_3^+$, FA) and methylammonium ($CH_3NH_3^+$, MA) cations in the A position of the $APbI_3$ perovskite structure generates an enhanced short-circuit current and thusproduces superior devices to those based on only $CH_3NH_3^+$.[12]

As electron-hole diffusion lengths in perovskites are long, the carriers created by absorption of photon can easily hop across the grain boundaries of one crystal to another. This enables the incorporation of nanosized perovskites in the active layer of highly performing solar cells. The PL quantum yield of $CH_3NH_3PbBr_3$ perovskite nanocrystals, synthesized using octylammonium bromide as surfactants, can be as high as 20%.[14] Different morphologies of $CH_3NH_3PbX_3$ (X = I,

Br) nanocrystals have been prepared by using various solvents and capping ligands. We showed that $CH_3NH_3PbX_3$ nanowires and nanorods exhibit relatively higher photoluminescence (PL) quantum yields and long PL lifetimes.[15] Also, $CH_3NH_3PbI_3$ single crystals can produce long (> 175 μm) diffusion lengths. This stems from greater carrier mobility, longer lifetime, and much smaller trap densities in the single crystals than in polycrystalline thin films.[16] But one should consider the difficulties in producing single crystals.

It has been reported that $CH_3NH_3PbI_3$ is less photo-stable than $CH_3NH_3PbBr_3$[17] and the doping of Br in the perovskite can lead to a slight improvement of device longevity mainly due to higher moisture-stability.[18] Based on calculations, the variations in the band gap in perovskites with different halides result from changes in the valence band.[19] There are a few reports of making perovskites with tunable PL emission and wide color gamut such as $CsPbX_3$ (X= Cl, Br, and I) nanocrystals[20] and $Pb(Br_xCl_{1-x})_3$, $Pb(Br_xI_{1-x})_3$, and $Pb(Cl_xI_{1-x})_3$ (x = 0-1) perovskites.[21] Many anomalous alloy properties have been observed in these materials, such as negligible formation energies at some concentrations and small or even negative band gap bowing parameters at high temperature. As expected from the differences in ionic radii, mixed (I-Cl) perovskites are more difficult to produce compared to (Br-Cl) and (I-Br) perovskites.[22] In this work, perovskites with tunable optical properties depending on the nature and ratio of the halides employed (X = Cl, Br, and I) were synthesized. We observed that upon doping of Cl and Br in the Br- and I-perovskite lattice respectively makes the charge recombination rates faster in the material. In agreement with the literature, we observed certain alloys of mixed halide perovskites initially shows multiple PL peak which blend to a single peak after few days.[23] Mixed halide perovskites $CH_3NH_3PbBr_{3-x}Cl_x$ with different compositions of halogens exhibit almost linear PL behavior. On the other hand, $(CH_3NH_3)Pb(Br_xI_{1-x})_3$ have shown deviation from linearity.
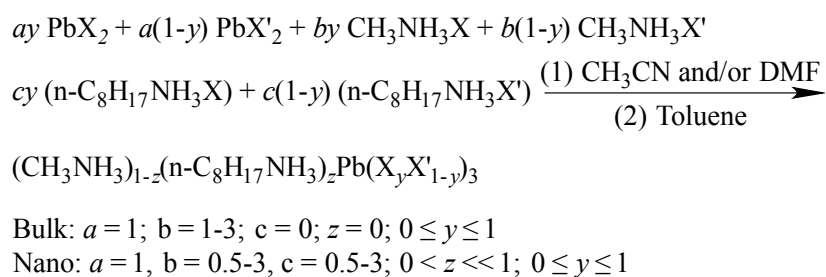
The surface trap states and grain boundaries of the perovskites are known to be the principal reason behind photocurrent hysteresis in solar cells. [24]The sub gap states affects the photoconductivity response in perovskite films and they also suffer from limited photovoltage by the sub gap states.[17] Elemental defects, such as Pb, I, and CH_3NH_3 vacancies derived from Frenkel defects have been showed to form shallow levels near band edges which makes them unintentional doping sources.[25] Similarly, in $CH_3NH_3PbBr_3$ perovskites, the dominant defects in $CH_3NH_3PbBr_3$ create shallow levels, thus, resulting in a low bulk non-radiative recombination rate.[26] Furthermore, under iodine-rich conditions, $CH_3NH_3PbI_3$ perovskites are likely to have a high density of deep electronic traps and the formation of key defects where Pb atoms are substituted by I. This can severely affect the photovoltaic performance. A deep defect state ~0.16 eV above the valence band was reported. Iodine interstitials (I_i) are believed to be responsible for this and they serve as non-radiative recombination centers.[27] Furthermore, Pb dimers and I trimers can result in intrinsic defects and is responsible for deep trap states acting as recombination centers.[28] Also the trap states are more significant in 2D $(C_4H_9NH_3I)_2(CH_3NH_3I)_{n-1}(PbI_2)_n$ (n = 1, 2, 3) perovskites.[29] Here we studied reversible photo-induced spectral changes, which results from trap states in $(CH_3NH_3)PbX_3$ films. We also studied the PL shift in the perovskites as the sample ages, which may be a result of phase segregation.

MATERIALS AND METHODS

Materials. Lead (II) iodide (99%), lead (II) bromide (≥98%), methylamine solution (33 wt % in absolute ethanol), N, N-dimethylformamide (DMF, anhydrous, 99.8%) and n-octylamine (99%) were purchased from Sigma-Aldrich. Hydroiodic acid (ACS, 55-58%), hydrobromic acid (ACS, 47.0-49.0%) and oleic acid (tech., 90%) were from Alfa-Aesar; acetonitrile (99.9%) and toluene (99.9%) were from Fisher. All chemicals were used as received unless specified otherwise.

Synthesis of Ammonium Halides. Ammonium halides were prepared by a modified literature procedure. Briefly, Hydroiodic acid (10 mL, 0.075 mol) or hydrobromic acid (8.6 mL, 0.075 mol) or hydrochloric acid (6.2 mL, 0.075 mol) was added to a solution of excess methylamine (24 mL, 0.192 mol) in ethanol (100 mL) at 0 °C, and the mixture stirred for 2 h. The solution was concentrated under vacuum and the resulting powder was dried under dynamic vacuum at 60 °C for 12 h, then recrystallized from ethanol. n-octylammonium iodide ($CH_3(CH_2)_7NH_3I$), n-octylammonium bromide ($CH_3(CH_2)_7NH_3Br$) and n-octylammonium chloride ($CH_3(CH_2)_7NH_3Cl$) were washed repeatedly with ethyl ether and dried under dynamic vacuum before use.

Scheme 1. Synthesis of mixed-halide organolead perovskites of different dimensionality (bulk *vs.* nano).

$$ay \, PbX_2 + a(1\text{-}y) \, PbX'_2 + by \, CH_3NH_3X + b(1\text{-}y) \, CH_3NH_3X'$$

$$cy \, (\text{n-}C_8H_{17}NH_3X) + c(1\text{-}y) \, (\text{n-}C_8H_{17}NH_3X') \xrightarrow[\text{(2) Toluene}]{\text{(1) } CH_3CN \text{ and/or DMF}}$$

$$(CH_3NH_3)_{1\text{-}z}(\text{n-}C_8H_{17}NH_3)_z Pb(X_y X'_{1\text{-}y})_3$$

Bulk: $a = 1$; $b = 1\text{-}3$; $c = 0$; $z = 0$; $0 \le y \le 1$
Nano: $a = 1$, $b = 0.5\text{-}3$, $c = 0.5\text{-}3$; $0 < z \ll 1$; $0 \le y \le 1$

Synthesis of polycrystalline and low-dimensional Br-I perovskites. For low-dimensional $CH_3NH_3Pb(Br_xI_{1\text{-}x})_3$, PbI_2 (3.7 mg, 0.008 mmol), CH_3NH_3I (1.9 mg, 0.012 mmol) and $CH_3(CH_2)_7NH_3I$ (3.1 mg, 0.012 mmol) were added into a mixture of acetonitrile (20mL) and DMF (200 µL) (a polar solvent), labeled as precursor solution A. $PbBr_2$ (2.9 mg, 0.008 mmol), CH_3NH_3Br (1.3 mg, 0.012 mmol) and $CH_3(CH_2)_7NH_3Br$ (2.5 mg, 0.012 mmol) were added into a mixture of acetonitrile (20mL) and DMF (0.2 mL), labeled as precursor solution B. According to different percentages of bromide loading, fractions of solution A and B were mixed up to 4 mL and the precursor mixture was rapidly mixed with 15 mL toluene (a less polar solvent) while stirring. In order to systematically synthesize Br-I perovskites, we kept all conditions the same for every sample including the precursor solvents, the concentration of ions other than halides, and

the injection rate. In our previous experiments,[15] acetonitrile and DMF serve as the iodide and bromide perovskite precursor solvent, respectively; however, acetonitrile has difficulty dissolving $PbBr_2$ and DMF will not crash out I-Br perovskites when injecting the precursor solution into toluene. Early failures of using a single precursor solvent lead us to try a mixture of acetonitrile and DMF. We observed that PbX_2 (X = Br or I) fails to dissolve in solvent mixtures with equimolar alkylammonium halides (RCH_3^+), where a : (b + c) = 1 : 1 (**Scheme 1**). However, the solubility can increase with a decreasing a : (b + c) ratio. When a : (b + c) is too small, impurities or perovskites with other stoichiometries can be introduced. Thus, finding a suitable Pb^{2+}: RCH_3^+ ratio is crucial to synthesize Br-I perovskites. We found that when a : (b + c) = 1 : 3, all precursors dissolve and the products are in pure phases. For low dimensional Br-I perovskites with an a: b: c = 1: 1.5: 1.5 ratio, we used octylammonium cations ($C_8H_{17}NH_3^+$) for preventing perovskite particles from growing larger. $C_8H_{17}NH_3^+$ cations are too large to penetrate the lattice and thus they would tangle on the surface of particles resulting in z << 1 in Scheme 1 and the prevent particle growth. Samples were subsequently allowed to stand for 24h before isolating the product by centrifugation (10 min at 4000 rpm) and washing with toluene (5 mL). Polycrystalline $CH_3NH_3Pb(I_xBr_{1-x})_3$ followed a similar synthesis method except the amount of methylammonium halide and no $CH_3(CH_2)_7NH_3X$ added in the precursor solution. PbI_2 (3.7 mg, 0.008 mmol) and CH_3NH_3I (3.8 mg, 0. 024 mmol) were added into a mixture of acetonitrile (20 mL) and DMF (200 µL), labeled as precursor solution A. $PbBr_2$ (2.9 mg, 0.008 mmol) and CH_3NH_3Br (2.6 mg, 0. 024 mmol) were added into a mixture of acetonitrile (20mL) and DMF (0.2 mL), labeled as precursor solution B. By following the same procedure in low-dimensional $CH_3NH_3Pb(Br_xI_{1-x})_3$, polycrystalline $CH_3NH_3Pb(Br_xI_{1-x})_3$ particles can be obtained.

Synthesis of polycrystalline and low-dimensional Cl-Br perovskites. $CH_3NH_3Pb(Cl_xBr_{1-x})_3$.
For low-dimensional $CH_3NH_3Pb(Cl_xBr_{1-x})_3$, $PbCl_2$ (11.1 mg, 0.04 mmol), CH_3NH_3Cl (1.4 mg,
0.02 mmol) and $CH_3(CH_2)_7NH_3Cl$ (3.3 mg, 0.02 mmol) were added into DMF (1 mL), labeled as
precursor solution A. $PbBr_2$ (14.7 mg, 0.04 mmol), CH_3NH_3Br (2.3 mg, 0.02 mmol) and
$CH_3(CH_2)_7NH_3Br$ (4.2 mg, 0.02 mmol) were added into DMF (1 mL), labeled as precursor solution
B. According to different percentages of bromide loading, fractions of solution A and B were mixed
up to 100 μL and the precursor mixture was rapidly mixed with 10 mL toluene while stirring.
Samples were allowed to stand for 24h before isolating the product by centrifugation (10 min at
4000 rpm) and washing with toluene (5 mL). Bulk $CH_3NH_3Pb(Cl_xBr_{1-x})_3$ follows similar synthesis
method except the amount of methylammonium halide and no $CH_3(CH_2)_7NH_3X$ added in the pre-
cursor solution. $PbCl_2$ (11.1 mg, 0.04 mmol) and CH_3NH_3Cl (2.8 mg, 0.04 mmol) were added into
DMF (1 mL), labeled as precursor solution A. $PbBr_2$ (14.7 mg, 0.04 mmol) and CH_3NH_3Br (4.6
mg, 0.04 mmol) were added into DMF (1 mL), labeled as precursor solution B. By following the
same procedure in low-dimensional $CH_3NH_3Pb(Cl_xBr_{1-x})_3$, polycrystalline $CH_3NH_3Pb(Br_xI_{1-x})_3$
particles can be obtained. Compared to Br-I perovskites, synthesizing Cl-Br perovskites are more
facile for two reasons: (1) all of the precursors are soluble in DMF and therefore excess RCH_3^+ is
unnecessary and (2) the products crashed out from DMF are pure Cl-Br perovskites. We used a
ratio of a : b : c = 1 : 1 : 0 in polycrystalline Cl-Br perovskite synthesis whereas a ratio of a: b: c =
1: 0.5: 0.5 for low-dimensional Cl-Br perovskites.

Structural Characterization. *Powder X-ray Diffraction (XRD).* XRD data were measured using
Cu KR radiation on Rigaku Ultima IV (40 kV, 44 mA). Samples were prepared by drop casting
from toluene onto a "background-less" quartz sample holder.

Transmission Electron Microscopy (TEM). TEM was conducted using a FEI Technai G2 F20 field emission TEM operating at up to 200 kV with a point-to-point resolution of less than 0.25 nm and a line-to-line resolution of less than 0.10 nm. Samples were prepared by placing 2 or 3 drops of dilute toluene solutions onto carbon-coated copper grids.

Size and Morphology Analysis. Material dimensions were measured manually or with ImageJ or both. Uncertainties in all measurements are reported as standard deviations.

Optical Characterization. *Optical Extinction.* Optical extinction (absorption plus scattering) spectra of solutions were measured with a photodiode-array Agilent 8453 UV/vis spectrophotometer. Solvent absorption was recorded and subtracted from all spectra.

Diffuse Reflectance. Diffuse reflectance spectra of solid films were measured with a SL1 Tungsten Halogen lamp (vis-IR), a SL3 Deuterium Lamp (UV), and a BLACK-Comet C-SR-100 Spectrometer. Samples were prepared by drop-casting toluene solutions onto glass.

Steady-State Photoluminescence (PL). Steady-state PL spectra were measured with a Horiba-Jobin Yvon Nanolog scanning spectrofluorometer equipped with a photomultiplier detector. Relative PL quantum yields (QYs) were measured following literature procedures, using either Rhodamine 590 or Rhodamine 640 dye as standard. Absorption and PL emission spectra were measured as replicates of three or more and the average QYs were recorded.

Lifetime Measurements. Excited state lifetime measurements were performed with the time-correlated single-photon counting (TCSPC) technique. The time correlated single-photon counting apparatus is described elsewhere.[30] For the work described here, we used different wavelengths of excitation, 500 nm, 570 nm and 638 nm. 500 nm and 570 nm excitation wavelengths were obtained from a supercontinuum laser (Fianium Ltd.) with proper 10 nm bandpass filters. Repetition rate of

the laser is 1 MHz. Whereas, a pulse diode laser from PicoQuant (model PDL 800-B) was used as an excitation source for the wavelength of 638 nm with a repetition rate of 5-MHz. A Becker & Hickl photon counting card (model SPC-630) has been used along with a MCP-PMT detector. With the system described, the full width at half-maximum of the instrument response (IRF) is ~200 ps. A 1 cm path length cuvette was used. Longpass filters or a monochormator were introduced for the collection of emission to eliminate scattered excitation light and collect the decay for a particular wavelength band. The decay parameters were calculated by fitting the decay to sum of exponentials after deconvolution of IRF from the decay.

Time-resolved emission spectral measurements. Time-resolved emission spectra (TRES) were measured with a home built nanosecond setup. A Continuum Surelite II laser (5ns, 20 Hz) was used. A 532 nm or a third-harmonic 355 nm were used as excitation wavelengths as mentioned in the figures. The spectra at different times from laser pulse were collected with a synchronized ICCD camera coupled with a spectrograph. The samples in toluene solution were kept in a 1 cm path length cuvette. Absorption and photoluminescence intensity were monitored before and after laser experiment to test goodness of sample.

Raman microscopy. A lab-built Raman microscope based on a DM IRBE platform (Leica, Wetzlar, Germany) with 532 nm (for $CH_3NH_3PbI_3$, Sapphire SF 532 nm, Coherent, Santa Clara, CA, USA) and 488 nm (for $CH_3NH_3PbBr_3$, Argon Ion 488 nm, Uniphase, San Jose, CA) laser excitation was used. A 100× HCX PL APO, 0.25 numerical aperture oil-immersion objective (Leica) was used to achieve a laser spot with a diameter of 0.28 ± 0.03 μm. The excitation power density at the sample was 1.6×10^5 W·cm^{-2}. Photoluminescence (PL) was collected from the epi-direction and focused onto a HoloSpec f/1.8i spectrograph (Kaiser Optical Systems, Ann Arbor, MI, USA) equipped with

a broad range grating (HFG-650, Kaiser Optical Systems) then directed to a charged coupled device (CCD) (Newton 940, Andor Technology, Belfast, UK). Collection times were 0.05 s. A series of 2400 spectra were collected every 0.09873 seconds.

Single particle fluorescence microscopy. Single particle fluorescence microscopy was performed using an inverted microscope (Nikon Eclipse TE2000U, Melville, NY, USA). Perovskites were sonicated for 60 minutes before drop casting 50 μL on a glass microscope coverslip (Carlson Scientific, Peotone, IL). A mercury lamp was used for excitation (XCite 120 PC, EXFO Photonic Solutions Inc., Quebec City). All excitation and emission filters were from Omega Optical (Brattleboro, VT, USA), unless noted otherwise. A filter set consisting of 545/30 nm excitation and 700/75 nm emission were used for the 100% iodide perovskites. A filter set consisting of 620-650/25 nm excitation and 690/70 nm emission filters were used for the 25% bromide and 75% iodide perovskites. An 500/20 nm excitation and an 629/56 nm emission filter from Semrock, Inc. (Lake Forest, IL, USA) were used for the 50% bromide and 50% iodide perovskites. A filter set consisting of 500/20 nm excitation and 535/30 nm emission filters were used for the 75% bromide and 25% iodide as well as the 100% bromide perovskites. A 100× PlanApo, 1.49 numerical aperture oil-immersion objective was used and PL images were collected using a PhotonMAX 512 EMCCD camera (Princeton Instrument, Trenton, NJ, USA) with a 20 ms exposure time. A gain of 3000 was used for all of the samples except no gain was used for the 100% iodide perovskites.

RESULTS AND DISCUSSION

According to Hume-Rothery rules,[31] substitutional solid solution can only form when (1) difference of the atomic radius of the two components is less than 15%; (2) they share a similar crystal structure and have the same charge in order to achieve complete solubility and similar electronegativity. Based on these rules, synthesis of chloride- bromide (Cl-Br) or bromide-iodide

(Br-I) perovskites is theoretically feasible while Chloride-iodide (Cl-I) is not. Even though all three halides have the same charge (-1) and similar electronegativities (3.16 for chloride, 2.96 for bromide and 2.66 for iodide in Pauling units),[32] chloride anions have a radius of 181 pm and the radii expand to 195 pm for bromide anions and 216 pm for iodide anions.[33] The radius difference is less than 15% for the Cl-Br and Br-I systems whereas for the Cl-I system it is over 15%. This radius difference allows Cl-Br and Br-I to form a solid solution but not Cl-I. In addition, the organometal bromide and chloride perovskites share the same cubic crystal structure while the iodide perovskite has a tetragonal structure (**Figure 1**), which may lead to unique behaviors when Br-I perovskites form a solid solution.

Morphology and size distribution of organometal mixed-halide perovskites. TEM images (**Figure 2**) show the dominant morphology of mixed halide perovskites is dot with an average grain size of 7-10 nm. The Bohr radii for bromide and iodide perovskites are 2 and 2.2 nm,[34] so no quantum confinement effect should take place in absorption or emission spectra, which further agrees with the results of our optical measurements. Another minor morphology for Br-rich mixed-halide perovskites is sheet, which also might account for the preferred orientation observed in the powder XRD patterns (**Figure 4**). As reported by our group before, mixed halide particles are also quite unstable under electron beam. The particles will 'evaporate' several minutes after the electron beam focuses on them, which implies low-dimensional perovskites are photo-/thermal-sensitive. This may result from the alkylammonium organic group.

Optical properties of polycrystalline organometal mixed-halide perovskites. A series of mixed-halide perovskites were systematically fabricated by tuning the ratio of the halide perovskite precursor concentrations as shown in **Figure 3**. Under UV light, 100%Br perovskite emits intensely but other samples emit weakly **(Figure 3 left panel (a), top)**. Emission spectra (**Figure**

3 left panel (b)) show the PL maxima cover all visible light region from 400 nm to 760 nm. Diffuse reflectance spectra (**Figure 3 left panel (c)**) demonstrates absorption edges shift from 400nm to 760 nm, indicating the bandgaps change as a function of halide compositions. The solution colors show a gradual change from milky white to dark brown under ambient light, also implying the bandgaps are composition-tunable (**Figure 3 left panel (a), bottom**). **Figure 3d** in the left panel shows the relationship between halide PL maximum/absorption edge and halide composition. It exhibits linear behavior for Cl-Br perovskites but for Br-I perovskites it is non-linear, or to be more specific, semi quadratic. All the Br-I perovskites prefer bromide perovskite phases. We attribute this to a larger ionic size and structural difference for Br-I than Cl-Br. The ionic radius difference for Cl-Br is only 14 pm, but for Br-I it is 21 pm. In addition, Cl-Br perovskites share the same cubic structure but $CH_3NH_3PbI_3$ has a tetragonal phase, thus causing Br-I to undergo a phase transformation from 100%Br to 100%I.

Optical properties of low-dimensional organometal mixed-halide perovskites. Adding $C_8H_{17}NH_3X$ can effectively reduce the particle size and enhance photoluminescence (**Figure 3 right vs. left panel**), but it sometimes introduces impurities into the system. Especially for 100%Br in the Br-I series, the quantum yield has reached 44%. As expected, PL spectra (**Figure 3 right panel (b)**) covers visible light region with brighter emission and absorption spectra indicate bandgaps are composition-tunable (**Figure 3 right panel (c)**). **Figure 3d** in the right panel exhibits PL maximum and 1st excitonic peak as a function of halide composition, further illustrating the linear behavior in the Cl-Br region and the Br-preferred behavior at the Br-I region. However, adding octylammonium may introduce some impurities into the system. For example, 25%Br 75%I shows peaks in addition to the main peak at 646 nm. This red PL peak might come from

Iodine-enriched domains in the samples or some species produced by the reaction of octylammonium halides and lead halides on the surface of perovskite nanocrystals. It is reported that RNH_3PBI_3 has a smaller bandgap with longer carbon chains in R.[35]

Crystallography study of organometal mixed-halide perovskites. The relationship between optical properties and crystal structures was studied by powder XRD experiment for each sample. From **Figure 4a**, all the samples are pure mixed halide perovskites because all the diffraction peaks match the standard patterns and no other peaks are visible. The diffraction peaks gradually shift from $CH_3NH_3PbCl_3$ to $CH_3NH_3PbI_3$, indicating that the mixed-halide perovskites are in solid solution. Low-dimensional perovskites exhibit fewer peaks than polycrystalline ones, possibly due to aggregation of the particles along a preferred orientation when we drop-casted samples on the XRD slide. Not surprisingly, similar peak shift also occured. However, 100%Cl shows several diffraction peaks that don't match standard pattern. These impurities may come from reactions between octylammonium chloride and lead chloride that need further study. **Figure 4c** demonstrates pseudocubic[18b] or cubic lattice parameters as a function of halide composition and, similar to the optical properties, it illustrates a linear behavior in the Cl-Br region and a non-linear behavior in the Br-I region. Since the Br^- ionic radius is 21 pm smaller than I^-, the concave curve in Br-I region indicates Br-phases are favored in the Br-I perovskite series.

Photoluminiscence lifetimes organometal perovskites, $CH_3NH_3Pb(I_{1-x}Br_x)_3$ and $CH_3NH_3Pb(Br_{1-x}Cl_x)_3$. We have carried out photoluminescence experiments with different morphologies and dimensions of $CH_3NH_3PbI_3$ perovskites (**Figure 5**). The lifetime decays can be best fitted with a bi-exponential curve. The long component can be attributed to the intrinsic recombination rate of the exciton or free carriers. Whereas, recombination through surface states is responsible for the faster component. The PL lifetimes in bulk $CH_3NH_3PbI_3$ is faster with a value of 9.1

ns and the quantum yield is also small. Thus, in bulk $CH_3NH_3PbI_3$, the dominant channel of recombination is *via* the fast carrier trapping through surface states. In anisotropic $CH_3NH_3PbI_3$ nanostructures, the slower component becomes more dominant with longer average lifetimes of 30.4 ns for 1500 nm × 34 nm $CH_3NH_3PbI_3$ nanowires and 65.6 ns 810 nm × 54 nm $CH_3NH_3PbI_3$ nanorods. In longer $CH_3NH_3PbI_3$ nanowires, where surface-to-volume ratio is larger than the shorter $CH_3NH_3PbI_3$ nanorods, more nonradiative surface states are present resulting in shorter lifetime. We also carried out experiments varying laser excitation power in perovskites. With increasing excitation power, the lifetime becomes faster. The PL lifetime decay curves of the low-dimensional perovskites are given in **Figure 6**. In all the mixed-halide perovskites we observed that polycrystalline perovskites show faster lifetime compared to that in low-dimensional perovskites. **Table I** and **Table II** summarize the PL lifetime observed in low- dimensional mixed-halide perovskites. The lifetime gradually becomes faster with increasing percentage of Br in bromide-iodide (Br-I) perovskites, though the lifetime in pure Br-perovskites is slower compared to the 50% and 75% Br perovskites (Br-I). Similar trend has been observed in Br-Cl perovskites. In general, lifetimes of Br-Cl perovskites are faster compared to Br-I perovskites consistent with the low QY in Br-Cl perovskites.

Photoluminescence Stability. Reversible PL Behavior: Thermal Red-Shifting of PL (Annealing) vs. Photo-Induced Blue-Shifting of PL. **Figure 7** shows the spectra of low-dimensional $CH_3NH_3PbI_3$ as sample ages after preparation. Two distinct features have been observed. First, the dominant PL peak is much bluer just after preparation of the perovskites. With time, the peak gradually red shifts to ~750 nm. Secondly, at the beginning, a blue peak at ~620 nm appears. This peak essentially disappears as the sample ages. On the other hand, **Figure 8a** provides the spectra

of aged low-dimensional $CH_3NH_3PbI_3$ as the perovskites are illuminated with different laser powers. The excitation wavelength was 532 nm. The figure shows with increasing power, the blue peak at 620 nm becomes more intense whereas the peak at 750 nm is shifting towards bluer wavelength. This perovskites were prepared with a synthetic method where we used a 1: 6 ratio of lead halide and alkylammonium halides (a: b: c = 1: 3: 3) to fabricate low-dimensional perovskites. The ratio of the "blue peak" to the "red peak" with respect to excitation energy has been presented in the inset of the figure. This "blue peak" might be result of defects or change in crystal structure due to illumination of laser. We carried out *in situ* XRD experiment with laser illumination. The lack of evidence of different crystal formation from XRD result indicates that this blue PL peak comes from surface trap states. We collected lifetime of the two peaks separately (**Figure 9**). The blue peak decays much faster compared to the red peak. Thus, we can assume this blue peak is coming from some surface defects. This photo-induced spectral change is thermally reversible. **Figure 8b** shows the spectra of the perovskites at different times after laser illumination. Initial the intense blue peak gradually disappears and ~730 nm peak shifts towards longer wavelength. To eliminate the blue peak, we optimized the synthetic method and successfully fabricated perovskites without the bluer peak. **Figure 8c** shows time resolved emission spectra (TRES) of a fresh, low-dimensional $CH_3NH_3PbI_3$ solution made from the optimized synthetic method (a: b: c = 1: 1.5: 1.5). Apparently, no blue peak is observed in this sample, which implies the optimized method can synthesize trap-free organometal mixed-halide perovskites. To further examine our hypothesis that excess precursor, CH_3NH_3I is responsible for introduction of defects in the perovskites, we performed experiments by first making the perovskites with our optimized scheme of synthesis and subsequently, adding excess of CH_3NH_3I. Addition of excess precursor induces spectral shifts in the PL and thus confirms the effect of excess precursor. We carried out similar experiments with

CH$_3$NH$_3$PbBr$_3$. We observed similar characteristic spectral changes upon laser illumination. The only notable difference being the rate of reversibility of the photoinduced changes is much slower compared to CH$_3$NH$_3$PbI$_3$. Similar, photo-stability behaviors were observed in solid state photo-luminescence measurements and the effect of "washing" (purification) on the optical properties were studied (**Figure 10**). The "washing" was seen to be effective to reduce PL shift.

CONCLUSION

This work, thus, suggest a linearly tunable band-gap can be achieved varying the amount of doping in perovskites, though, deviation from linear behavior in I-Br perovskites can be attributed to bigger difference in size of the halide ions. Also, as the Br perovskites are more stable in atmosphere, the mixed halide perovskites are most likely to have more stability. Furthermore, we observed low-dimensional perovskites have longer carrier recombination rate, which facilitates extraction of charges when they are used in active layers. Although, Cl-Br perovskites were easier to synthesize, but they have, usually, low quantum yield and faster PL lifetime. Also, we focused on the effect of stoichiometry of the precursors of the synthesis on the quality of the material. To use in well performing solar cell device, materials are expected to have a single bandgap and single carrier recombination rate. Although to enhance solubility of the precursor in the used solvents higher a: b: c ratio was preferred, we found out higher stoichiometric ratio materials with defects. The trap-states in perovskites are more abundant in presence of excess precursor. We studied reversible nature of the spectral shifts under laser illuminations. Thus, using the knowledge obtained from spectroscopic studies, we found a: b: c ratio of 1: 1.5: 1.5 is preferable for an optimum synthesis.

Author Contributions

L. M. carried out all the synthesis and structural characterizations. U. B. performed steady-state and time-resolved spectroscopic studies in bulk toluene solvent. D. J. F. carried out the microscopic solid-state measurements.

REFERENCES

1.   Green, M. A.; Ho-Baillie, A.; Snaith, H. J., The emergence of perovskite solar cells. *Nat Photon* **2014,** *8*, 506-514.

2.   Park, N.-G., Organometal Perovskite Light Absorbers Toward a 20% Efficiency Low-Cost Solid-State Mesoscopic Solar Cell. *The Journal of Physical Chemistry Letters* **2013,** *4*, 2423-2429.

3.   Snaith, H. J., Perovskites: The Emergence of a New Era for Low-Cost, High-Efficiency Solar Cells. *The Journal of Physical Chemistry Letters* **2013,** *4*, 3623-3630.

4.   Kazim, S.; Nazeeruddin, M. K.; Grätzel, M.; Ahmad, S., Perovskite as Light Harvester: A Game Changer in Photovoltaics. *Angewandte Chemie International Edition* **2014,** *53*, 2812-2824.

5.   Kamat, P. V., Evolution of Perovskite Photovoltaics and Decrease in Energy Payback Time. *J. Phys. Chem. Lett.* **2013,** *4*, 3733-3734.

6.   Liu, M.; Johnston, M. B.; Snaith, H. J., Efficient Planar Heterojunction Perovskite Solar Cells by Va-pour Deposition. *Nature* **2013,** *501*, 395-398.

7.   Bisquert, J., The Swift Surge of Perovskite Photovoltaics. *J. Phys. Chem. Lett.* **2013,** *4*, 2597-2598.

8.   Grätzel, M., The Light and Shade of Perovskite Solar Cells. *Nature mater.* **2014,** *13*, 838-842.

9.   Stoumpos, C. C.; Malliakas, C. D.; Kanatzidis, M. G., Semiconducting Tin and Lead Iodide Perovskites with Organic Cations: Phase Transitions, High Mobilities, and Near-Infrared Photoluminescent Prop-erties. *Inorg. Chem.* **2013,** *52*, 9019-9038.

10.   Edri, E.; Kirmayer, S.; Cahen, D.; Hodes, G., High Open-Circuit Voltage Solar Cells Based on Organ-ic–Inorganic Lead Bromide Perovskite. *J. Phys. Chem. Lett.* **2013,** *4*, 897-902.

11.   Eperon, G. E.; Stranks, S. D.; Menelaou, C.; Johnston, M. B.; Herz, L. M.; Snaith, H. J., Formamidinium Lead Trihalide: A Broadly Tunable Perovskite for Efficient Planar Heterojunction Solar Cells. *En-ergy Environ. Sci.* **2014,** *7*, 982-988.

12.   Pellet, N.; Gao, P.; Gregori, G.; Yang, T. Y.; Nazeeruddin, M. K.; Maier, J.; Grätzel, M., Mixed Organic Cation Perovskite Photovoltaics for Enhanced Solar-Light Harvesting. *Angew. Chem. Int. Ed.* **2014,** *53*, 3151-3157.

13.   Ogomi, Y.; Morita, A.; Tsukamoto, S.; Saitho, T.; Fujikawa, N.; Shen, Q.; Toyoda, T.; Yoshino, K.; Pandey, S. S.; Ma, T., $CH_3NH_3Sn_xPb_{(1-x)}I_3$ Perovskite Solar Cells Covering up to 1060 nm. *J. Phys. Chem. Lett.* **2014,** *5*, 1004-1011.

14.   Schmidt, L. C.; Pertegás, A.; González-Carrero, S.; Malinkiewicz, O.; Agouram, S.; Mínguez Espallargas, G.; Bolink, H. J.; Galian, R. E.; Pérez-Prieto, J., Nontemplate Synthesis of $CH_3NH_3PbBr_3$ Perovskite Nanoparticles. *Journal of the American Chemical Society* **2014,** *136*, 850-853.

15.   Zhu, F.; Men, L.; Guo, Y.; Zhu, Q.; Bhattacharjee, U.; Goodwin, P. M.; Petrich, J. W.; Smith, E. A.; Vela, J., Shape Evolution and Single Particle Luminescence of Organometal Halide Perovskite Nano-crystals. *ACS nano* **2015,** *9*, 2948-2959.

16.   Dong, Q.; Fang, Y.; Shao, Y.; Mulligan, P.; Qiu, J.; Cao, L.; Huang, J., Electron-hole diffusion lengths > 175 μm in solution-grown $CH_3NH_3PbI_3$ single crystals. *Science* **2015,** *347*, 967-970.

17.   Leijtens, T.; Stranks, S. D.; Eperon, G. E.; Lindblad, R.; Johansson, E. M.; McPherson, I. J.; Rensmo, H.; Ball, J. M.; Lee, M. M.; Snaith, H. J., Electronic properties of meso-superstructured and planar organometal halide perovskite films: Charge trapping, photodoping, and carrier mobility. *ACS nano* **2014,** *8*, 7147-7155.

18.   (a) Suarez, B.; Gonzalez-Pedro, V.; Ripolles, T. S.; Sanchez, R. S.; Otero, L.; Mora-Sero, I., Recombination Study of Combined Halides (Cl, Br, I) Perovskite Solar Cells. *J. Phys. Chem. Lett.* **2014,** *5*, 1628-1635; (b) Noh, J. H.; Im, S. H.; Heo, J. H.; Mandal, T. N.; Seok, S. I., Chemical management for colorful, efficient, and stable inorganic-organic hybrid nanostructured solar cells. *Nano Lett* **2013,** *13*, 1764-9.

19.   Butler, K. T.; Frost, J. M.; Walsh, A., Band Alignment of the Hybrid Halide Perovskites $CH_3NH_3PbCl_3$, $CH_3NH_3PbBr_3$ and $CH_3NH_3PbI_3$. *Mater. Horiz.* **2015,** *2*, 228-231.

20.   Protesescu, L.; Yakunin, S.; Bodnarchuk, M. I.; Krieg, F.; Caputo, R.; Hendon, C. H.; Yang, R. X.; Walsh, A.; Kovalenko, M. V., Nanocrystals of Cesium Lead Halide Perovskites ($CsPbX_3$, X = Cl, Br, and I): Novel Optoelectronic Materials Showing Bright Emission with Wide Color Gamut. *Nano Letters* **2015**.

21.   Papavassiliou, G. C.; Pagona, G.; Karousis, N.; Mousdis, G. A.; Koutselas, I.; Vassilakopoulou, A., Nanocrystalline/microcrystalline materials based on lead-halide units. *Journal of Materials Chemistry* **2012,** *22*, 8271-8280.

22.   Yin, W.-J.; Yan, Y.; Wei, S.-H., Anomalous Alloy Properties in Mixed Halide Perovskites. *The Journal of Physical Chemistry Letters* **2014,** *5*, 3625-3631.

23.   Sadhanala, A.; Deschler, F.; Thomas, T. H.; Dutton, S. E.; Goedel, K. C.; Hanusch, F. C.; Lai, M. L.; Steiner, U.; Bein, T.; Docampo, P.; Cahen, D.; Friend, R. H., Preparation of Single-Phase Films of $CH_3NH_3Pb(I_{1-x}Br_x)_3$ with Sharp Optical Band Edges. *The Journal of Physical Chemistry Letters* **2014,** *5*, 2501-2505.

24.   Shao, Y.; Xiao, Z.; Bi, C.; Yuan, Y.; Huang, J., Origin and elimination of photocurrent hysteresis by fullerene passivation in $CH_3NH_3PbI_3$ planar heterojunction solar cells. *Nat Commun* **2014,** *5*.

25.   Kim, J.; Lee, S.-H.; Lee, J. H.; Hong, K.-H., The Role of Intrinsic Defects in Methylammonium Lead Iodide Perovskite. *The Journal of Physical Chemistry Letters* **2014,** *5*, 1312-1317.

26.   Shi, T.; Yin, W.-J.; Hong, F.; Zhu, K.; Yan, Y., Unipolar self-doping behavior in perovskite $CH_3NH_3PbBr_3$. *Applied Physics Letters* **2015,** *106*, 103902.

27.   Duan, H.-S.; Zhou, H.; Chen, Q.; Sun, P.; Luo, S.; Song, T.-B.; Bob, B.; Yang, Y., The identification and characterization of defect states in hybrid organic–inorganic perovskite photovoltaics. *Physical Chemistry Chemical Physics* **2015,** *17*, 112-116.

28.   Agiorgousis, M. L.; Sun, Y.-Y.; Zeng, H.; Zhang, S., Strong Covalency-Induced Recombination Centers in Perovskite Solar Cell Material $CH_3NH_3PbI_3$. *Journal of the American Chemical Society* **2014,** *136*, 14570-14575.

29.   Wu, X.; Trinh, M. T.; Niesner, D.; Zhu, H.; Norman, Z.; Owen, J. S.; Yaffe, O.; Kudisch, B. J.; Zhu, X., Trap States in Lead Iodide Perovskites. *Journal of the American Chemical Society* **2015,** *137*, 2089-2096.

30.   Bhattacharjee, U.; Beck, C.; Winter, A.; Wells, C.; Petrich, J. W., Tryptophan and ATTO 590: Mutual Fluorescence Quenching and Exciplex Formation. *J. Phys. Chem. B* **2014,** *118*, 8471–8477.

31.   Hume-Rothery, W.; Powell, H. M., *Z. Kristallogr.* **1935,** *91*, 23.

32.   Pauling, L., The Nature of the Chemical Bond. IV. The Energy of Single Bonds and the Relative Elec-tronegativity of Atoms. *J. Am. Chem. Soc.* **1932,** *54*, 3570-3582

33.   Shannon, R. D.; Prewitt, C. T., Effective Ionic Radii in Oxides and Fluorides. *Acta Crystallogr. Sect. B* **1969,** *25*, 925-946.

34.   Tanaka, K.; Takahashi, T.; Ban, T.; Kondo, T.; Uchida, K.; Miura, N., Comparative Study on the Exci-tons in Lead-Halide-Based Perovskite-Type Crystals $CH_3NH_3PbBr_3$ $CH_3NH_3PbI_3$. *Solid State Commun.* **2003,** *127*, 619-623.

35.   Papavassiliou, G. C., Three-and low-dimensional inorganic semiconductors. *Prog. Solid St. Chem.* **1997,** *25*, 125-270.

TABLES

Table 1. Structural and optical properties of mixed-halide organolead perovskites: $CH_3NH_3Pb(X_yX'_{1-y})_3$.[a]

Loading	a:b:c[a]	a (nm)	Size (nm)		Abs. edge (nm)	PL_{max} (nm)	QY (%)	τ (ns)
	(Pb:C1:C8)		XRD	TEM				
Polycrystalline (bulk)								
100% I, 0% Br	1:3:0	0.628	-[b]	n.d.[c]	765	763	n.d.[c]	20.2
50% I, 50% Br	1:3:0	0.594	-[b]	n.d.[c]	532	576	n.d.[c]	7.69
0% I, 100% Br	1:3:0	0.591	-[b]	n.d.[c]	527	519	n.d.[c]	5.64
100%Br, 0% Cl	1:1:0	0.598	72	n.d.[c]	526	527	n.d.[c]	n.d.[c]
50%Br, 50% Cl	1:1:0	0.581	-[b]	n.d.[c]	466	466	n.d.[c]	n.d.[c]
0%Br, 100%Cl	1:1:0	0.572	-[b]	n.d.[c]	399	412	n.d.[c]	n.d.[c]
Low-dimensional (nano)								
100% I, 0% Br	1:1.5:1.5	0.634	-[b]	7 ± 2	774[d]	745	1.5	83.9
50% I, 50% Br	1:1.5:1.5	0.599	-[b]	8 ± 3	560[d]	540	0.02	13.6
0% I, 100% Br	1:1.5:1.5	0.587	7	8 ± 2	527[d]	506	44	23.6
100%Br, 0% Cl	1:0.5:0.5	0.596	86	160 (plates)	515[d]	518	5	22.6
50%Br, 50% Cl	1:0.5:0.5	0.579	40	10 ± 3	449[d]	459	3	10.6
0%Br, 100%Cl	1:0.5:0.5	0.567	14	9 ± 3	387[d]	398	0.03	n.d.[c]

[a]According to Scheme 1. [b]Too large for Scherrer equation (>0.1-0.2 μm). [c]Not determined. [d]1st excitonic peak.

FIGURES
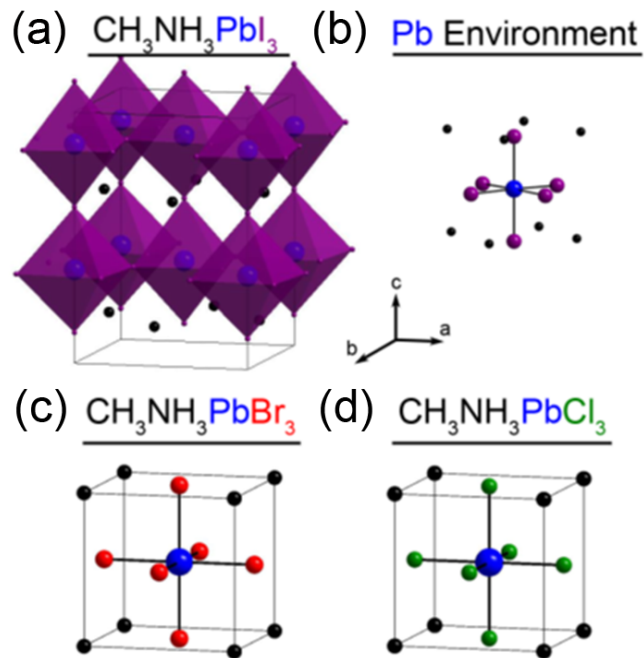
Figure 1. Organometal halide perovskite unit cells of (a) $CH_3NH_3PbI_3$, (c) $CH_3NH_3PbBr_3$ and (d) $CH_3NH_3PbCl_3$ and (b) Pb environment in $CH_3NH_3PbI_3$ unit cell.
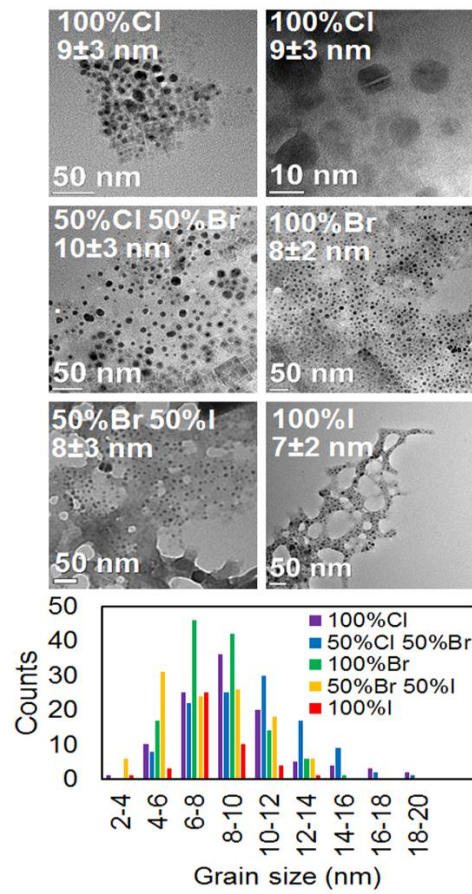
Figure 2. Typical transmission electron microscopy (TEM) images of Organometal halide perovskite nanocrystals and its histogram of grain size distribution.
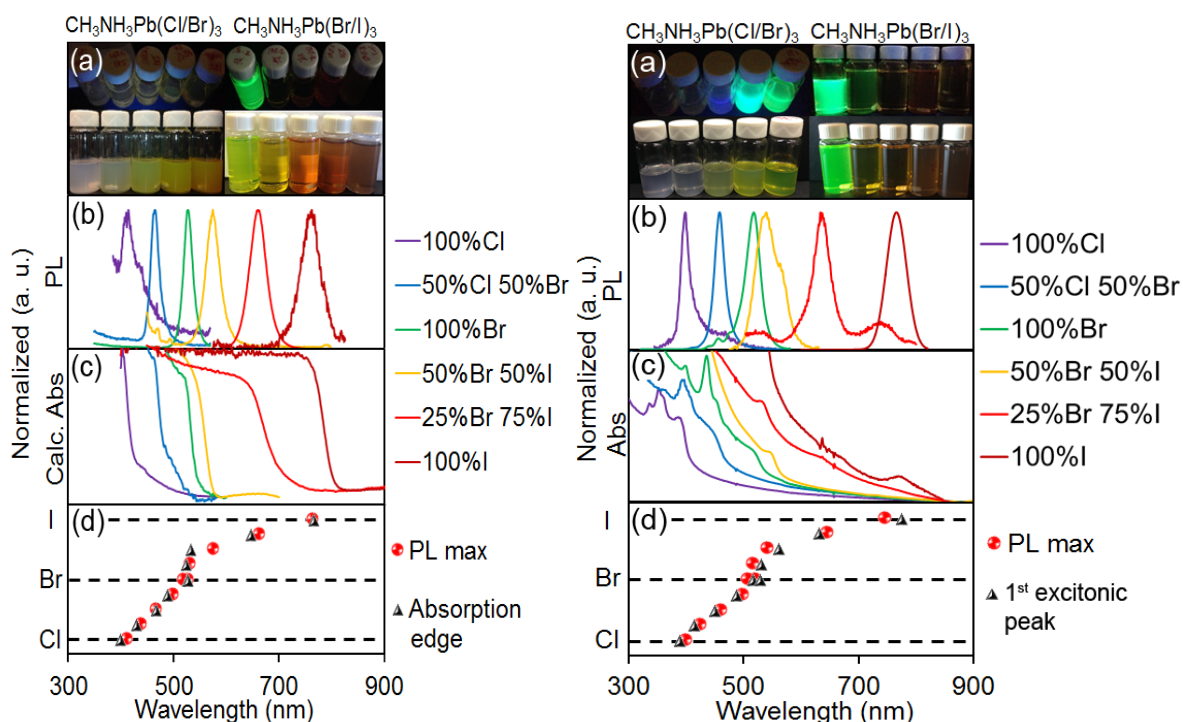
Figure 3. Left Panel. Polycrystalline organometal mixed-halide perovskites $CH_3NH_3PbX_3$ (X=Cl, Br, I) exhibit composition-tunable emission and diffuse reflectance spectra. (a) samples in toluene under UV lamp (top) and ambient light (bottom); (b) typical emission spectra ($\lambda_{exc} = 300$nm for $CH_3NH_3Pb(Cl/Br)_3$ and 430nm for $CH_3NH_3Pb(Br/I)_3$; (c) representative diffuse reflectance spectra in thin film; (d) PL maximum and absorption edge as a function of halide composition. **Right Panel.** Low-dimensional organometal halide perovskites $CH_3NH_3PbX_3$ (X=Cl, Br, I) exhibit composition-tunable emission with higher intensity and solution absorption spectra. (a) samples in toluene under UV lamp (top) and ambient light (bottom); (b) typical emission spectra ($\lambda_{exc} = 300$nm for $CH_3NH_3Pb(Cl/Br)_3$ and 430nm for $CH_3NH_3Pb(Br/I)_3$; (c) representative absorption spectra in toluene solution; (d) PL maximum and 1st excitonic peak as a function of halide composition.
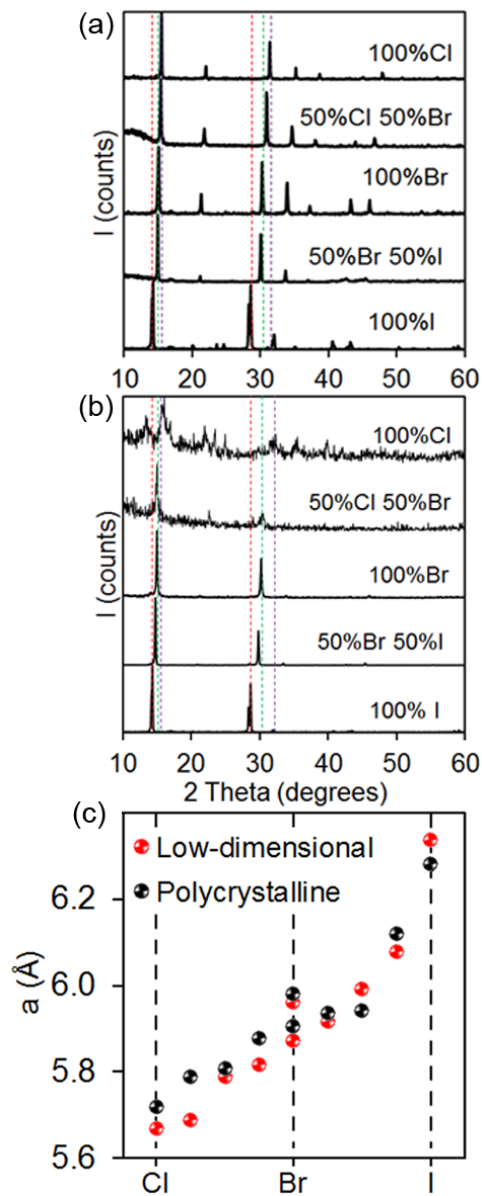
Figure 4. Powder XRD of polycrystalline (a) and low-dimensional (b) mixed halide perovskites. Red, green and purple dashed lines correspond to the main peaks of iodide, bromide and chloride perovskite standard patterns. (c) Lattice parameters of pseudocubic or cubic as a function of halide composition.
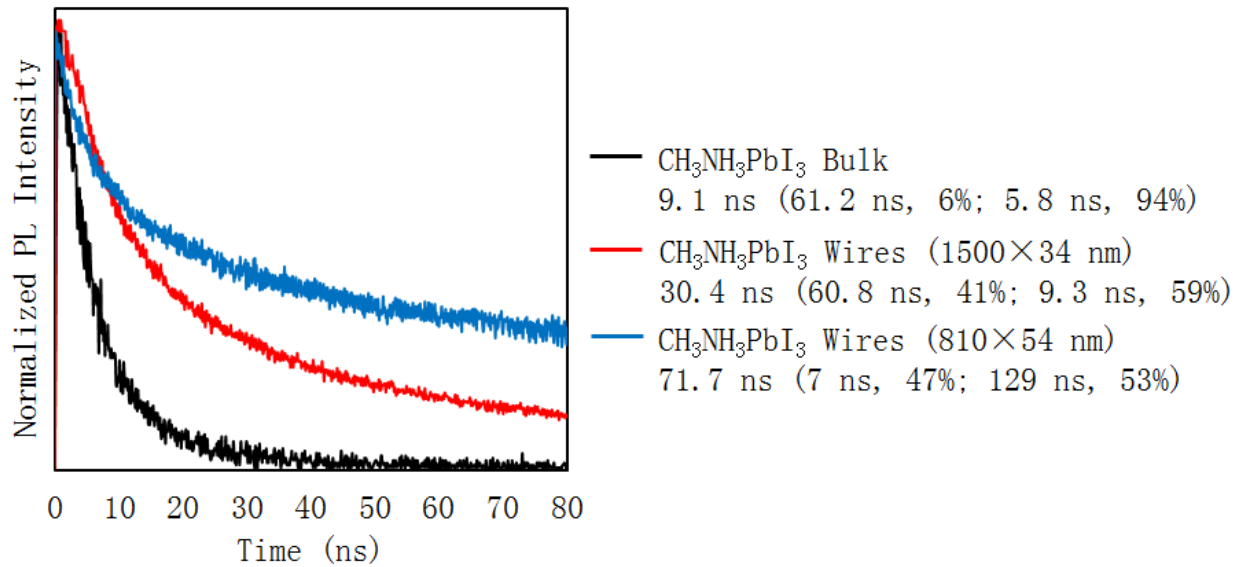
Figure 5. Photoluminescence decay lifetimes of solutions containing crystalline CH₃NH₃PbI₃ particles of different sizes and morphologies (λexc = 638 nm). (Reprinted with permission from *ACS Nano* **2015**, *9*, 2948-2959. Copyright (2015) American Chemical Society.)

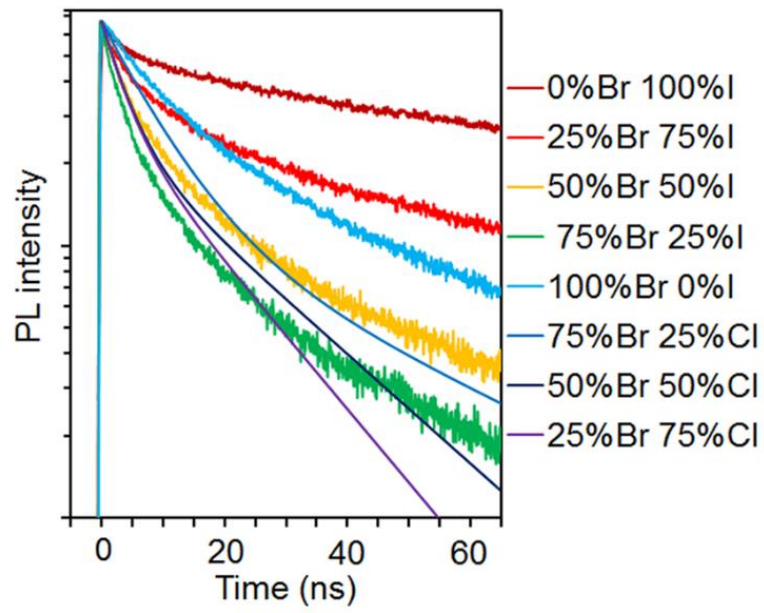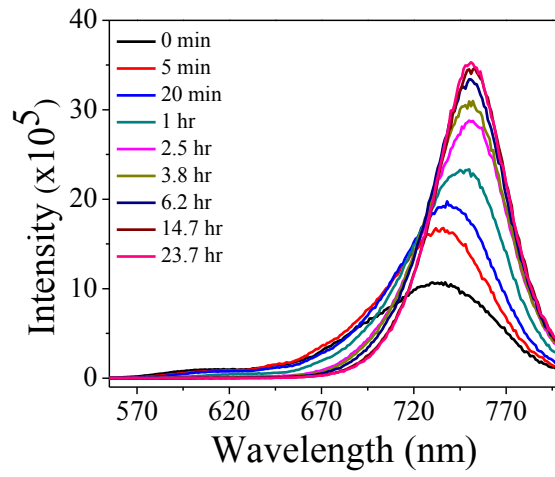**Figure 6.** Time-resolved PL decays for all the low dimensional samples except 100%Cl.

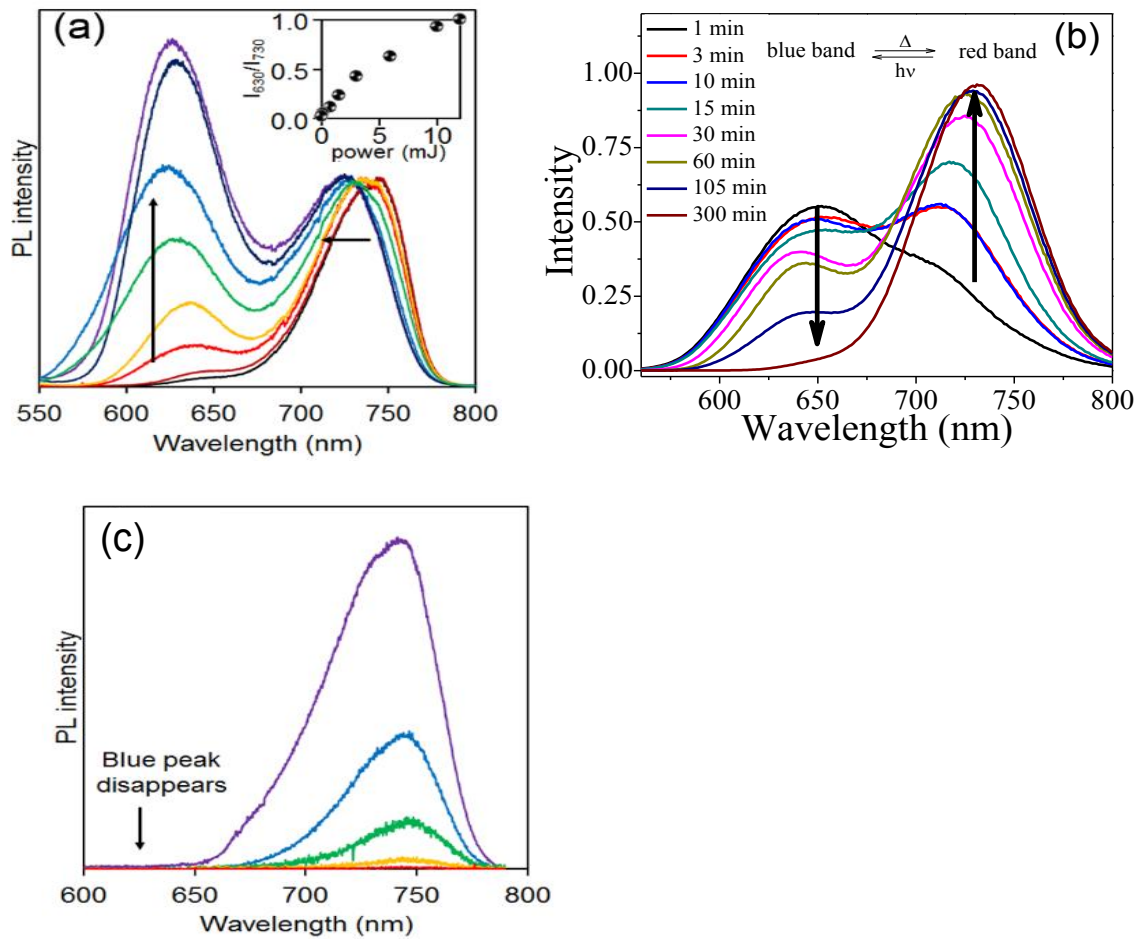**Figure 7.** PL spectra of low-dimensional CH₃NH₃PbI₃ after certain times from preparation.

Figure 8. (a) Emission spectra of low-dimensional $CH_3NH_3PbI_3$ as a function of excitation power, normalized at 730 nm; (b) PL spectra of $CH_3NH_3PbI_3$ after different times after illumination with laser. (c) Time resolved emission spectra (TRES) of low-dimensional $CH_3NH_3PbI_3$ taken at a gap of 5 ns. The laser energy is 5 mJ.

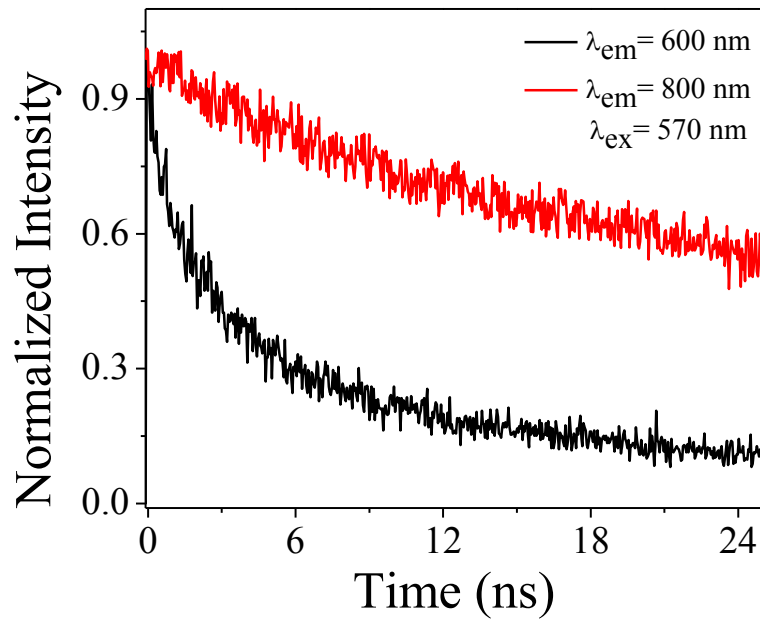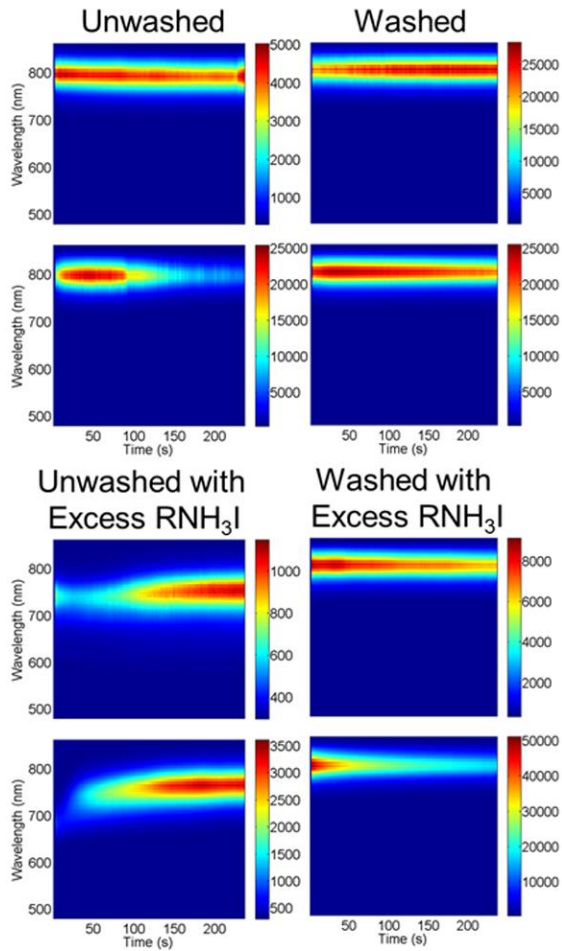**Figure 9**. Lifetime of the blue and the red peak of $CH_3NH_3PbI_3$.

Figure 10. All samples represent 100%I perovskite samples. A control experiment where samples are made with and without purification and addition and relief of excess precursor revealed that unless the samples were not purified, a PL emission peak at near 800 nm is observed, and excess precursor changes the photoluminescence spectra to a maxima of approximately 740 nm.

UJJAL BHATTACHARJEE

Academic Qualification

- ➢ **Ph. D.**: Iowa State University, USA, Dept. of Chemistry. Under supervision of Prof. Jacob. W. Petrich. Aug, 2010 – Aug, 2015.
- ➢ **M.Sc.**: IIT Bombay, India, Dept. of Chemistry, 2008 –2010. M.Sc. 1-yr project and summer project under supervision of Prof. Sambhu N. Datta. Feb, 2009 – June, 2010.
- ➢ **B.Sc.**: Ramakrishna Mission Residential College, Narendrapur, Under Calcutta University, India July, 2005 – July, 2008.

Academic Achievements

- ➢ Scholarships obtained: MCM Scholarship, IIT Bombay
- ➢ Joint Admission Test to M.Sc. to IIT(JAM-2008) all India rank: 33
- ➢ College Rank(B.Sc.): 5
- ➢ NET, June 2009 all India rank: 26
- ➢ GATE 2010 all India rank: 3
- ➢ Fellowships: Offer for summer research fellowship from *Indian Academy of Sciences*, *Bangalore*

Technical skills

- ➢ *Instruments Handled:*
  UV-VIS spectrometer, Fluorimeter, Time Correlated Single Photon Counting, Fluorescence Upconversion, Nano-second transient absorption and time resolved emission spectrometer, Stimulated emission depletion (STED) microscopy, Fluorescence correlation spectroscopy, Fluorescence recovery after photo-bleaching (FRAP), Infrared spectrometer (both Dispersive and FT-IR), Cyclic voltammetry, Viscometer, Karl-Fisher coulometric titration, X.R.D., In synthesis lab used inert atmosphere slink, glove box for reactions, Rota vapor, spin coater, centrifuge, column chromatography.

- ➢ *Instrument fabrication:*
  - Hands on experience in fabricating a nano-second transient absorption and time resolved emission spectrometer with an ICCD camera and a 5 ns Nd:YAG laser.
  - Explicit experience in designing a TCSPC instrument with a Ti-Saphire laser with picosecond time resolution.
  - Direct experience on making a STED instrument with 40 nm spatial and 200 ps time resolutions and combining STED microscopy with fluorescence correlation spectroscopy.
  - Hands-on experience on making a fluorescence up-conversion instrument with a regenerative amplifier and OPA.
- ➢ *Computer* Languages *Known:* FORTRAN 77, GAUSSIAN-03.
- ➢ *Technical softwares used*: Matlab, Origin, ImageJ, Molden, Molkel, Gauss view, ChemDraw.

.

Seminars

- ➢ Computational studies on molecular magnetism. Department of chemistry, IIT Bombay, April 29, 2010.
- ➢ Tryptophan and ATTO 590: Mutual Fluorescence Quenching and Exciplex Formation. Department of Chemistry, Iowa State University, September 3, 2014.
- ➢ Spectroscopy-Driven Development of Defect-Free Perovskites for Highly Efficient Photovotaics. Gordon Research Conference on Photochemistry, Easton, MA, July 19, 2015.

Publications

1. Kambakam, S.; **Bhattacharjee, U.**; Petrich, J. W.; Rodermel, S., Etiorespiration, a Novel Process Dependent on PTOX, NDH and PGR5, that Poises the Etioplast for Chloroplast Biogenesis. *Submitted to Molecular Plant* **2015**.

2. **Bhattacharjee, U.**; Men, L.; Alvarado, S.; Vela, J.; Petrich, J. W., Quenching of the Fluorescence of Atto Dyes by Au-Cds Nanoparticles. *Manuscript under preperation*.

3. **Bhattacharjee, U.**; Men, L.; Freppon, D.; Zhu, F.; Smith, E. A.; Petrich, J. W.; Vela, J., Mixed Halide Organolead Perovskites: The Role of Excess Precursor on Photoluminescence Stability. *Manuscript under preperation*.

4. **Bhattacharjee, U.**; Dudas, S.; Rasmussen, M. A.; Casey, T. A.; Petrich, J. W., Fluorescence Spectroscopy of the Retina for the Screening of Bovine Spongiform Encephalopathy. *Accepted in Journal of Agricultural and Food Chemistry* **2015**.

5. **Bhattacharjee, U.**; Santra, K.; Bobbit, J. M.; Elshobaki, M.; Chaudhary, S.; Smith, E. A.; Petrich, J. W., Characterizing Electric Field Oriented P3ht Thin Films Using Polarized-Light Spectroscopies. *Submitted to The Journal of Physical Chemistry B* **2015**.

6. Zhu, F.; Men, L.; Guo, Y.; Zhu, Q.; **Bhattacharjee, U.**; Goodwin, P. M.; Petrich, J. W.; Smith, E. A.; Vela, J., Shape Evolution and Single Particle Luminescence of Organometal Halide Perovskite Nanocrystals. *ACS Nano* **2015,** *9* (3), 2948-2959.

7. **Bhattacharjee, U.**; Beck, C.; Winter, A.; Wells, C.; Petrich, J. W., Tryptophan and ATTO 590: Mutual Fluorescence Quenching and Exciplex Formation. *The Journal of Physical Chemistry B* **2014,** *118* (29), 8471-8477.

8. Syed, A.; Lesoine, M. D.; **Bhattacharjee, U.**; Petrich, J. W.; Smith, E. A., The Number of Accumulated Photons and the Quality of Stimulated Emission Depletion Lifetime Images. *Photochemistry and Photobiology* **2014,** *90* (4), 767–772.

9. Lesoine, M. D.; **Bhattacharjee, U.**; Guo, Y.; Vela, J.; Petrich, J. W.; Smith, E. A., Subdiffraction, Luminescence-Depletion Imaging of Isolated, Giant, CdSe/CdS Nanocrystal Quantum Dots. *The Journal of Physical Chemistry C* **2013,** *117* (7), 3662-3667.

10. Hanway, P. J.; Xue, J.; **Bhattacharjee, U.**; Milot, M. J.; Ruixue, Z.; Phillips, D. L.; Winter, A. H., Direct Detection and Reactivity of the Short-Lived Phenyloxenium Ion. *Journal of the American Chemical Society* **2013,** *135* (24), 9078-9082.

11. Sainz, M.; Pérez-Rontomé, C.; Ramos, J.; Mulet, J. M.; James, E. K.; **Bhattacharjee, U.**; Petrich, J. W.; Becana, M., Plant hemoglobins may be maintained in functional form by reduced flavins in the nuclei, and confer differential tolerance to nitro-oxidative stress. *The Plant Journal* **2013,** *76* (5), 875–887.

12. **Bhattacharjee, U.**; Panda, A.; Latif, I. A.; Datta, S. N., Unusually Large Coupling Constants in Diradicals Obtained from Excitation of Mixed Radical Centers: A Theoretical Study on Potential Photomagnets. *The Journal of Physical Chemistry A* **2010,** *114* (24), 6701-6704.

13. Latif, I. A.; Singh, V. P.; **Bhattacharjee, U.**; Panda, A.; Datta, S. N., Very Strongly Ferromagnetically Coupled Diradicals from Mixed Radical Centers. II. Nitronyl Nitroxide Coupled to Tetrathiafulvalene via Spacers. *The Journal of Physical Chemistry A* **2010,** *114* (24), 6648-6656.